UNIVERSIDADE FEDERAL DE MINAS GERAIS

PROGRAMA DE PÓS-GRADUAÇÃO EM ENGENHARIA
METALÚRGICA, MATERIAIS E DE MINAS

DISSERTAÇÃO DE MESTRADO

“MATHEMATICAL MODELING OF INCLUSION REMOVAL FROM STEEL DURING LADLE TEEMING THROUGH INERT GAS INJECTION”

Autor: Alexandre Dolabella Resende

Orientador: Prof. Roberto Parreiras Tavares

Março de 2019

Alexandre Dolabella Resende

MATHEMATICAL MODELING OF INCLUSION REMOVAL FROM STEEL DURING LADLE TEEMING THROUGH INERT GAS INJECTION

Dissertação apresentada ao Programa de Pós-Graduação em Engenharia Metalúrgica, Materiais e de Minas da Escola de Engenharia da Universidade Federal de Minas Gerais, como requisito parcial para obtenção do Grau de Mestre em Engenharia Metalúrgica, Materiais e de Minas.

Área de Concentração: Metalurgia Extrativa

Orientador: Prof. Roberto Parreiras Tavares

Belo Horizonte

Universidade Federal de Minas Gerais

Escola de Engenharia

2019

R433m

Resende, Alexandre Dolabella.
Mathematical modeling of inclusion removal from steel during ladle teeming during inert gas injection [manuscrito] / Alexandre Dolabella Resende. – 2019.
xvii, 167 f., enc.: il.

Orientador: Roberto Parreiras Tavares.

Dissertação (mestrado) - Universidade Federal de Minas Gerais, Escola de Engenharia.

Bibliografia: f. 163-167.

1. Engenharia metalúrgica - Teses. 2. Metalurgia extrativa - Teses. 3. Aço - Inclusões - Teses. 4. Modelos matemáticos - Teses. I. Tavares, Roberto Parreiras. II. Universidade Federal de Minas Gerais. Escola de Engenharia. III. Título.

CDU: 669(043)

Aos meus pais e à minha madrinha pelo apoio à minha educação e à Mariana pela paciência e pelo carinho.

O autor agradece a todos aqueles que, direta ou indiretamente, colaboraram na preparação deste trabalho e, em particular:

Ao Professor Roberto Parreiras Tavares pela orientação, pelo empenho na revisão dos trabalhos e pelo aprendizado proporcionado ao longo desses anos.

Aos Professores Leandro Rocha Lemos e Aline Lima da Silva, por comporem a banca avaliadora, dedicando seu tempo a fim de contribuir com o trabalho.

Aos colegas e aos profissionais do PPGEM pelas participações nos trabalhos anteriores desenvolvidos, que serviram de ponto de partida para esse trabalho.

À RHI Magnesita, em especial aos gestores Rubens Freire e Afonso Portugal, pelo incentivo ao meu mestrado e pelo apoio em seu desenvolvimento.

SUMMARY

2. OBJETIVO GERAL

6. CONCLUSÕES

7. SUGESTÕES PARA TRABALHOS FUTUROS

LIST OF FIGURES

LIST OF TABLES

LIST OF SYMBOLS

Bo = Bond Number

b_α = Radial Coordinate of the Boundary of the Bubble Dispersion Region

C_d = Drag Coefficient

$C_{\varepsilon 1}$ = Calibration constant for the ε transport equation

$C_{\varepsilon 2}$ = Calibration constant for the ε transport equation

C_μ = Eddy viscosity constant for the standard k-ε model

d = Inclusion diameter

e_n = Coefficient of restitution in the normal direction

e_t = Coefficient of restitution in the tangential direction

Eu = Euler Number

$\mathrm{F_i}$ = Force in the i-direction

F_{Drag} = Drag Force

F_{Lift} = Lift Force

F_S = Surface Tension Force

F_{VM} = Virtual Mass Force

F_{PG} = Pressure Gradient Force

Fr = Froude Number

$\mathrm{Fr_m}$ = Modified Froude Number

g = Acceleration due to Gravity

k = Turbulent kinetic energy

L = Flow Characteristic Length

L_t = Turbulent length scale

$\overline{L_g}$ = Mean free path of the gas molecules

M = Mach Number

Mo = Morton Number

P_k = Turbulence production due to mean velocity gradients and buoyancy.

P_ω = Production of turbulent eddy frequency.

r_{cl} = Radial position of eccentric plug centerline

Re = Reynolds Number

$\mathrm{R}_{\mathrm{inc,mod}}$ = Inclusion Radius in the Physical Model

$\mathrm{R}_{\mathrm{inc,real}}$ = Inclusion Radius in the Real Full Scale Model

u_i = Local Flow Velocity in the i-direction

$\bar{u}_i$ = Time averaged velocity in the i-direction

$\overline{u'}_i$ = Fluctuating velocity component after time averaging in the i-direction

u_p = Particle Velocity

$\overrightarrow{u_q}$ = Velocity vector for phase q,

V = Flow Characteristic Velocity

$\overline{v_g}$ = Mean velocity of gas molecules

V_p = Average Plume Rising Velocity

V_s = Sound Velocity

V_t = Turbulent velocity scale

v_t = Inclusion Terminal Rising Velocity

x_i = i-coordinate

x_p = Particle Position

We = Weber Number

α = Volume Fraction of a given phase, often the gas.

α_{cl} = Gas Volume Fraction at the Ladle Centerline

α_{ecc} = Gas Volume Fraction for Eccentrically Located Plug

α_q = Volume fraction of phase q

β = Calibration constant for the k-ω model.

β' = Calibration constant for the k-ω model.

Δp = Pressure Difference

ε = Dissipation rate of the Turbulent kinetic energy

ζ = Normally distributed random number

λ = Geometric Scale Factor of the Reduced Scale Model

μ = Dynamic Viscosity of the Main Fluid

μ_{eff} = Effective Viscosity

μ_t = Eddy Viscosity

ν = Kinematic Viscosity of the Main Fluid

ρ = Density of the Main Fluid

$\rho_{\mathrm{inc,real}}$ = Density of the Inclusions in the Real Full Scale Equipment

$\rho_{\mathrm{inc,mod}}$ = Density of the Inclusion Particles used in the Physical Model

ρ_g = Gas Density

ρ_p = Particle Density

ρ_q = Density of the phase q

ρ_s = Density of Solid Inclusion

ρ_{steel} = Density of the Molten Steel

ρ_{water} = Density of Water

σ = Surface Tension

σ_k = Turbulent Prandtl number for the turbulent kinetic energy

σ_ε = Turbulent Prandtl number for the turbulence dissipation rate

σ_ω = Turbulent Prandtl number for the turbulent eddy frequency

${\tau^t}_{ij}$ = Reynolds Stress in the i-j plane

τ_r = Particle Relaxation Time

$\overline{\tau_q}$ = Stress-strain tensor for phase q

ω = Turbulent eddy frequency

RESUMO

Produtos siderúrgicos estão presentes em diversas aplicações no mundo contemporâneo, das quais muitas exigem controle do teor de impurezas. Com o progresso tecnológico e a competição globalizada, tais requisitos vêm se tornando cada vez mais rigorosos. Nesse contexto, a melhoria contínua dos processos se faz necessária. No entanto, as altas temperaturas e os riscos operacionais dificultam o estudo do processo diretamente no equipamento industrial. Dessa forma, modelos experimentais e matemáticos são frequentemente utilizados com o fim de analisar fenômenos físicos envolvidos na produção do aço e prever a eficácia de diferentes alternativas na qualidade do produto final. Nesse trabalho, um modelo matemático foi desenvolvido com o objetivo de estudar a remoção de inclusões não-metálicas do aço durante a drenagem da panela. Diferentes abordagens de modelagem matemática foram testadas a fim de se obter o modelo que melhor representasse o fenômeno a ser estudado, o que foi verificado através da comparação com resultados experimentais obtidos em um modelo físico de uma panela industrial. Verificou-se que o modelo matemático no qual as movimentações da superfície livre foram representadas apresentou resultados mais compatíveis com os experimentos. Além disso, observou-se que os resultados de remoção de inclusões foram bastante sensíveis ao critério de remoção utilizado nos modelos, de forma que um critério customizado foi adotado. Através do modelo desenvolvido, foram estudados os efeitos da vazão de gás e do tempo de tratamento de rinsagem. Observou-se que, nas faixas de valores estudados, ambos mostraram correlação positiva com a remoção de inclusões do aço na panela, com maior relevância para o tempo de rinsagem.

Palavras-chave:

Fluidodinâmica Computacional; Metalurgia Secundária; Limpidez do Aço; Inclusões; Injeção de Gás Inerte

ABSTRACT

Steel products are present in various applications in the contemporary world, in which many of them require control of the amount of impurities. With technological advancement and globalized competition, such requirements are becoming stricter. In this context, continuous improvement of the processes is necessary. However, the high temperatures and operational risks make it difficult for studies to be performed directly on the industrial equipment. Therefore, experimental and mathematical models are frequently used with the goal of analyzing physical phenomena involved in steelmaking and to predict the performance of alternative proposals in the final product quality. In the present work, a mathematical model was developed with the objective of studying non-metallic inclusion removal from the molten steel during ladle teeming. Different mathematical modeling approaches have been tested in order to obtain the model which would better represent the phenomenon to be studied, what has been verified through the comparison with experimental results obtained in a physical model of an industrial ladle. It has been verified that the mathematical model in which the free surface motion was represented has shown results more consistent with the experiments. Moreover, it has been observed that the inclusion removal results were very sensitive to the inclusion removal criterion adopted, so that a custom criterion has been adopted. Through the developed model, the effects of the gas flow rate and time duration of the purging treatment have been studied. It has been observed that, in the ranges of values studied, both parameters have shown a positive correlation with the inclusion removal from steel in the ladle, with greater relevance for the time duration of the purging treatment.

Keywords:

Computational Fluid Dynamics; Secondary Metallurgy; Steel Cleanliness; Inclusions; Inert Gas Injection

1. INTRODUÇÃO

Produtos siderúrgicos são utilizados em várias aplicações, desde a indústria automotiva até bens de capital e construção civil. A previsão para a demanda de produtos siderúrgicos acabados em 2017 foi de 1.548,5 milhões de toneladas e para 2018 seu crescimento era esperado que fosse igual a 0,9%, alcançando 1548,5 milhões de toneladas[1]. Dessa forma, a indústria siderúrgica cumpre uma função vital no mundo contemporâneo e a melhoria contínua dos seus processos é de grande interesse para a sociedade.

Uma parcela significativa da demanda por produtos siderúrgicos requer que a quantidade de impurezas seja limitada a somente poucos ppm, como, por exemplo, chapas finas utilizadas na fabricação de automóveis e eletrodomésticos ou placas pesadas utilizadas em plataformas de extração de petróleo. Consequentemente, os siderurgistas precisam assegurar a qualidade de seus produtos caso desejem fornecer para esses mercados. Por outro lado, a indústria siderúrgica é constantemente pressionada a reduzir seus custos. A globalização e a competição mundial forçam os siderurgistas a seguir reduzindo seus custos de produção de forma a permanecer competitivos. É um grande desafio conciliar a produtos de alta qualidade e baixos custos de produção. Para fazer isso, os siderurgistas precisam maximizar a eficiência de seus processos produtivos, evitando a ocorrência de defeitos como trincas ou inclusões e minimizando os índices de sucateamento.

Uma etapa da cadeia de produção do aço que tem um impacto direto na qualidade e nos custos do processo siderúrgico é o refino secundário. Nessa etapa, o aço líquido passa por diversos tratamentos na panela. Injeção de gás inerte pelo fundo da panela é geralmente adotada de forma a homogeneizar a composição e a temperatura do banho através da agitação provocada pelo movimento ascendente do gás. O padrão de fluxo gerado pela pluma de gás ascendente também contribui para a flotação de inclusões não-metálicas, que são absorvidas pela camada de escória sobrenadante. Esse fenômeno contribui para a produção de aços limpos.

Embora a injeção de gás inerte seja uma prática muito comum, ainda há espaço para melhorias na compreensão das correlações entre os parâmetros do processo e os resultados de remoção de inclusões. Muitas plantas siderúrgicas operam de forma empírica, ajustando o processo de acordo com os resultados coletados a partir de amostras do produto final. Existem vários problemas com essa abordagem, incluindo:

dificuldade em rastrear com precisão a origem do defeito, falta de compreensão da física envolvida na formação de defeitos e grande número de variáveis de processo que poderiam estar potencialmente envolvidas no defeito, entre muitas outras.

Uma alternativa à abordagem empírica é o uso de modelos matemáticos para avaliar o efeito dos parâmetros do processo nos indicadores desejados de qualidade do produto, como a quantidade e a distribuição de tamanho das inclusões no banho. Através destes, é possível estudar fenômenos específicos, como o efeito da injeção de gás inerte na remoção da inclusão na panela, e entender como variáveis de processo como vazão de gás, projeto do plugue e tempo de rinsagem afetam os resultados de interesse, como, por exemplo, remoção de inclusões.

No presente trabalho, um modelo matemático foi desenvolvido para estudar a remoção de inclusões da panela durante a fase de drenagem, logo após a injeção de gás inerte. Os resultados do modelo devem fornecer uma compreensão sobre como os parâmetros de rinsagem podem ser otimizados para fornecer uma melhor flotação de inclusões. A validação do modelo numérico foi realizada através dos resultados experimentais obtidos a partir do trabalho de Silva[2].

O trabalho experimental de Silva[2] teve o diferencial de usar uma sonda APS (Aqueous Particle Sensor) que detecta e conta as partículas que passam por ela, e também fornece sua distribuição de tamanho. Este é um resultado muito importante para entender quais tamanhos das inclusões são mais bem removidos através do processo de rinsagem. No entanto, os modelos experimentais em geral demoram muito para serem construídos e costumam ser muito caros. Eles também têm a limitação de escala e propriedades do material. Embora seja quase impossível, para a maioria dos pesquisadores, construir um modelo 1: 1 de uma panela industrial, também é impossível respeitar totalmente todos os critérios de similaridade relevantes de fluxos multifásicos complexos, como o que está sendo estudado, com modelos de escala reduzida.

A inovação proposta por este estudo foi a incorporação das capacidades de simulações numéricas aos resultados experimentais obtidos por Silva[2]. Por meio do modelo matemático, foi possível ampliar o conhecimento obtido anteriormente, pois o modelo computacional permite uma visualização mais fácil dos resultados de interesse, como a distribuição da velocidade e da turbulência no domínio. Isso fornece uma compreensão mais profunda da eficácia de uma determinada configuração com relação à remoção de inclusões. Além disso, o desenvolvimento de um modelo numérico facilita o estudo de diferentes configurações de panelas não estudadas anteriormente, já que é mais rápido e mais barato alterar a geometria CAD (Computer Aided Design) no modelo do que construir outro protótipo. Como o modelo matemático desenvolvido neste trabalho não necessita da composição química do aço como dado de entrada, o modelo é aplicável a qualquer tipo de aço cuja rota de produção inclua a etapa de metalurgia secundária.

1. INTRODUCTION

Steel products are used in a wide range of applications, from the automotive industry to capital goods and construction. The forecast for the global demand of finished steel products in 2017 was 1535.2 million tonnes and for 2018 it was expected to grow 0.9%, reaching 1,548.5 million tonnes[1]. Therefore, the steelmaking industry plays a vital role in the contemporary world and continuous improvement of its processes are of great interest for the society.

A significant fraction of the demand for steel products requires the amount of impurities in it to be limited to only a few ppm, like, for example, thin sheets used in the manufacturing of automobiles and home appliances or heavy plates used in offshore platforms for oil extraction. Consequently, steelmakers need to assure the quality of their products if they wish to supply for such markets. On the other side, the steel industry is constantly pressured to reduce its costs. Globalization and the worldwide competition force the steelmakers to keep reducing their production costs in order to remain competitive. It is a great challenge to accomplish both high product quality and low production costs. In order to do that, the steelmakers must maximize their manufacturing processes efficiencies, avoiding the occurrence of defects such as cracks or inclusions and minimizing the scrapping index.

One step of the steel production chain, which has a direct impact on the quality and costs of the steelmaking process, is the secondary steelmaking. At this stage, the molten steel goes through various treatments in the ladle. Inert gas purging at the ladle bottom is usually adopted in order to homogenize the bath composition and temperature through stirring caused by the ascending gas trajectory. The flow pattern generated by the upward gas plume also contributes to non-metallic inclusions flotation, which are absorbed by the upper slag layer. This phenomenon contributes to the production of cleaner steels.

Although inert gas purging is a very common practice, there is still room for improvement on the understanding of the correlations between the process parameters and the inclusion removal results. Many steelmaking shops operate on an empirical basis, adjusting the process according to the results collected from samples of the final product. There are several problems with this approach including: difficulty to accurately track the source of the defect, lack of comprehension of the physics involved in the defect formation and large number of process variables which could be potentially involved in the defect, among many others.

One alternative to the empirical approach is the use of mathematical models to assess the effect of the process parameters on the desired indicators of product quality, such as the amount and size distribution of inclusions on the bath. Through these, it is possible to study specific phenomenon, such as the effect of inert gas purging on inclusion removal in the ladle, and to understand how process variables such as gas flow rate, plug design and purging time affect the results of interest, like, for example, inclusion removal.

In the present work, a mathematical model was developed to study the inclusion removal on the ladle during the teeming stage, right after inert gas purging. The model results should provide understanding about how the purging parameters could be optimized in order to provide better inclusion flotation. Validation of the numerical model was performed through the experimental results obtained from the work of Silva[2].

The experimental work from Silva[2] had the differential of using an APS (Aqueous Particle Sensor) probe which detects and counts the particles which pass through it, and also provides their size distribution. This is a very important result for understanding which sizes of the inclusions are better removed through the purging process. However, experimental models in general take a long time to build and are often very expensive. They also have the limitation of scale and material properties. While it is almost impossible for most researchers to build a 1:1 model of an industrial ladle, it is also impossible to fully respect all relevant similarity criteria of complex multiphase flows, such as the one being studied, with reduced scale models.

The innovation proposed by this study was the incorporation of the capabilities of numerical simulations to the experimental results obtained by Silva[2]. Through the mathematical model, it was possible to expand the knowledge obtained previously, as the computational model allows for an easier visualization of results of interest, such as velocity and turbulence distribution in the domain. This provides a deeper understanding of the effectiveness of a given configuration with respect to inclusion removal. Moreover, the development of a numerical model makes it easier for studying different ladle configurations not previously studied, as it is faster and cheaper to change the CAD (Computer Aided Design) geometry in the model than it is to build another prototype. Since the mathematical model developed in this work does not need the steel chemical composition as an input, the model is applicable to any steel grade whose production route includes the secondary metallurgy step.

2. OBJETIVO GERAL

Estudar a remoção de inclusões durante a drenagem da panela, logo após a rinsagem com gás inerte, por meio de um modelo matemático, identificando a abordagem de modelagem matemática que melhor reproduza os resultados experimentais.

2.1. Objetivos Específicos

- Desenvolver um modelo matemático para o cálculo do fluxo e do comportamento das inclusões durante a drenagem da panela;
- Validar o modelo matemático com os resultados experimentais de Silva[2];
- Comparar diferentes abordagens de modelagem numérica em termos de concordância com os resultados experimentais e eficiência computacional;
- Avaliar os resultados que não são facilmente obtidos a partir do modelo experimental, como a energia cinética turbulenta e os contornos de velocidade, e correlacionar esses resultados com a eficiência de remoção da inclusão;
- Analisar os efeitos de diferentes parâmetros do processo na remoção da inclusão, como a vazão de gás e a duração do tratamento de rinsagem.

2. GENERAL OBJECTIVE

To study inclusion removal during ladle teeming, right after inert gas purging, by means of a mathematical model, identifying the mathematical modeling approach that better reproduces the experimental results.

2.1. Specific Objectives

- To develop a mathematical model for fluid flow and inclusion behavior during ladle teeming;
- To validate the mathematical model with the experimental results from Silva[2];
- To compare different numerical modeling approaches in terms of their agreement to the experimental results and computational efficiency;
- To evaluate results which are not easily obtainable from the experimental model such as turbulent kinetic energy and velocity contours and to correlate these results to the inclusion removal efficiency;
- To analyze the effects of different process parameters on inclusion removal, such as the gas flow rate and time duration of the purging treatment.

3. LITERATURE REVIEW

3.1 Secondary Steelmaking

3.1.1 Introduction

In this section, an introduction about secondary steelmaking processes will be made, mostly based on the contents of a book by Ghosh[3].

The history of secondary steelmaking goes back to 1950 or so, when steel was made in furnaces such as open hearths, converters and electric furnaces. Back then, ladle treatment was limited to deoxidation, carburization by addition of coke or ferro-carbon alloy and some minor alloying. However, more stringent demands on steel quality and consistency in its properties require controls that are beyond the capability of steelmaking furnaces. This has led to the development of various kinds of treatments of liquid steel in ladles, besides deoxidation, which are known today as *secondary metallurgy*.

The growth of secondary steelmaking is associated with that of the continuous casting process. This route has become the dominant process to produce steel, against ingot casting which was used mostly up to the 1960s. As the tolerance levels of interstitial impurities and inclusions are lower in continuous casting compared to ingot casting, secondary refining processes grew in importance.

Harmful impurities in steel are sulphur, phosphorus, oxygen, hydrogen and nitrogen. The main effects of these impurities in steel are loss of ductility, reduction in impact strength and corrosion resistance. Oxygen and sulphur are also constituents of nonmetallic particles in steel, which are known as *inclusions*. These particles are very harmful to the steel properties and should be removed as much as possible. Secondary steelmaking processes include treatments that aim to reducing the amount of impurities in the molten steel such as desulfurization, decarburization, degassing, and also heating, alloying, homogenization and inclusion removal and modification.

The requirements of steel quality are becoming more and more stringent over the years, which means fewer impurities, lower inclusion content, less variation from cast to cast and better surface quality and homogeneity. Such demands, combined with the constant need for cost reduction, environmental pollution control and relatively stagnant world steel market, pose a huge challenge for steelmakers. In this context, it is critical to understand the underlying phenomena affecting the efficiency of the secondary steelmaking and to take action in order to improve them. Of particular interest in this study is the relationship between the stirring practice and its effectiveness to remove inclusions. Therefore, these aspects will be covered in more detail in the next sections.

3.1.2 Deoxidation

Among the many treatments applied to the molten steel in secondary steelmaking, the deoxidation is particularly relevant for this work, as one source of nonmetallic inclusions is the reaction product of this process. Therefore, a review of this topic will be made in this section.

According to Holappa[4], at the beginning of the secondary steelmaking stage, the molten steel has a significant amount of oxygen, typically in the range of 200-800 ppm. These values are far below the solubility of oxygen in liquid iron which is about 2300 ppm. However, when steel solidifies, its solubility of oxygen drops to 30 ppm or less. The excess oxygen is transferred to the residual melt during solidification. As its concentration and activity increases, it starts to react with carbon forming CO gas, which causes a foamy structure in solidified steel. In the great majority of steel production, such a structure is unacceptable; consequently, the free oxygen must be brought to very low levels in liquid steel. This is usually accomplished by the addition elements with great affinity for oxygen, such as aluminum, silicon and manganese.

Deoxidation reactions may happen due to addition of one or more deoxidizers. When only one deoxidizer is considered, the reaction is known as *simple deoxidation*. On the other hand, when multiple deoxidizers are used simultaneously, the deoxidation is known as *compl*ex. A simple deoxidation reaction may be represented as shown in Eq.3.1:[3]

$$x[M] + y[O] = (M_X O_Y) \tag{3.1}$$

Where M is the deoxidizer, and M_xO_Y is the deoxidation product. The deoxidation products are oxides such as Al_2O_3 and SiO_2, which precipitate as nonmetallic inclusions in the molten steel. These should be removed from the molten steel before it solidifies, if a clean steel is desired.

According to Ghosh[3], the formation of the deoxidation products as a new phase occur by processes of *nucleation and growth*. *Nucleation* refers to a formation of a small embryo of a new phase that is capable of growth. Such embryo consists of a small number of molecules and has a dimension in the order of 10 Å or so. Nucleation can happen through two different mechanisms:

1. *Homogeneous* nucleation, which occurs within the matrix;
2. *Heterogeneous* nucleation, which occurs with the aid of a substrate, such as already existing inclusions or refractory walls.

The nucleation rate was found to be proportional to the supersaturation ratio of the reactants, in this case, dissolved oxygen and the deoxidizer. Therefore, just after the addition of the deoxidizer, rapid nucleation and decrease of dissolved oxygen is possible, as the supersaturation is maximum at this moment. However, as a result of the reaction, the supersaturation of the melt comes down drastically, eventually ceasing nucleation.[3] The oxides resulting from the deoxidation reactions must be removed from the bath in order to actually lower the total oxygen content of the steel, and, therefore, these nuclei must grow into bigger inclusions in order to acquire a reasonable floating velocity.

There are several mechanisms by which the growth of nuclei to inclusions take place, including: diffusion, Ostwald ripening and collision between particles, leading to coalescence or agglomeration of particles. Diffusion happens due to the concentration gradient between the bulk and the surface of the nuclei, bringing reacting atoms to the surface of the nuclei. Ostwald ripening is a growth mechanism in which larger inclusions grow at the expense of smaller ones due to the larger surface energy of many small particles compared to less bigger particles. Finally, collision between particles can happen through the mechanisms of Brownian collisions, Stokes collisions and turbulent collisions. The first two are important in submicron scale, while turbulent collisions are decisive for micron scale inclusions.[4] Zhang and Pluschkell[5] studied the nucleation and growth mechanisms of inclusions and found that when their radius is smaller than 1 µm, particle growth is dominated by diffusion and Brownian collisions. Growth by Brownian collisions was found to be not directional and independent of fluid flow due to the irregular thermal motion typical of these collisions. Such behavior would cause particles to assume an approximately spherical shape. On the other side, for inclusions bigger than 2 µm, turbulent collisions would be the dominant mechanism. Differently from the Brownian collisions, turbulent collisions would be fluid flow dependent and directional, which would cause the particles to grow in irregular shapes.

As inclusions grow, they are also transported to the surrounding interfaces where they can be adhered and removed. In large industrial ladles, this is the slowest stage in deoxidation. In gas stirred ladles, most inclusions leave the steel through the top slag, with their floating due to buoyancy being defined by Stokes Law, as shown in Eq.3.2[4]:

$$v_t = \frac{gd^2(\rho_s - \rho)}{18\mu} \tag{3.2}$$

Where v_t is the inclusion terminal velocity, g is the acceleration due to gravity, d is the inclusion diameter, ρ_s is the density of the solid particle, ρ_f is the fluid density and μ is the viscosity of the steel.

As the terminal velocity depends on the particle diameter, it can be concluded that inclusions of various sizes would have different rising velocities. The smallest inclusions would have a very long transport time to the slag under the effects of buoyancy forces only. In this context, argon purging through the bottom of the ladle can be an effective way to enhance inclusion removal, through the following mechanisms:

3. Attachment of inclusions to floating gas bubbles. As the bubbles have a much lower density and higher diameter than the inclusions, their terminal velocities are considerably higher. The inclusions, especially the smaller ones, which are captured by the rising bubbles, are carried much faster to the slag surface.

4. The injected gas increases the turbulence of the fluid flow in the ladle, which promotes inclusion growth by turbulent collisions, thereby increasing their terminal velocity.

5. The gas plume promotes a recirculating flow pattern in the ladle, which drags inclusions to the top surface.

In the next section, a review about fundamental aspects of the fluid flow in steel ladles during argon purging will be made.

3.1.3 Fluid Flow in the Ladle during Argon Purging

Ladle stirring through inert gas purging was developed with the primary objective of homogenization of temperature and composition of the melt. It was found that it also offered the additional advantage of faster floating out of inclusions.[3]

For moderate gas bubbling rates, less than 0.6 Nm^3/min, gas purging is usually performed through porous refractory plugs, usually mounted at the bottom of the ladle. An illustration of a porous plug assembly in the ladle is shown in Figure 3.1.[6]

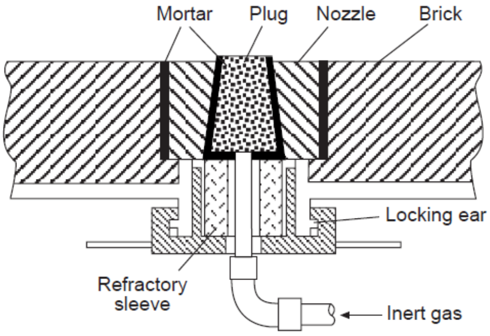

Figure 3.1: Schematic of a porous refractory plug mounted in the ladle bottom.[6]

Homogenization of bath temperature and composition by gas purging is primarily due to the effect of dissipation of buoyant energy of the injected gas. Figure 3.2 shows a sketch of the fluid flow in the ladle during gas purging[3]. The buoyancy of the injected gas causes an upward flow above the purging plug, which expands in diameter as it flows up due to diffusion and bubble expansion. This region, known as the *plume,* contains both molten steel and gas bubbles. It promotes recirculation of the molten steel, as the molten steel that flows upward above the plug flows downward close to the vessel walls. Such flow pattern is turbulent and drives mixing in the ladle.

Several researchers have performed fundamental studies in order to establish empirical correlations to characterize the plume in gas stirred melts. Ghosh[3] makes a review of many of these studies. Some of these will be presented in the next paragraphs.

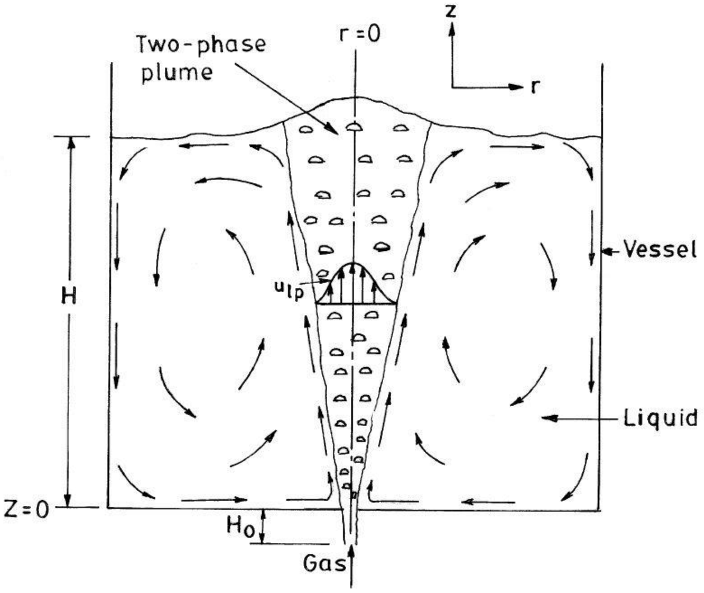

Figure 3.2: Fluid flow sketch during ladle stirring.[3]

Iguchi et al.[7] measured the bubble frequency, the gas holdup *(α)* and the mean and fluctuating velocity components in an air-water vertical bubbling jet in a cylindrical vessel. The gas holdup was defined as the total passing time of bubbles through a probe tip during an interval of 1 second and gave a measurement of the gas fraction at a given location. Its value at the vessel centerline *(α_{cl})* was adopted as a reference. Based on the results, the plume was divided in 4 different regions with respect to the distance from the nozzle tip: *momentum, transition, buoyancy and surface*. More detailed investigations on the bubble behavior in the buoyancy region were performed in a subsequent study[8]. Figure 3.3 shows the location of each region where b_α represents the boundary of the bubble dispersion region.

The *momentum* region is located where the ratio of inertia to buoyancy forces is high and the flow is affected mainly by the momentum of the gas discharging from the nozzle. The gas fraction at the centerline would be above 10% and the shape of the plume in this region is independent of the vessel diameter and height. Turbulence generation is primarily caused by entrainment of the surrounding fluid, similarly to a turbulent free jet.[7] In the *transition* region, the plume diameter remains approximately unchanged, for reasons that are not very clear. The gas fraction at the centerline was found to be about 10% in this region.[7]

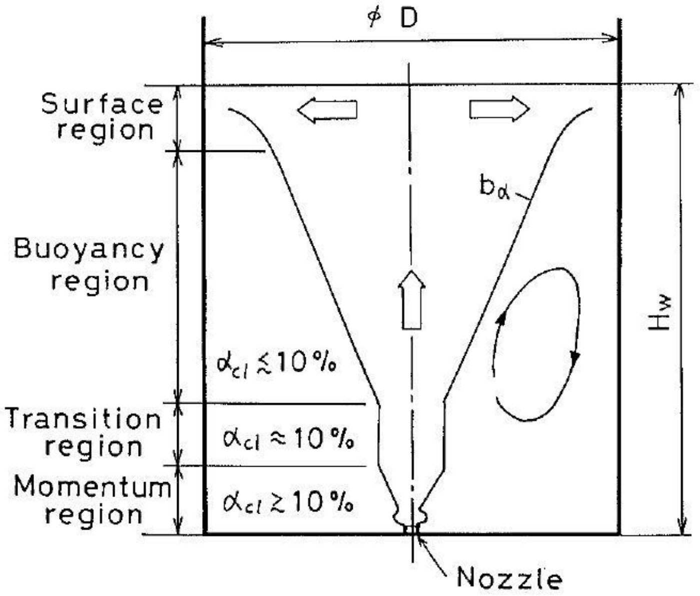

Figure 3.3: Classification of the plume in 4 different regions.[8]

The *buoyancy* region was defined as the region where α_{cl} is lower than 10% and the flow is governed mostly by buoyant effects. The gas holdup was found to follow a Gaussian distribution around the plume axis and its shape is dependent only on the injected gas flow rate. The mean bubble rising velocity and the mean flow velocity at the centerline were constant in the buoyancy region[8]. The turbulence profile also follows a Gaussian distribution in this region, which was attributable to mechanisms of turbulence generation due to the wake behind the bubbles as well as to the entrainment of the surrounding fluid.[7] Finally, the *surface* region was defined by a sudden broadening of the plume due to horizontal velocity components close to the top surface. It was reported that it was difficult to determine the limit between the buoyancy and the surface regions.[7]

Although the classification provided by Iguchi et al.[7,8] is useful to analyze the flow fundamentals in a bottom stirred ladle, it must be kept in mind that the density of the molten steel is much higher than that of the water. Therefore, in an industrial ladle the plume would likely behave almost entirely accordingly to the buoyant region, since the region where gas inertia effects is dominant is very small. Xie et al.[9] performed experimental studies of bubble behavior in a system in which the main fluid was a low melting point alloy denominated *Wood's Metal.* This alloy has a melting point of 70°C and therefore is liquid at the experiment temperature of 100°C. The results of gas fraction distribution confirmed the statement of earlier papers that it could indeed be represented by a Gaussian function and are shown as a function of distance to the nozzle tip in Figure 3.4[9]. Therefore, the local gas fraction could be written as a function of the radial position, as shown in Eq.3.3, for any given axial distance to the nozzle:

$$\alpha = \alpha_{cl} \exp(-r^2/b_\alpha{}^2) \tag{3.3}$$

Where α is the gas fraction at a given radial position, α_{cl} is the gas fraction at the centerline, *r* is the radial position and b_α is the boundary of the plume.

Experiments were also performed for plugs located eccentrically in the ladle bottom, which is a very common industrial configuration. Figure 3.5 shows the gas fraction profile for this situation.[9] It can be seen that, under such configuration, the plume deflects toward the closer wall of the vessel. The reason reported for such behavior is that the different velocities of the surrounding fluid causes a traction on the bubble plume on the side with higher velocities. The bubble plume, then, displaces to this direction.[9]

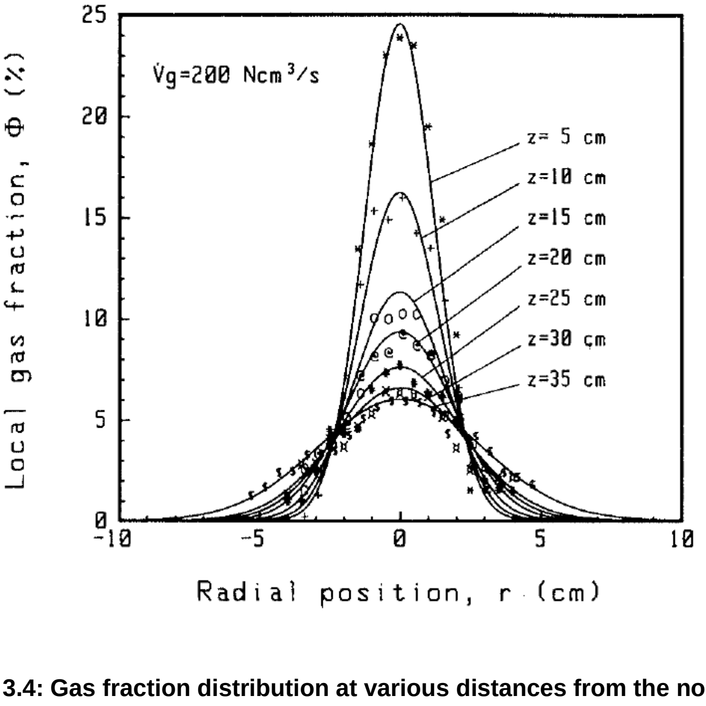

Figure 3.4: Gas fraction distribution at various distances from the nozzle.[9]

The gas fraction distribution for the eccentrically located plug was also found to obey a Gaussian function, modified to account for the displacement. Eq.3.4 shows the gas fraction distribution for the eccentrically located plug, where r_{cl} is the radial position of the plug centerline:

$$\alpha_{ecc} = \alpha_{cl}\exp(-(r - r_{cl})^2/{b_\alpha}^2) \tag{3.4}$$

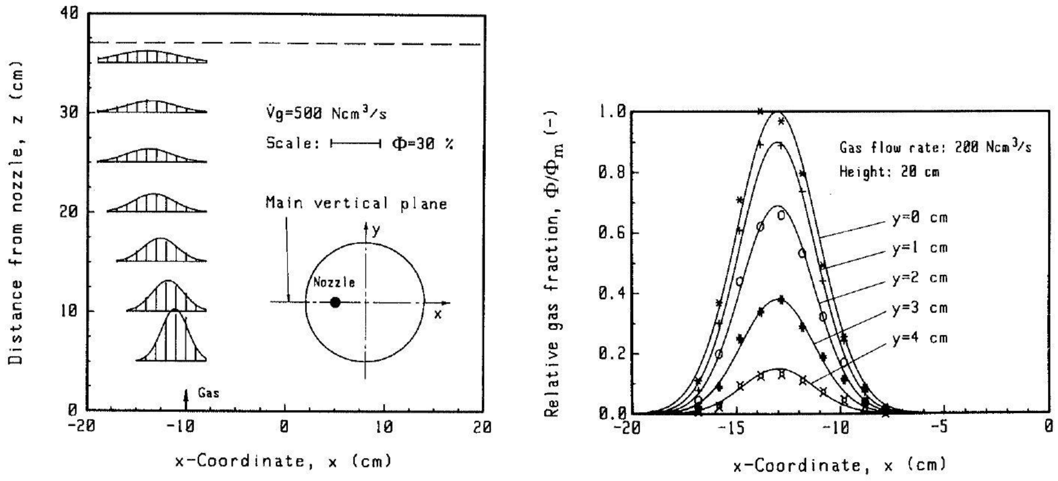

Figure 3.5: Gas fraction profile for eccentrically located nozzle.[9]

Regarding the rising velocity at the plume, the reported studies[7,8,9] agree that it also follows a Gaussian curve, similarly to the gas fraction. The average rising velocity was found to have negligible variation in the vertical direction, except in the close proximity to the nozzle. The liquid and bubble rising velocities obtained by Sheng and Irons[10] are shown in Figure 3.6. These results confirm the previous findings that the average velocity indeed does not show significant variations along the vertical direction.

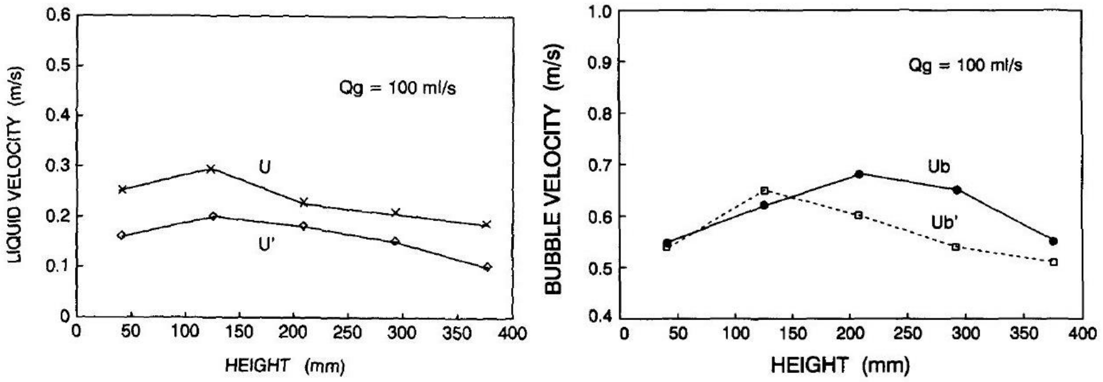

Figure 3.6: Liquid (left) and bubble(right) rising velocity in the plume.[10]

Ghosh[3] compares the behavior of the gas plume in the experiments to a free gas jet where the axial velocity decreases rapidly with the distance from the nozzle. It was pointed out that the difference lies in the fact that the rising bubbles impart momentum to the entrained liquid throughout the plume volume due to buoyancy force, while the momentum of a free jet derives solely from its momentum upon exiting the nozzle. Therefore, the buoyant plume may be visualized as a pump, making the liquid flow upward.

The region near the surface of the bath, also known as *spout*, was studied by Sahajwalla et al.[11]. It was found that the general behavior of the flow in this region was opposite to that in the plume, as the gas fraction distribution was found to be minimum at the axis and increasing in the radial direction, due to horizontal velocity components of the flow when it reaches the surface. The bubble velocities within the spout were also found to decrease as the vertical distance increased, opposed to what happens in the plume, where shortly beyond the nozzle, the rising velocities have an approximately constant value.[11]

The studies mentioned so far have considered gas purging through a nozzle at the ladle bottom. Anagbo and Brimacombe[12] performed similar investigations for gas injection through a porous plug, finding similar trends to those reported for injection through the nozzle. This agrees with what was stated by Mazumdar and Guthrie[13], who pointed out that under ladle refining conditions, hydrodynamic conditions at the orifice only marginally influence the physical characteristics of the plume. In this context, Ghosh[3] lists the forces that are expected to govern the nature of the flow:

1. Buoyant force of the rising plume;
2. Inertial force due to liquid motion;
3. Surface forces at the top of the bath;
4. Viscous shear forces at ladle wall.

Mazumdar et al.[14] performed water modeling experiments using an oil layer to account for the effects of the top slag phase in an industrial ladle. Three different configurations were analyzed in the experiments, one without the upper layer phase, another with oil as the upper phase, and other using a wooden block as a replacement for the oil to represent a rigid or pasty slag. The velocities were measured at several points of the domain and a total specific kinetic energy of motion was calculated. These values were expressed as a function of the input of potential energy from the gas flow for the three configurations. Figure 3.7 presents the results.

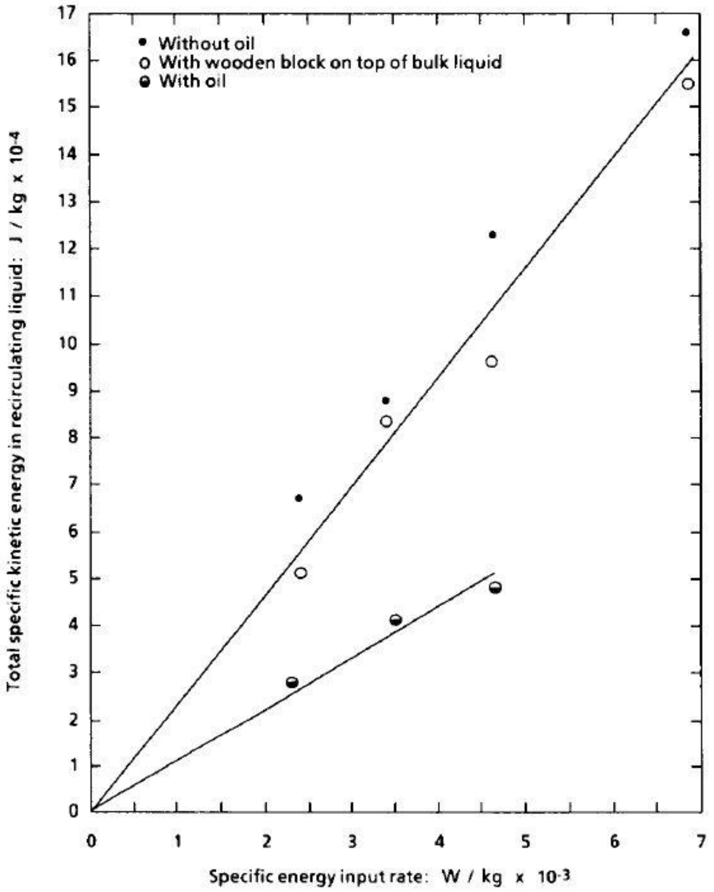

Figure 3.7: Total Kinetic Energy of Fluid Flow vs Input Energy from Gas Purging.[14]

It can be seen that the kinetic energy of the flow is much lower when the oil phase is present. This indicates that interactions between the bulk liquid and the upper layer promote severe energy dissipation. Moreover, there is virtually no difference between the fluid flow in the configuration without oil compared to that with the wooden block. It was concluded that the mechanism of energy dissipation in the presence of a deformable oil phase was not dominated by tangential friction at the interface.

Three modes of energy dissipation were then considered as hypotheses:

- the surface energy required for multiple droplet formation, as this phenomenon was observed at the interface;
- the potential energy required for keeping these droplets entrained in the lower phase liquid, as these were carried down by convection despite its natural tendency to float up;
- the potential energy required to maintain a deformed oil mass at the interface.

Of these, the experiments showed the third mode, deformation of the upper layer, to be the dominant energy dissipation mode. Such energy dissipation would be responsible for lowering the velocity of fluid recirculation and the level of turbulence in the bath, which could significantly affect numerous processing operations. Therefore, it was recommended that the slag-metal interface should not be modeled as a flat, rigid surface in order to account for these effects.[14]

Even for the configuration without the upper layer, it can be seen from Figure 3.7 that only a small fraction of the total energy input is actually converted into fluid flow kinetic energy, with the rest being lost. Ghosh[3] listed several mechanisms by which it could occur, such as: bubble slippage in the plume, formation of waves and droplets at the surface and friction at the vessel wall. Bubble slippage was regarded as the dominant one. Consequently, the plume should be regarded as *two-phase flow* rather than *quasi-single phase flow*[3], in order to account for this effect.

In this section, the fundamental aspects of fluid flows in gas stirred ladle systems were presented. The literature in this field is extensive and it is beyond the scope of this work to make a comprehensive evaluation of every publication regarding this subject. Nevertheless, what has been presented provides a solid base for understanding the underlying physics in complex mathematical modeling studies regarding inclusion transport in the ladle, which is the main objective of this work. In the next section, a review of the fundamentals of physical and mathematical modeling procedures will be made, followed by a review on recent publications regarding physical and mathematical modeling of gas stirred ladle systems focused on inclusion removal.

3.2 Fluid Dynamics Modeling Techniques

The nature of steelmaking operations makes studying its fluid dynamics phenomena a very difficult task. Factors such as the high operating temperatures, the opacity of liquid steel and the relatively large size of the industrial vessels pose a huge challenge for studying the process dynamics of steelmaking operations in the plant.[15]

As a consequence, such processes are commonly studied through models which try to represent relevant parts of what is happening in the process. Physical modeling of metallurgical processing operations dates back to the early 1960s, while mathematical models came later, around the mid-1970s.[15] The former consists of representing the system through lab experiments, usually using reduced-scale water models. The latter simulates the system in a computational environment using numerical methods to solve the fluid motion equations.

Mazumdar[15] points that these two modeling approaches should not be regarded as alternatives but must be pursued in a complementary fashion. Along with plant data, both are necessary ingredients of a successful investigation, as shown in Figure 3.8. In this section, a review about the fundamental aspects of these modeling techniques will be made.

3.2.1 Physical Modeling

Physical models of metallurgical processes usually consist of reduced-scale models using water as the main fluid. Although there are rare reports of 1:1 scale water models, the most common practice is to adopt reduced-scale models due to the large size of the industrial vessels and very high flow rates necessary to feed a real scale model.

However, for the model to give useful information, the experiments should provide data that could be scaled up to the real scale phenomena. The conditions that the lab model must follow in order to be similar to its real-world counterpart are denominated *similarity criteria*. Fox and McDonald[16], in their book, explain three types of similarity that should be achieved in a successful experiment: geometric, kinematic and dynamic.[16]

There most basic type of similarity is *geometric*. For a model to be geometric similar to the prototype, it must have the same shape and all its dimensions should be related to the prototype by a constant ratio.

Next, there is the *kinematic similarity*. Two flows are kinematically similar when velocities at equivalent locations have the same direction and their magnitude is related by a constant scale factor. Therefore, for kinematically similar flows, the streamlines are also related by the same constant scale factor. As the geometric boundaries limit the streamlines, kinematically similar flows must also be geometrically similar.

Finally, the strictest similarity criterion is the *dynamic*. It is fulfilled when two flows have all forces of the same type parallel and related by a constant scale factor in every equivalent location. In order to be dynamically similar, the flows must necessarily be geometrically and kinematically similar. To assess the necessary conditions for complete dynamical similarity, all relevant forces acting in the flow must be considered. Experimental conditions must be established in such a way that all important forces for a given problem are related by a constant scale factor between the model and the prototype.

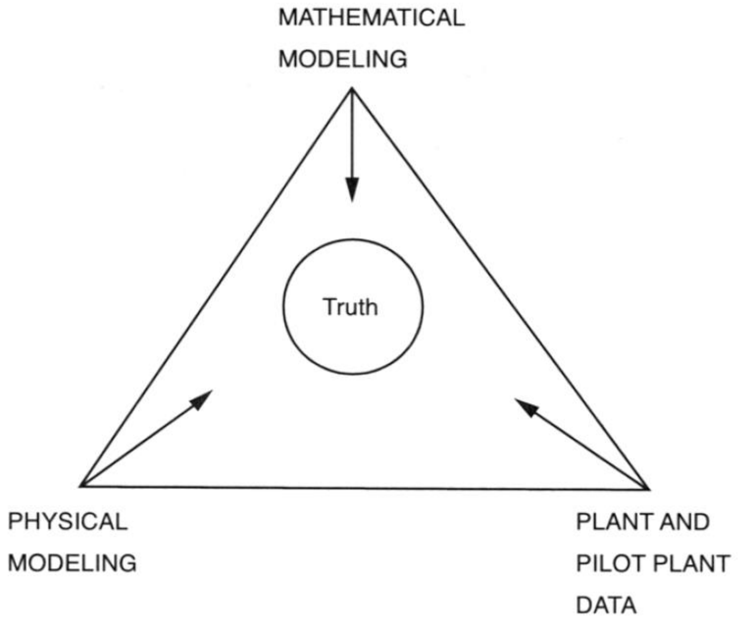

Figure 3.8: Three Essential Components of a successful investigation.[15]

Typical forces usually found in fluid dynamics problems are:[16]

- Inertial Forces;
- Viscous Forces;
- Pressure Forces;
- Gravitational Forces;
- Surface Tension Forces;
- Compressibility Forces.

Inertia forces are very important in the majority of flows. The ratio between inertial forces and each of the others listed above provides fundamental dimensionless numbers which can be used to assess dynamical similarity between geometrically similar flows. Which dimensionless parameters should be analyzed will depend of the governing forces for each particular problem.

The ratio between inertia and viscous forces gives the most famous dimensionless parameter in fluid mechanics: the *Reynolds number*. Its value is a criterion by which the flow regime can be determined, *laminar* or *turbulent,* and is expressed by Eq.3.5, where *V* is the flow characteristic velocity, *L* is the flow characteristic length and ν is the fluid kinematic viscosity:

$$Re = \frac{\rho V L}{\mu} = \frac{VL}{\nu} \tag{3.5}$$

The ratio between pressure forces and inertia forces gives the *Euler number,* which is commonly used in aerodynamic models and is given by Eq.3.6, where Δp is the pressure difference in the flow:

$$Eu = \frac{\Delta p}{\frac{1}{2}\rho V^2} \tag{3.6}$$

The *Froude number* is the ratio between inertia and gravitational forces and is represented by Eq.3.7:

$$Fr = \frac{V^2}{gL} \tag{3.7}$$

The *Weber number* is the ratio between inertia and surface tension forces, and is given by Eq.3.8, where σ is the surface tension at the main fluid interface with other fluids:

$$We = \frac{\rho V^2 L}{\sigma} \tag{3.8}$$

And finally, the *Mach number* is the ratio between inertia forces and compressibility forces, represented by Eq.3.9, where V_s is the sound velocity:

$$M = \frac{V}{V_s} \tag{3.9}$$

Ghosh[3] lists the dimensionless numbers most relevant for secondary steelmaking flows and their specific application:

- Reynolds Number: General fluid flow;
- Froude Number: Forced convection;
- Modified Froude Number: Gas-liquid systems;
- Weber Number: Gas bubble formation in liquid;
- Morton Number: Velocity of gas bubbles in liquid.

The *modified Froude Number* is also a ratio between inertia and gravitational forces, given by Eq.3.10, where ρ_g is the gas density:

$$Fr_m = \frac{\rho_g V^2}{(\rho - \rho_g) g L} \tag{3.10}$$

The *Morton number* is a ratio between the product of gravitational and viscous forces divided by the surface tension forces and is represented by Eq.3.11:

$$Mo = \frac{g\mu^4}{\rho\sigma^3} \tag{3.11}$$

Mazumdar[17] expressed the balance between the various forces acting on a fluid element in a multidimensional flow under steady-state conditions through the Navier-Stokes equation, shown in Eq.3.12:

$$\frac{\partial}{\partial x_j}(\rho u_j u_i) = -\frac{\partial P}{\partial x_j} + \frac{\partial}{\partial x_j}\left(\mu \frac{\partial u_i}{\partial x_j}\right) + F_i \tag{3.12}$$

The dimensionless equivalence of Eq.3.12 is typically represented as shown in Eq.3.13:

$$\frac{1}{Eu} = f(Re, Fr) \tag{3.13}$$

Equation 3.13 states that the ratio of pressure forces to the kinetic energy of the fluid in a flow system is a function of the inertial, viscous and body (buoyancy in this case) forces. Therefore, to achieve similar ratios of pressure force to kinetic energy in the model and in the full-scale system, the Reynolds and Froude number equivalence must be maintained between the two. However, it is not possible to attain both similarities simultaneously in reduced-scale water models. Consequently, the influence of one of these dimensionless groups must be ignored as an approximation. Assuming flows in typical gas stirred ladles to be dominated largely by inertial forces ($Re \gg Fr$), the dynamical similarity criterion between the model and the full-scale ladle can be obtained through the Froude number similarity.

For the calculation of the Froude number for a gas stirred ladle, characteristic values for velocity and length scale must be defined. The characteristic length is usually defined as the bath height. For the characteristic velocity, an initial assumption would be to consider the linear velocity of the gas at the injection point. However, it has been pointed out[3,13,17] that, as already discussed, the fluid dynamics condition close to the injection orifice only marginally influence the overall flow in the ladle, with buoyant effects being much more significant. Therefore, a similarity criterion considering the injection velocity as a parameter would not be very representative of the actual flow conditions. Mazumdar[17] proposed the following expression for the Froude number in gas stirred ladles:

$$Fr = \frac{{V_p}^2}{gL} \tag{3.14}$$

Where V_p is the average plume rising velocity.

The Froude number similarity is a widely used and accepted criterion in physical modeling of metallurgical reactors. Nevertheless, additional similarity numbers may have to be considered depending on the phenomena to be analyzed. When inclusion removal analysis is performed in the physical model, the following relationship must be respected in order to make sure the particles will have similar trajectories, where R denotes the radius of the inclusions in the model and in the real full scale model and λ is the geometric scale factor:[18]

$$R_{inc,mod} = R_{inc,real} . \lambda^{0,25} \left[\frac{1 - \frac{\rho_{inc,real}}{\rho_{steel}}}{1 - \frac{\rho_{inc,mod}}{\rho_{water}}} \right]^{0,5} \tag{3.15}$$

Another example of study where additional similarity parameters have to be considered is for models in which the slag phase is simulated with oils or emulsions. In this case, the Weber and Bond numbers similarities become important.[19] The Bond number expresses the ratio between body and surface tension forces and is represented by:

$$Bo = \frac{\rho g L^2}{\sigma} \tag{3.16}$$

Although it is sometimes possible to achieve multiple similarities in reduced scale models, in most experiments some criteria must be neglected as an approximation. Therefore, it is very difficult to model complex phenomena relying only on physical modeling. An alternative is to complement the physical modeling with mathematical modeling, which can represent the full-scale equipment and therefore, overcomes the challenge of respecting multiple similarity criteria. As it will be seen in the next section, mathematical modeling has its own limitations, consequently the best approach for a complete investigation is to use physical modeling studies to calibrate the mathematical model, in order to get the best accuracy possible.

3.2.2 Mathematical Modeling

3.2.2.1 Modeling Turbulent Flow

A mathematical model consists on a set of differential equations for the physical process of interest. However, as pointed by Patankar[20], if the methods of classic mathematics were used to solve such equations, there would be little hope of predicting many phenomena of practical interest, as only a tiny fraction of heat transfer or fluid mechanics problems can be solved in closed form.

With the development of computing technology and numerical methods capable of solving the set of differential equations, the possibility of solving practical engineering problems through mathematical modeling became a reality. The most widely used numerical technique for fluid flow problems is the *Finite Volume Method*. It consists in discretizing the domain geometry into a finite number of smaller volumes, or cells, for which the fluid motion differential equations can be applied. Usually, for obtaining accurate solutions, the method requires the cells to be many times smaller than the domain, which can easily make the total number of cells reach millions, for complex engineering problems.

Equations 3.17 and 3.18 represent the differential equations for fluid motion, where Equation 3.17 accounts for the continuity and Equation 3.18 represents the momentum conservation equation:[21]

$$\frac{\partial \rho}{\partial t} = -\frac{\partial}{\partial x_i}(\rho u_i) - \frac{\partial}{\partial x_j}(\rho u_j) - \frac{\partial}{\partial x_k}(\rho u_k) \tag{3.17}$$

$$\begin{aligned}\rho\left(\frac{\partial u_i}{\partial t} + u_i\frac{\partial u_i}{\partial x_i} + u_j\frac{\partial u_i}{\partial x_j} + u_k\frac{\partial u_i}{\partial x_k}\right)\\ = -\frac{\partial}{\partial x_i}\left[-2\mu\frac{\partial u_i}{\partial x_i} + \frac{2}{3}\mu\left(\frac{\partial u_i}{\partial x_i} + \frac{\partial u_j}{\partial x_j} + \frac{\partial u_k}{\partial x_k}\right)\right]\\ - \frac{\partial}{\partial x_j}\left[-\mu\left(\frac{\partial u_i}{\partial x_j} + \frac{\partial u_j}{\partial x_i}\right)\right] - \frac{\partial}{\partial x_k}\left[-\mu\left(\frac{\partial u_i}{\partial x_k} + \frac{\partial u_k}{\partial x_i}\right)\right] - \frac{\partial P}{\partial x_j}\\ + \rho g_{xj}\end{aligned} \tag{3.18}$$

For a Newtonian fluid with constant density and viscosity, Equation 3.18 can be rewritten as:

$$\begin{aligned}\rho\left(\frac{\partial u_i}{\partial t} + u_i\frac{\partial u_i}{\partial x_i} + u_j\frac{\partial u_i}{\partial x_j} + u_k\frac{\partial u_i}{\partial x_k}\right)\\ = \left(\mu\frac{\partial^2 u_i}{\partial {x_i}^2} + \mu\frac{\partial^2 u_i}{\partial {x_j}^2} + \mu\frac{\partial^2 u_i}{\partial {x_k}^2}\right) - \frac{\partial P}{\partial u_i} + \rho g_x\end{aligned} \tag{3.19}$$

This set of differential equations describes the flow of a single phase in an Eulerian frame of reference. As for most problems of interest such equations cannot be solved in closed form, numerical algorithms have to be used in order to linearize and obtain a solution. The details of such procedures are extensive and deeply analyzed in many textbooks[20,22,23] and therefore will not be discussed in the present work.

A great source of complexity in mathematical modeling of fluid flows is the turbulent nature of many fluid dynamics phenomena of practical interest. One possible alternative is to try and solve Equations 3.17-3.19 directly for turbulent flows, in an approach known as DNS (*Direct Numerical Simulation*). In this method, all turbulent features of the flow are fully resolved up to the Kolmogorov length scale (where the energy of the smallest eddies is of the same magnitude as the viscous dissipation, which usually happens at approximately 10^{-9}m). Naturally, such method is unsteady and requires extremely fine meshes (extremely small cells) and equally small time steps to capture all flow details, and its computational cost is prohibitive for practical applications and even in academy its usage is extremely limited.

An alternative is to fully represent only the largest turbulent eddies, which were found to be responsible for the majority of the turbulent transport phenomena. The smallest eddies would be modeled instead of being resolved. This approach receives the name of LES (*Large Eddy Simulation*) and despite being many times less expensive than DNS, its applications are still currently limited due to its still high computational demand for practical problems of interest.

For most practical engineering problems, the preferred approach is to use time-averaged equations which model all scales of turbulence. Through such method, it is even possible to obtain pseudo steady-state solutions for turbulent flows solved for time-averaged results. This approach is known as RANS (*Reynolds Averaged Navier Stokes*) and the time-averaged equations are given by:[24]

$$\frac{\partial \rho}{\partial t} = -\frac{\partial}{\partial x_i}(\rho \bar{u}_i) - \frac{\partial}{\partial x_j}(\rho \bar{u}_j) - \frac{\partial}{\partial x_k}(\rho \bar{u}_k) \qquad \textbf{(3.20)}$$

$$\frac{\partial(\rho\bar{u}_i)}{\partial t} = -\frac{\partial}{\partial x_i}(\rho\bar{u}_i\bar{u}_i) - \frac{\partial}{\partial x_j}(\rho\bar{u}_j\bar{u}_i) - \frac{\partial}{\partial x_k}(\rho\bar{u}_k\bar{u}_i) + \mu\nabla^2\bar{u}_i - \frac{\partial\bar{P}}{\partial x_i} + \rho g_{xj} + \left[-\frac{\partial}{\partial x_i}\left(\rho\overline{u'}_i\overline{u'}_i\right) - \frac{\partial}{\partial x_j}\left(\rho\overline{u'}_j\overline{u'}_i\right) - \frac{\partial}{\partial x_k}\left(\rho\overline{u'}_k\overline{u'}_i\right)\right] \tag{3.21}$$

As it can be seen, Equations 3.20-3.21 are identical to Equations 3.17-3.19, except for the three terms in brackets in the momentum equation. These terms are residuals from the statistical averaging operation and are denominated *Reynolds Stresses*. RANS turbulence models seek to model the Reynolds Stresses so that the time-averaged equations can be solved.

The most general approach in RANS turbulence modeling is to solve six additional differential equations to account for the *Reynolds Stresses Transport*. However, a less expensive and more popular approach for practical engineering flows is to assume that the Reynolds Stresses can be written analogously to viscous shear stresses, meaning that its magnitude would be proportional to the mean flow strain rate, as shown in Equation 3.22:

$$\tau^t{}_{ij} = \rho\overline{u'}_i\overline{u'}_j = -\mu_t\left(\frac{\partial u_i}{\partial x_j} + \frac{\partial u_j}{\partial x_i}\right) \tag{3.22}$$

The proportionality constant μ_t is denominated *eddy viscosity* due to the analogy with Newton's Law of Viscosity. This proposal is known as the *Boussinesq Approximation*. The advantage of this approach is that the effective viscosity of the flow can be written as the sum of the dynamic and eddy viscosity:

$$\mu_{eff} = \mu + \mu_t \tag{3.23}$$

By substituting the Reynolds Stresses components in Equation 3.21 using Equations 3.22-3.23, the turbulence problem reduces to determining the value of μ_{eff}. This approach proved to be successful to a wide array of practical engineering problems and various different turbulence models have been proposed, suggesting different ways to calculate μ_{eff}.

The first turbulence models to be developed used an analogous expression for the eddy viscosity based on the kinetic theory of gases. The viscosity of an ideal gas can be expressed as:[24]

$$\mu = \frac{1}{3}\rho_g \overline{v_g}\,\overline{L_g} \tag{3.24}$$

Where ρ_g is the gas density, $\overline{v_g}$ is the mean velocity of the gas molecules and $\overline{L_g}$ is the mean free path of the molecules. Similarly to the motion of a gas, the turbulent flow has its eddies moving in a random fashion, therefore it seemed reasonable to assume that diffusion effects could be expressed by an analogous expression. Then, the eddy viscosity would be expressed as:

$$\mu = C\,\rho\,V_t\,L_t \tag{3.25}$$

Where C is a constant, V_t is a characteristic turbulent velocity and L_t is a characteristic turbulent length scale. The first and simplest turbulence models, known as *Zero-Equation Models,* tried to estimate characteristic values of turbulent velocity and length for the global flow, so that a global eddy viscosity value could be obtained. However, real turbulent flows have several velocities and length scales in wide ranges. Therefore, such estimations would be inappropriate for most practical applications.[24,25]

In order to account for the different scales of turbulence which exist in most flows, some models expressed the eddy viscosity in terms of additional turbulent transport variables. The most successful of these models are Two-Equation models based on the transport of turbulent kinetic energy, k, and either turbulent eddy dissipation rate ε or turbulent eddy frequency ω. These are known as k-ε and k-ω turbulence models.

The turbulent kinetic energy gives the turbulent velocity scale and is proportional to the average of the square values of the velocity fluctuations:

$$k = \frac{1}{2}\left(\left(\overline{u_i'}\right)^2 + \left(\overline{u_j'}\right)^2 + \left(\overline{u_k'}\right)^2 \right) \tag{3.26}$$

Thus, a characteristic turbulent velocity can be obtained by:

$$V_t \propto \sqrt{k} \tag{3.27}$$

Viscous dissipation of turbulence occurs at the smallest eddies, which have such small diameter that viscous effects are of similar magnitude as inertial effects. On the other hand, most of the turbulent energy is carried by the larger eddies. Therefore, for turbulent dissipation to occur, the turbulent energy must be transferred from the large eddies to the small eddies. The rate of energy transfer from the large to the small eddies is proportional to the characteristic eddy frequency, ω. Assuming that the smaller eddies cannot sustain turbulent energy, then all the energy received from the larger eddies is dissipated.[25] Thus:

$$\varepsilon = k\,\omega \tag{3.28}$$

Physically, the frequency of a turbulent eddy can be understood as the ratio between the eddy velocity and length. Assuming these to be proportional to the characteristic turbulent velocity and length:[25]

$$\omega \propto \frac{V_t}{L_t} \tag{3.29}$$

Thus, substituting Eq. 3.27 in Eq.3.29, the turbulent length scale can be expressed as a function of the turbulent transport variables k and ω:

$$L_t \propto \frac{V_t}{\omega} \propto \frac{k^{\frac{1}{2}}}{\omega} \tag{3.30}$$

By substituting Eq. 3.28 in Eq.3.30, the length scale can be obtained in terms of k and ε:

$$L_t \propto \frac{V_t}{\omega} \propto \frac{k^{\frac{1}{2}}}{\frac{\varepsilon}{k}} \propto \frac{k^{\frac{3}{2}}}{\varepsilon} \tag{3.31}$$

By combining Eqs. 3.27 and 3.31 into Eq.3.25, the eddy viscosity expression for the standard k-ε model can be obtained:

$$\mu = C_\mu \, \rho \, \frac{k^2}{\varepsilon} \tag{3.32}$$

C_μ is a constant for the standard k-ε model. For the standard k-ω model, the equivalent expression can be obtained by substituting Eq. 3.28 in Eq.3.32:

$$\mu = \rho \, \frac{k}{\omega} \tag{3.33}$$

Through Eqs. 3.32 and 3.33, it is possible to determine the eddy viscosity value for each cell in the domain, depending on the state of turbulence at each location. This is a huge step forward compared to the *Zero-Equation Model* and this approach is regarded as a good compromise between accuracy and computational effort.

For the eddy viscosity to be computed at each location, transport equations must be defined for the additional turbulent variables. Eqs. 3.34 and 3.35 show the transport equations for the standard k-ε model:[26]

$$\frac{\partial(\rho k)}{\partial t} = -\,div(\rho \bar{u} k) \; + div\left[\left(\mu + \frac{\mu_t}{\sigma_k}\right)\nabla\, k\right] + \; P_k - \; \rho\varepsilon \tag{3.34}$$

$$\frac{\partial(\rho\varepsilon)}{\partial t} = - \, div(\rho\bar{u}\varepsilon) + \, div\left[\left(\mu + \frac{\mu_t}{\sigma_\varepsilon}\right)\nabla\,\varepsilon\right] + \frac{\varepsilon}{k}(C_{\varepsilon 1}P_k - \, C_{\varepsilon 2}\rho\varepsilon) \tag{3.35}$$

P_k accounts for turbulence production due to mean velocity and buoyancy effects. σ_k, σ_ε, $C_{\varepsilon 1}$ and $C_{\varepsilon 2}$ are model constants. These constants need to be calibrated through experimental data.

The standard k-ε model has been used in several different practical applications and is very well established, with a good overall performance. Nevertheless, it has also shown some weaknesses, such as a poor performance when modeling flows with strong curvature or adverse pressure gradients. Attempting to solve these limitations, alternative versions of the k-ε model were proposed. The RNG k-ε and the Realizable k-ε models introduce corrections to calculate the turbulent variables and eddy viscosity, softening the weaknesses of the standard k-ε model.[26]

Similarly to Eqs. 3.34 and 3.35, the transport equations for the standard k-ω model:[27]

$$\frac{\partial(\rho k)}{\partial t} = - \, div(\rho\bar{u}k) \; + \; div\left[\left(\mu + \frac{\mu_t}{\sigma_k}\right)\nabla\,k\right] + \, P_k - \, \beta'\rho k\omega \tag{3.36}$$

$$\frac{\partial(\rho\omega)}{\partial t} = - \, div(\rho\bar{u}\omega) + div\left[\left(\mu + \frac{\mu_t}{\sigma_\omega}\right)\nabla\,\omega\right] + P_\omega - \, \beta\rho\omega^2 \tag{3.37}$$

The standard k-ω model has the advantage of being more robust than the k-ε models for near-wall calculations. On the other side, on the free stream regions, it is very sensitive to the initial guess and generally leads to less accurate results than ε based models.[27]

In order to use the strengths of both formulations, the Baseline (BSL) k-ω model was proposed. The BSL k-ω model adopts the standard k-ω formulation in the near-wall regions and uses a transformed version of the k-ε model in the far field. This was done through writing the k-ε model using a k-ω formulation and using a blending function which activates the standard k-ω in the boundary layer region and the transformed k-ε in the free stream.[28]

Further improvement came with the Shear Stress Transport (SST) k-ω model, which accounts for the transport of turbulence shear stresses in the definition of the turbulent viscosity. The SST k-ω model introduces a limiter to the formulation of the eddy viscosity that makes it more accurate and reliable for wider classes of flows due to its enhanced prediction of flow separation from smooth surfaces.[28] One serious limitation of turbulence modeling is that, unlike the dynamic viscosity, μ_{eff} is not a fluid property, but a flow property. Therefore, it is impossible to obtain one single general μ_{eff} value, through a set of experiments that would be suitable for any flow calculation. For practical engineering calculations, a turbulence model must be chosen considering the experimental conditions of its formulation and if they relate to the actual flow physics to be simulated. Some turbulence models have been proved to be applicable to a wide range of flows with acceptable accuracy and affordable computational cost, such as the k-ε model (and its variants) or the SST model. As the development and calibration of a specific turbulence model is outside the scope of this study, these models will be the first choices for turbulence modeling in the present work.

3.2.2.2 Modeling Multiphase Flow

Another significant source of complexity in mathematical modeling is when more than one phase needs to be represented in the system. So far, the equations shown in this section account for flows where there is only one phase in the system. However, for simulating the phenomena of inclusion removal in a gas stirred ladle, several phases coexist in the flow and must be accounted for in an accurate investigation, such as:

1. Main liquid phase (molten steel in the industrial equipment or water in the physical model);
2. Gas bubbles from purging;
3. Inclusions;
4. Atmospheric air (if a free surface model is used);
5. Slag layer (if it is not neglected in the modeling assumptions);

Currently, there are two general approaches for dealing with multiphase flows: the Eulerian-Eulerian or the Eulerian-Lagrangian. Both approaches aim at calculating how the different phases are distributed in the domain and how they interact. For each different modeling approach, different assumptions are made regarding the phases distributions and the interphase momentum and energy transfer.

In the Euler-Lagrange approach, the main fluid phase is treated as a continuum by solving the Navier-Stokes equations, while the dispersed phase is solved by tracking a large number of discrete particles through the calculated flow field. Such approach is considerably simpler when particle-particle interactions can be neglected, which requires the volume fraction of the second phase to be small.[29] In the context of the problem to be analyzed in this study, secondary phases which could be suitable for being modeled in a Lagrangian framework are the inclusions and the gas bubbles.

On the other side, the Euler-Euler approach consists of modeling the different phases as interpenetrating continua. Since the volume of a phase cannot be occupied by the other phases, the concept of phasic volume fraction is introduced. The volume fractions are assumed to be continuous functions of space and time and their sum is always equal to one. Conservation equations for each phase are derived to obtain a set of equations, which have a similar structure for all phases.[30] Conservation of momentum can be accounted for either by a single set of momentum equations shared by the fluids (suitable for free surface modeling) or by solving separate equations for each phase (suitable for dispersed fluid modeling). If the slag layer and the atmospheric air are present in the model, they must necessarily be modeled through an Eulerian-Eulerian approach. The inclusions and gas bubbles can also be modeled through this method, with the spatial distributions being given by the volume fraction transport variable.

As it can be seen from this section, there are many different approaches for dealing with complex phenomena in fluid flow problems, especially regarding turbulent and multiphase flows. In this context, physical modeling results are very useful, as these bring a dose of reality to the mathematical model results, allowing the evaluation of the accuracy of each different modeling approach. Through a balance between the verified accuracy of each modeling method and its computational cost for a given phenomenon, a mathematical model can be developed and its results regarded as trustworthy. From there, new hypothetical situations can be simulated, with the possibility of predicting the outcome of each scenario before it is put to practice. This is the motivation for the development of mathematical models in general, and in the context of inclusions removal in gas stirred ladles, is the main objective of the present study.

In the next section, other publications related to modeling fluid flow and/or inclusion removal in gas stirred ladles are presented. This is an important step to assess which modeling methods have successfully (or unsuccessfully) represented the physics involved in this phenomenon and where this study could contribute to the existing knowledge in the field.

3.3 Inclusion Removal Modeling

Sheng et al.[31] studied the growth and separation of alumina micro inclusions using both static and dynamic modeling. The initial micro-inclusion size was obtained from experimental data. A 2-D axisymmetric CFD model was developed to analyze fluid flow in the ladle, with turbulence being modeled using the k-ε model. The inclusion concentration was modeled through a scalar transport variable. The results of the CFD model were used as input for equations predicting the growth and removal of inclusions. The static modeling results have shown that the predicted removal of micro-inclusions due to bubble flotation was highly dependent on the flotation theory employed. The main conclusion reported for this study was the existence of concentration gradients for the inclusions: after 1 minute of stirring, fewer inclusions were found close to the steel/slag interface and plume area than in the other regions. This was attributed to inclusion growth due to turbulent collisions in these regions.

Söder et al[32] performed a similar study, using a static modeling approach fed with data obtained by a CFD model. It has been found that the two most significant mechanisms of inclusion removal were removal to the top slag by buoyancy and removal by bubble flotation, assuming spherical-cap bubbles and plane contact. When bubbles were assumed to be spherical, resulting removal rates were lower than when they were assumed to be spherical caps. Inclusions larger than 25 µm were found to be removed mostly by Stokes flotation while smaller inclusions would be separated primarily by spherical cap bubbles flotation.

Aoki et al.[33] modeled inclusion removal by bubbles in three steps. First, an Eulerian-Lagrangian model was developed to model the transient multiphase turbulent flow in the ladle during argon purging. Turbulence was modeled by the k-ε model and its effects on the bubbles were accounted for by means of the “random walk” method, where random fluctuating velocity components are added to the bubble velocity proportional to the local turbulence levels. The second step of the study was an axisymmetric model for the flotation of an individual bubble and the random motion of an inclusion in such flow field, to determine the probability of collision and attachment between them. A statistical analysis was performed using thousands of simulations to assess the probability of inclusion attachment. Finally, the third step of the study consisted in the modeling of inclusion transport in the turbulent flow field through a scalar variable for the inclusion concentration. A source term in the transport equation was created to account for inclusion removal due to bubble collision, as calculated in the previous step. The calculated flow field and gas volume fraction matched well with an experiment using Wood's metal. It was also found that, considering turbulent random effects, the attachment probability between the inclusion and the bubble was 10 to 100 times higher than if these effects were neglected.

Wang et al.[34] developed a three-dimensional mathematical model to predict the growth and removal of inclusions during gas stirring in a multi-tuyère ladle. The inclusion transport was modeled adopting a scalar transport variable for its concentration. The efficiency of inclusion removal was studied under three collision mechanisms: Brownian, Stokes and turbulent collisions. The results indicated that inclusion growth resulting from turbulent collision is the most important and the effect of Stokes collision is remarkable as inclusion size increases. Inclusion growth resulting from Brownian collisions was found to be negligible. Inclusion removal by wall adhesion was also found to be negligible.

Zheng and Zhu[35] studied the effects of gas blowing time and flow rate on inclusion removal in a ladle through physical modeling. Emulsion drops were used to simulate the collision and aggregation of inclusions in steel. The model was built on a 1:9 scale and considered a gas flow rate range from 1.19×10^{-2} to 16.63×10^{-2} Nm^3/h in the experiments, which translates to a flow rate of 5 to 70 Nm^3/h (or 83 to 1667 NL/min) in an equivalent industrial ladle. The emulsion drops used to simulate the inclusions had an equivalent diameter of 379 µm, which translates to 112.5 µm diameter Al_2O_3 inclusions in the molten steel. Samples were collected from the mixture in the ladle in fixed time intervals, in order to evaluate the inclusion removal rate. Figure 3.9 shows the variation of inclusion removal rate with the gas blowing time for various flow rates. Figure 3.10 compares the final inclusion removal rates for the different flow rates studied.

In the experiments, lower gas flow rates were found to be more efficient than higher gas flow rates for inclusion removal within a shorter blowing time. This effect can be seen clearly in Figure 3.9, where by the 8 minute mark, the lower flow rates have already removed a significant amount of inclusions, compared to the higher flow rates, which take a much longer time to achieve similar removal rates. On the contrary, when longer blowing times are considered, the higher flow rates showed superior results, which can be seen in Figure 3.10.

It was also found that inclusion removal was in an exponential relationship with gas blowing time in a gas stirred ladle. It was suggested that at lower flow rates, inclusions may be attached to bubbles and at higher flow rates they may be captured by wakes.

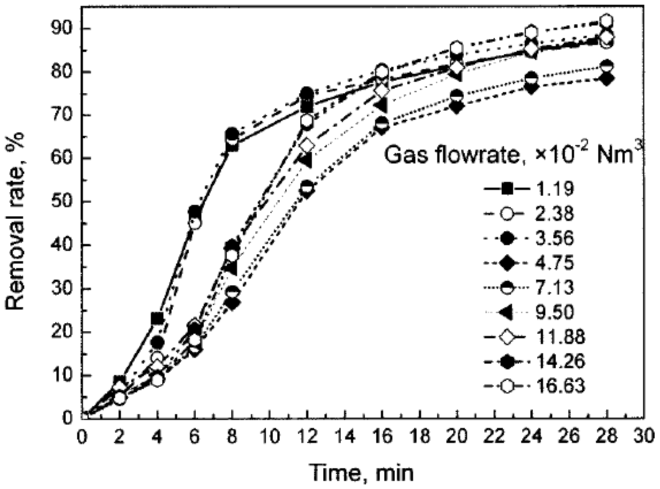

Figure 3.9: The variation of inclusion removal rate with gas blowing rate for various flow rates. Zheng and Zhu (2008)[35]

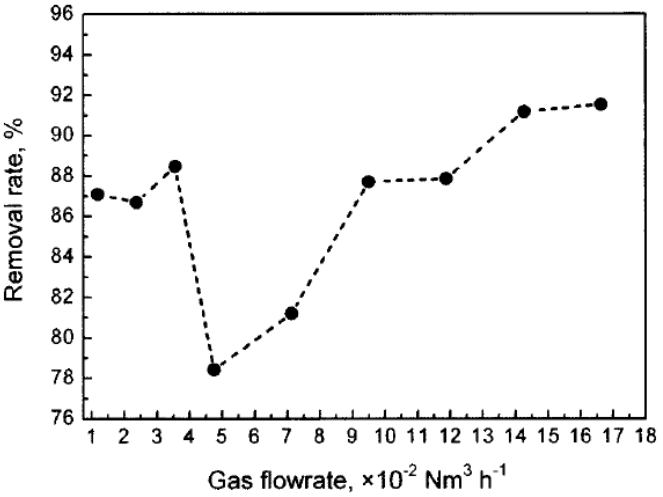

Figure 3.10: Variation of final inclusion removal rate with gas blowing rate. Zheng and Zhu (2008)[35]

Ek et al[36] conducted industrial trials and water modeling experiments in order to find an optimum flow rate range for argon purging in the ladle, studying the mixing time and the inclusion removal. The water modeling experiments were performed in a 1:5 scale model which replicated a 200ton industrial ladle. The studied gas flow rates are shown in Table 3.1. CFD calculations were used as an auxiliary tool to gain a semi quantitative understanding of the effect of argon flow rate in ladle treatment. In both industrial trials and water model, homogenization of alloying elements happened very fast, usually within 2-3 minutes. The fast mixing was further confirmed by the CFD calculation. Charcoal particles in the range of 63-75 µm were used to simulate the inclusions in the water model, while silicon oil was applied to simulate the slag. The effect of the gas flow rate on the rate of inclusion removal was not found to be significant. Figure 3.11 shows the measured inclusion concentration with time for the experiments, comparing different gas flow rates, and no significant differences have been observed. For all configurations, the inclusion concentration gets lower as time progresses, following an approximately exponential relationship. Taking into account mixing, inclusion removal and inclusion generation, it was suggested that a low argon flow rate should be employed in the ladle treatment, when slag-metal reaction was not the main objective of the ladle treatment.

Table 3.1: Gas blowing rates studied. Ek et al. (2010)[36]

Configuration	Blowing rates			
1/5 scale model (m^3/h)	0.15	0.21	0.36	0.45
Equivalent industrial ladle (m^3/h)	2.4	3.4	5.8	7.3
Equivalent industrial ladle (L/min)	40.00	56.67	96.67	121.67

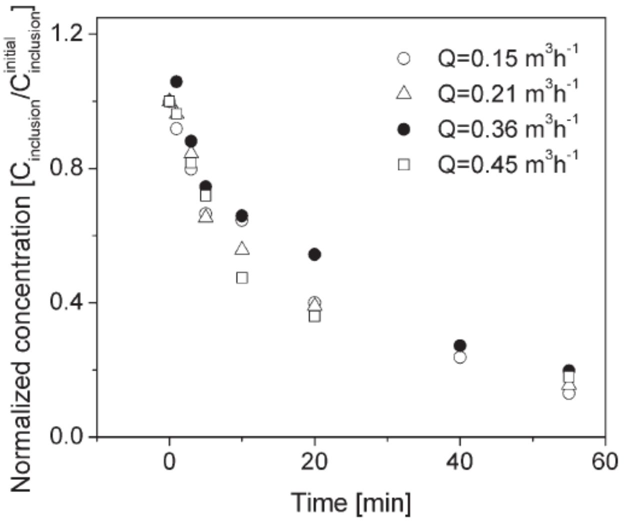

Figure 3.11: Normalized inclusion concentration as a function of time for different gas flow rates. Ek et al. (2010)[36]

Qu et al.[37] modeled inclusion removal under gas blowing in a teeming ladle. Both physical and mathematical modeling were adopted. For the physical model, a 1:10

scale water model was built, corresponding to a 150ton industrial ladle. Through the physical model, the effects of different nozzle arrangements, gas blowing rates and blowing time were analyzed regarding the inclusion removal rate. The studied blowing rates are shown in Table 3.2.

Table 3.2: Studied gas blowing rates. Qu et al. (2010)[37]

Configuration	Blowing rates			
1/10 scale model (m^3/s)	2.70E-06	4.00E-06	5.30E-06	6.70E-06
Equivalent industrial ladle (m^3/s)	5.09E-03	7.55E-03	1.00E-02	1.26E-02
Equivalent industrial ladle (L/min)	305.40	453.00	600.00	756.00

As for the mathematical model, it was used with the goal of showing the fluid flow characteristics in the teeming ladle and to reveal the effect of fluid flow on inclusion removal. An Eulerian-Eulerian multiphase model was used to calculate the fluid flow in the numerical simulations. It was found that under the study conditions, soft gas blowing with a single nozzle and a blowing rate of 2.7 x 10^{-6} m^3 s^{-1} was the best condition to float inclusions into the slag layer, showing a relative inclusion removal rate of 69%. Such a gas blowing rate could be translated, through the similarity criterion, for an industrial ladle blowing rate of 5.09 x 10^{-3} m^3 s^{-1} or 305 L/min. The inclusion removal rate increased with the bottom blowing time, as shown in Figure 3.12, however it was suggested to end the gas blowing when the draining percentage reached 50% to avoid re-entrainment of floated inclusion particles into the bath and to avoid reoxidation due to surface exposure.

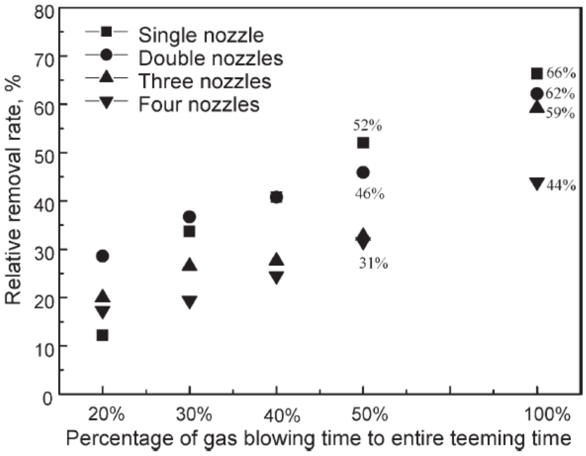

Figure 3.12: Effect of gas blowing time on the inclusion removal rate. Qu et al. (2010)[37]

Marins[38] studied inclusion removal in the ladle through inert gas injection by means of a Population Balance model (PBM) based on the results of a CFD study of the flow in the ladle. The PBM considered the value of Dissipation of Turbulent Kinetic Energy, ε, extracted from the CFD calculations, as the input for its calculations. Samples of the molten steel from an industrial ladle were collected for the evaluation of the amount of inclusions. The samples were collected through the method TOS (Total Oxygen Sampler) and analyzed through the SEM (Scanning Electron Microscope) technique in order to assess the amount of inclusions and the area occupied by them. The study was performed for a 125ton industrial ladle and the industrial results showed that the Total Oxygen concentration, under a gas flow rate of 33.5 Nm^3/h, was lower than when a flow rate of 16.7 Nm^3/h was applied. It was suggested that, for the flow rates studied, the benefits provided by increasing the kinetic energy of the flow would surpass the deleterious effects of turbulence close to the slag interface.

Lou and Zhu[39] used a coupled CFD-PBM model to investigate the bubbly plume flow and inclusion behavior, including growth, size distribution and removal. To model turbulence, a modified k-ε model with extra source terms to account for bubble-induced turbulence was adopted. For the inclusions, the turbulent random motion, bubbles wakes and slag eye forming on the molten steel surface were considered. The results showed that, under low gas flow rates, the inclusion growth is mainly attributed to both turbulent shear collision and Stokes collision and inclusion removal is mainly attributed to bubble-inclusion buoyancy collision and inclusion own flotation near the slag interface. At higher flow rates, both inclusion-inclusion and inclusion-bubble collisions due to turbulent random motion were found to be significant for inclusion growth and removal. For a 150ton ladle, an increase in the gas flow rate increased the total amount of inclusion removal, up to 200 NL/min. Flow rates above this value did not show significant change on the inclusion removal rate.

Bellot et al.[40] also used a coupled CFD-PBM model to simulate the mechanisms of transport, aggregation, flotation and removal of inclusions in a gas stirred ladle. The multiphase flow was modeled according to the Eulerian-Eulerian approach and turbulence was calculated with the standard k-ε model with an additional term to account for bubble induced turbulence. The inclusion population was modeled through a scalar transport variable. The mathematical model was applied to simulate inclusion removal in a 60ton ladle with argon injection through two porous plugs, each with a gas flow rate of 70 L/min. A 0-D model, where only the Population Balance Equation was solved and the ladle was considered perfectly agitated was also solved. The results showed that the aggregation mechanism plays a major role by translating the particle size distribution towards larger diameters. This can be seen in the results shown in Figure 3.13. For the smaller sizes, the inclusion number density is smaller after 300 seconds than at the beginning of the simulation, while for the larger sizes, the number density is larger after 300 seconds than it was at the beginning.

Sa[41] studied the effect of an upper slag phase in the flow in the ladle during inert gas injection. The study was performed through physical and mathematical modeling considering different plug arrangements, gas flow rates and slag thicknesses and the main result of interest was the mixing time in the ladle. The results showed that the slag layer has a significant influence in the mixing time and as the thickness of the slag layer increases, the mixing time also increases, which suggests that there is a reduction in the overall flow velocities for the cases with thicker slag layers.

Liu et al.[42] reviewed the research performed in gas stirring in ladles over the past few decades. It was observed that to describe the gas-liquid two phase flow in the plume, there would be four main mathematical methods: (1) the quasi-single phase model, (2) the volume of fluid (VOF) model, (3) the Eulerian multiphase model and (4) the Eulerian-Lagrangian model. More recently, commercial codes coupled with user-defined functions (UDFs) have been employed for the study of gas bubbling in ladles. Due to the ability of the VOF model to track sharp interfaces, it has been used in three main analysis points: for modeling the gas-liquid phase interfaces, coupled with the discrete phase model and coupled with thermodynamic models. As for the Eulerian multiphase model, multiple sets of equations for continuity, momentum and turbulence are solved for each phase. This increased complexity negatively affects convergence behavior, however these models can be used to include effects of additional forces such as virtual mass force, drag force, lift force and turbulence dissipation force on the flow pattern, which can greatly improve the model results. Figure 3.14 shows a schematic view of the preferred models applied in different areas of research in ladle metallurgy. Considering the topics of interest in the present study, it is possible to notice that:

- For the inclusion behavior at the top interface, the preferred approach has been the VOF multiphase model coupled with LES turbulence model.
- For calculations of velocity and turbulence distributions and general flow pattern analysis, the quasi-single phase model, the Eulerian multiphase model and the

Eulerian-Lagrangian multiphase model have been widely adopted. For turbulence, the k-ε model has been the most popular choice.

- For inclusion removal in molten steel, the VOF or Eulerian multiphase model have been used together with the Discrete Phase model. Some studies have also adopted the Population Balance model. For turbulence, the k-ε model has been mostly used.

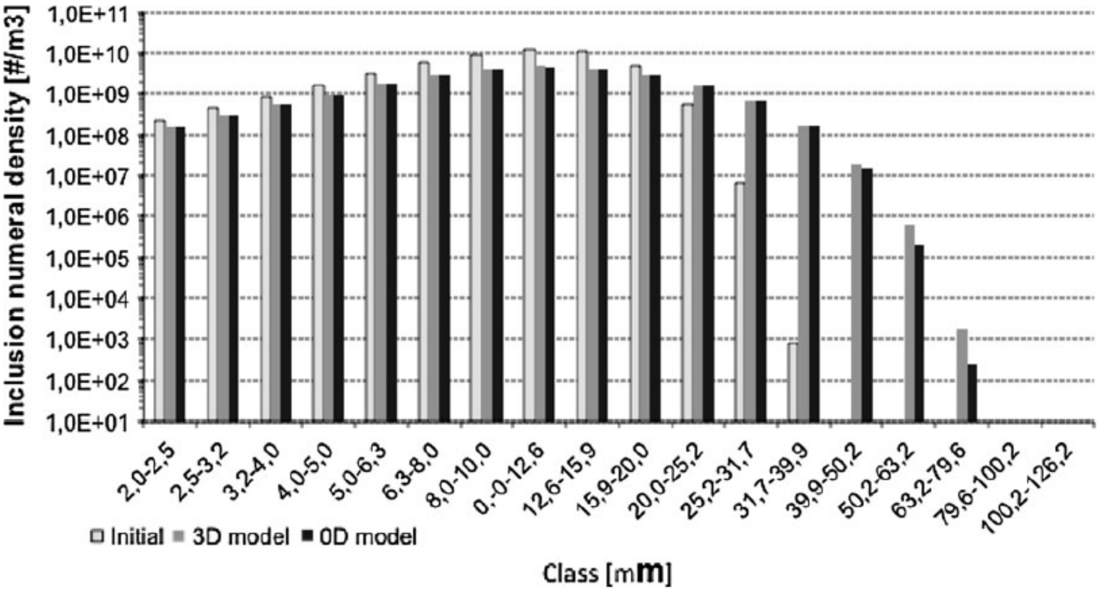

Figure 3.13: Particle Size Distribution at the beginning of the simulations and after 300 seconds for 3D and 0D model. Bellot et al. (2013)[40]

In this section, other publications related to the phenomenon of inclusion removal in a gas stirred ladle were presented. It is possible to find some trends in these publications regarding modeling assumptions and relevant mechanisms of inclusion growth and removal. The k-ε turbulence model was a popular choice in these publications, and due to its wide applicability and acceptance, it was adopted in the present work. For the models that considered interactions between the inclusions, such as collisions and agglomeration, the scalar transport variable approach seemed to be more used than the Lagrangian approach. This is probably due to the difficulties in considering interactions between the discrete particles in the DPM approach.

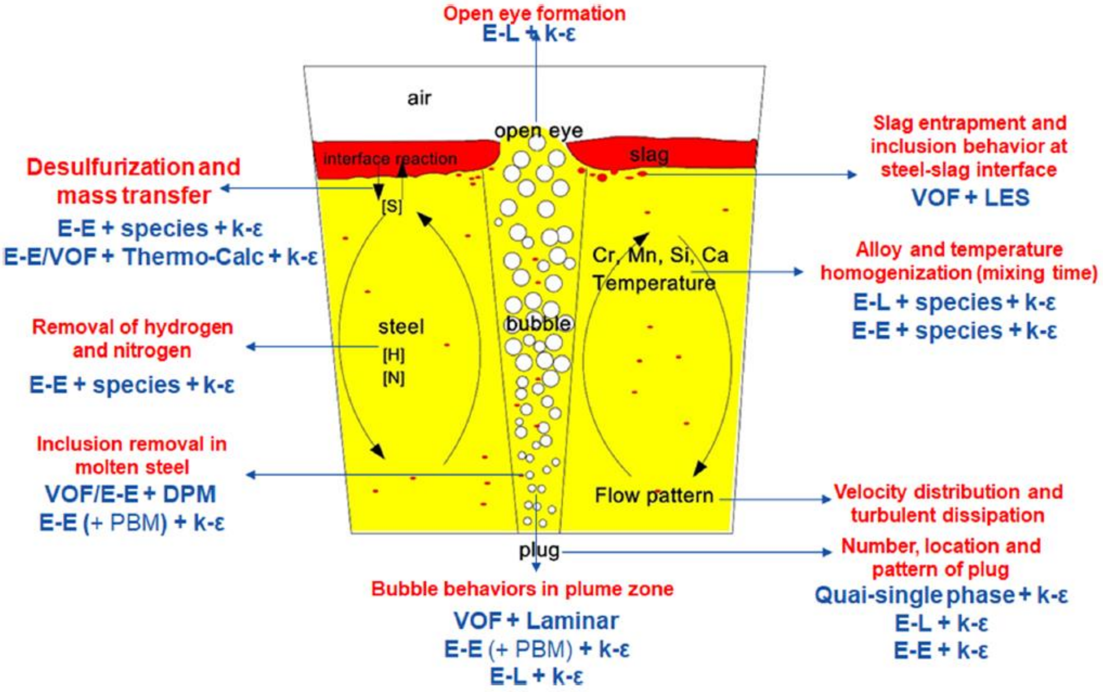

Figure 3.14: Schematic diagram of preferred numerical models in different research areas in ladle metallurgy. Liu et al. (2018)[42]

Most studies in the literature show that the inclusion concentration in the ladle reduces with longer gas blowing times, often showing an exponential relationship. Most inclusions would be removed at the early stages of purging and the effectiveness would get gradually lower as less inclusions would remain in the bulk flow.

Finally, many of the publications in the area seem to agree that lower gas flow rates are preferable than high flow rates in order to promote inclusion flotation. Even though some studies show an increase in the inclusion removal rate with higher gas blowing rates, the higher stirring intensity often bring other problems such as slag eye opening and emulsification, therefore, from a practical perspective, the optimum purging rate would not be as high. However, care must be taken when analyzing such trends from the other works in literature. The ranges of blowing rates studied vary greatly from study to study, therefore what one author defines as a “high blowing rate” could be different from what another author understand as a high gas flow rate. Especially since many water modeling experiments adopt different scale factors, it is important to analyze the reported results scaling the gas blowing rates back to the equivalent values of an industrial ladle. This has been done in this section of the present study and provides a common base for comparison with the results obtained in this work.

4. METHODOLOGY

4.1 Mathematical Model

4.1.1 General Workflow for the Mathematical Model Development

The phenomenon to be studied in the present work is the inclusion removal from the ladle during inert gas purging right before the ladle teeming. There are three main different process steps that are of interest for this study:

i. The first step is when the fluid is at rest. At this stage, the system has a homogeneous distribution of inclusions. In an equivalent industrial system, this step would correspond to the time taken by the ladle to be transported to the turret, after the relevant secondary metallurgy treatments have been performed and the steel is ready to be cast.

ii. The second step is the purging treatment right before the ladle teeming. This treatment would be performed with the sole goal of inclusion removal, since the conventional purging treatments typical of the secondary metallurgy have already been performed before.

iii. The third and final step is the ladle teeming.

The mathematical model developed in the present work replicated the experimental conditions adopted by Silva[2,43,44], as it is convenient to have the experimental results for comparison with the results obtained through the simulations. In the next paragraphs, the basic information about the experiments will be described, as this is necessary for the introduction of the work developed in the present study. Further details about the experiments are going to be provided at a later section of this text.

The reduced scale model of the ladle was built on a 1:5 scale representing a 180ton industrial ladle. The model has a height of 72.5 cm, a bottom diameter of 64.5 cm and an upper diameter of 72.5 cm. The experiments were conducted with a bath height of 60 cm. The total water volume in the model was 227 liters. A schematic picture of the prototype is shown in Figure 4.1 and Figure 4.2. The plug size considered in the simulations of the present work had a surface area of 15 cm^2.

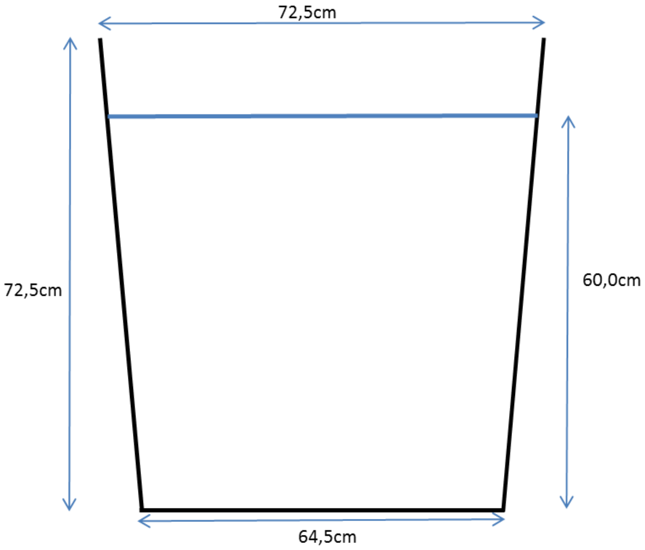

Figure 4.1: Schematic of the reduced scale model for the ladle.[2]

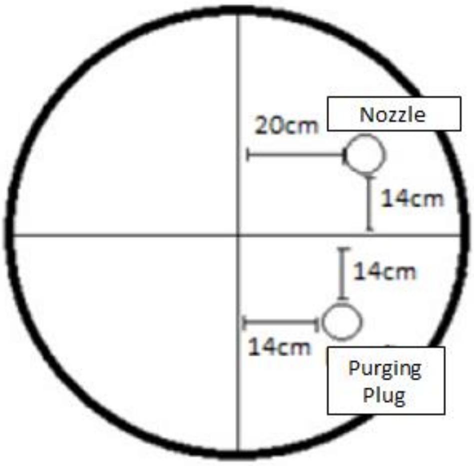

Figure 4.2: Position of the purging plug and nozzle in the ladle set-up.[2]

In the experimental work developed by Silva[2,43,44] , the inclusions were simulated using hollow spherical boron-silicate particles, with size distribution as shown in Figure 4.3. This analysis shows that 10% of the samples have diameter up to 14.20 µm, 90% of the samples have diameter up to 64.51µm and the average diameter of the sample is 38.28 µm.

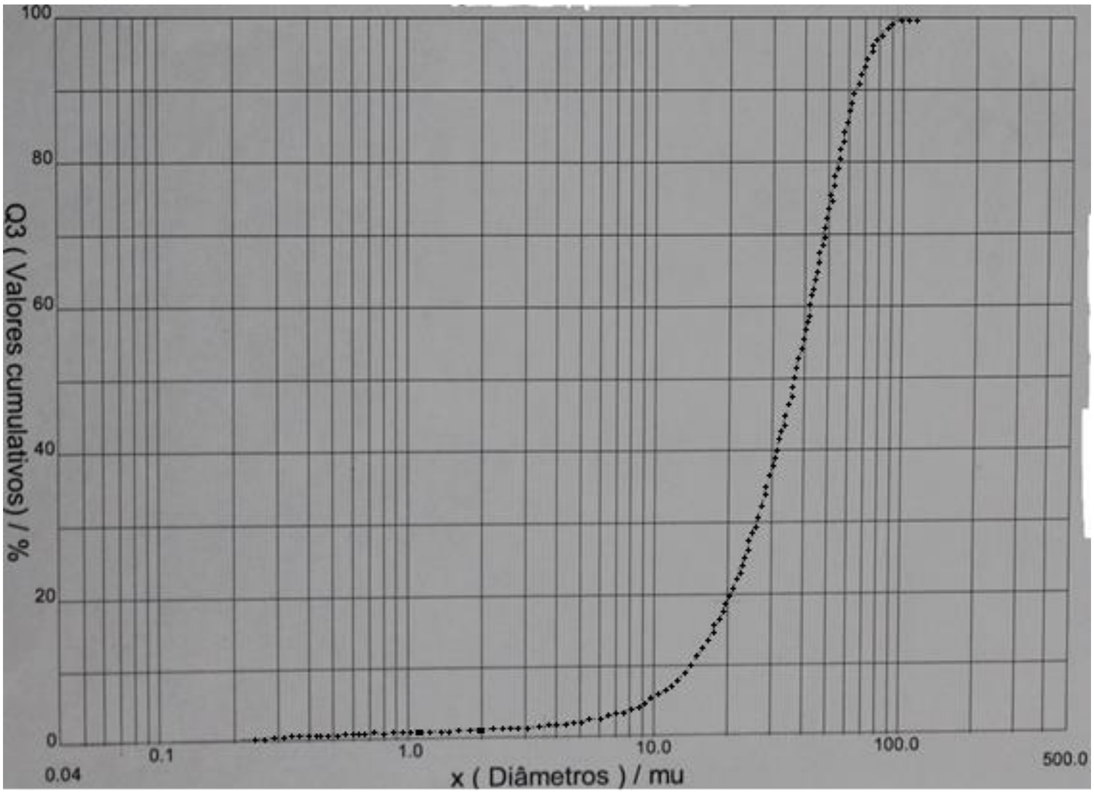

Figure 4.3: Size Distribution of the Inclusion Particles used in the Water Model.[2]

In the experiments, the following steps were followed:

1. Injection of the inclusion particles and homogenization of its distribution in the bath;
2. Gas purging with varying flow rates and process times;
3. After the gas purging finishes, the probe software is initialized and it starts counting the particles at the same time that the ladle teeming starts. The particles are counted until the ladle is almost totally drained.

The APS probe used in the experiments was able to measure inclusions in the range of 20 µm to 170 µm diameter. In an equivalent industrial ladle, this would be equivalent to a size range of 32 µm to 272 µm. The mass of inclusions injected was calculated in order to result in a concentration of 4.24×10^8 inclusions per cubic meter in the experiments.

Table 4.1 shows the equivalence between the conditions studied in the present work and the corresponding industrial parameters. This correlation is important for the comparison of the results of this work and other studies in the literature. It is also necessary for practical application of the conclusions of this work in the industrial practice.

Table 4.1: Equivalent industrial parameters for the configurations studied in the present work.

Model time (s)	Industrial time (s)	Model flow rate (NL/min)	Industrial flow rate (NL/min)
25	56	2	35
55	123	5	87
80	179	10	174

As discussed previously, many different approaches exist for modeling the same physical phenomenon. The choice of which method is the most appropriate depends on two basic aspects: accuracy and computational cost. The latter is easy to evaluate, the longer the model takes to carry out the simulations, the higher its computational cost. For the assessment of the former, the predictions of the model should be compared to experimental results.

The basic steps in the development of the proposed mathematical model were:

1. Representing the system geometry in a CAD platform;
2. Meshing of the geometric domain;
3. Setting up fluid flow models and boundary conditions;
4. Solving the model;
5. Post-processing the results.

In the post-processing stage, the predictions of the mathematical model results were compared to the experimental data and the validity of the results was verified. As the ladle geometry is very simple and the numerical methods for solving the conservation equations of the mathematical model are very robust in today's commercial codes, steps 1 and 4 listed above are not likely to cause any mismatch between the model results and the experimental data. Therefore, the development of the mathematical model was focused in making sure that the adopted mesh was appropriate and that the fluid flow models, boundary conditions and interaction models between the liquid, gas and particles adequately represented the physical phenomena.

For the assessment of the mesh adequacy, a mesh independence study was performed. This consists of solving the same problem with meshes of different levels of refinement in order to obtain a solution which is mesh independent. Usually the mesh needs to be locally refined in regions of steeper gradients, such as in the proximity of the walls and in the plume region. Such requirements will be evaluated during the model development. The mesh study is considered complete when there is no significant variation between the results of further refined meshes.

Nevertheless, for turbulent multiphase flows, such as the one being studied, the complexity usually goes beyond the mesh generation. The modeling of such flows requires the choice of one among several available models, each with its own advantages and limitations. The selection of appropriate turbulence and multiphase models is probably be the most critical step in obtaining reliable results from the mathematical model.

The simulations have been divided in three different stages:

Transport stage: Right after the inclusions were injected and homogenized in the water modeling experiments, the system was allowed to rest for some minutes. This would be equivalent, in the industry perspective, to the time taken by the real ladle to be transported to the turret. During this time, no purging is performed and the inclusions float towards the slag due to buoyancy effects. In the physical modeling experiments, this time was considered to be equal to 7 minutes, and this was also the time considered in the present work simulations. Such time corresponds to a transport time of 15 minutes in the melt shop, which was taken as an average representative value of the industrial practice;

Purging stage: After the resting time, the gas purging treatment is performed. The evaluation of the effectiveness of such treatment as well as the influence of its parameters are the main objective of the present work. The simulations were performed replicating the water modeling experiments conditions. In an equivalent industrial situation, this stage would correspond to a purging treatment being applied when the ladle is already at the turret, instants before teeming started;

Teeming stage: Right after the purging treatment finishes, the ladle teeming starts and the water flows through the nozzle at the bottom of the ladle. At this time, the APS probe located in the nozzle counts how many inclusions are in the flow and the effectiveness of various purging treatments can be compared. In an equivalent industrial situation, this stage corresponds to the teeming of the molten steel from the ladle to the tundish. At this moment, inclusions present in the molten steel may be carried over to the tundish, or they may be captured by the slag before they pass through the nozzle.

Even though these three stages follow a logical order from a process perspective, each of them requires a different approach for mathematical modeling. It would be theoretically possible to build a single comprehensive model which would encompass all the three stages, however such approach would not be the most efficient. A mesh refinement in the plume region is necessary in the purging simulation but is a waste in the teeming simulation. On the other side, modeling an air layer free board is mandatory for the teeming simulation, however it is optional for the purging simulation, where a boundary condition could be applied directly at the water/air interface. This makes the choice of modeling each stage separately a more convenient approach for the present work. To account for the sequential nature of the process, a report describing the inclusions position and velocity is exported as an output of each stage model and imported as the initial condition for the next stage model. Figure 4.4 shows a schematic view of the modeling steps in the present work:

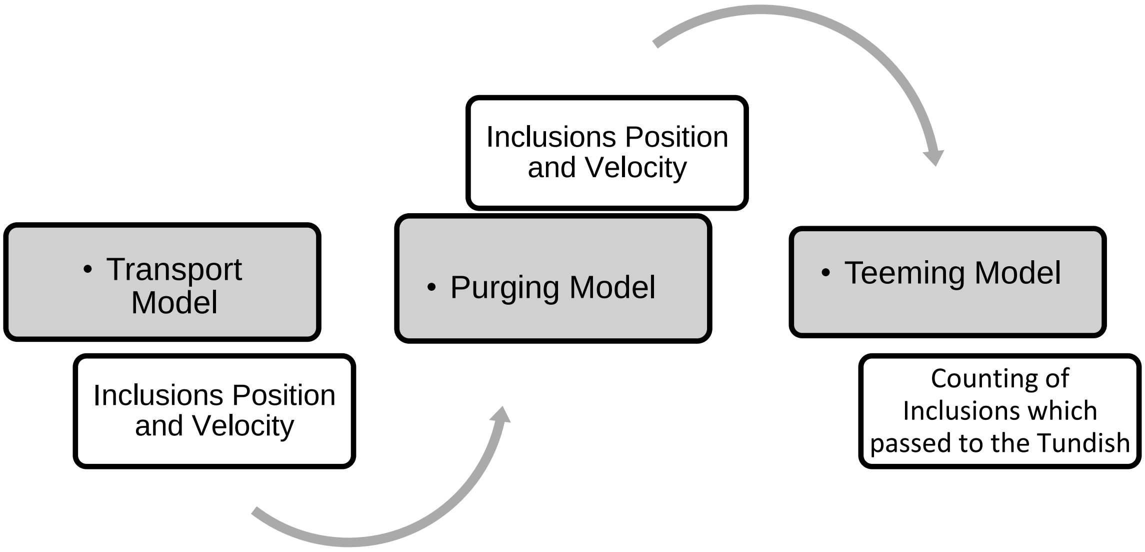

Figure 4.4: Sequence of the modeling stages in the present work.

To model the behavior of the inclusions, the Lagrangian approach was chosen in the present work. In the experiments with the physical model, the amount of inclusions injected in the domain was in the range of 10^8. Tracking such a number of inclusions in the mathematical model would be prohibitive, therefore a representative number of inclusions were tracked in the mathematical model and the results were translated into the real number of inclusions of the experiments, accounting for their size distribution. The calculations performed to translate the results of inclusion counting predicted by the mathematical model into the results of the physical model are described later in this chapter, in section 4.3 Validation of the Mathematical Model.

The next three sections describe the modeling methods adopted in the first mathematical models developed in this work. Then, the following section describes alternative mathematical modeling approaches also tried in the present work in order to determine which approaches are more appropriate to model inclusion removal during ladle purging.

4.1.2 Transport Model Description

The transport phase is very simple from the mathematical modeling perspective. The flow is theoretically at rest, and the inclusions float subject exclusively due to a force balance between buoyancy and drag effects. Therefore, the governing equations for the fluid flow are not solved in this step, only the ordinary differential equations for the discrete phase representing the inclusions.

The differential equation that needs to be solved to obtain each particle instantaneous velocity is given by Eq. 4.1:[45]

$$\frac{d\overrightarrow{u_p}}{dt} = \frac{\vec{u} - \overrightarrow{u_p}}{\tau_r} + \frac{\vec{g}\,(\rho_p - \rho)}{\rho_p} + \vec{F} \tag{4.1}$$

Where $\frac{\vec{u} - \overrightarrow{u_p}}{\tau_r}$ is the drag force per unit mass, $\frac{\vec{g}\,(\rho_p - \rho)}{\rho_p}$ is the buoyancy force per unit mass and $\vec{F}$ is an additional force term per unit mass, and is equal to zero for the simulations of the transport stage, in which the fluid is at rest. The particle relaxation time τ_r is given by Eq. 4.2:

$$\tau_r = \frac{\rho_p {d_p}^2}{18\mu} \frac{24}{C_d Re} \tag{4.2}$$

The particle velocity is represented by $\overrightarrow{u_p}$, the fluid velocity is represented by $\vec{u}$, C_d is the drag coefficient, the molecular viscosity of the fluid is represented by μ, the fluid density is ρ, the particle density is ρ_p and the particle diameter is d_p. Integration of Eq. 38 provides the particle velocity value, which is then used to calculate the particle trajectory, as shown in Eq. 4.3:

$$\frac{dx_p}{dt} = u_p \tag{4.3}$$

As a consequence of not solving the fluid flow equations, there are not many requirements for the mesh in this stage. Since the only equations to be solved in this step are for the particle motion in the Lagrangian frame of reference, the only influence of the mesh is that the finite volumes store the information of the fluid flow velocities that are used in the particle motion calculations. But since the fluid flow velocities are constant and equal to zero in the entire domain, all the mesh volumes store the same value and consequently, do not influence the particle calculations. Therefore, a general mesh has been created using ANSYS Meshing default settings for Fluent CFD, with a maximum element size of 30 mm. The maximum value of 30 mm was chosen in order to have enough representative volumes in a cross-section for the particle injections, since it was found that the most convenient way to inject the inclusions would be at the mesh volumes. Figure 4.5 shows the resulting mesh for the Transport Stage Calculations. A ½ symmetric geometry was considered in this model. An even smaller fraction of the geometry could be modeled, due to axial symmetry, but a ½ fraction was chosen due to convenience for exporting the results for the purging model. The density of the inclusions was considered to be equal to the density of the borosilicate particles used in the physical model, which corresponds to 340 kg/m^3.

The inclusions were injected through several horizontal planes with a close space between them. The goal here was to consider as if the inclusions were perfectly homogeneous in the ladle. To represent that, 11 planes were created normal to the ladle's Y-axis (vertical direction), with a spacing of 5 mm between each plane, and one inclusion of each size was injected at each mesh cell contained in a plane. Altogether, 279 inclusions of each size were injected in each plane. The inclusion sizes considered were: 20 µm, 30 µm, 38 µm, 45 µm, 56 µm, 75 µm, 80 µm, 90 µm, 112 µm and 140 µm. The sizes were based on the inclusion size distribution shown in Figure 4.3. The first injection plane was located 5 mm above the ladle bottom.

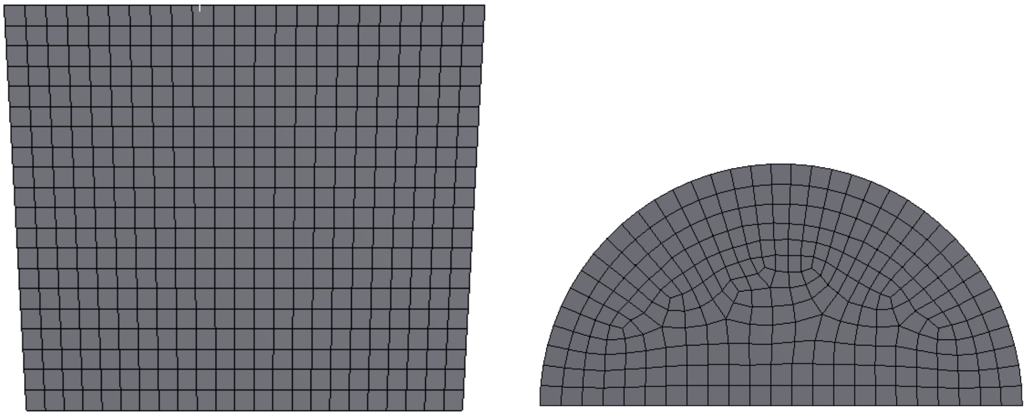

Figure 4.5: Mesh for the Transport Stage Simulation.

After the simulation of the behavior of the inclusions floating in the bath at rest during 7 minutes, the resulting positions of all simulated inclusions were exported to an ".his" file, which can be opened by programs such as *Microsoft Excel* and allows for the creation of injection files for the initial locations of the inclusions in the next simulation stages.

4.1.3 Gas Purging Model

In the gas purging stage, the objective is to model how the gas injection in the ladle affects the flow pattern and inclusion behavior. The inclusions could be captured at the top surface or they could move with the flow and end up being carried into the tundish during the teeming stage, if they are not removed before.

A region of great interest in the geometric domain in this stage is the plume region. Since there will be high velocity gradients and different phases coexisting at this location, it is important to have a more refined mesh there. High quality cells are also very important when doing multiphase mathematical modeling. Therefore, a hexahedral mesh was built for the purging model, with a local refinement in the plume region. Further details about the mesh are described in the mesh independency study section of the present work, located in the Results and Discussion chapter. The mesh has approximately 106,000 cells. In order to reduce the computational effort, only ½ of the geometric domain was modeled, with the symmetry plane passing through the purging plug.

Another region of concern during meshing is the boundary layer at the walls. Since there are velocity gradients close to the walls, it is important to have at least a few elements in the boundary layer. To reduce computational costs, the near-wall flow was modeled with the use of scalable wall functions. This approach does not resolve the flow all the way to wall, but uses semi-empirical formulas instead, to bridge the wall-affected flow results to the bulk flow. This reduces significantly the need for mesh refinement at the walls, with consequent economy of computational resources. Scalable wall functions have also the advantage of allowing for arbitrary refinement of the near-wall mesh, being better than Standard wall-functions which show poor results if the near-wall mesh is refined too much.

Several different approaches are available to mathematically model the gas purging phenomenon. In the present work, this stage was modeled through two different methods. In the first method, the Eulerian multiphase model was adopted to account for the dispersed gas phase. The water/air interface was modeled through a free-slip wall boundary condition. Thus, this modeling approach will be referred in the present work as “Eulerian Flat Surface”. In the second method, the Volume of Fluid (VOF) multiphase model was adopted to represent both the injected gas and the air layer above the fluid domain, in order to represent the free surface at the interface. This modeling approach will be referred to as “VOF model” henceforward in the present work.

4.1.3.1 Eulerian Flat Surface Model

The modeling of this stage was divided in two steps: first a steady-state flow field obtained during the gas purging was calculated. Then, using this calculated flow field, the motion of the inclusions was calculated. This approach had the advantage of decoupling the simulations of the flow field and inclusions motion, however it had the disadvantage of not capturing the transient evolution of the flow. If the considered time for gas injection is not long enough for the steady state to be achieved, the velocities in the recirculating flow in the ladle might be over predicted. In order to check the validity of this approach, the cases in which the VOF model was adopted were run under a full transient approach.

The governing equations for the flow according to the Eulerian multiphase model are shown from Eq.4.4 to Eq.4.6, considering no mass transfer between the different phases:[46]

$$\frac{\partial}{\partial t}\left(\alpha_q \rho_q\right) = -\nabla \cdot \left(\alpha_q \rho_q \overrightarrow{u_q}\right) \tag{4.4}$$

$$\frac{\partial}{\partial t}\left(\alpha_q \rho_q \overrightarrow{u_q}\right) = -\nabla \cdot \left(\alpha_q \rho_q \overrightarrow{u_q}\,\overrightarrow{u_q}\right) - \alpha_q \nabla p + \nabla \cdot \overline{\overline{\tau_q}} + \alpha_q \rho_q \vec{g} + \vec{F}_{Drag,q} + \vec{F}_{Lift,q} + \vec{F}_{Virtual\ Mass,q} + \vec{F}_{Turbulent\ Dispersion,q} \tag{4.5}$$

$$\sum \alpha_q = 1 \tag{4.6}$$

Where α_q is the volume fraction of phase *q*, ρ_q is the density of phase *q*, $\overrightarrow{u_q}$ is the velocity vector for phase *q*, p is the pressure field shared by all phases, $\overline{\overline{\tau_q}}$ is the stress-strain tensor for phase *q*. This set of equations is solved separately for each phase when the Eulerian multiphase model is adopted and separate velocity fields are obtained for each phase. This model has the advantage of accounting for the relative velocity between the liquid and gas phase and also of giving accurate results for both regions of high and low gas holdup. Therefore, it is valid both in the vicinity of the plug, where gas holdup is high, and in the upper plume region, where significant dispersion has already occurred.

The drag law defined for the gas/liquid interaction was the Grace model. This drag correlation is calibrated for water/air bubbly systems, similarly to the experiment being modeled. The Eulerian model requires the mean bubble diameter as an initial input and this data was obtained from the camera measurements performed by Silva[2,48] and is shown in Table 4.2:

Table 4.2: Mean Bubble Diameters considered in the simulations.

Gas Flow Rate (L/min)	Mean Bubble Diameter (mm)
2	2,5
5	4,0
10	3,5

Non-drag interaction forces are also important in water/air bubbly systems. In the present study, the additional forces of lift, virtual mass and turbulent dispersion were considered. The lift force was modeled accordingly to the Tomiyama model, the virtual mass coefficient adopted was the default value of 0.5 and turbulent dispersion was modeled accordingly to the Simonin[45] model. The interfacial area model for the phase interaction was defined as the Particle model. Surface tension was enabled for this model, considering the Continuum Surface Force (CSF) model.

Turbulence was modeled through the Realizable k-ε model with turbulence generation by the bubbles motion enabled, through the Sato Turbulence Transfer model.

For the flow field calculation, the gas was injected through a mass-flow inlet boundary condition, applied to the porous plug surface area. Simulations were performed for the gas flow rates of 2, 5 and 10 L/min. A free-slip wall degassing boundary condition was applied at the top surface of the fluid domain. This boundary condition considers this surface as an outlet for the gas and a zero-shear stress surface for the liquid. For the ladle walls, a no-slip wall boundary condition was applied.

The numerical solver was configured to adopt the Phase-Coupled SIMPLE scheme for the pressure-velocity coupling. Spatial discretization was defined as 2nd Order Upwind for the Momentum equations and 1st Order Upwind for the other variables. The under-relaxation parameters had to be modified from the default values, due to solution divergence happening during the calculations. Table 4.3 lists the adopted values in the present study.

Table 4.3: Under-relaxation parameters for the Purging Simulation.

Variable	Under-relaxation factor
Pressure	0.03
Density	0.1
Body Forces	0.1
Momentum	0.07
Volume Fraction	0.05
Turbulent Kinetic Energy	0.08
Turbulent Dissipation Rate	0.08
Turbulent Viscosity	0.1

The limit for residuals convergence was set as equal to 10^{-4}. However, residuals convergence alone is not the most adequate measurement of convergence, especially for complex multiphase flows. A more suitable assessment of convergence is the monitoring of results of interest as the iterations progress. When the monitored results stop varying, that means the solution has achieved convergence. Therefore, in the simulations of the present work, the average velocity and average turbulent kinetic energy were monitored in order to make sure a converged solution was obtained, since these two variables give a good notion of the flow pattern development in the ladle. Also, the mass conservation for the gas phase is an important result to monitor, since for a converged solution, the rate of mass of gas leaving the domain through the top surface must be equal to the rate of mass flowing in at the inlet.

Once a converged solution for the flow field was obtained, the inclusions paths were solved. The inclusions were injected at the same positions where they were located at the end of the ladle transport stage (7 minutes at rest). For the inclusion fate calculation, just a single iteration needs to be performed, with the flow equations being deactivated. Similarly to what was done in the Transport stage, the inclusions were modeled as a discrete phase. The drag law chosen to model the interaction between the inclusions and the liquid phase was the Spherical drag law. Additional forces included in the calculations were the Virtual Mass and Pressure Gradient forces. Finally, to account for the random motion of particles in the turbulent flow, the Discrete Random Walk model was activated. The governing equation for the particle motion is very similar to what has been considered in the Transport stage, but with the additional forces of Virtual Mass and Pressure Gradient, as shown in Eq.4.7:[46]

$$\frac{d\overrightarrow{u_p}}{dt} = \frac{\vec{u} - \overrightarrow{u_p}}{\tau_r} + \frac{\vec{g}\,(\rho_p - \rho)}{\rho_p} + \overrightarrow{F_{VM}} + \overrightarrow{F_{PG}} \qquad \textbf{(4.7)}$$

When the flow is turbulent, such as is the case for the purging stage in a ladle, the Discrete Random Walk model estimates the instantaneous fluid velocity at any location through the local value of the Turbulent Kinetic Energy, as shown in Eq.4.8 and Eq.4.9:

$$u = \bar{u} + u'(t) \qquad \textbf{(4.8)}$$

$$u' = \zeta \sqrt{\frac{2k}{3}} \qquad \textbf{(4.9)}$$

Here, $\bar{u}$ is the averaged flow velocity, $u'(t)$ is the random fluctuating velocity at a given time, ζ is a normally distributed random number and k is the turbulence kinetic energy.

The implication of including turbulent dispersion effects in the particle trajectory calculation is that, in regions of high turbulence, the particle is going to be subject to significant random velocity components by the surrounding fluid. When this effect is applied to a high number of different particles, the resulting effect is that each particle will follow a different trajectory, thus promoting a dispersion of the particles in these locations of high turbulence.

The boundary conditions for the inclusion fate calculation were reflection at the ladle walls with perfect momentum restitution (restitution coefficient equal to 1.0) and capture at the top surface (restitution coefficient equal to zero). The effect of varying the restitution coefficient at the top surface was also investigated in the present work.

The normal coefficient of restitution defines the amount of momentum in the direction normal to the wall that is retained by the particle after the collision with the boundary, as shown in Eq.4.10:[49]

$$e_n = \frac{u_{p2,n}}{u_{p1,n}} \tag{4.10}$$

Where $u_{p,n}$ is the particle velocity normal to the wall and subscripts 1 and 2 refer to before and after collision, respectively. Similarly, the tangential coefficient of restitution, e_t, defines the amount of momentum in the direction tangential to the wall that is retained by the particle. A normal or tangential coefficient of restitution equal to 1.0 implies that the particle retains all of its initial normal or tangential momentum after the rebound. If the coefficient is equal to zero, it means that the particle retains none of its normal or tangential momentum after the collision. Intermediate values mean that the particle will rebound but will retain only a fraction of its initial momentum.

After one iteration covering a time step of 80 seconds, which is equivalent to the time duration of the water modeling experiments, the number of inclusions captured by the top surface can be obtained. The more efficient the gas purging treatment, the more inclusions should be captured by the top layer. Moreover, the final positions and velocities of the remaining inclusions can be exported for the next stage, where the liquid is going to be drained from the ladle.

4.1.3.2 Volume of Fluid (VOF) Model

Many studies in the literature[14,41,42] have shown that the behavior of the top liquid surface in a ladle purging simulation should not be approximated by a flat wall. The agitation caused by the bubbles disturbs the top surface and its oscillations affect the overall flow pattern in the ladle. Consequently, it would also have an effect on the inclusion motion in the ladle.

In the present study, the first attempt to consider this behavior was through the Eulerian model with the Multi Fluid VOF enabled. The advantages of this approach would be that both the velocity fields for the liquid and gas phases would be calculated separately, and the gas/liquid interface would also be captured. However, the disadvantage was that the model showed a very unstable initialization, diverging in the first iterations. Moreover, solving the flow for both the liquid and bubble phases with the additional complexity of calculating the free surface would be computationally expensive.

The alternative was to model the gas purging stage not through the Eulerian model, but instead through the Volume of Fluid method. By choosing the VOF model, just a single velocity field would be solved and shared by all phases. While this is a disadvantage regarding not capturing the bubble slip velocities and other relevant phenomena such as bubble dispersion and turbulence generation by bubbles, the model showed much more stability and did not diverge at the beginning. Computational time was also improved under this approach, since solving a single velocity field greatly reduced the processing time. Therefore, this approach was chosen to model the purging stage considering the free surface at the top. The governing equations for the VOF model are shown from Eq.4.11 to 4.14:[49]

$$\frac{\partial \rho}{\partial t} = -\frac{\partial}{\partial x_i}(\rho u_i) - \frac{\partial}{\partial x_j}(\rho u_j) - \frac{\partial}{\partial x_k}(\rho u_k) \tag{4.11}$$

$$\begin{aligned} &\rho\left(\frac{\partial u_i}{\partial t} + u_i\frac{\partial u_i}{\partial x_i} + u_j\frac{\partial u_i}{\partial x_j} + u_k\frac{\partial u_i}{\partial x_k}\right) \\ &\quad = \left(\mu\frac{\partial^2 u_i}{\partial {x_i}^2} + \mu\frac{\partial^2 u_i}{\partial {x_j}^2} + \mu\frac{\partial^2 u_i}{\partial {x_k}^2}\right) - \frac{\partial P}{\partial u_i} + \rho g_x + F_S \end{aligned} \tag{4.12}$$

$$\frac{\partial \alpha_q}{\partial t} + \vec{u} \cdot \nabla \alpha_q = 0 \tag{4.13}$$

$$\sum \alpha_q = 1 \tag{4.14}$$

It is interesting to notice that Eq. 4.11 and 4.12 are very similar to the conservation equations for a single-phase flow, as shown in Section 3.2.2.1 (Eq. 3.17 and 3.19). The main difference is the addition of the surface tension force term F_S in Eq. 4.12. The surface tension force acts in the interface in order to minimize the free energy by decreasing the interfacial area.

For this model, there are not as many available options to consider varied drag formulations and non-drag forces, as there were for the Eulerian model. Moreover, since a single velocity field is solved and shared by all phases, the plume is treated as a continuum instead of a dispersed phase. If the mesh was refined enough, it would be even possible to solve the bubbles formation directly. However, for it to be possible, the mesh cell size would need to be significantly smaller than the bubbles, which is clearly not viable for most applications due to the high associated computational cost.

Since the oscillations at the top surface and its influence on the overall flow pattern are of interest, a steady-state model cannot be applied when following this approach. Therefore, a transient run was performed. A time step size of 0.001 second was considered to simulate a purging time of 80 seconds. Therefore, 80,000 time steps were necessary for the simulation. Since a transient calculation was performed, the equations for the Discrete Phase representing the inclusions were solved simultaneously with the transient flow calculations. The governing equations for the inclusions motion are the same as shown for the Eulerian Flat Surface model (Eq.4.7 to 4.9). For the inclusion behavior at the interface, since there is not a boundary condition to be specified at this location (due to the interface being in the interior of the domain), an User Defined Function (UDF) was adopted to specify the inclusion behavior there. More details about this UDF are described in Section 4.2 of the present study.

For these simulations, the pressure-velocity coupling was handled by the SIMPLE scheme. 2nd order upwind discretization schemes were applied for the momentum equation and 1st order upwind for the other equations. The Compressive scheme was chosen for the volume fraction discretization. Although the Geo-Reconstruct gives a sharper interface, this model also includes the gas plume, which would not be adequately represented by a too sharp interface, since the mesh is not fine enough to directly model the bubbles. Moreover, as the top interface is composed only of good quality structured cells, the Compressive scheme would give good results for interface resolution, at a lower computational cost. Table 4.4 shows the under relaxation parameters used for the simulations performed under this approach.

Table 4.4: Under relaxation parameters for the VOF Purging Simulation.

Variable	Under-relaxation factor
Pressure	0.3
Density	0.1
Body Forces	0.1
Momentum	0.7
Turbulent Kinetic Energy	0.8
Turbulent Dissipation Rate	0.8
Turbulent Viscosity	1

4.1.4 Ladle Teeming Model

After all the necessary treatments were performed during the secondary metallurgy step of steelmaking, the steel must be teemed into the tundish, beginning the Continuous Casting step of the production. In many steelmaking plants, the steel in the ladle is not completely transferred to the tundish because vortex formation and collapse of the slag interface. This condition can cause severe contamination of the steel in the tundish. For many applications, the steel in the tundish should be as clean as possible. Therefore, many steelmakers interrupt the ladle teeming just before the slag layer collapses.

Inclusions which, at the end of the purging stage, stay in the upper portion of the bath, have a higher chance of not flowing into the tundish and either become entrapped in the top surface or stay in the ladle in the residual steel melt after the teeming process is interrupted. Therefore, a more efficient purging treatment would also contribute to have more inclusions displaced towards the upper ladle region, in such a way that even if they are not captured by the slag, at least they would not flow into the tundish before the nozzle is closed.

Therefore, in the teeming stage of the present work, the objective of the simulation is to count how many inclusions are carried into the tundish. The counting is performed until air starts flowing into the nozzle, which would be analogous to a slag layer collapse. Moreover, in the experiments, the counting was interrupted also when air started flowing into the nozzle, because it caused interference with the APS probe. Consequently, it makes sense from both the experimental and industrial perspectives, to perform the inclusion counting only up until this moment.

At this stage, the most relevant feature which needs to be resolved in the flow is the position of the water/air interface, since it will influence the moment when the counting will be interrupted and also whether an inclusion reaches the free surface before it flows down the nozzle. Therefore, a finer mesh resolution was adopted in the vertical direction. A region of interest for mesh refinement is the cylinder just above the nozzle. Since the water/air interface collapsing phenomenon occurs just above the nozzle, it is desirable to have a finer mesh resolution at this location to capture more accurately the interface deformation at this moment. More details about the mesh are described in the mesh independency study, in the Results and Discussion section (Section 5.2.1).

The modeling of the ladle teeming was performed according to the VOF model, since the interface position was the most relevant flow feature to be resolved. The governing equations for this model have been shown in the previous section (Eq.4.11 to 4.14 in Section 4.1.3.2) and are the same for the teeming model. Figure 4.6 show the initial phase distribution for the ladle teeming calculations, where phase-1 is the water phase.

A mass-flow outlet boundary condition was applied at the nozzle, with the flow rate value defined as 20.6 L/min. This value caused the ladle to be completely drained after 11 minutes of teeming. In the experiments by Silva[2,42,48], the flow rate decreased as the teeming progressed, due to the reduction of the height of the water column. However, in the real industrial conditions, the flow rate is usually kept steady by flow control systems. Taking this into account, Silva[48] normalized his inclusion counting results in order to make them equivalent to a constant flow rate scenario. In the present work, since it is actually simpler to set up a constant flow rate in the mathematical model, and it is also closer to the industrial reality, the flow rate was kept constant for the entire simulation.

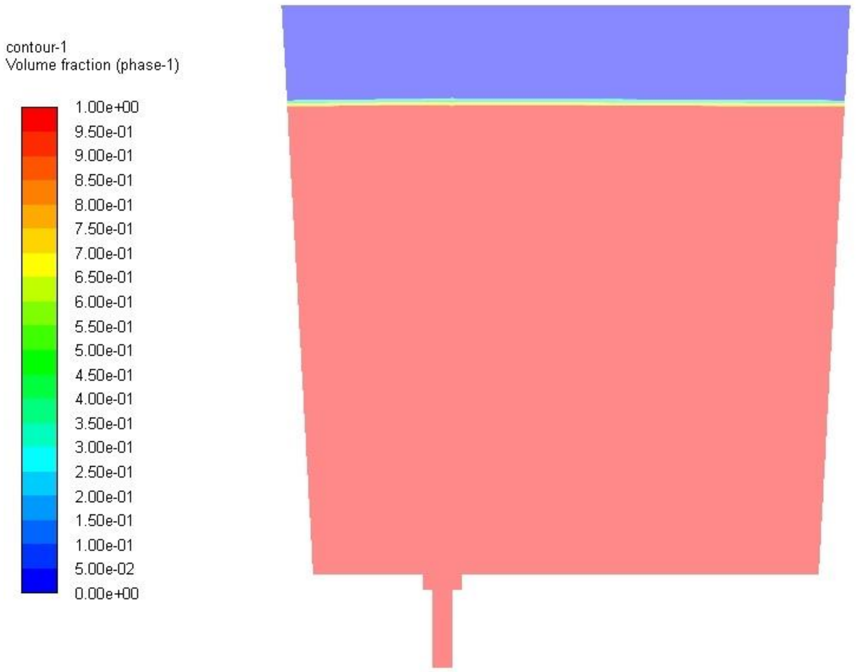

Figure 4.6: Initial phase distribution for the teeming stage model.

Since the boundary condition at the top of the ladle is an opening where air can flow freely inwards or outwards, it is necessary to account for an air layer free board, so as not to apply the boundary condition at the steel domain. A pressure inlet boundary condition was applied at the top surface. Only air was allowed to enter the domain through this surface. No-slip boundary conditions were applied at the walls. The surface tension between the phases was considered constant according to the Continuum Surface Force model. Turbulence was modeled with the Standard k-ε model with scalable wall functions.

For the solver settings, the PISO scheme was chosen to handle the pressure-velocity coupling, due to its good performance for transient flows. The momentum equations were discretized with the 2nd order upwind scheme, while the other variables used 1st order upwind. For the volume fraction equation, the Geo-Reconstruct scheme was adopted, which gives the best interface capturing performance among all available schemes in ANSYS Fluent. The underrelaxation parameters adopted were the same used in the purging model calculations, already described in Table 4.3.

Residual convergence was defined as 10^{-3}, which is the default value for ANSYS Fluent. Since this stage requires a transient simulation, a too tight convergence criterion could be too expensive computationally. The time step for the calculation was defined as 0.01 second, therefore 66,000 time steps were necessary to cover the whole time range of the teeming.

The inclusions which were not captured by the top layer in the purging stage were injected at the same positions where they were at the end of the previous stage. Their velocity at that moment was also recorded and input as an initial condition for the teeming simulation. In order to count how many inclusions passed through the nozzle, an inclusion report was written at every 1000 time steps (10 seconds). These reports give the positions and velocities of every inclusion in the domain. Using it, it is possible to calculate how many inclusions passed through the outlet, since they would disappear from the domain. The report also gives information on the size of the inclusions. From this information, it is possible to evaluate the inclusion removal efficiency of a given purging treatment and compare different configurations.

Two different conditions for the inclusion behavior at the interface were simulated. In the first condition, the inclusions which reached the interface stayed there for the rest of the computations. In the second condition, the inclusions which floated into the interface were removed from the computations through an UDF. Since using both conditions for all simulations would make for a very high number of simulations, the first condition was applied to the simulations in which the Eulerian Flat Surface model was adopted in the purging stage, while the second condition was applied to the simulations in which the VOF model was adopted in the purging stage. The influence of the inclusion capture condition was evaluated.

4.2 User-Defined functions to Modify Inclusion Capture Behavior

User-Defined functions (UDFs) are C or C++ functions that can be dynamically loaded with the ANSYS Fluent solver to enhance its standard features. UDFs can be used to customize mathematical models such as the multiphase or discrete phase models used in a simulation.

In the present work, UDFs were adopted mainly to modify the inclusion capture behavior at the top surface. A simple inclusion capture criterion by the mathematical model would have the inclusion capture rate consistently increasing with the flow rate, as the collision probability would be higher with increased flow kinetic energy. In reality, under intense stirring conditions, the inclusion would likely not be able to attach to the top surface and would revert to the bulk flow. Thus, it is necessary to prepare the mathematical model to limit the inclusion capture only to regions below a certain intensity of stirring.

Another issue which demanded the usage of UDFs was the definition of inclusion capture at locations which were not boundaries of the domain. In the simulations in which the VOF model was used, the interface between the liquid phase and the atmospheric air was in the interior of the domain, not in the boundaries. Thus, the standard DPM capture boundary conditions available in Fluent could not be used. It was necessary to write an UDF to define that, at the fluids interface, the inclusions would be captured. The condition of capture only in low stirring areas was also included in this UDF. The condition of inclusion capture adopted was that an inclusion would be captured only if it touched the top surface having a velocity smaller than 0.1 m/s. This criterion was defined arbitrarily, based on the order of magnitude of the velocities observed in the ladle in the results of the present work, with the objective of limiting the capture of the inclusions with the most kinetic energy. Although this is a reasonable assumption, it is definitely necessary that a more advanced criterion based on physical principles such as interfacial forces between the particles and the interface be developed. Unfortunately, such a development was not done in the present work.

Although the UDFs presented in this section have a significant effect on the final result of inclusion capture ratio, they did not change significantly the mathematical model robustness. Therefore, all other assumptions and boundary conditions were kept the same as already described in the previous sections.

Figure 4.7 shows the UDF adopted for the conditional inclusion capture criterion as a boundary condition in the Eulerian Flat Surface model. Since this UDF was defined as a DPM Boundary Condition, it can only be applied at a boundary of the domain, thus being useful only for the Eulerian Flat Surface model, in which the water/air interface is located at the boundary of the domain.

```
/* boundary condition for conditional inclusion capture criterion */
#include "udf.h"
DEFINE_DPM_BC(inc_capture,tp,t,f,f_normal,dim)
{
real vn = 0.;
real vmax = 0.1;
real nor_coeff = 1.0;
real tan_coeff = 1.0;
real normal[3];
int i;
int idim;

idim = dim;

```

```
for(i=0; i<idim; i++)
normal[i] = f_normal[i];

if (NV_MAG(TP_VEL0(tp)) > vmax)
{
/* Compute normal velocity. */
for(i=0; i<idim; i++)
vn += TP_VEL(tp)[i]*normal[i];

/*Subtract off normal velocity. */
for (i=0; i<idim; i++)
TP_VEL(tp)[i] -= vn*normal[i];

/*Apply tangential coefficient of restitution. */
for(i=0; i<idim; i++)
TP_VEL(tp)[i] *= tan_coeff;

/*Add reflected normal velocity. */
for(i=0; i<idim; i++)
TP_VEL(tp)[i] -= nor_coeff*vn*normal[i];

/* Store new velocity in TP_VEL0 of particle. */
for(i=0; i<idim; i++)
TP_VEL0(tp)[i] = TP_VEL(tp)[i];

return PATH_ACTIVE;
}

else
{
return PATH_ABORT;
}
}
```

Figure 4.7: UDF for the conditional inclusion capture criterion as a boundary condition in the Eulerian Flat Surface model.

For the inclusion removal criterion to be considered in the simulations in which the VOF model was adopted, a different UDF needed to be developed. Figure 4.8 shows the UDF adopted in the VOF model simulations.

```
/* inclusion capture condition at the water air interface in the VOF model */
#include "udf.h"
DEFINE_DPM_SCALAR_UPDATE(inc_capture_vof,c,t,initialize,tp)
{
real vn = 0.;
real vmax = 0.1;
real nor_coeff = 0.001;
real tan_coeff = 1.0;
real normal[3];
real f_normal[3];
real vof_surface = 0.1;
real bath_height = 0.6;
int i;
int air;
int idim;

/*Problem Dimensions: */
idim = 3;

/*Phase Domain index for the air phase:*/
air = 1;

/*Margin of error for the bath height, considering oscillations: */
bath_height *= 0.95;

/*Since it is not a boundary, i need to specify the normal direction to the free surface: */

f_normal[0] = 0;
```

```
f_normal[1] = 1;
f_normal[2] = 0;

for(i=0; i<idim; i++)
normal[i] = f_normal[i];

/*Condition of the particle touching the free surface and/or the plume in the homogeneous model:*/

Thread *psink;
psink = THREAD_SUB_THREAD(t,air);

if (C_VOF(c, psink)>vof_surface)
{
if (TP_POS(tp)[1] > bath_height) /*Differentiating plume from surface */
{
if (NV_MAG(TP_VEL0(tp)) > vmax) /*Reflect particle */
{
/* Compute normal velocity. */
for(i=0; i<idim; i++)
vn += TP_VEL(tp)[i]*normal[i];

/*Subtract off normal velocity. */
for (i=0; i<idim; i++)
TP_VEL(tp)[i] -= vn*normal[i];

/*Apply tangential coefficient of restitution. */
for(i=0; i<idim; i++)
TP_VEL(tp)[i] *= tan_coeff;

/*Add reflected normal velocity. */
for(i=0; i<idim; i++)
TP_VEL(tp)[i] -= nor_coeff*vn*normal[i];

/* Store new velocity in TP_VEL0 of particle. */
for(i=0; i<idim; i++)
TP_VEL0(tp)[i] = TP_VEL(tp)[i];

}

else
{
tp -> stream_index = -1; /*Abort particle */
}
}
}
}
```

Figure 4.8: UDF for the conditional inclusion removal at the water/air interface in the VOF model.

Finally, there was also an UDF developed to be adopted in the teeming stage simulations, to consider inclusion removal when they reached the interface during teeming. This UDF is very similar to the one shown in Figure 4.8, with the difference that it needs less inputs, so that some lines of the code were deactivated. The effect of including this UDF was assessed by comparing the inclusion removal results obtained with and without its adoption.

```
/* inclusion removal criterion at the water air interface in the VOF model for the teeming stage */
#include "udf.h"
DEFINE_DPM_SCALAR_UPDATE(inc_capture_vof,c,t,initialize,tp)
{
/* real vn = 0.;
real vmax = 0.1;
real nor_coeff = 0.001;
real tan_coeff = 1.0; Not used in teeming, only purging stage*/
real normal[3];
real f_normal[3];
```

```
real vof_surface = 0.1;
/* real bath_height = 0.6; Not used in teeming, only purging stage */
int i;
int air;
int idim;

/*Problem Dimensions: */
idim = 3;

/*Phase Domain index for the air phase:*/
air = 1;

/*Margin of error for the bath height, considering oscillations: */
/* bath_height *= 0.95; */

/*Since it is not a boundary, i need to specify the normal direction to the free surface: */

f_normal[0] = 0;
f_normal[1] = 1;
f_normal[2] = 0;

for(i=0; i<idim; i++)
normal[i] = f_normal[i];

/*Condition of the particle touching the free surface and/or the plume in the homogeneous model:*/

Thread *psink;
psink = THREAD_SUB_THREAD(t,air);

if (C_VOF(c, psink)>vof_surface)
{
/* if (TP_POS(tp)[1] > bath_height)*/ /*Differentiating plume from surface */
/* {
if (NV_MAG(TP_VEL0(tp)) > vmax)*/ /*Reflect particle */
/* {*/
/* Compute normal velocity. */
/* for(i=0; i<idim; i++)
vn += TP_VEL(tp)[i]*normal[i];*/

/*Subtract off normal velocity. */
/* for (i=0; i<idim; i++)
TP_VEL(tp)[i] -= vn*normal[i];*/

/*Apply tangential coefficient of restitution. */
/* for(i=0; i<idim; i++)
TP_VEL(tp)[i] *= tan_coeff;*/

/*Add reflected normal velocity. */
/* for(i=0; i<idim; i++)
TP_VEL(tp)[i] -= nor_coeff*vn*normal[i];*/

/* Store new velocity in TP_VEL0 of particle. */
/* for(i=0; i<idim; i++)
TP_VEL0(tp)[i] = TP_VEL(tp)[i];*/

/* }

else*/
/* { */
tp -> stream_index = -1; /*Abort particle */
/* }
} */
}
}
```

Figure 4.9: UDF for the conditional inclusion removal at the water/air interface in the VOF model for the teeming stage.

4.3 Validation of the Mathematical Model

The predictions of the different mathematical models discussed in the previous sections were compared to the results of the water modeling experiments developed by Silva[2].The objective of this comparison is to identify the mathematical model that is more adequate to describe the behavior of the inclusions during gas injection and ladle teeming.

The experimental setup considered the same ladle geometry adopted in the simulations shown previously. Many of the relevant information about the experiments have already been presented in the mathematical model description section of the present study. Therefore, only specific details not yet mentioned are going to be described in the next paragraphs.

Counting of inclusions at the outlet of the ladle during its drainage was carried out using an APS probe, which also determines the size distribution of the inclusions. Figure 4.10 shows a picture of the APS probe used in the lab experiments. This probe consists of a glass tube with an orifice in its edge where the particles can pass through. The orifice has 500 µm and sucks the liquid continuously while the experiments are performed. Two electrodes, one inside and another outside the tube, measure the voltage of the fluid.

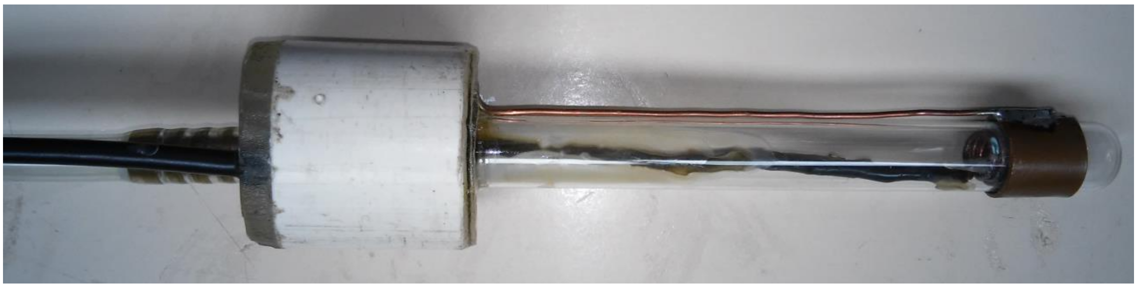

Figure 4.10: APS Probe.[36]

The working principle of the probe is described in detail in the works of Silva[2,43,44] and Chakraborty[51]. The steps for the execution of the experiments are described in detail in the work by Silva[2,43,44].

The APS probe used in the experiments was able to measure inclusions in the range of 20 µm to 170 µm. For the probe to work properly, the principle of the “Electric Sensing Zone” (ESZ) had to be respected, which means that only one particle could pass through the orifice at a time. The meaning of this was that there would be a maximum particle concentration in the system to assure that there would not be more than one particle passing through the probe at a given time, confusing the system and leading to errors. (CHAKRABORTY[51])

The maximum inclusion concentration allowed in the system for the ESZ principle to be respected was calculated by Silva[2] and found to be equal to 4.24×10^9 particles per cubic meter. A safety factor of 10 was adopted in the experiments, therefore the number of inclusions injected was calculated to be proportional to 4.24×10^8 inclusions per cubic meter.

Considering that the ladle being considered in the experiments and simulations has 227 liters of water, the initial number of inclusions in the ladle can be estimated through Eq. 4.15:

$$4.24\ x\ 10^8\ \frac{inclusions}{m^3}\ x\ 0.227\ m^3 = 9.62\ x\ 10^7\ inclusions \tag{4.15}$$

The value of 9.62×10^7 inclusions in the ladle has been obtained considering the estimated inclusion concentration predicted by Silva[2], in which the average inclusion diameter of 38 µm has been considered for the calculations.

Another way to calculate the amount of inclusions in ladle at the beginning of the experiments is through the injected mass of inclusions reported by Silva[2].

Multiplying the reported concentration of the injection solution (48 g/L) by the volume of solution injected (20 mL):

$$48\ \frac{g}{L}\ x\ 0.020\ L = 0.96\ g\ of\ inclusions\ injected \tag{4.16}$$

Table 4.5 and Table 4.6 show the calculations of the number of inclusions in the ladle based on the mass of inclusions injected and the size distribution data from analyses performed on samples of the particles injected in the experiments. Q3 is the accumulated percentage of inclusions up to the diameter value being considered. For example, at the third row, the Q3 value of 5.53% together with a diameter value of 10 µm means that 5.53% of the sample has diameter equal or less than 10 µm.

Table 4.5: Calculations of the initial number of inclusions in the Ladle based on the inclusions size distribution. First Sample.

Q3 (%)	d (µm)	Accumulated mass (kg)	Inclusions mass at each diameter range (kg)	Mass of a single inclusion (kg)	Number of Inclusions at each diameter range
1.27	1	1.21E-05	1.21E-05	1.78E-16	6.81E+10
2.61	5	2.49E-05	1.28E-05	2.23E-14	5.75E+08
5.53	10	5.28E-05	2.79E-05	1.78E-13	1.57E+08
10.21	15	9.75E-05	4.47E-05	6.01E-13	7.44E+07
16.05	20	1.53E-04	5.58E-05	1.42E-12	3.92E+07
30.3	30	2.89E-04	1.36E-04	4.81E-12	2.83E+07
42.41	38	4.05E-04	1.16E-04	9.77E-12	1.18E+07
52.5	45	5.01E-04	9.64E-05	1.62E-11	5.94E+06
67.16	56	6.41E-04	1.40E-04	3.13E-11	4.48E+06
86.83	75	8.29E-04	1.88E-04	7.51E-11	2.50E+06
90.08	80	8.60E-04	3.10E-05	9.11E-11	3.41E+05
94.7	90	9.05E-04	4.41E-05	1.30E-10	3.40E+05
99.12	112	9.47E-04	4.22E-05	2.50E-10	1.69E+05
100	140	9.55E-04	8.41E-06	4.88E-10	1.72E+04

Table 4.6: Calculations of the initial number of inclusions in the Ladle based on the inclusions size distribution. Second Sample.

Q3	d (mu)	Accumulated mass (kg)	Inclusions mass at each diameter range (kg)	Mass of a single inclusion (kg)	Number of Inclusions at each diameter range
1.27	1	1.30E-05	1.30E-05	1.78E-16	7.30E+10
2.61	5	2.52E-05	1.22E-05	2.23E-14	5.49E+08
5.53	10	4.98E-05	2.45E-05	1.78E-13	1.38E+08
10.21	15	8.83E-05	3.85E-05	6.01E-13	6.41E+07
16.05	20	1.37E-04	4.89E-05	1.42E-12	3.43E+07
30.3	30	2.59E-04	1.22E-04	4.81E-12	2.53E+07
42.41	38	3.64E-04	1.06E-04	9.77E-12	1.08E+07
52.5	45	4.55E-04	9.01E-05	1.62E-11	5.55E+06
67.16	56	5.90E-04	1.36E-04	3.13E-11	4.35E+06
86.83	75	7.90E-04	1.99E-04	7.51E-11	2.65E+06
90.08	80	8.26E-04	3.67E-05	9.11E-11	4.02E+05
94.7	90	8.81E-04	5.52E-05	1.30E-10	4.25E+05
99.12	112	9.41E-04	5.92E-05	2.50E-10	2.37E+05
100	140	9.55E-04	1.44E-05	4.88E-10	2.95E+04

Table 4.7 show the average values over the two samples and the total number of inclusions in the ladle at the beginning of the experiments. For this calculation, the inclusions which had a diameter less than 20 µm were not considered, since the APS

probe is not able to detect particle sizes smaller than 20 µm. Therefore, the total number of countable inclusions at the beginning is 8.86 x 10^7 inclusions. The second column shows the fraction of the total number of inclusions that is represented by each diameter value. It can be seen that the smaller inclusions, with diameter equal or less than 30 µm, make for more than 70% of the total amount of inclusions in the system. On the other side, larger inclusions, which diameter is larger than 90 µm represent less than 1% of the total amount of inclusions.

Table 4.7: Initial number of inclusions at the beginning of the experiments. Average values from the two samples.

Number of inclusions at the diameter range	%	Diameter (µm)
3.68E+07	41.5%	20
2.68E+07	30.3%	30
1.13E+07	12.8%	38
5.75E+06	6.5%	45
4.41E+06	5.0%	56
2.58E+06	2.9%	75
3.71E+05	0.4%	80
3.83E+05	0.4%	90
2.03E+05	0.2%	112
2.34E+04	0.0%	140
8.86E+07	**100.0%**	**Sum of countable inclusions**

In order to calculate the total number of inclusions counted in the mathematical model, its results are going to be extracted from the model in terms of percentages of inclusions of each size that stay in the top surface or pass through the nozzle, relative to the initially injected number of inclusions in the model. Then, these percentage values were multiplied by the initial number of inclusions in the experiments, as calculated in Table 4.7. By following this procedure, it is possible to relate the mathematical results to the size distribution considered in the experiments. All results show in the present work follow this calculation procedure, unless stated otherwise.

4.4 APS Probe Model

In order to understand the relationship between the number of inclusions counted by the APS probe and the total amount of inclusions which flow through the nozzle, a separate model was developed to simulate the inclusions flow into the probe. The flow through the probe is much lower than the total flow in the nozzle, as has been measured by Silva[2]. Therefore, it was necessary to verify whether the number of inclusions counted by the probe would be representative of the total amount of inclusions passing in the nozzle. Figure 4.11 shows the geometric domain considered in the model developed to simulate the flow of inclusions through the APS probe.

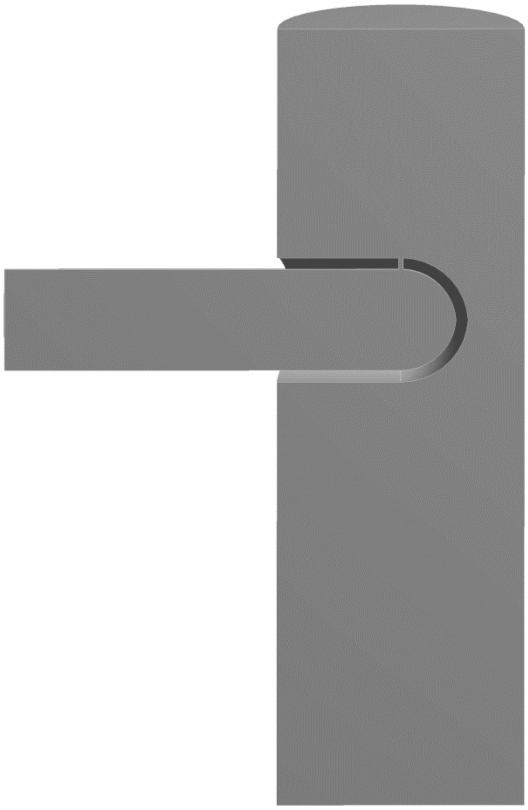

Figure 4.11: Geometric Domain for the APS Probe Simulation.

The APS probe dimensions were measured to provide the necessary information for its geometric modeling. The inner diameter of the probe was found to be equal to 12.8 mm and the horizontal distance between the orifice and the tip of the tube was found to be equal to 7 mm. The inner diameter of the nozzle was found to be equal to 25 mm. The orifice diameter was equal to 0.5 mm.

Figure 4.12 shows the mathematical model mesh for the APS probe simulation. The mesh had a total of 107,000 nodes and 432,000 elements. Particularly the probe orifice was a region which drove up the mesh requirements, since the orifice had much lower dimensions that the rest of the domain. Therefore, smaller cells had to be adopted to mesh this region.

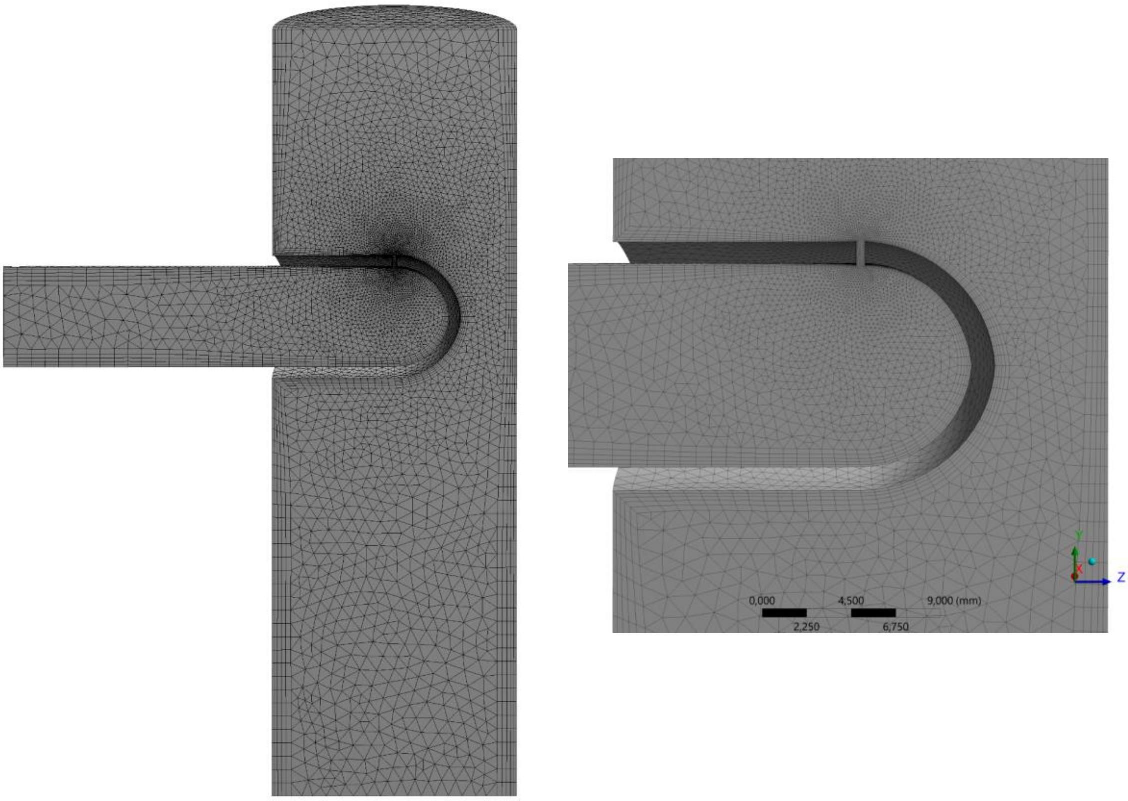

Figure 4.12: Mesh for the APS probe simulation.

The boundary conditions applied to this model were:

- Mass-flow-inlet at the top boundary, corresponding to the water mass flow rate through the nozzle;
- Mass-flow-outlet at the probe outlet boundary, corresponding to the measured water flow rate at the probe in the experiments;
- Constant pressure-outlet at the lower boundary, corresponding to where the water flow leaves the experimental system;
- Symmetry at the front plane, which passes through the probe orifice;
- No-slip walls at all other boundaries;

The steady-state flow field was calculated for the system through the SIMPLE scheme for pressure-velocity coupling and the 1st order upwind scheme was chosen for the discretization of all variables except the momentum, which adopted a 2nd order upwind discretization.

After the flow field was calculated, a representative number of inclusions was injected into the system representing the inclusion sizes of 20, 30, 38, 45 and 56 µm, which were the most representative sizes which were counted in the teeming stage calculations. The inclusions calculations were performed according to the Discrete Phase model, considering a spherical drag law and the additional non-drag forces of virtual mass and pressure gradient. Turbulent dispersion effects were considered according to the Discrete Random Walk model. The governing equations for the Discrete Phase are the same as Eq. 4.7 to 4.9, presented in Section 4.1.3.1 of the present study.

The results of these calculations allowed for the estimation of the ratio between the number of inclusions counted by the probe and the real number of inclusions flowing through the ladle nozzle. This knowledge was necessary in order to compare the experimental results with the results obtained from the mathematical model.

4.5 Presentation of the Results

The inclusion counting results obtained from the mathematical model were presented according to the percentage of removed inclusions (PRI). Since there are several different steps in the developed mathematical model, the PRI can also be measured in several different ways.

The *Absolute PRI* was defined as the percentage of removed inclusions comparing the amount of inclusions which passed through the nozzle during the ladle teeming and the initial amount of inclusions in the system, as shown in Eq.4.17:

$$Absolute\ PRI = \left(1 - \frac{Inclusions\ passing\ through\ the\ nozzle}{Initial\ amount\ of\ inclusions\ in\ the\ system}\right) x\ 100\% \qquad \textbf{(4.17)}$$

The *Relative PRI* was defined as the ratio between the amount of inclusions passing through the nozzle during teeming after a given purging treatment and the amount of inclusions passing through the nozzle during teeming when no purging treatment was applied (Reference configuration), as shown in Eq.4.18:

$$Relative\ PRI = \left(1 - \frac{Inclusions\ counted\ in\ the\ Case\ being\ studied}{Inclusions\ counted\ in\ the\ Reference\ Case}\right) x\ 100\% \qquad \textbf{(4.18)}$$

Another relevant result for the present work is the *Purging Stage PRI*. Since the teeming stage simulations are time consuming, it is sometimes convenient to evaluate the amount of inclusions removed considering only the Purging Stage, such as when evaluating the effect of the time duration of the purging treatment on the PRI. The definition of the *Purging PRI* is shown in Eq.4.19:

$$Purging\ PRI = \left(1 - \frac{Inclusions\ in\ the\ system\ after\ purging}{Inclusions\ in\ the\ system\ before\ purging}\right)\ x\ 100\% \tag{4.19}$$

Alternatively, the Purging PRI can also be measured regarding the initial amount of inclusions in the system, before the resting time, giving the *Absolute Purging PRI*:

$$Abs.Purg.PRI = \left(1 - \frac{Inclusions\ in\ the\ system\ after\ purging}{Initial\ amount\ of\ inclusions\ in\ the\ system}\right)\ x\ 100\% \tag{4.20}$$

5. RESULTS AND DISCUSSION

5.1 Flow field results during the Purging Stage – Eulerian Flat Surface Model

5.1.1 Mesh Independency Study and General Flow Pattern Evaluation

In order to evaluate the influence of the mesh in the purging simulations results, the results for three meshes of different resolutions were compared. Such comparison will be shown in this section. Figure 5.1, Figure 5.2 and Figure 5.3 show the meshes which were studied. For this section, a gas flow rate of 5 L/min was considered.

The parameters which determine the resolution of each of these meshes are shown in Table 5.1, which also lists the number of cells of each mesh. Figure 5.4 shows the edges where the radial divisions mesh control was applied. The example shown is for Mesh 1.

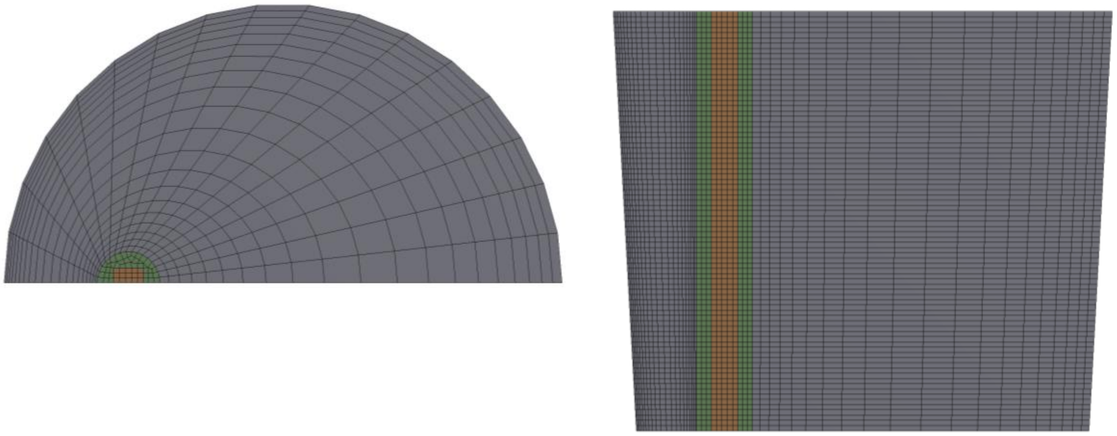

Figure 5.1: Mesh 1.

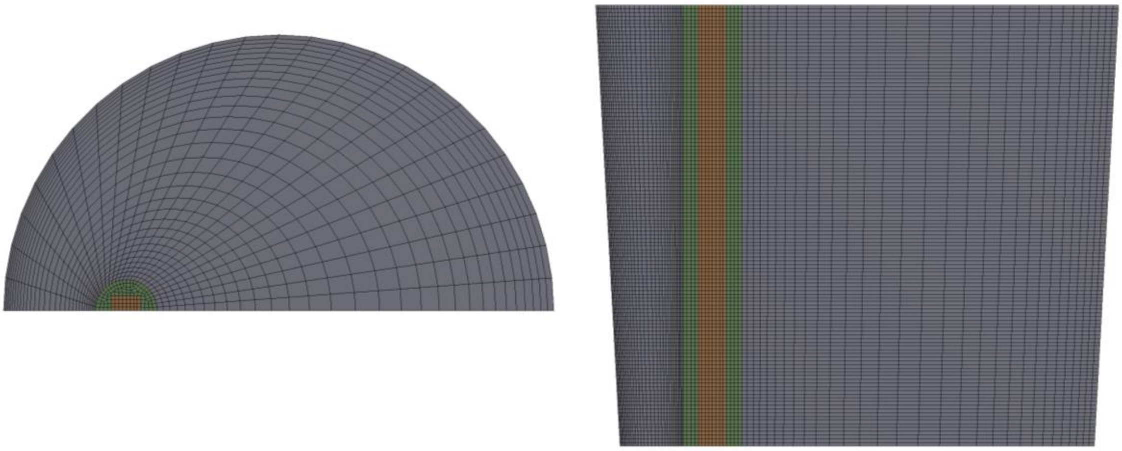

Figure 5.2: Mesh 2.

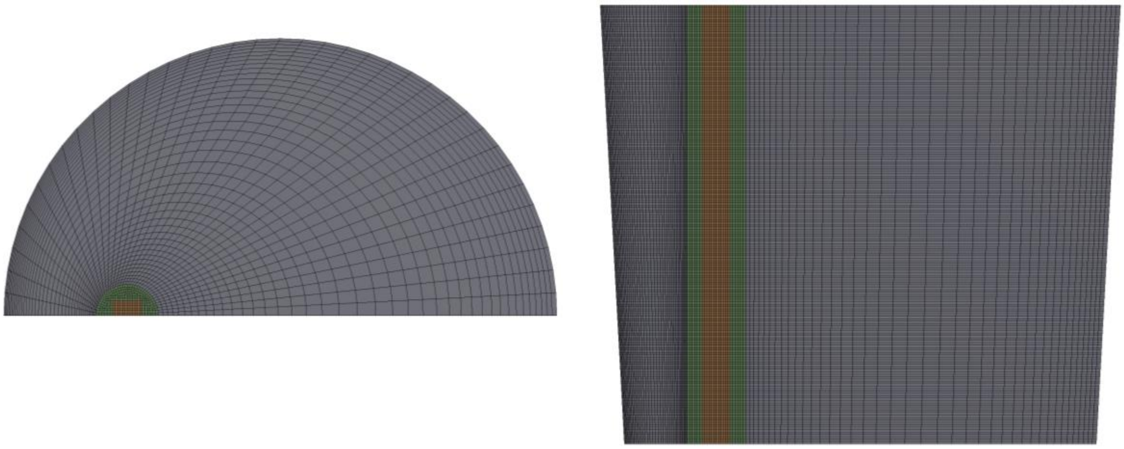

Figure 5.3: Mesh 3.

Table 5.1: Mesh Independency Study Parameters. Purging stage simulations.

Configuration	Element Size	Body Sizing Plume	Radial Divisions	Cells
Mesh 1	45 mm	7.5 mm	20	32,000
Mesh 2	30 mm	5 mm	30	107,000
Mesh 3	30 mm	3.3 mm	40	324,000

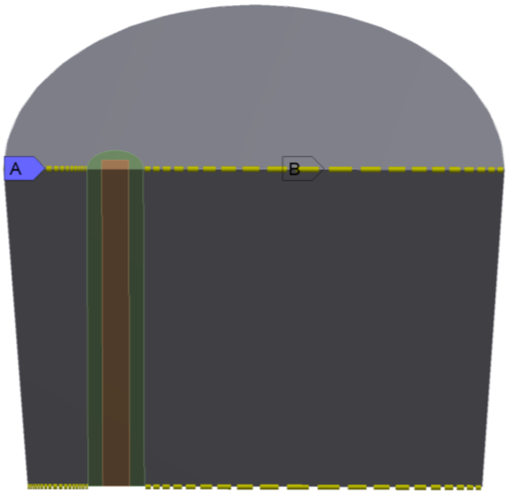

Figure 5.4: Mesh Radial Divisions. (Mesh 1)

Figure 5.5 and Figure 5.6 show the velocities contours for the three different meshes. Figure 5.5 shows the results for the front symmetry plane, while Figure 5.6 shows the results for the top surface. It can be seen that the existing differences between the results are very small, especially considering that the mesh resolution has been significantly altered (by a factor of approximately 3, as can be seen in Table 5.1).

The main features of the flow are the strong upward velocities in the plume region, which cause a large recirculation loop that encompasses almost the entire ladle.

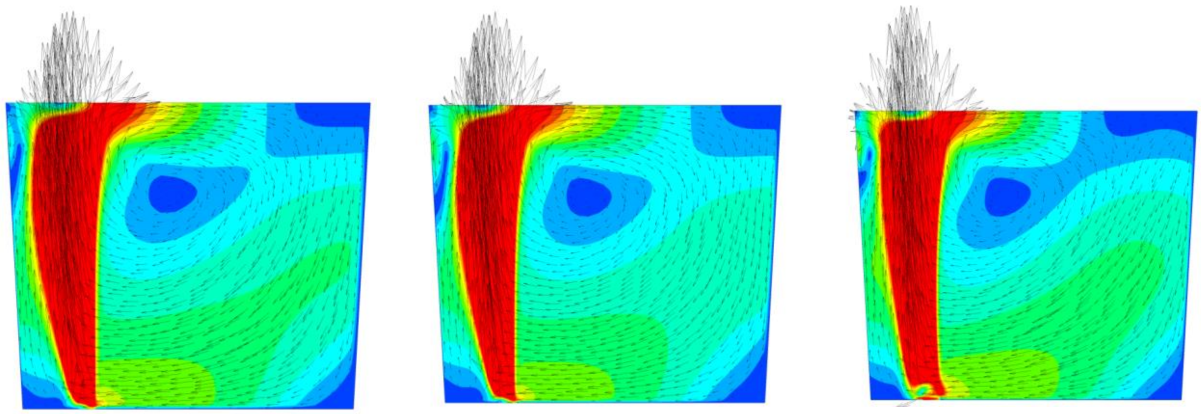

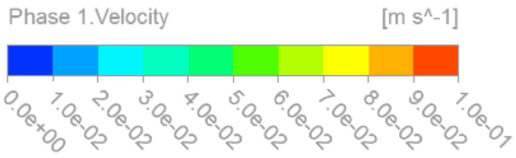

Figure 5.5: Velocities Contour for the Mesh Independency Study.

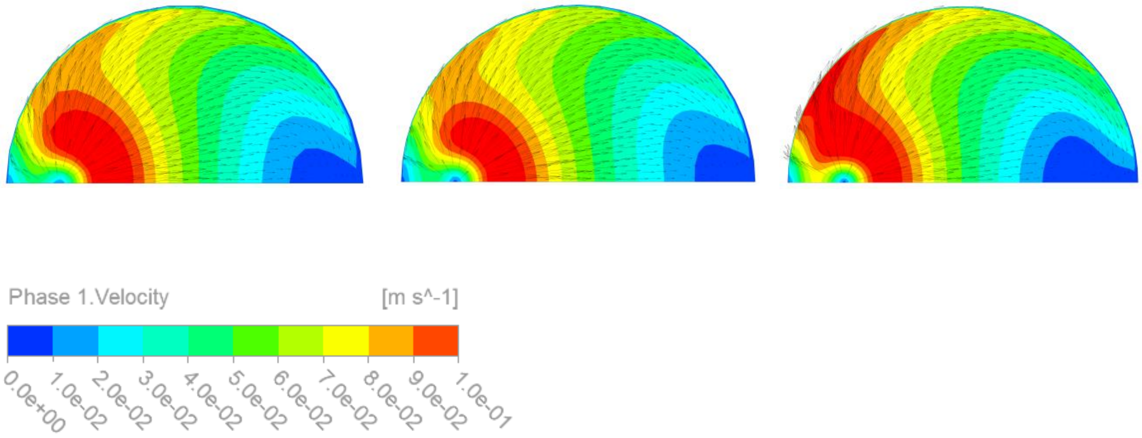

Figure 5.6: Velocity Contour at the Top Surface for the Mesh Independency Study.

Figure 5.7 and Figure 5.8 show the distribution of Turbulent Kinetic Energy for the three different meshes. The results show that the turbulence is concentrated in the plume region, which makes sense since turbulence generation in this case is driven by:

- Shear between the high velocities at the plume and the low velocities in the rest of the ladle;
- Bubbles upward motion;
- Sudden change of direction of the flow when the plume reaches the top surface;

All of these factors contribute to concentrated turbulence in the plume vicinity and in the spout region. The three configurations showed the same pattern of turbulence in these regions, with some local differences at the plume rising region. The turbulence levels close to the top surface do not show significant variations, as it can be seen in Figure 5.8.

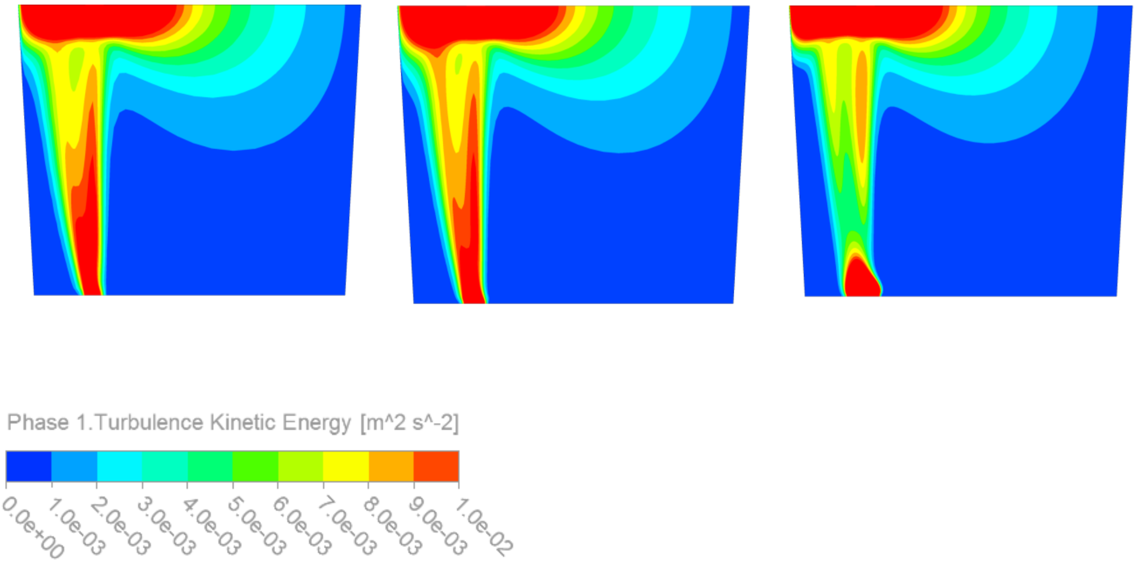

Figure 5.7: Turbulence Kinetic Energy Contour for the Mesh Independency Study.

Table 5.2 shows a comparison between results obtained with each mesh configuration. It can be seen that increasing the mesh resolution threefold led to variations in the range of 2-3% for average values of velocity and turbulence and for the amount of inclusions removed during the purging stage. The number of inclusions removed during the purging stage considers that 9207 inclusions were tracked at this stage in the mathematical model. Here, it is important to reinforce that the number of inclusions tracked in the mathematical model is not the same as the real number of inclusions in the experiments. The mathematical model tracks a representative number of inclusions and, according to the percentage of inclusions removed, the results are translated to the real amount of inclusions according to the size distribution being considered.

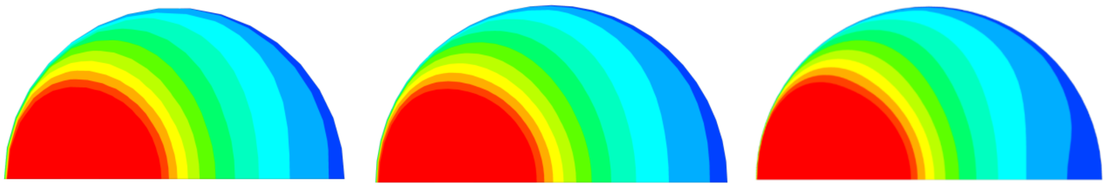

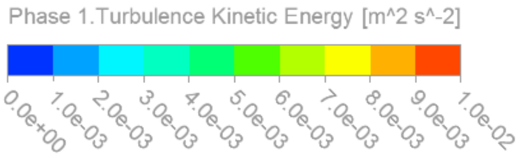

Figure 5.8: Turbulence Contour at the Top Surface. Mesh Independency Study.

Figure 5.9, Figure 5.10 and Figure 5.11 show the distribution of the remaining inclusions in the ladle after 80 seconds of purging. The distribution is similar for the three cases and it can be observed that the remaining inclusions are dispersed around the ladle, due to the stirring caused by the gas purging. There is a higher concentration of inclusions in the middle of the ladle, matching the core of the recirculation loop that can be seen in the velocity contours shown in Figure 5.5. A possible reason for this phenomenon is that, due to turbulent random effects, inclusions are driven off regions where the turbulence is higher, such as the plume and the top surface. Some inclusions might end up in the core of the recirculation loop. Since at this location the velocities and turbulence levels are lower, the inclusions remain there for a long time, which leads to an accumulation of inclusions there.

Table 5.2: Mesh Independency Study Results.

Configuration	Average Velocity Steel(m/s)	Average Turbulence Kinetic Energy x 10^-3 (m^2 s^-2)	Removed Inclusions by Purging (for 1/2 ladle)
Mesh 1	0.4194	1.741	7434
Mesh 2	0.4027	1.702	7226
Mesh 3	0.4076	1.669	7362

Considering the results provided by the mesh independency study, Mesh 2 was adopted for the further simulations of the gas purging.

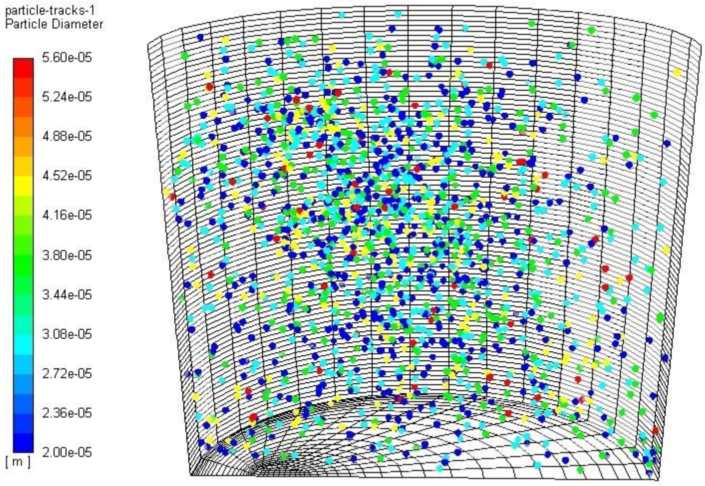

Figure 5.9: Inclusions remaining on the flow after 80 seconds of purging. Mesh 1.

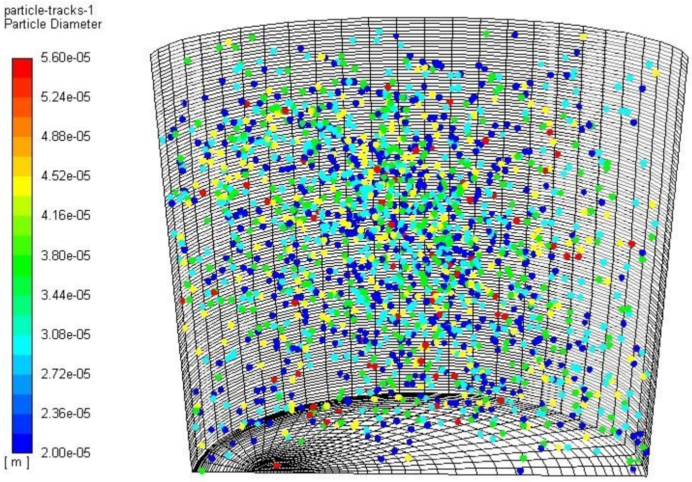

Figure 5.10: Inclusions remaining on the flow after 80 seconds of purging. Mesh 2.

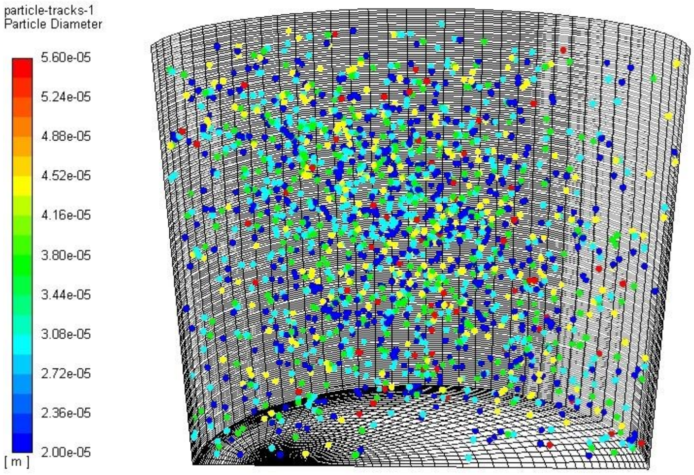

Figure 5.11: Inclusions remaining on the flow after 80 seconds of purging. Mesh 3.

In order to assess the overall quality of the mesh, there are some metrics which can be employed. The default quality measure in ANSYS Meshing is the *Skewness* metric. The *Skewness* of a mesh cell indicates how close this cell is to the ideal shape of an equilateral and equiangular cell. Figure 5.12 illustrates the difference between cells of ideal shape (zero *Skewness*) and highly skewed cells. Highly skewed cells should be avoided because they lead to less accurate results as compared to equilateral and equiangular cells.[52]

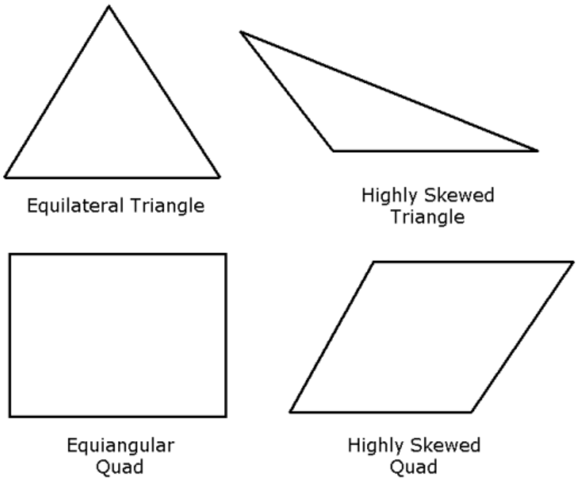

Figure 5.12: Skewness Mesh Metric.[41]

Table 5.3 shows a classification of cell quality according to its *Skewness* value:[52]

Table 5.3: Classification of Cell Quality according to the Skewness Value.[52]

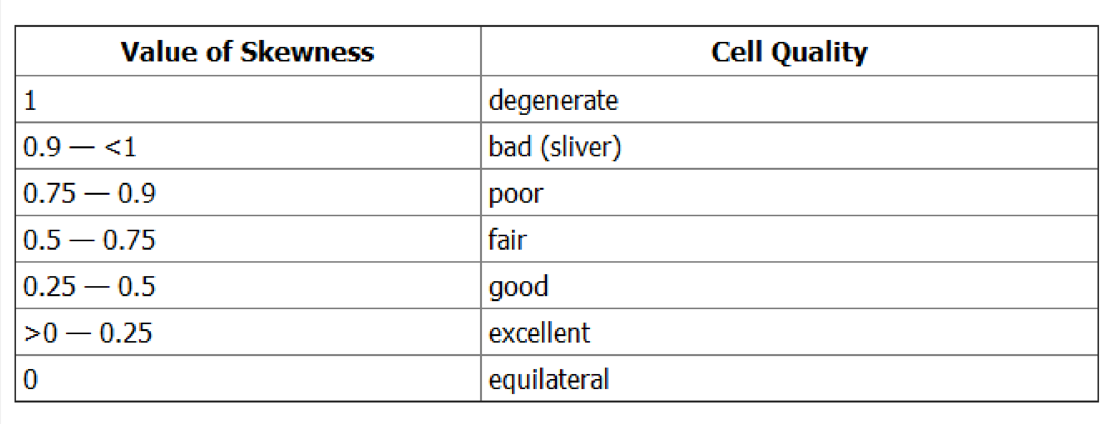

Value of Skewness	Cell Quality
1	degenerate
0.9 — <1	bad (sliver)
0.75 — 0.9	poor
0.5 — 0.75	fair
0.25 — 0.5	good
>0 — 0.25	excellent
0	equilateral

The *Skewness* measurement for the generated mesh is shown in Figure 5.13. The y-axis of the graph shows the number of cells which fall in the *Skewness* range shown in the x-axis. It can be seen that the huge majority of the cells are in the *Skewness* range classified as “Good” (< 0.5). The maximum S*kewness* obtained was equal to 0.58, and less than 2% of the cells (2,000 out of 106,000) show this value, which is fairly acceptable. Therefore, the mesh is adequate for the simulations to be performed in this study.

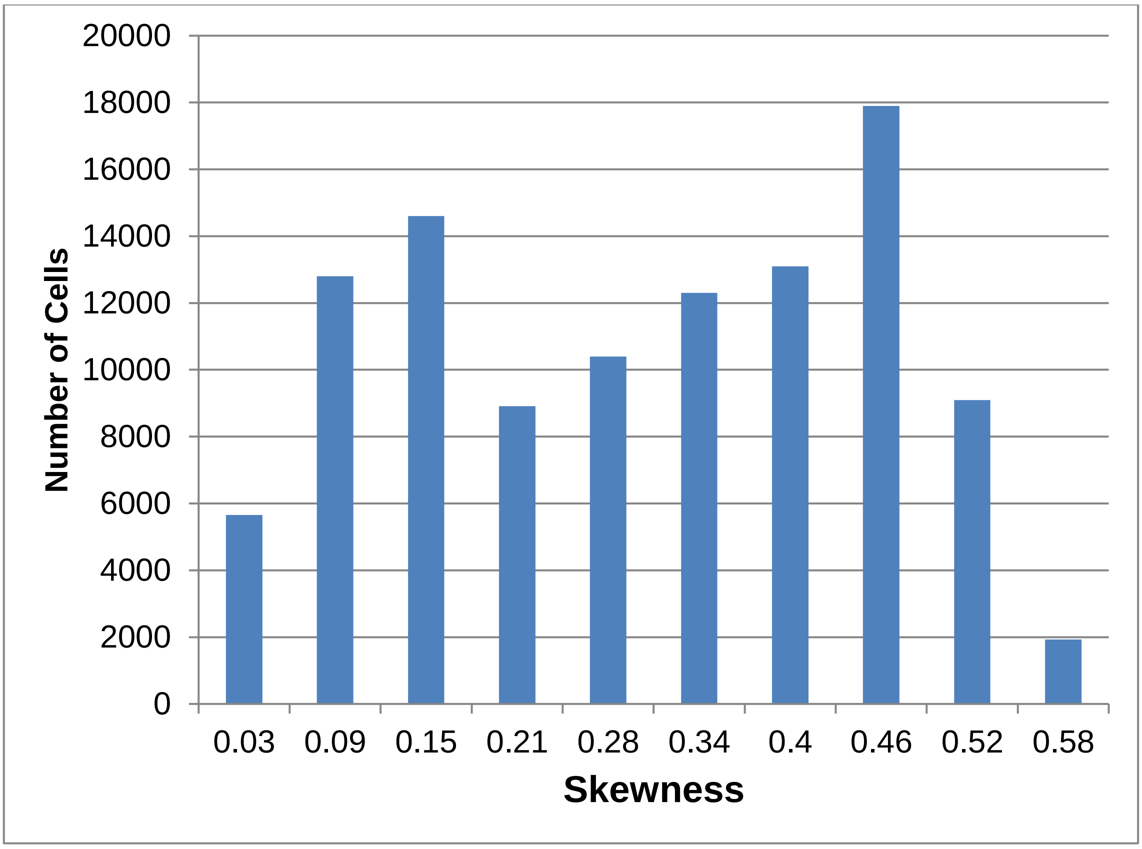

Figure 5.13: Measurement of Cell Skewness for the Purging Model Mesh.

5.1.2 Comparison of Flow Patterns for different gas purging flow rates

In this section, the flow patterns obtained through different gas flow rates were compared. The simulated configurations had the flow rates of 2, 5 and 10 NL/min. Figure 5.14 shows the velocity contours for the front symmetry plane, comparing the three configurations. Figure 5.15 shows the results for the top surface.

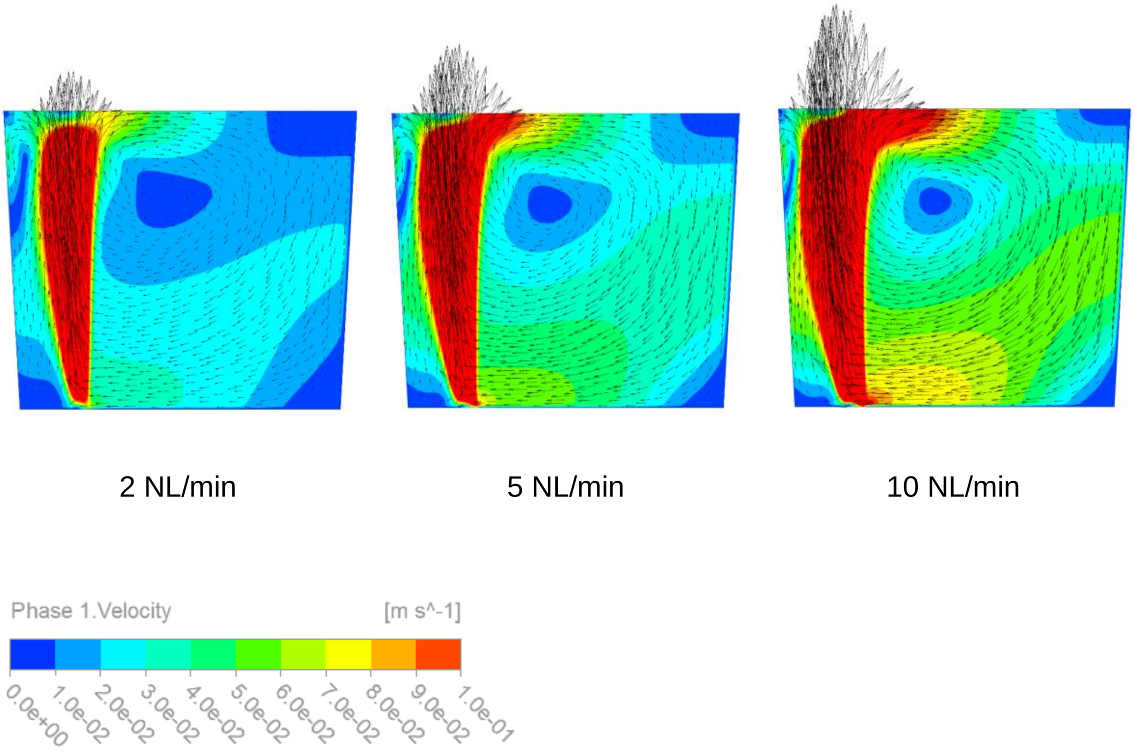

2 NL/min

5 NL/min

10 NL/min

Figure 5.14: Velocity Contours for different gas purging rates.

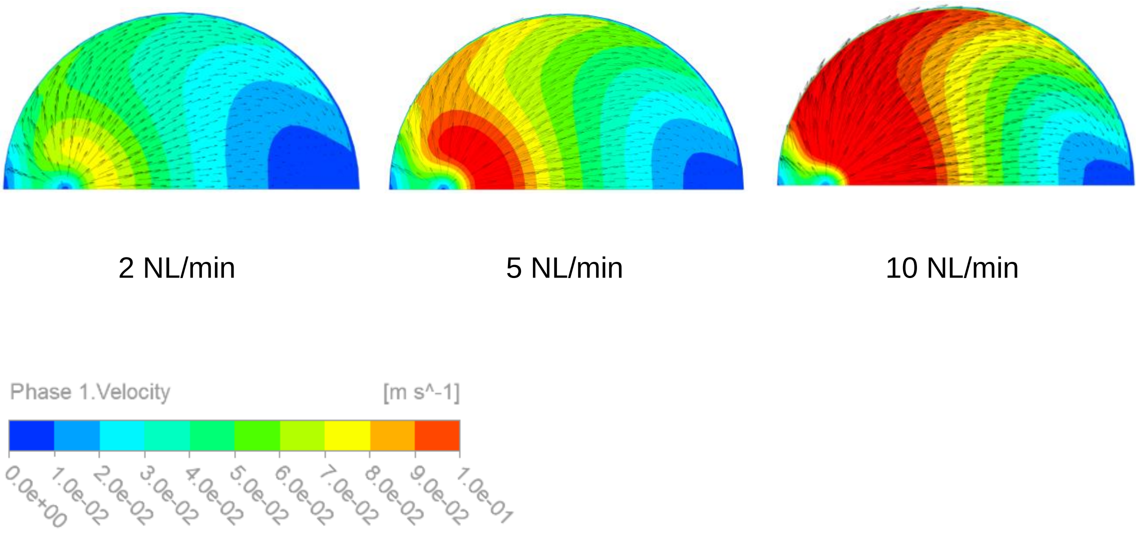

2 NL/min

5 NL/min

10 NL/min

Figure 5.15: Velocities at the Top surface for different gas flow rates.

It can be seen that the overall flow pattern is the same, regardless of the gas flow rate. All configurations show a similarly shaped recirculating flow driven by the upward plume bubbles motion. However, there is a significant increase in the overall velocities magnitude as the flow rate increases, which would be naturally expected.

At this point, it is important to highlight one limitation of the Eulerian multiphase model, adopted in these simulations. When applying this model, it is necessary to input the bubble diameter, which then is used to obtain relevant parameters of interphase transfer such as drag and interfacial area between the fluids. These parameters drive how much momentum is transferred from the plume to the bulk flow and have a profound influence in the entire ladle flow pattern. The problem arises when the same bubble diameter is adopted in the calculations for the entire domain. In real flows, there are complex phenomena of bubbles breakage and coalescence and these are significantly influenced by variations in the gas flow rate. Unfortunately, a simulation including all the effects of bubble breakage and coalescence would demand comprehensive experimental results for validation and a significant computational capacity and therefore is outside the scope of the present study. Nevertheless, it is important to account for the adopted model limitations when evaluating the results.

Figure 5.16 and Figure 5.17 show the contours for the turbulence kinetic energy. As the gas flow rate increases, the extent of the region subject to higher agitation increases together with the magnitude of the turbulence. Such a trend is expected, as it is straight forward that with higher gas flow rates, the stirring in the ladle should also be higher.

Figure 5.18 shows the gas volume fraction distribution, where phase-1 is the water phase and phase-2 is the gas phase. The plume dispersion effect can be seen for the three flow rates being studied. Furthermore, the values are higher for the case with the higher flow rate, as would be expected.

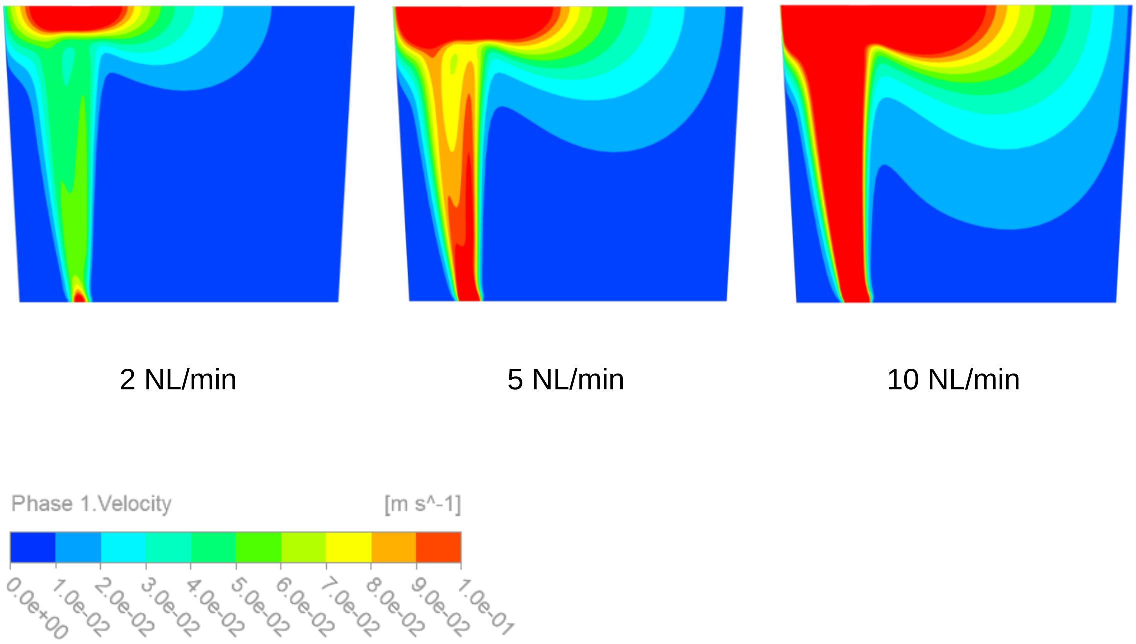

2 NL/min

5 NL/min

10 NL/min

Figure 5.16: Turbulence Kinetic Energy Contour for different gas flow rates.

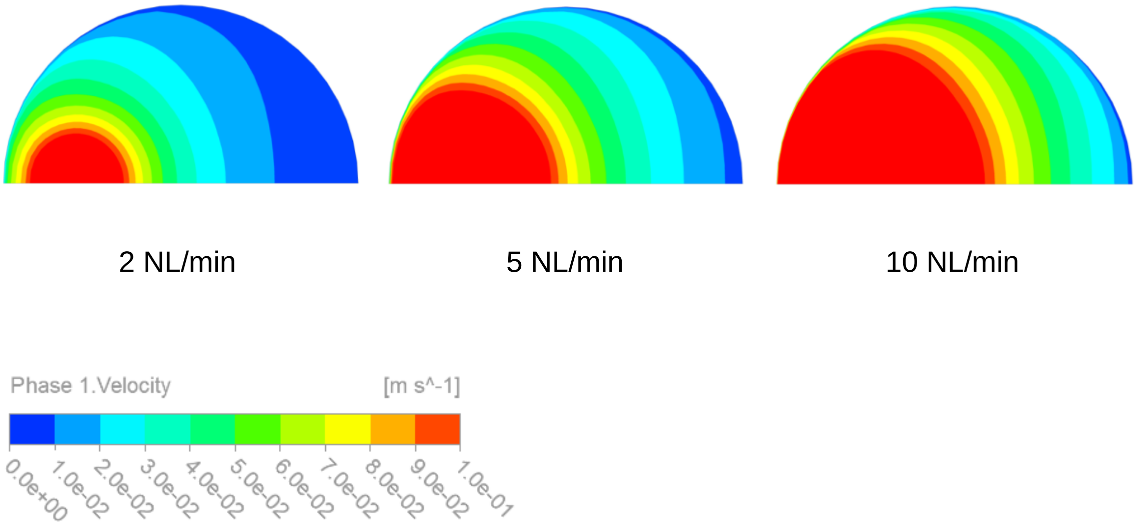

2 NL/min

5 NL/min

10 NL/min

Figure 5.17: Turbulence Kinetic Energy Contour at Top Surface for different gas flow rates.

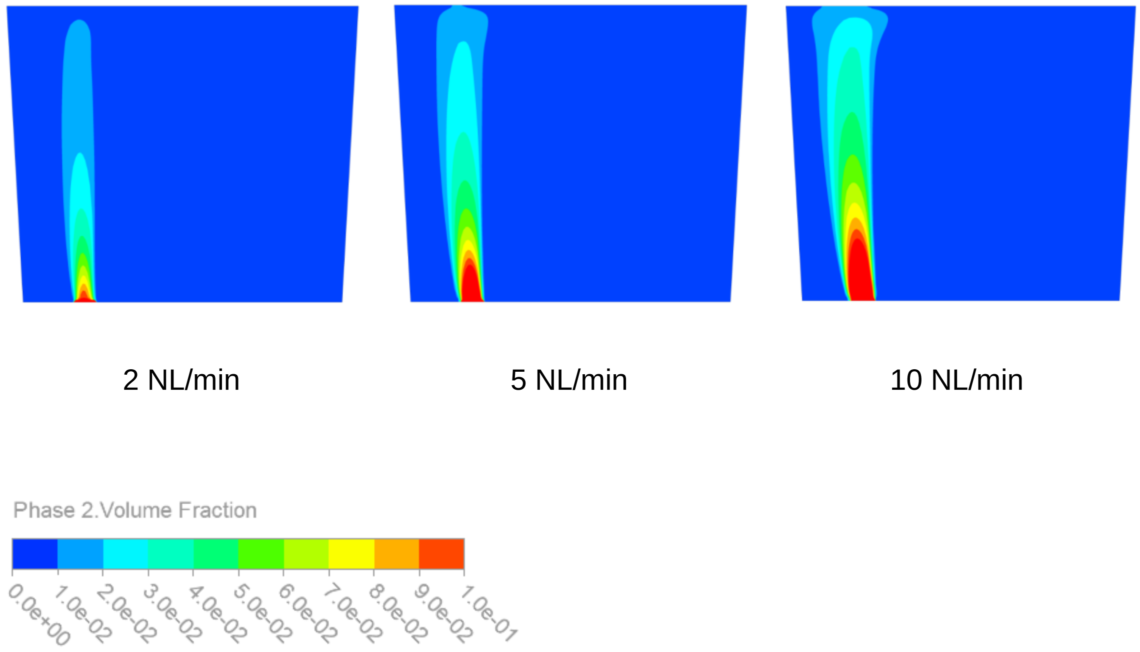

2 NL/min 5 NL/min 10 NL/min

Figure 5.18: Gas Volume Fraction contours for different gas flow rates.

5.2 Teeming Stage Flow Field Results

5.2.1 Mesh Independency Study

In order to evaluate the influence of the mesh in the results of the teeming simulations, the predictions for three meshes of different resolutions were compared. Such comparison will be shown in this section. Figure 5.19, Figure 5.20 and Figure 5.21 show the meshes which were studied. For this section, the inclusion distribution corresponding to the configuration with no gas purging was considered. This choice has the advantage of having a symmetric inclusion distribution, which allows for the adoption of a symmetric mesh, reducing the computational cost of these simulations.

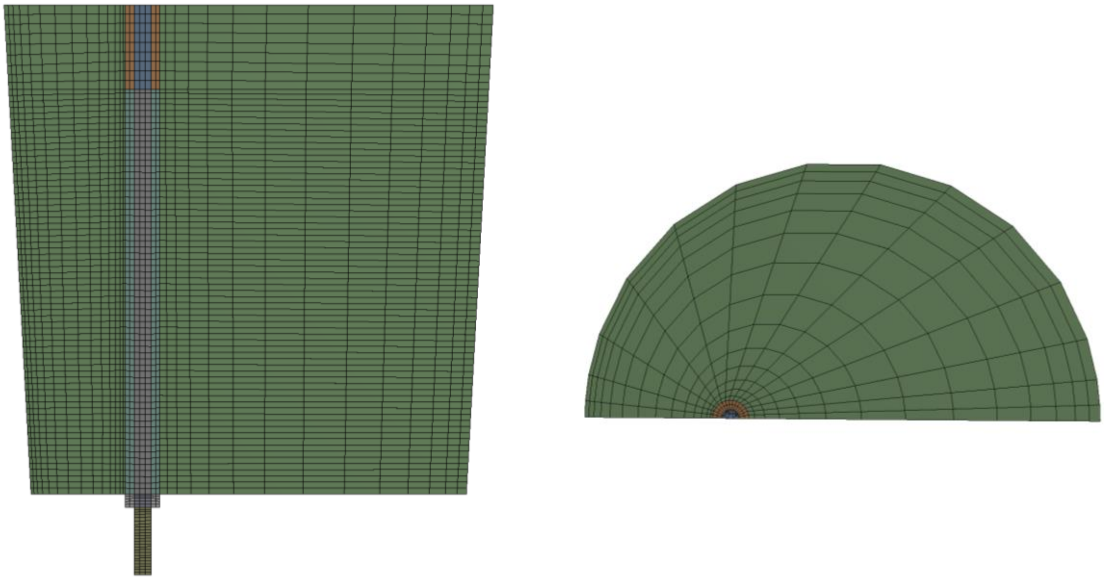

Figure 5.19: Mesh 1. Teeming stage mesh independency study.

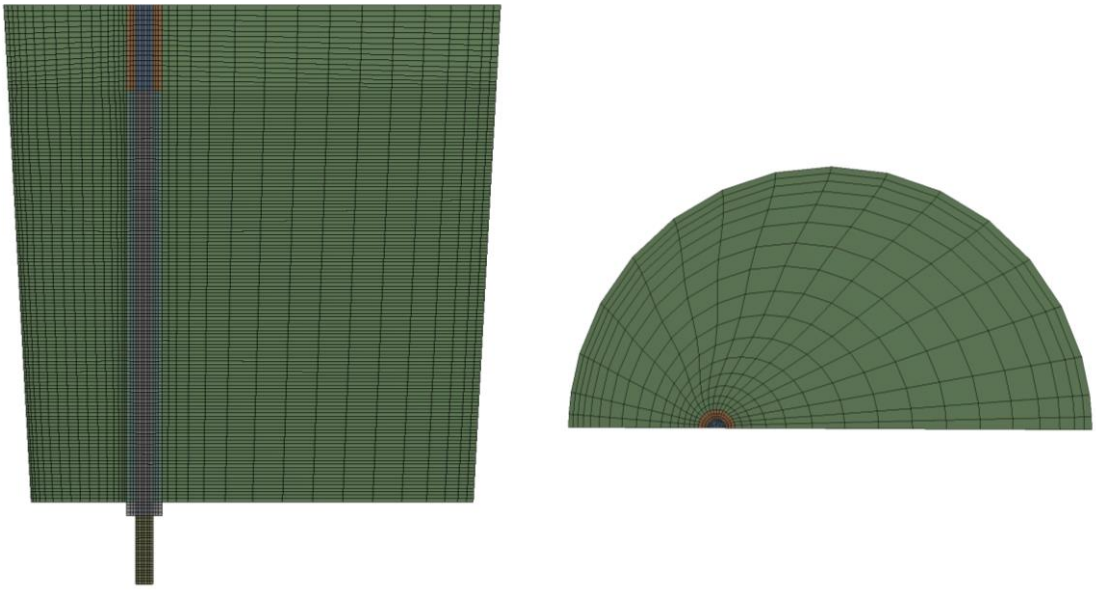

Figure 5.20: Mesh 2. Teeming stage mesh independency study.

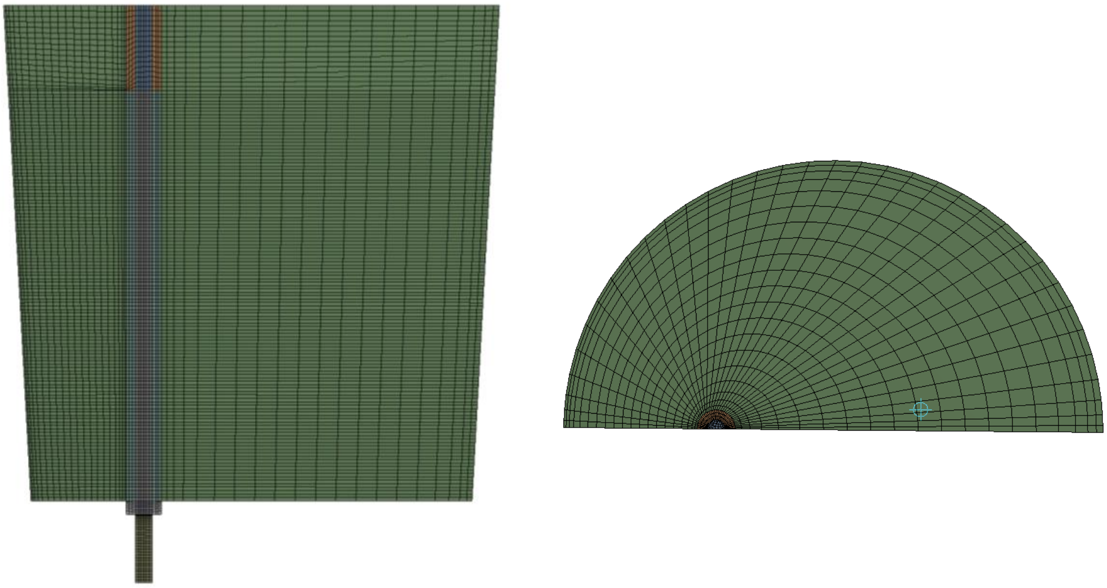

Figure 5.21: Mesh 3. Teeming stage mesh independency study.

Table 5.4 shows the considered parameters for each of the three meshes analyzed in the mesh independency study.

Table 5.4: Mesh Independency Study parameters. Teeming stage simulations.

Configuration	Element Size	Vertical Divisions (Liquid Region)	Cells
Mesh 1	50 mm	60	20,438
Mesh 2	30 mm	100	52,515
Mesh 3	20 mm	120	124,000

Figure 5.22 shows the volume fraction contour after 9 minutes of teeming time. It can be seen that the progress of the teeming process was not affected by the mesh resolution for the three meshes analyzed. The water/air interface is located at the same height for all cases. The interface gets sharper in the meshes with higher resolution, which is expected, but this did not have had a significant effect on the calculations.

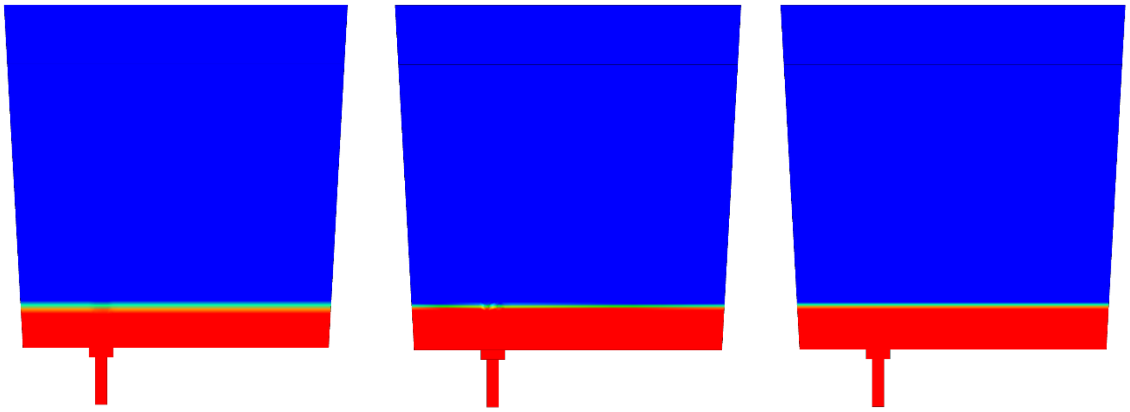

Figure 5.22: Volume Fraction Distribution after 9 minutes of teeming. Mesh Independency Study.

Figure 5.23 shows the velocity contours for the same time step, at 9 minutes of teeming.

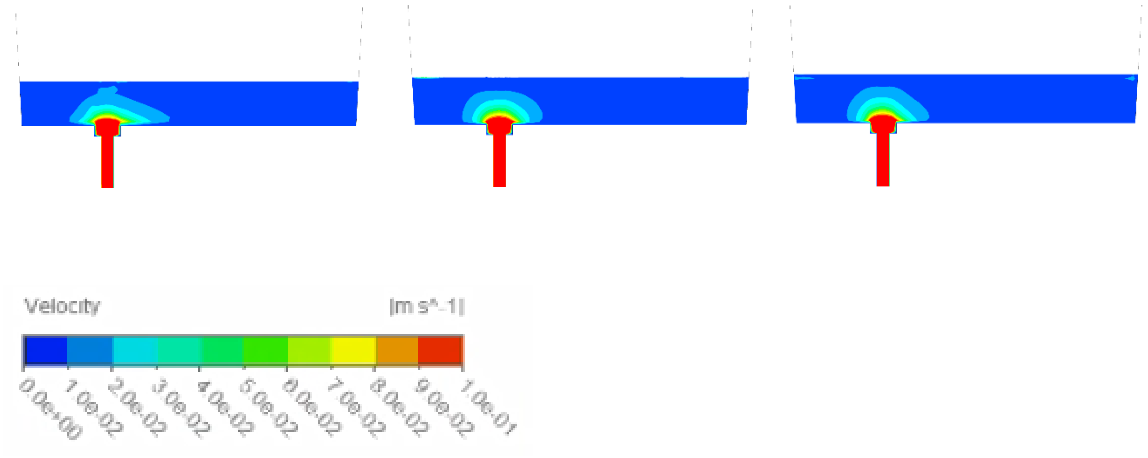

Figure 5.23: Velocity contours after 9 minutes of teeming.

There are some minor differences comparing Mesh 1 and 2, regarding the shape of the velocity contours. From Mesh 2 to Mesh 3, there are no significant variations that can be detected, even though the number of cells doubled from Mesh 2 to Mesh 3.

Figure 5.24 shows the inclusion counting curves obtained for the three meshes, for the reference configuration where no purging treatment was performed. It can be seen that the overall inclusion removal efficiency is not significantly affected by the mesh choice, since the result which matters the most for the analysis in the present work is at 10 minutes. The shape of all curves is also the same, showing a linear trend from 1 minute until approximately 8 minutes, and then showing a sudden steep increase of the number of inclusions passing through the nozzle, corresponding to the moment when the inclusions at the interface start being sucked into the nozzle. The main difference observed is that, for both Meshes 1 and 3, the steep part of the curve occurs earlier than for Mesh 2. The reason why these two configurations showed an earlier suction of the inclusions at the top surface is not clear, especially since no earlier vortex formation was detected. Figure 5.22 shows the phases distributions at 9 minutes of teeming for the three cases and there is still a considerable amount of liquid to be drained in the ladle.

This slight mismatch should not pose significant problems for the analyses to be performed in the present study due to the following reasons:

- The suction effect of the inclusions at the top surface is more likely a model deviation than a real physical phenomenon of interest. In a real industrial ladle, with an adequate slag, these inclusions which accumulated in the top surface would most likely be absorbed by the slag instead of staying at the interface ready to be sucked by the nozzle. In a later section of the present work, an UDF will be applied to remove these inclusions at the water/air interface, which should eliminate this deviation.

- Even if the suction effect is accounted for, the result of most interest in this study and also for practical applications is the final inclusion removal rate at the end of teeming. At 10 minutes, the differences of inclusion removal efficiencies were very low, regardless of the earlier suction effect occurring for Mesh 1 and Mesh 3.

- The differences observed change the moment of the suction occurrence, but do not alter the shape of the curves. All curves show a delay at the beginning until approximately 1 minute, then show a linear trend and finally show a steeper section. Therefore, the main characteristics of the flow remain the same in all cases.

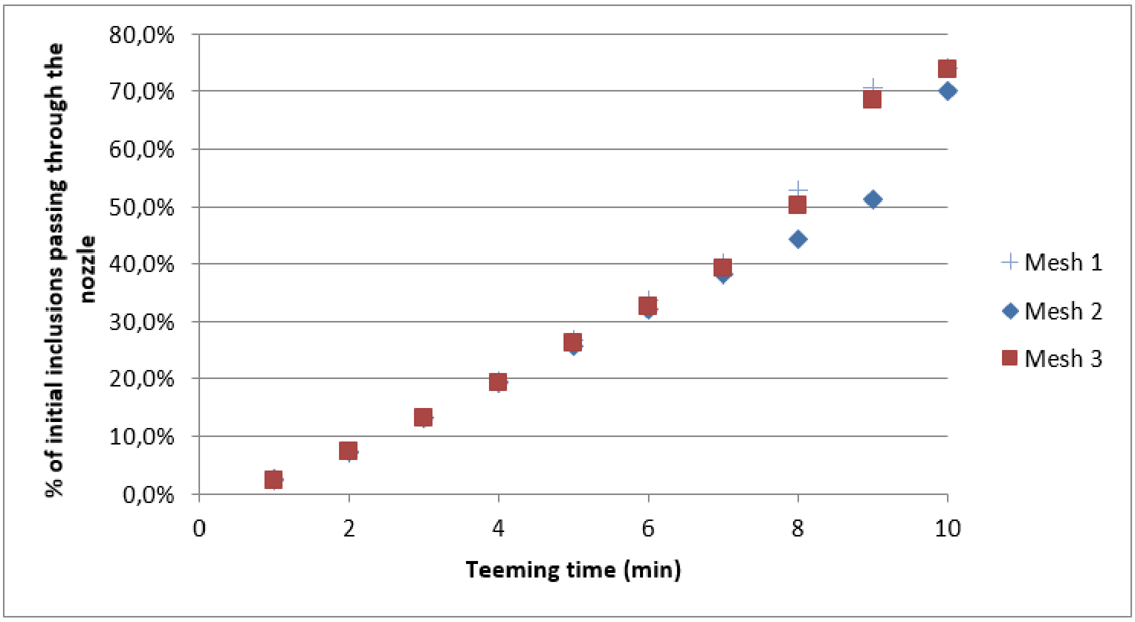

Figure 5.24: Curve for Inclusion Counting for the reference case. Mesh independency study.

Based on the results shown in this section, Mesh 2 was chosen to be adopted in the teeming simulations.

Another important analysis to be performed with respect to the adequacy of a given mesh is the quality of the cells. Figure 5.25 shows the skewness metric for the Teeming stage mesh 2. From the classification defined in Table 5.3, it can be seen that the vast majority of the cells are at least “Good”. A tiny fraction stays in the “Fair” range, which also supports that the mesh is adequate for the simulations.

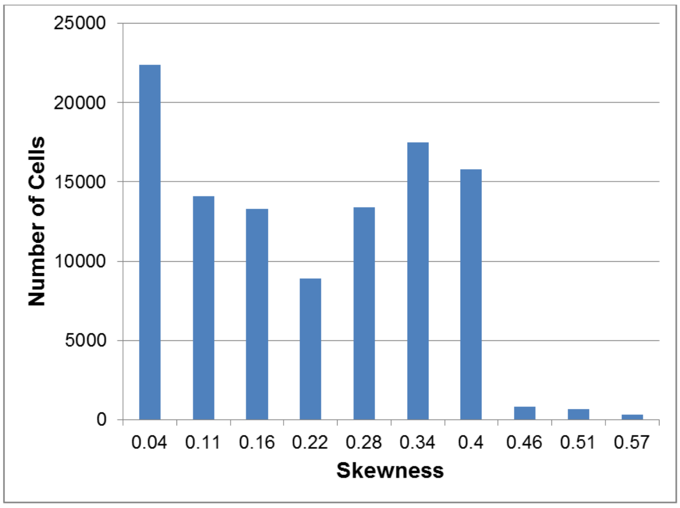

Figure 5.25: Measurement of Cell Skewness for the Teeming Stage Mesh.

5.2.2 Flow Pattern Evaluation

The transport of inclusions towards the nozzle during the teeming stage is governed by the force balance between buoyancy effects and the drag exerted by the downward flow.

A simple evaluation would be to compare the terminal rising velocity of the particles with the average teeming velocity. Under this assumption, particles that would have a rising velocity higher than the ladle teeming velocity would reach the top surface.

However, the velocity distribution in the teeming ladle is not homogeneous. Figure 5.26 shows the velocity vectors in regions where the velocity is higher than 0.001 m/s, which is approximately the average velocity of the downward flow, obtained by dividing the flow rate by the ladle cross-section. It can be seen that the region just above the nozzle has higher velocities than the rest of the ladle. The analysis of the inclusions distributions for the Reference case (no purging) shows this effect clearly: the inclusions just above the nozzle are sucked into it, while the inclusions in the rest of the ladle keep an orderly undisturbed layered pattern.

Figure 5.27, Figure 5.28 and Figure 5.29 show the same results for different instants of time. It can be seen that, as the teeming progresses, stronger horizontal components of velocity start to develop in the regions which are not above the nozzle.

At the later stages of teeming, but still before atmospheric air starts to enter the nozzle, the inclusions which are at the water/air interface start to flow into the nozzle. This effect can be seen in Figure 5.30, where an almost continuous stream of inclusions can be seen flowing from the top surface. Since the mathematical model adopted in the present study does not account for interfacial forces which might keep the inclusions attached to the interface, they can be dragged down should the velocities in the vicinity get high enough. In an equivalent industrial system, such inclusions would most likely have had already enough time to be absorbed by the slag layer and should not pass to the tundish. Therefore, the model presented in this section has a limitation in its prediction capabilities in the final stages of teeming. This limitation will be dealt with by including an UDF which removes the inclusions which reach the water/air interface, preventing them from being sucked in the final stages of teeming. The results obtained through this alternative approach will be shown in a later section of the present study.

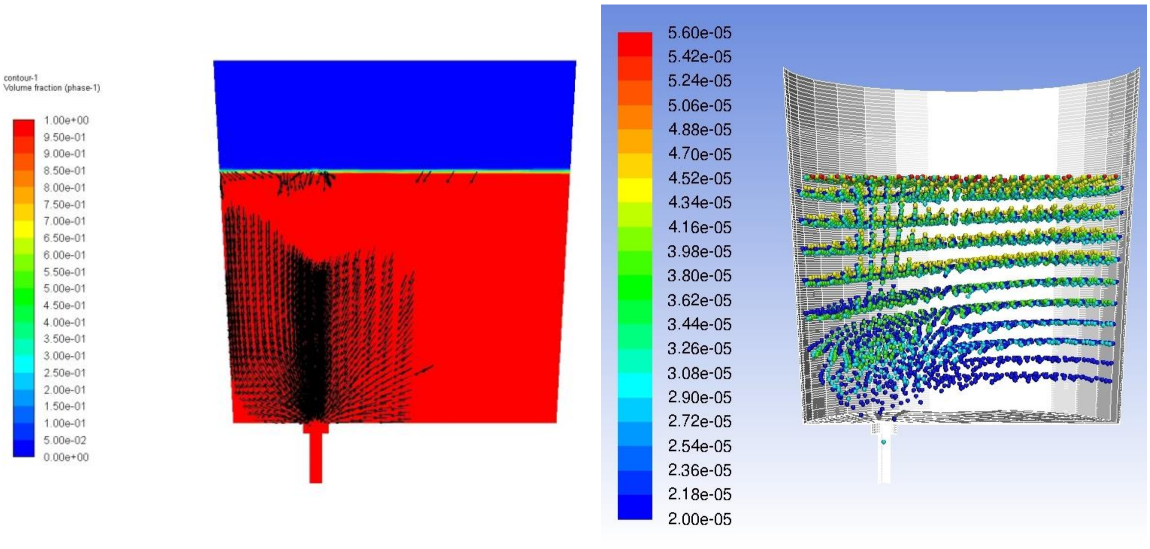

Figure 5.26: Volume Fraction Contour showing the velocity vectors where the velocity is above 0.001 m/s (Left). Inclusions in the ladle colored by their diameter (m) (Right). Results for 110 seconds after start of teeming.

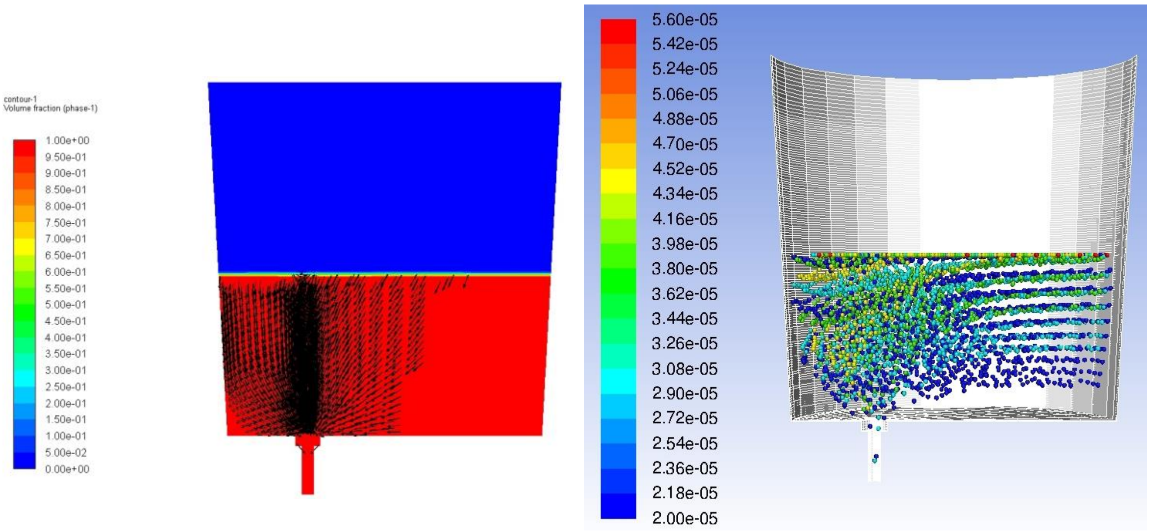

Figure 5.27: Volume Fraction Contour showing the velocity vectors where the velocity is above 0.001 m/s (Left). Inclusions in the ladle colored by their diameter (m) (Right). Results for 297 seconds after start of teeming.

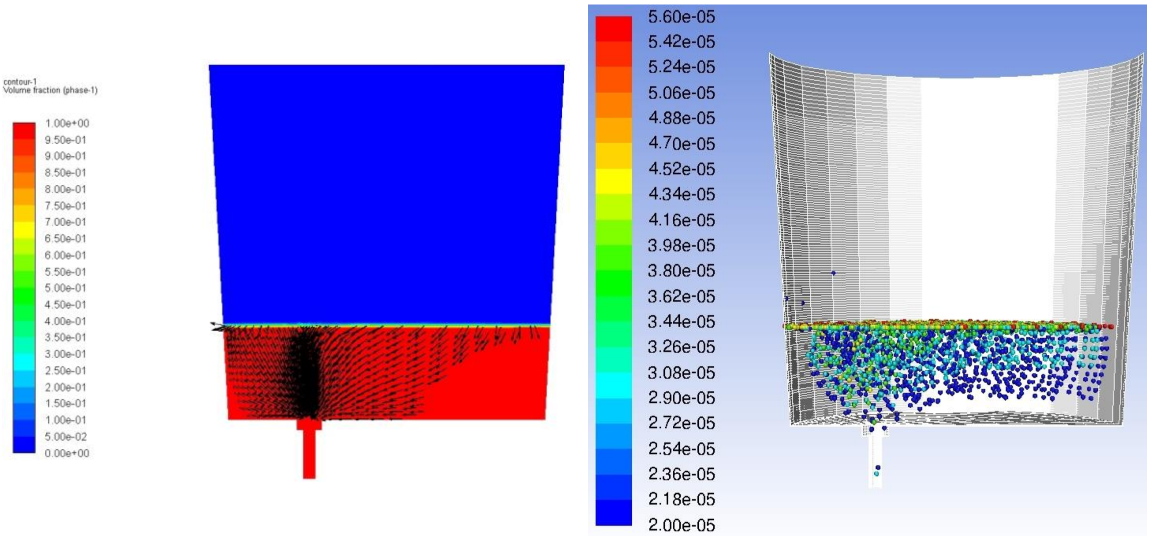

Figure 5.28: Volume Fraction Contour showing the velocity vectors where the velocity is above 0.001 m/s (Left). Inclusions in the ladle colored by their diameter (m) (Right). Results for 440 seconds after start of teeming.

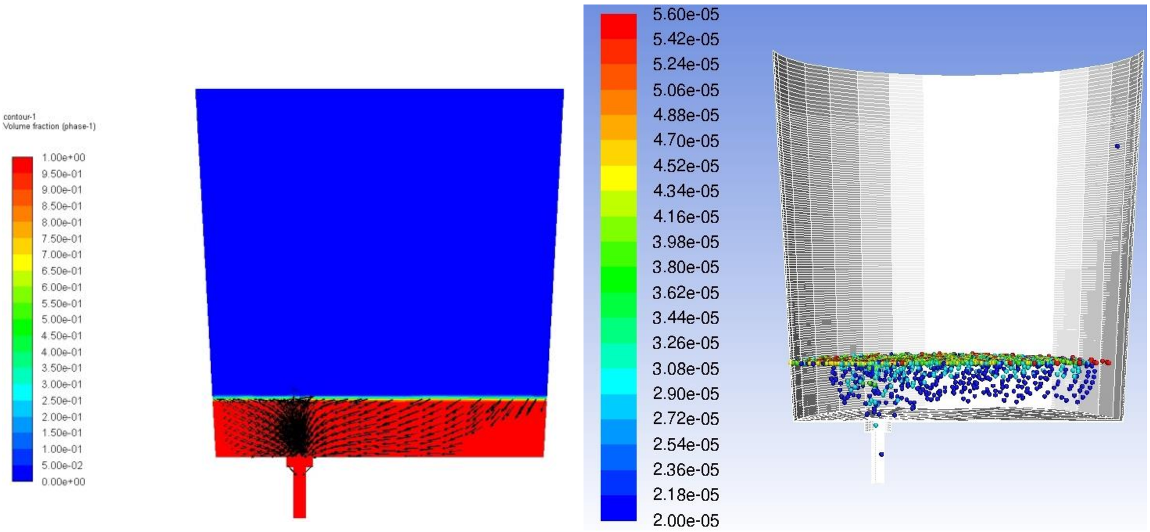

Figure 5.29: Volume Fraction Contour showing the velocity vectors where the velocity is above 0.001 m/s (Left). Inclusions in the ladle colored by their diameter (m) (Right). Results for 517 seconds after start of teeming.

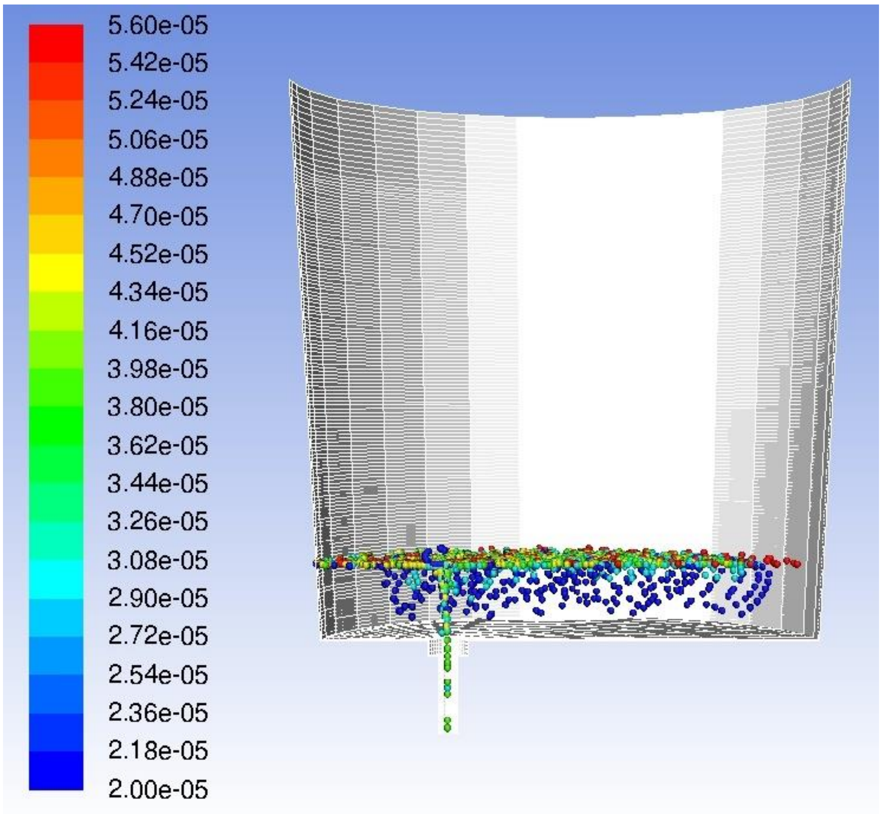

Figure 5.30: Inclusions in the ladle colored by their diameter. Result for 533 seconds after the start of teeming. A continuous stream of inclusions can be seen passing through the nozzle.

5.2.3 Instant of atmospheric air pick-up

It is important to know the instant when the water/air interface will collapse and air will start flowing through the nozzle. At such stage, the equivalent industrial system would most likely already have slag flowing through the nozzle, which is undesirable for clean steel production. Therefore, the equivalent industrial ladle would probably have the teeming interrupted before this moment. Thus, it does not make sense to count inclusions after air starts flowing into the nozzle.

In order to evaluate the instant when air starts flowing through the nozzle, the volume fraction contours were plotted for the final stages of teeming. Figure 5.31 and Figure 5.32 show that this occurs between 616 and 627 seconds after teeming starts. Therefore, the inclusion counting results presented in this study will be considered until the 10 minute mark.

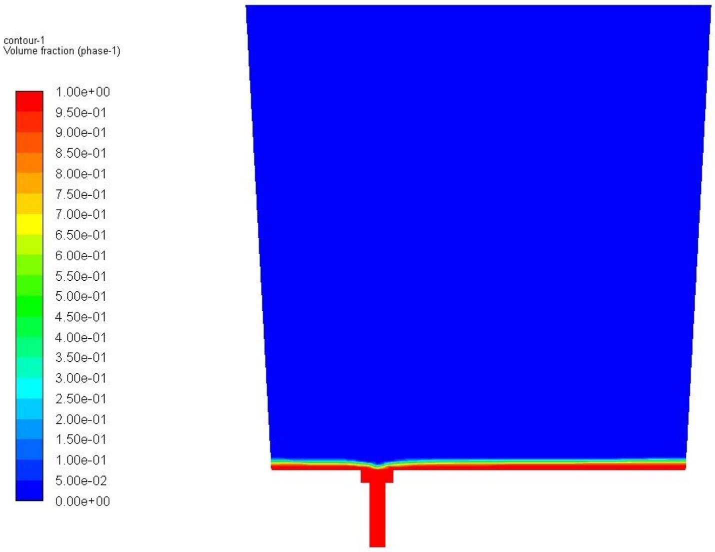

Figure 5.31: Volume fraction of the water phase (phase-1) at t = 616 s.

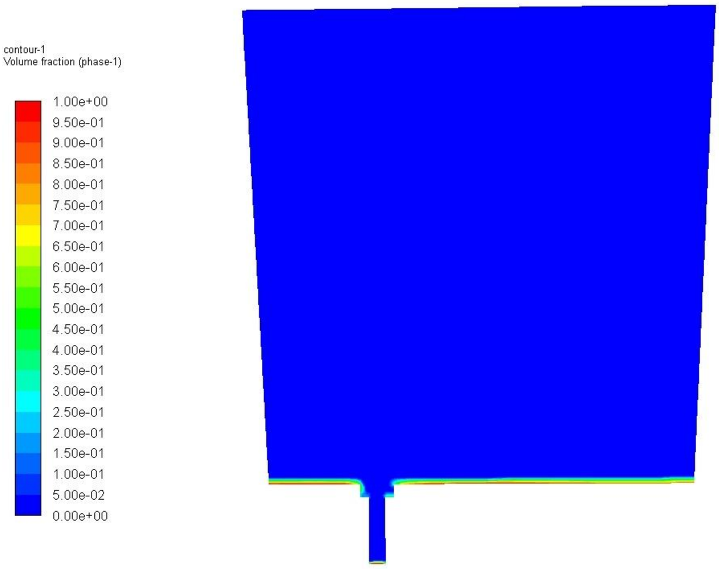

Figure 5.32: Volume fraction of the water phase (phase-1) at t = 627 s.

5.3 Results of the Inclusion Counting Simulations – Eulerian Flat Surface Model

5.3.1 Results for the Reference Configuration

At the beginning of the analysis, there are inclusions from sizes ranging from 20 to 140 µm distributed through the ladle. In the reference configuration, no purging treatment was be performed. The system stayed at rest during approximately 7 minutes and then the teeming started.

The 7 minutes of waiting time were enough to float all inclusions larger than 56 µm. Although it is a simple simulation, the results can also be verified by comparing them to the obtained values of terminal rising velocity of the particles, from Stokes' Law.

Recalling Equation 3.2, already presented at the literature review of the present study:

$$v_t = \frac{gd^2(\rho_s - \rho)}{18\mu} \tag{3.2}$$

From Equation 3.2, it is possible to obtain the terminal rising velocity for each size of inclusion simulated. These values are shown in

Table 5.5. The Reynolds number is also shown. The Stokes Law calculations are valid only until Re < 1, which is a condition fulfilled by almost all inclusion sizes studied. The size of 140 µm shows a slightly higher Reynolds number, but by a very small amount, which should not bring significant deviations for this calculation.

Table 5.5: Terminal rising velocities for the simulated particles.

Inclusion Diameter (µm)	Stokes Rising Velocity (m/min)	Distance covered in 7 minutes (cm)	Particle Reynolds Number
20	9.70E-03	6.79	0.003
30	2.18E-02	15.28	0.011
38	3.50E-02	24.51	0.022
45	4.91E-02	34.37	0.037
56	7.60E-02	53.23	0.071
75	1.36E-01	95.48	0.170
80	1.55E-01	108.64	0.207
90	1.96E-01	137.49	0.294
112	3.04E-01	212.93	0.567
140	4.75E-01	332.7	1.108

The results shown in

Table 5.5 confirm that, for the particle sizes simulated, the largest inclusions that can remain in the flow after 7 minutes are the 56 µm diameter inclusions. Moreover, since the 56 µm inclusions cover 53 cm in 7 minutes, only those whose initial position is below 7 mm (recalling that the bath height is 60 cm) in the vertical direction will remain in the flow after 7 minutes, which is naturally a small fraction of the initial quantity.

After the 7 minutes of waiting time, 74.4% of the initial amount of inclusions still have not floated to the top surface. Even though all inclusions larger than 56 µm have been removed, these constitute for a small fraction of the total amount of inclusions, in the size distribution considered in the present study.

The positions of these inclusions that remained in the flow were recorded and used as initial conditions for the teeming simulation. Figure 5.33 shows the remaining inclusions distribution in the ladle.

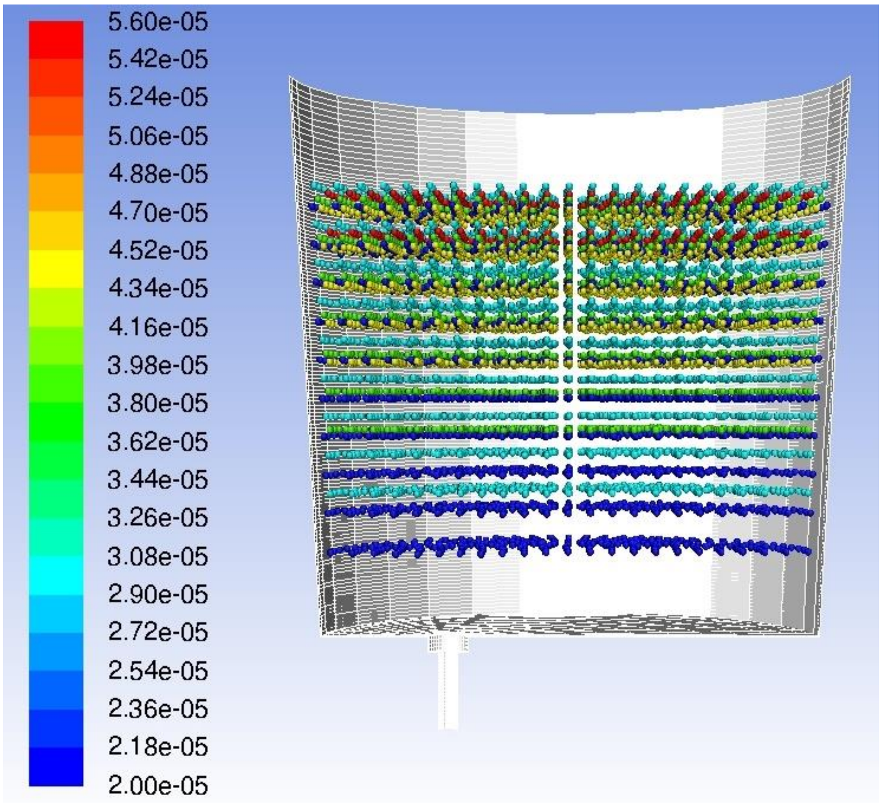

Figure 5.33: Inclusion distribution after 7 minutes of rest. Inclusions colored by their diameter (m).

The accumulated counting result of inclusions passing through the nozzle is shown in Figure 5.34 for the reference configuration. The data was collected every 1 minute, with a total of 10 points for 10 minutes.

From the obtained curve, three main regions can be identified:

I. First, there is a time period at the very beginning where very few inclusions are counted. This can be concluded by the low amount of inclusions counted at the 1 minute mark. In Figure 5.33, it can be seen that there are no inclusions at the lowest portion of the ladle. Since the inclusions take some time to cover this distance again towards the nozzle, the first instants of teeming should show very few inclusions being counted.

II. Then, the inclusions start to be detected in the nozzle. As the teeming progresses, the curve follows an approximate linear trend until approximately the 9 minute mark. Such a trend can be explained by the homogeneous distribution of inclusions in the ladle and the constant mass flow rate through the outlet. These two factors cause the flow of inclusions to not suffer significant changes during most of the process, which explains the linear behavior.

III. Finally, at the last stages of the simulation, the inclusions which have reached the top surface start flowing into the nozzle. The amount of inclusions which made it to the top surface through the entire process is a significant number and having them all flow through the nozzle over a short time causes the curve to have a steeper inclination.

At the 10 minute mark, approximately 70% of the initial amount of inclusions injected has passed through the nozzle. There has not been a significant gain in terms of steel cleanliness during the teeming process, since only 74.4% of the initial number of inclusions were in the flow at the start of teeming. Therefore, only 4.4% of the initial inclusion quantity was removed during the teeming phase.

5.3.2 Comparison of Inclusion Counting Results for Different Gas Flow Rates.

The curves showing the percentage of inclusions that passed through the nozzle comparing different purging flow rates is shown in Figure 5.35. It can be seen that significantly less inclusions remain in the flow when the purging treatment is performed. Table 5.6 describes the percentage of inclusions removed at the end of the purging stage, before teeming started. It can be seen that most inclusions were removed during the purging stage by adhering to the top surface. When the teeming stage started, the configurations in which the purging treatment was performed already began with much less inclusions than the reference configuration. The more inclusions are counted in the curves, the worse is the purging treatment being studied.

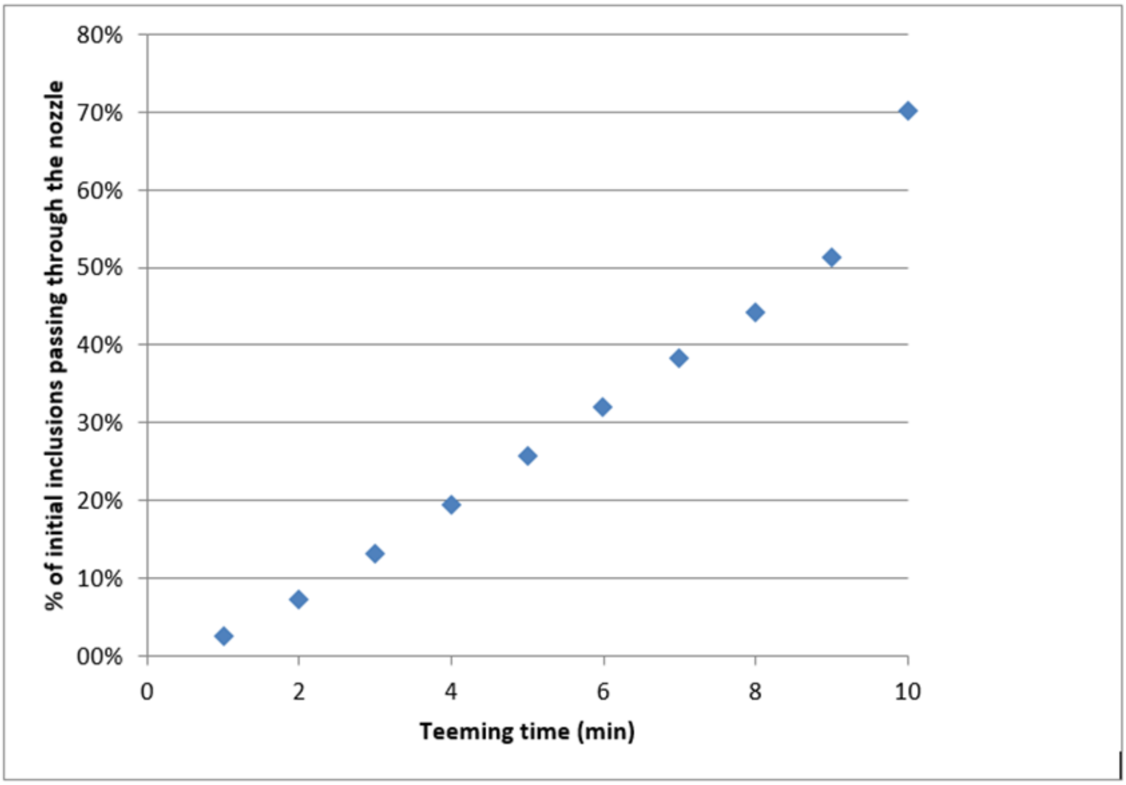

Figure 5.34: Inclusion Counting Results for the Reference Configuration.

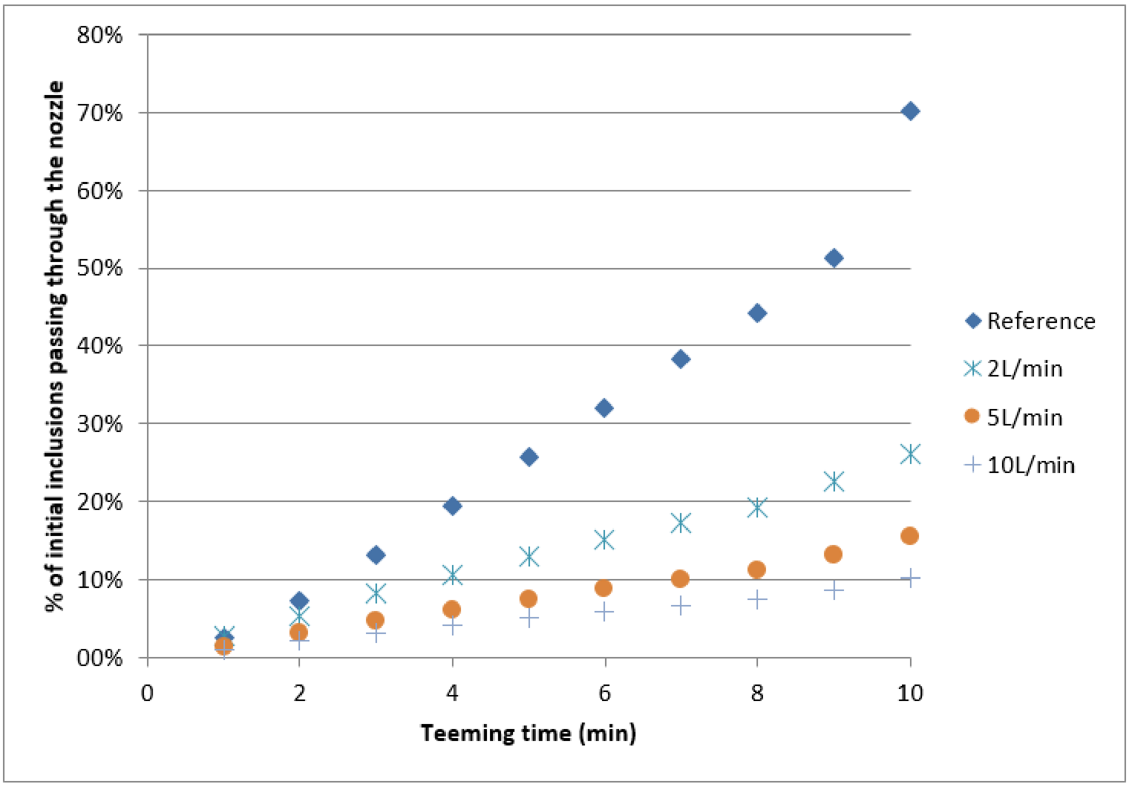

Figure 5.35: Inclusion Counting Results for different gas purging rates.

Table 5.6: Inclusion Removal Efficiency for each Flow Rate.

Configuration	Inclusion Removal Efficiency after Rest and Purging	Absolute PRI
No purging	25.6%	29.8%
2L_P1	72.3%	73.9%
5L_P1	83.4%	84.5%
10L_P1	89.1%	89.8%

Figure 5.36,Figure 5.37 and Figure 5.38 show the remaining inclusions distributions after the purging treatment, considering the three flow rates studied: 2, 5 and 10 L/min. The figures preserve the same view that was adopted in the contours of the purging flow pattern results (with the plug on the left side of the ladle).

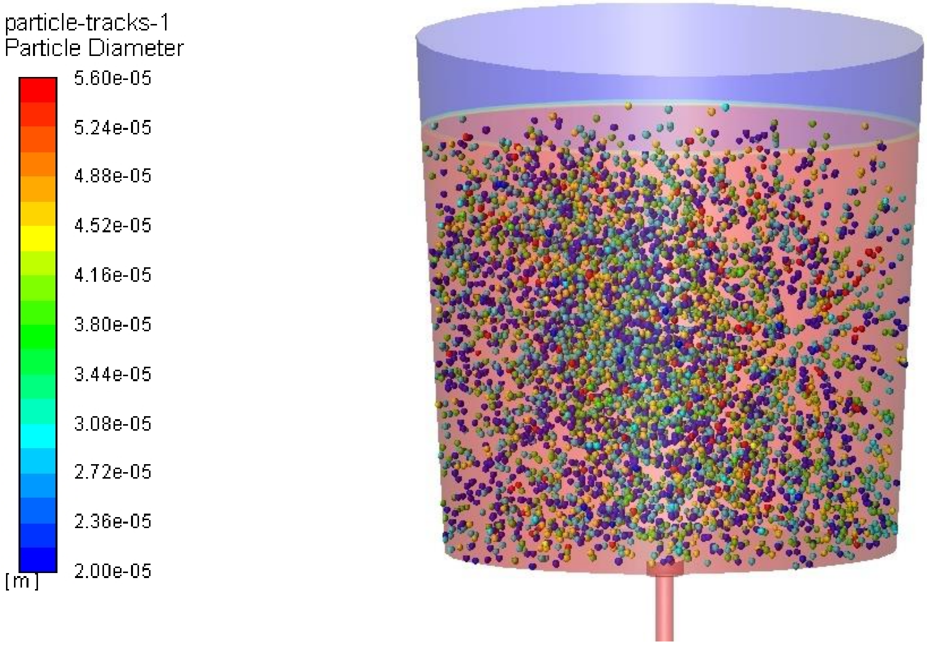

Figure 5.36: Inclusion Distribution after gas purging. 2 L/min.

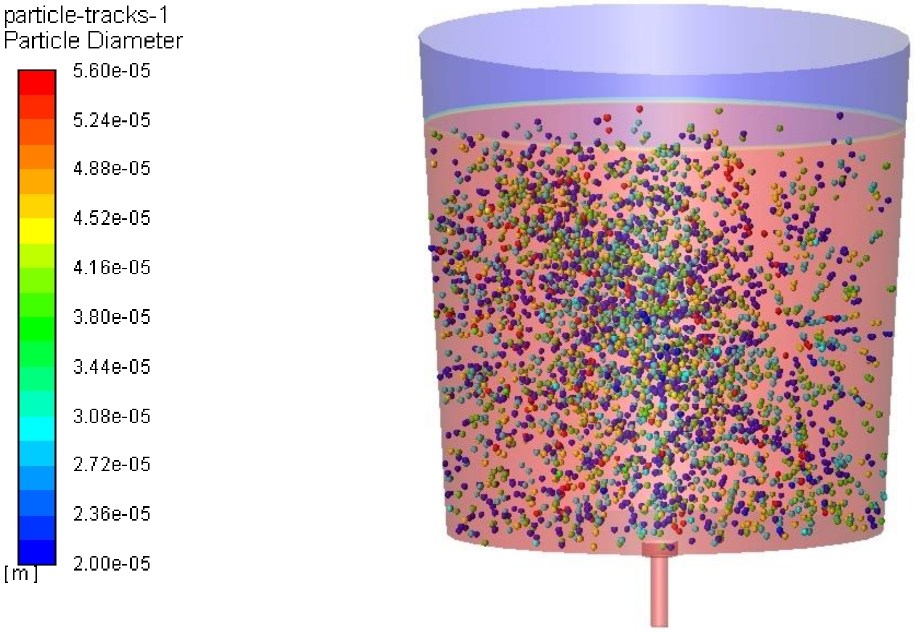

Figure 5.37: Inclusion Distribution after gas purging. 5 L/min.

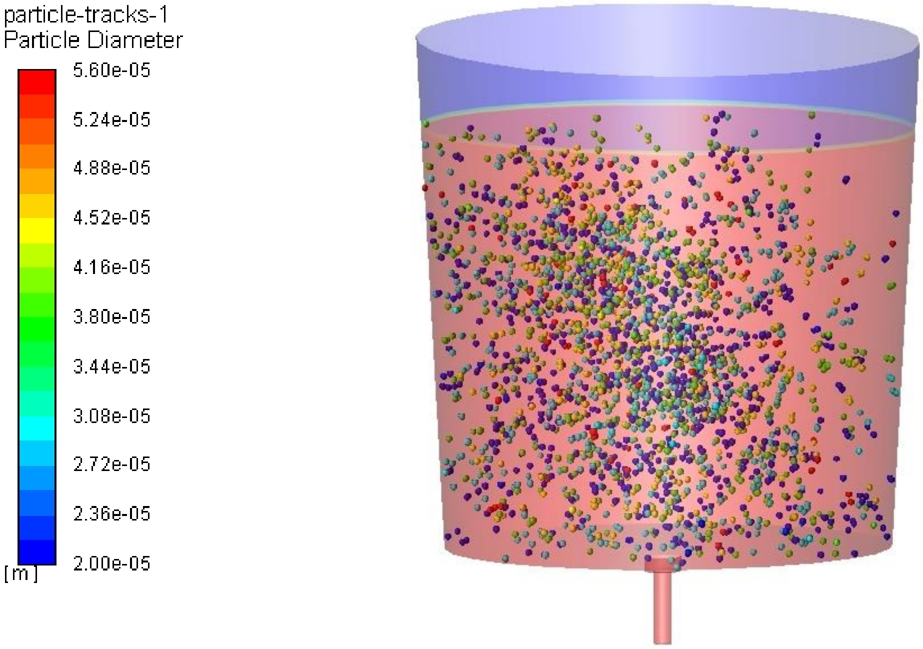

Figure 5.38: Inclusion Distribution after gas purging. 10 L/min.

In order to provide a better visualization of the curves for the purging cases, the same curves are shown with a modified axis scale in Figure 5.39, with the maximum value in the y-axis fixed in the value of 30%. It can be seen that the curves follow a linear pattern until approximately 8-9 minutes of teeming, when the curves start presenting a steeper slope. This is attributed to a transition in the teeming process, when the interface gets close enough to the nozzle, causing the suction of the inclusions which had reached the top surface during the teeming stage. This phenomenon is similar to what has been identified for the reference configuration, but since the purging cases have less inclusions in the ladle during the teeming and the remaining inclusions after purging are more evenly distributed due to the stirring (opposed to the reference case, which shows less inclusions close to the ladle bottom at the beginning of teeming), the phenomenon can be seen a little earlier than in the reference case.

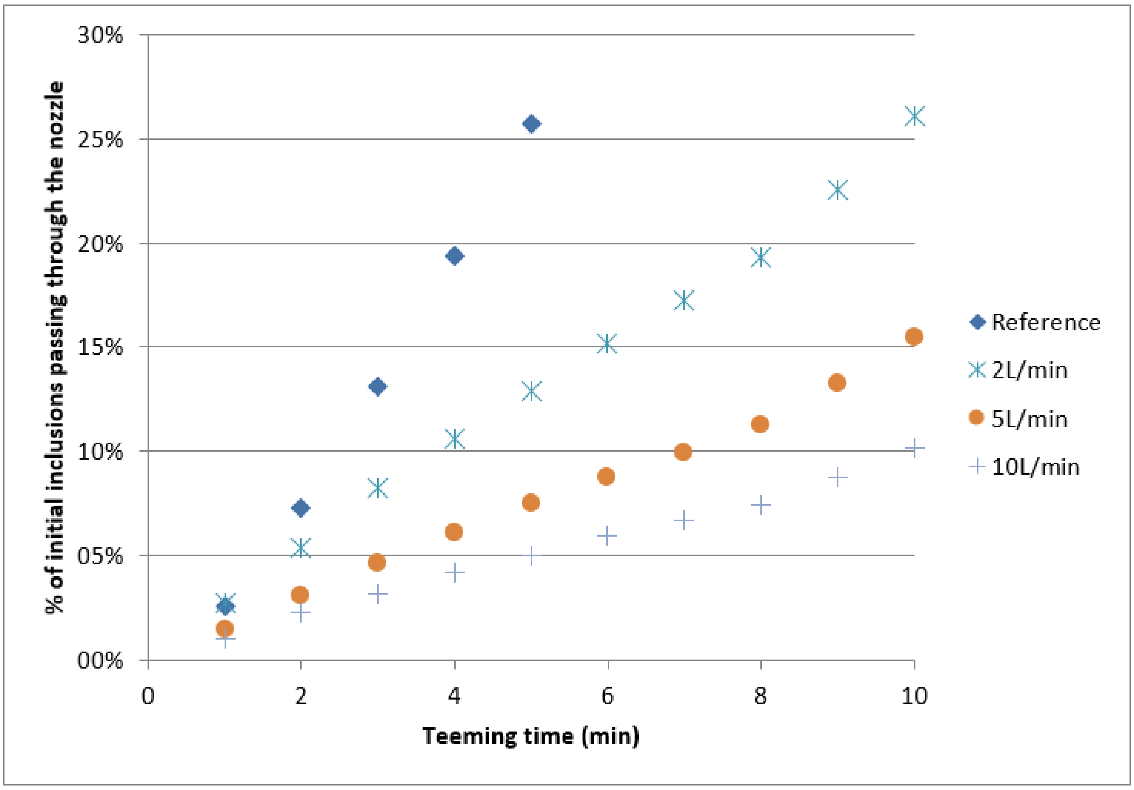

Figure 5.39: Inclusion Counting Results for different gas purging rates. Modified Scale.

For the most part of the curves, a linear trend can be seen. This can be explained by the following factors:

- For the size distribution being considered in the present study, only inclusions with low flotation velocities remain in the flow to be computed in the teeming stage. Moreover, from the remaining inclusions, the smaller ones (20 and 30 µm) represent most of the inclusions. The consequence is that the majority of inclusions in the present study are much more influenced by the flow conditions than by their own flotation velocity.

- The initial conditions before the 7 minutes waiting time had the inclusions evenly distributed in the fluid domain. The only deviation from the even distribution, for the reference case, is the accumulation of floated inclusions in the water/air interface. Apart from that, there is no reason for a sudden change of behavior in the inclusion counting during the teeming.

- For the cases in which purging was performed, there is significant stirring all over the ladle. Such stirring causes the remaining inclusions to be evenly distributed around the ladle. This effect is shown clearly in Figure 5.38Figure 5.36, Figure 5.37 and Figure 5.38.

- The teeming is performed according to a constant mass flow rate at the nozzle. Therefore, if the inclusions distribution is approximately homogeneous, especially for the predominant smaller inclusions, then it would be expected a constant rate of inclusions passing through the nozzle. This gives a linear curve for the accumulated counting of inclusions.

Figure 5.40 shows linear curve fits for the inclusion counting curves, covering the period from 1 to 8 minutes of teeming. It can be seen that the fit is very good for all cases.

5.3.3 Effect of Changing the Restitution Coefficient at the top surface.

The results shown in the previous analysis show an increase in the inclusion removal efficiency as the gas purging rate increases. However, under intense stirring conditions, the inclusion could not be able to attach to the top surface and could revert to the bulk flow.

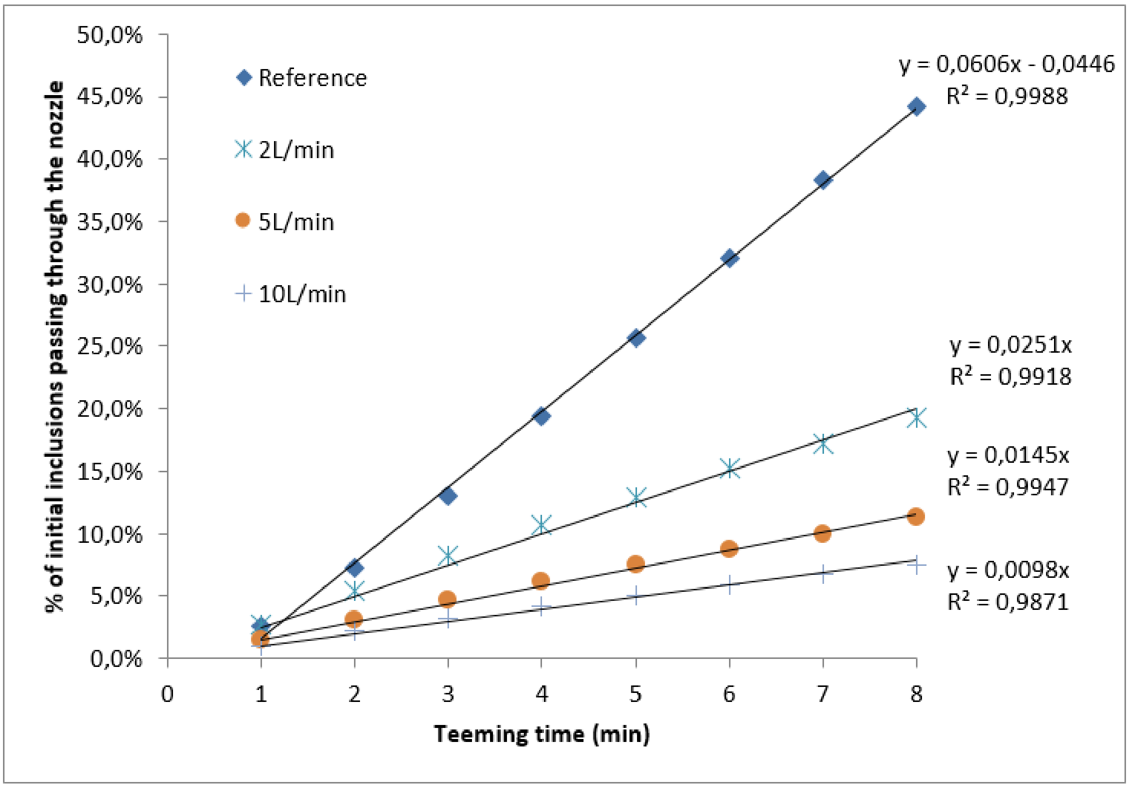

Figure 5.40: Linear curve fits for the inclusion counting curves.

The boundary condition for the inclusions at the top surface in the previous analysis considered a restitution coefficient equal to zero. This means that, when an inclusion touches the surface, regardless of the local velocities and agitation, the inclusion will be regarded as captured and will be removed from further computations. Such an assumption tends to overestimate the inclusion capture results, since with higher turbulence, there is a higher probability of collisions between the inclusions and the top surface. However, higher turbulence also decreases the probability that the inclusion remains attached to the interface. Consequently, the model tends to show an increasing inclusion capture rate as turbulence increases in the flow, despite strong evidence pointing otherwise for the real behavior.

In order to investigate the effect of changing the restitution coefficient, the results for the inclusion motion was recomputed, considering the flow rate of 10 L/min and a coefficient of restitution equal to 0.001 (instead of zero, as used in the previous calculations). The objective of this calculation was to verify if there would be an accumulation of inclusions in the upper part of the ladle, by not removing them from the computations at the moment of collision with the interface.

Figure 5.41 shows the evolution of the inclusion distribution in the ladle during the purging time of 80 seconds. It can be seen clearly that there is not a tendency of inclusion transport toward the upper ladle region. On the contrary, there is a strong tendency of homogenization of the inclusion concentration throughout the ladle.

The flow pattern results shown from Figure 5.14 toFigure 5.17 show the velocities and turbulence distribution in the ladle for the 10 L/min case. These results explain why the inclusion homogenization occurs so quickly. The significant recirculation loop carries the inclusions around the ladle, while the strong turbulence close to the surface contribute to drive the inclusions from the top toward the ladle inner region. Even considering the restitution coefficient to a very small number was not enough to keep the inclusions close to the top surface.

In order to understand this effect, it is important to recall the formulation of the Discrete Random Walk model for turbulent dispersion of particles, presented from Eq. 4.7 to 4.9 in Section 4.1.3.1 of the Methodology. The turbulent dispersion effect considers that a random fluctuating velocity component is added to the fluid velocity in the equation for the particle velocity calculation. This random fluctuating velocity is proportional to the turbulent kinetic energy in the cell where the particle velocity is being calculated. This effect is included in the model in order to represent the agitation typical of highly turbulent flows. In a real turbulent flow, it is highly unlikely that the particles would follow ordered trajectories in locations subjected to high turbulence intensities.

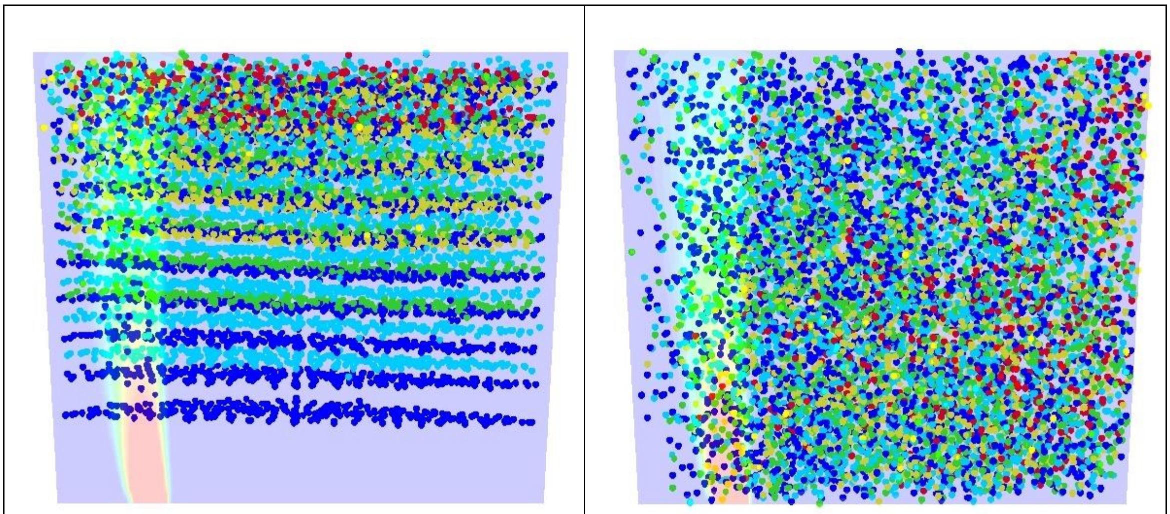

t = 0 seconds

t = 10 seconds

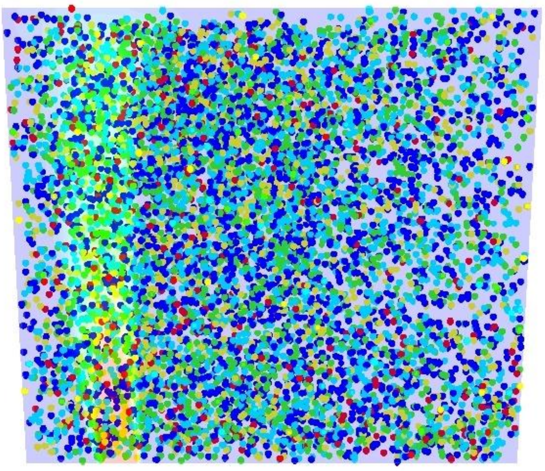

t = 20 seconds

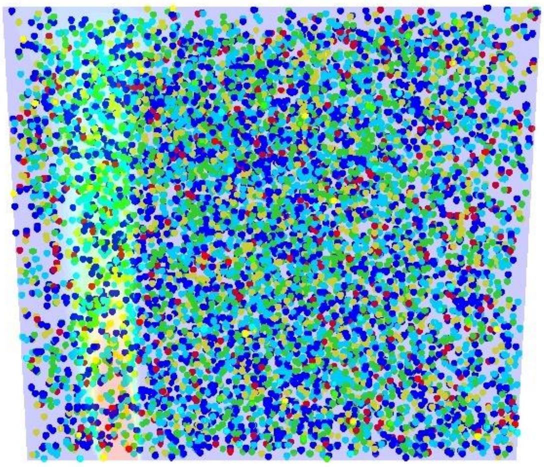

t = 30 seconds

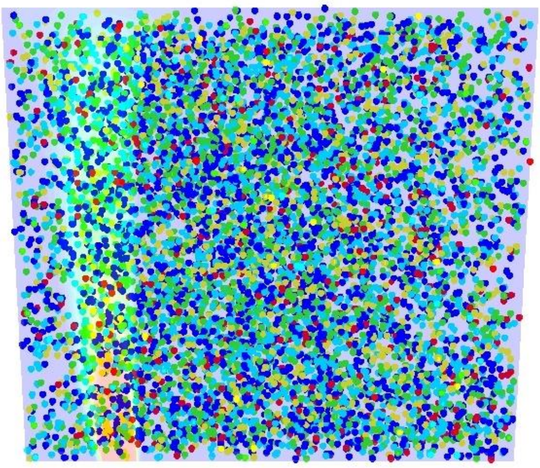

t = 40 seconds

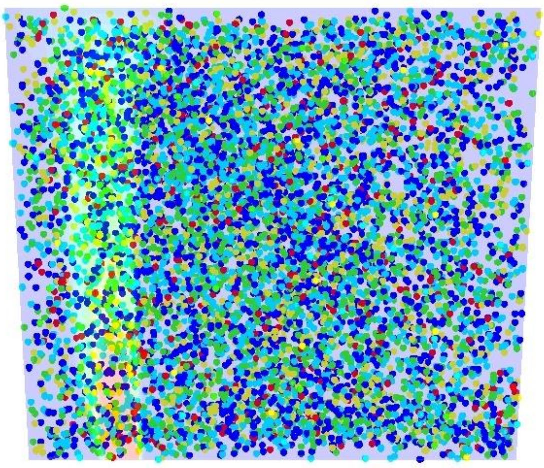

t = 50 seconds

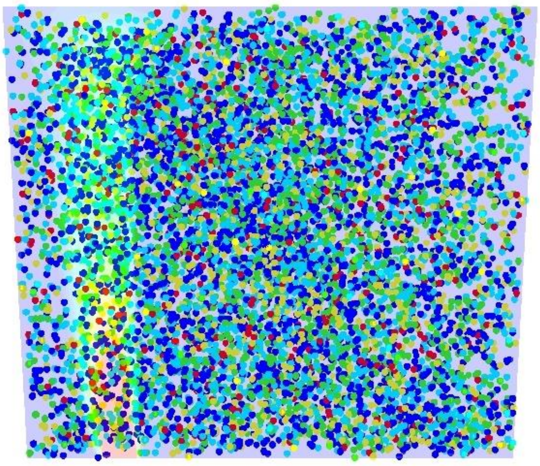

t = 60 seconds

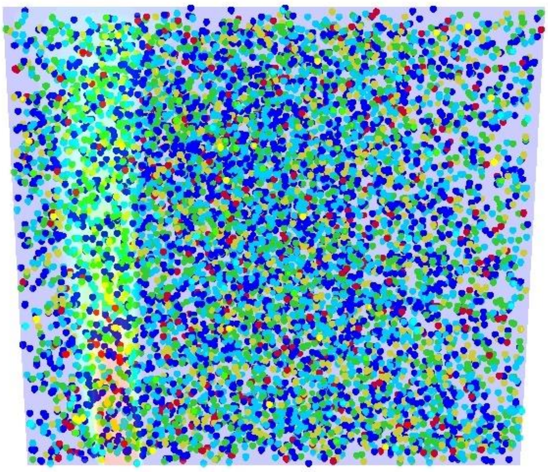

t = 70 seconds

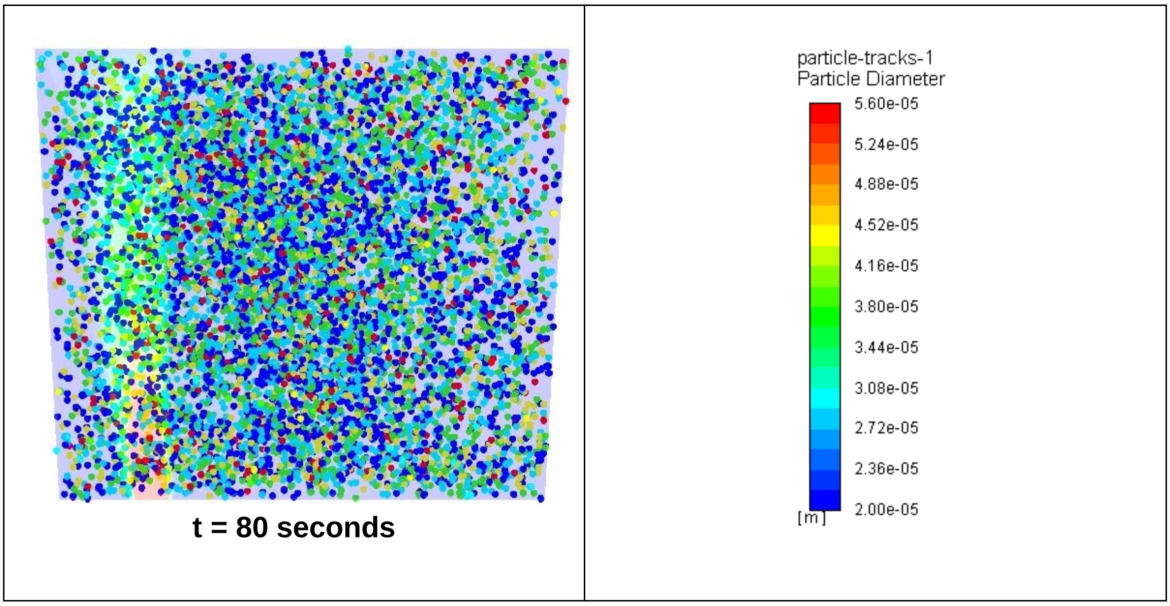

t = 80 seconds

Figure 5.41: Inclusion Distribution in the Ladle during purging considering a 10 L/min flow rate and a restitution coefficient of 0.001.

Thus, even if the low restitution coefficient causes the inclusion to lose almost its entire momentum and rebound very close to the top surface, most of the upper ladle region is subject to high turbulent agitation, as it could be seen in Figure 5.16 and Figure 5.17. As a consequence, random fluctuating velocities of significant magnitude are added to the average fluid velocities at these locations, impacting the calculation of the particle velocity in the subsequent time steps after the rebound. Eventually the inclusions close to the top surface would acquire downward velocities and return to the bulk flow. And since the inclusions considered in this simulation are 56 µm or smaller, their flotation velocity due to buoyancy is very low compared to the velocities induced by the flow. Therefore, there is not a tendency for the inclusions to stay at the upper portion of the ladle, if any coefficient of restitution higher than zero is considered. If the inclusions do not stick to the top surface, they will be carried back to the bulk flow and spread throughout the ladle. Comparing the inclusions distribution after 80 seconds of purging and at the beginning (t = 0 seconds) in Figure 5.41, it can be seen that, under the assumption considered in this model, the gas purging treatment would have a negative effect on the PRI, since the inclusions were initially closer to the top surface (at t = 0 seconds) than they were after the purging treatment (t = 80 seconds).

Figure 5.42 shows the curves of inclusion counting for this configuration during teeming, compared to the reference case. It can be seen that, under the assumption of no inclusion entrapment by the top surface, even with a very low restitution coefficient, the purging treatment yields worse results than no treatment at all. This would actually be expected, given the inclusion distribution shown in Figure 5.41. With no inclusions entrapped in the top surface and a homogeneous distribution of inclusions caused by the stirring, it would be expected that more inclusions would be counted. It is also interesting to note that both curves intersect at the 10 minute mark, which reinforces the hypothesis that the sudden change of inclination of the curve for the reference case is due to the suction of inclusions from the top surface towards the nozzle, as described previously in the present study.

From these results, it can be questioned whether the assumption of no inclusion capture is too extreme, given that it leads to the conclusion that the purging treatment is worse than no treatment at all. In the next section, another approach will be presented, adopting a custom criterion for inclusion capture at the top surface.

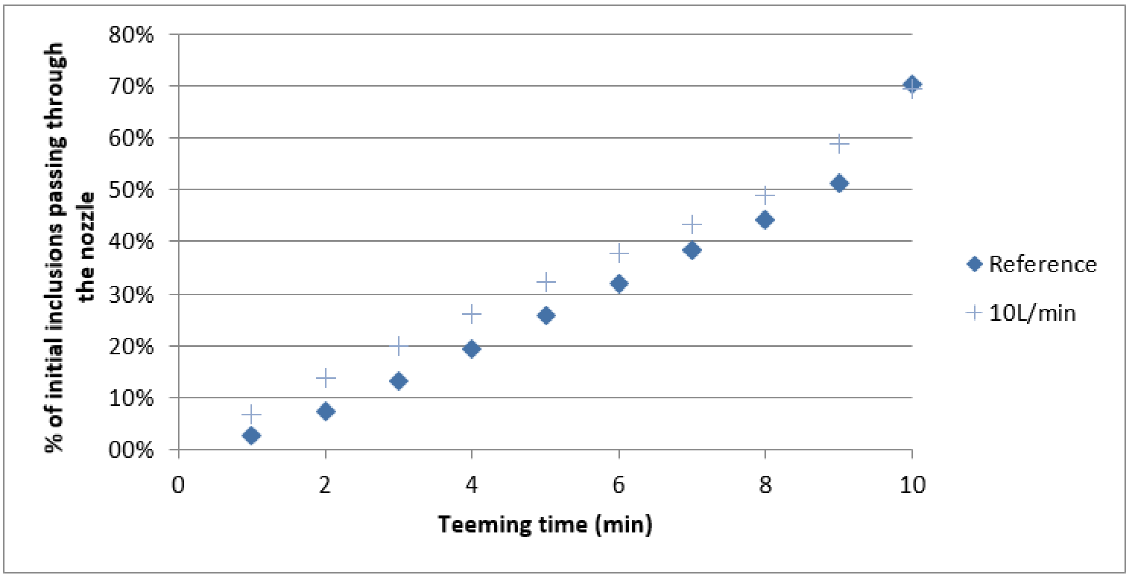

Figure 5.42: Inclusion Counting Results for the case with 10 L/min purging and no inclusion capture at the top surface.

5.3.3 Effect of Changing the Inclusion Capture Criterion through a User Defined Function.

Figure 5.43, Figure 5.44 andFigure 5.45 show the inclusions distribution in the ladle obtained after an analysis in which a custom capture criterion was defined at the top surface. The figures on the left side represent the already shown results of inclusion distribution after purging considering the standard capture criterion. The figures on the right side show the new results considering the custom criterion. The chosen criterion in the present study was that only inclusions which touched the surface at a velocity lower than 0.1 m/s would be captured. The choice of velocity value was arbitrary, based in the velocity values observed in the flow pattern results, with the sole goal of providing an estimation of what would happen if such a condition was applied. For the calculated velocity fields in the simulations of the present study, the value of 0.1 m/s was a suitable threshold to distinguish between the high stirring region above the plug and the rest of the ladle. In reality, there is a much more complex relationship between the inclusions and the interface, which very likely involves surface tension effects, and it is a topic of further study to determine more precisely what should be the condition for inclusion attachment in the top surface.

It can be seen that, as expected, there are more inclusions in the flow when the custom criterion is adopted, compared to the previously obtained results where the zero restitution coefficient (Standard capture criterion) was applied. Nevertheless, the overall distribution did not show significant differences, with an almost homogeneous inclusion distribution, with a slightly higher concentration at the middle of the ladle. By some unknown reason, the inclusions which were removed from the computations were still displayed when the custom criterion was adopted, but this did not have any influence in the results.

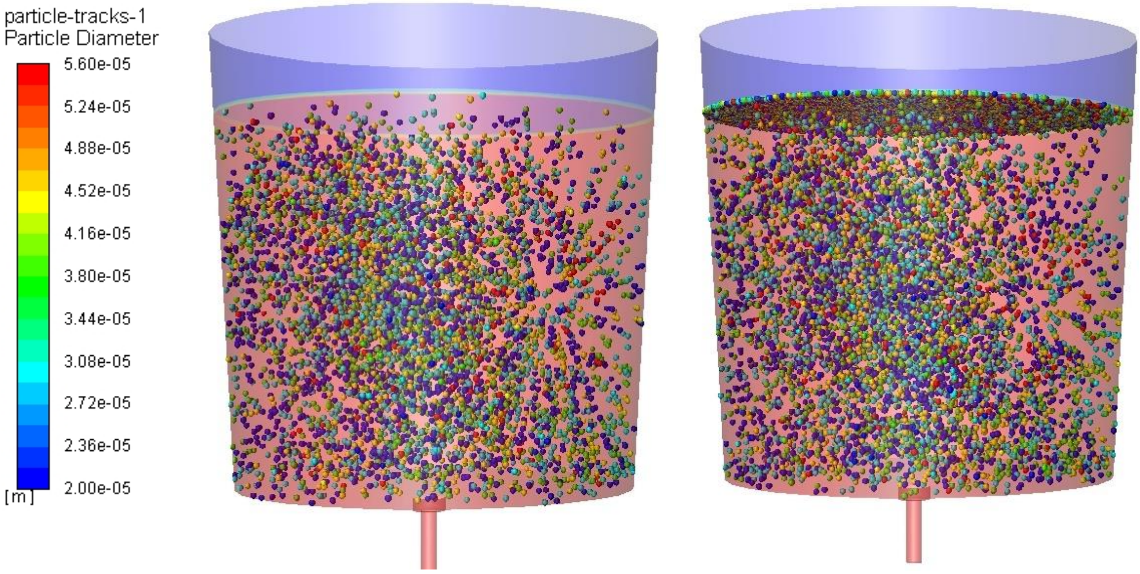

Figure 5.43: Inclusion Distribution after 2L/min purging during 80 seconds. Standard capture criterion (Left) and Custom capture criterion (Right).

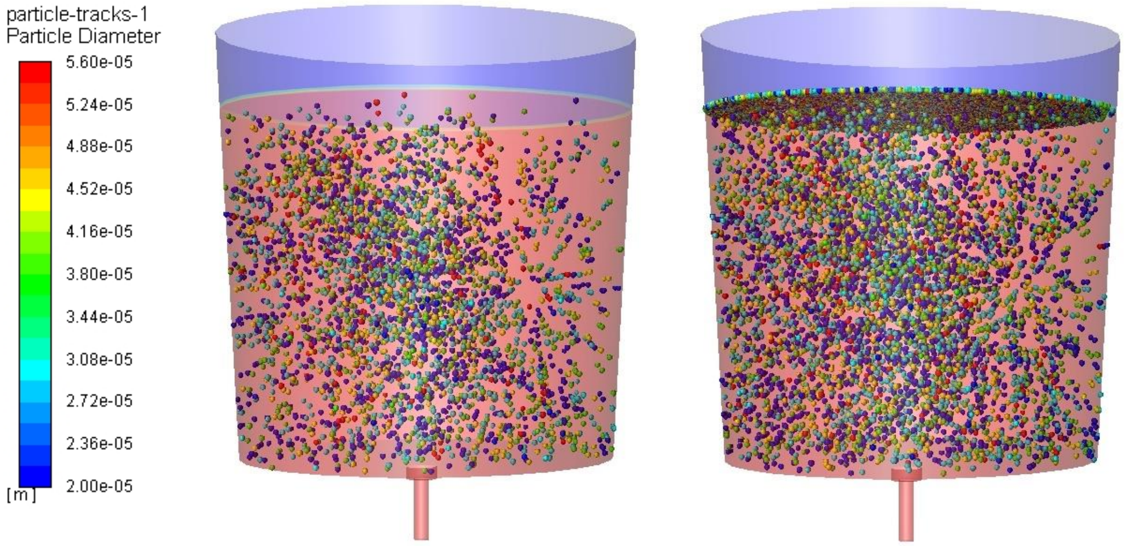

Figure 5.44: Inclusion Distribution after 5L/min purging during 80 seconds. Standard capture criterion (Left) and Custom capture criterion (Right).

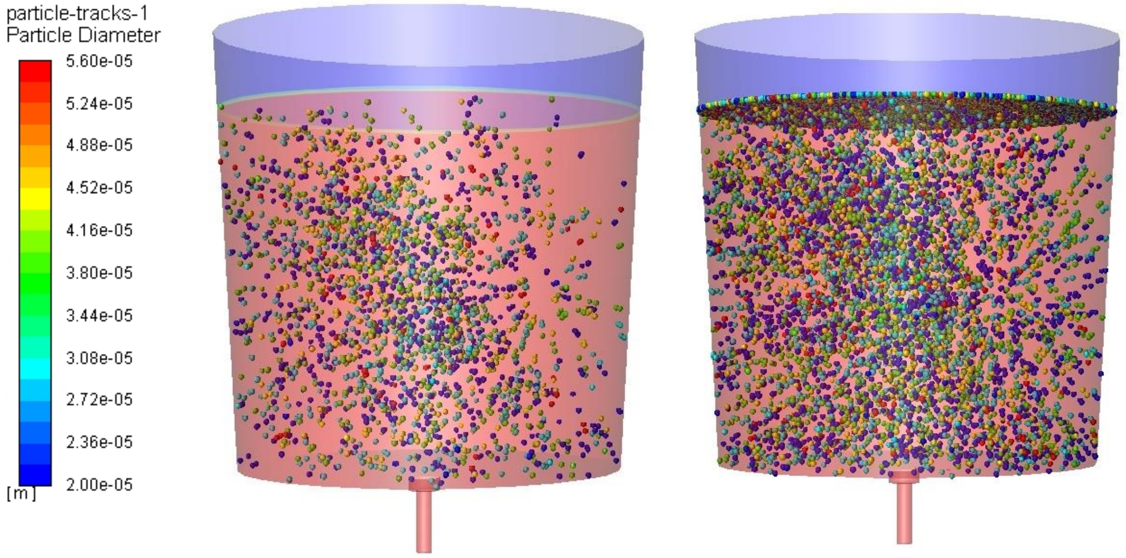

Figure 5.45: Inclusion Distribution after 10L/min purging considering a custom capture criterion.

Table 5.7 shows a comparison between the inclusion removal efficiencies (*Absolute Purging PRI*, as defined in the Methodology Chapter) obtained by using the UDF for the custom capture criterion, and by using the standard zero restitution coefficient criterion. As expected, there was a reduction in the inclusion capture ratio for all purging rates studied. The most interesting aspect of these results, however, is that there is almost no difference between the results obtained for the 5 L/min and the 10 L/min flow rates, when the UDF is applied. This means that the developed UDF was effective to counter balance the increase in the results of inclusion removal caused by excessive stirring, which is most likely not true in a real system, at least not in the extent observed in the results for the Standard Capture Criterion.

Table 5.7: Effect of the Inclusion Capture UDF. % of inclusions removed after purging considering the initial amount of inclusions at the beginning (Absolute Purging PRI).

Configuration	Standard Capture Criterion	Custom Capture Criterion
2L_P1	72.3%	67.2%
5L_P1	83.4%	72.2%
10L_P1	89.1%	72.3%

From the results shown in Table 5.6 previously, it was seen that the teeming stage had almost no effect on the final inclusion removal efficiency, with the purging stage results being the governing results for the overall inclusion removal efficiency. Therefore, the teeming simulations were not repeated for this section. Considering the results of Table 5.6 and the very similar inclusions distributions shown in Figure 5.43, Figure 5.44 and Figure 5.45, it can be concluded that no significant alterations in the results would be provided by the extra computational effort to run the teeming simulations.

5.4 VOF Model Results.

5.4.1 Flow Pattern Evaluation

In order to investigate the effects that the modeling choice for the top surface has on the inclusion counting results, the water/air interface was modeled through the VOF model in an alternative mathematical model configuration. The results were obtained again for the same three purging flow rates: 2, 5 and 10 L/min. Since a free surface could show oscillations, this model was run fully in transient mode. The advantage of this approach against the steady state approach is that it is possible to see the flow development over the time, as can be seen in Figure 5.46, for the 2 L/min flow rate.

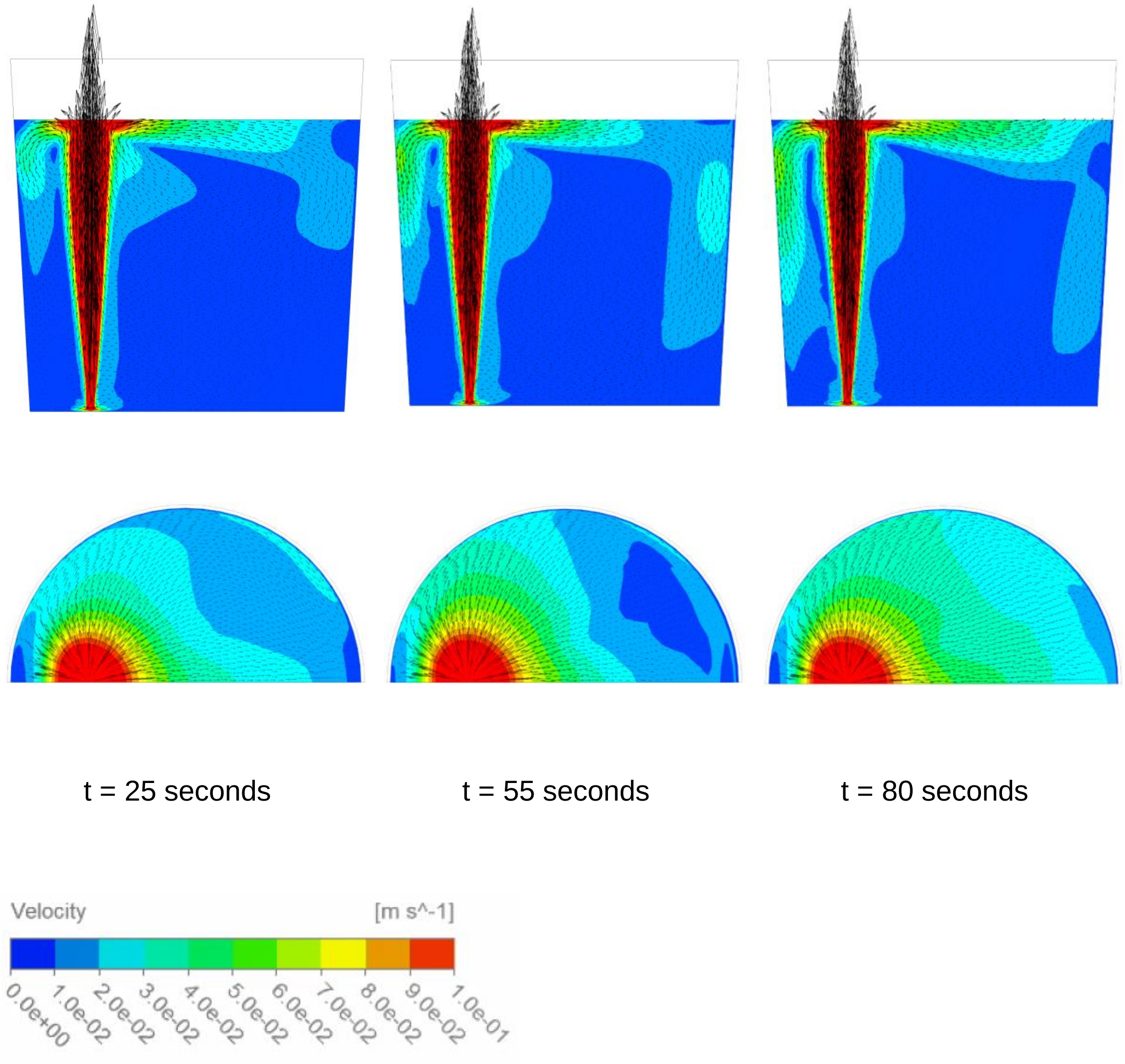
t = 25 seconds

t = 55 seconds

t = 80 seconds

Figure 5.46: Velocities Contour. Transient Results for 2L/min flow rate. 25s, 55s and 80s. Symmetry plane passing through the plug (Above) and horizontal plane located 60 cm above the ladle bottom, in the theoretical interface position (Below).

From Figure 5.46, it can be seen that the flow is still evolving by the 80 seconds mark, which evidences that a steady-state approach might not be adequate for the flow pattern evaluation in this case. It is also evident how much lower are the overall ladle velocities in this case, compared to the 2 L/min case simulated previously.

Figure 5.47 shows the flow pattern results obtained for the gas flow rate of 5 L/min.

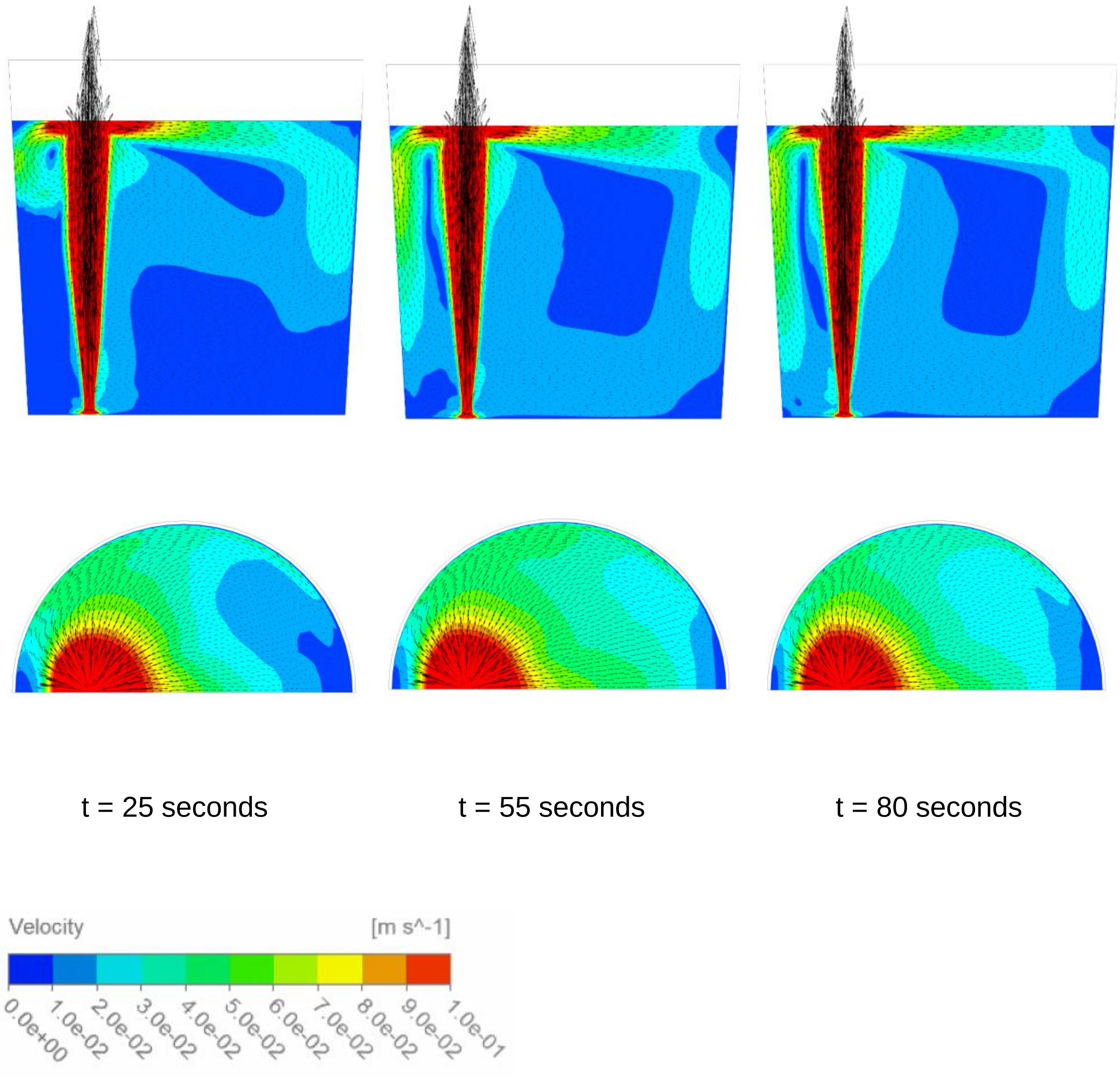

t = 25 seconds t = 55 seconds t = 80 seconds

Figure 5.47: Velocities Contour. Transient Results for 5L/min flow rate. 25s, 55s and 80s. Symmetry plane passing through the plug (Above) and horizontal plane located 60 cm above the ladle bottom, in the theoretical interface position (Below).

This time, it is possible to see that the flow is already fully developed by the 55 seconds mark, as there are no noticeable changes between the velocity contours for the times of 55 seconds and 80 seconds. Since the velocities are higher in overall for the 5 L/min case compared to the 2 L/min, the transport of momentum is also faster and therefore the flow reaches its fully developed state earlier. It is interesting to notice that, even though the flow is fully developed, the velocities in overall are still much lower than what was obtained through the flat top surface modeling approach adopted previously. Therefore, the differences in the velocities were not induced by the choice of steady-state or transient approach, although there might have been a slight contribution of the flow underdevelopment in the velocities result for the 2 L/min case.

Finally, Figure 5.48 shows the flow pattern for the 10 L/min case. Again, by the 55 seconds mark, the flow already seems to be well developed.

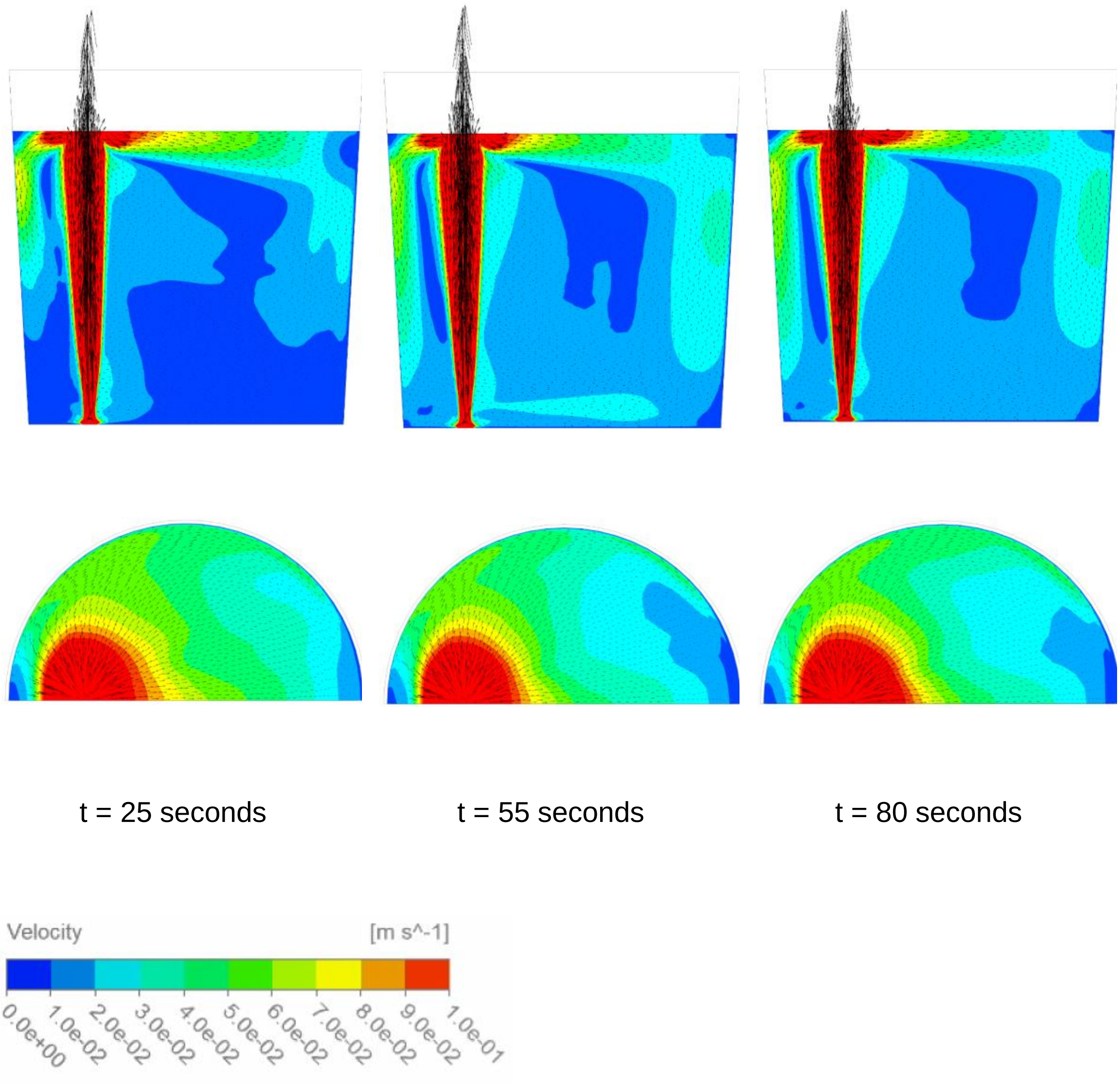

t = 25 seconds t = 55 seconds t = 80 seconds

Figure 5.48: Velocities Contour. Transient Results for 10L/min flow rate. 25s, 55s and 80s.

Figure 5.49 shows the water Volume Fraction contours for the three cases. Two main aspects should be observed from these results:

- The plume is very thin compared to the plume obtained through the Eulerian model. The standard VOF model available in Fluent does not allow for the adoption of turbulent dispersion models, as it is supposed to be used for interface tracking. This is surely a limitation from this model, as the real plume should be more disperse.

- The spout is visible, especially under higher purging rates. This provides an explanation for the lower overall velocities seen in the ladle when modeling the free surface. Significant momentum is lost by elevating the flow above the equilibrium height and a large fraction of the flow returns with a downward component, reducing the velocities parallel to the surface.

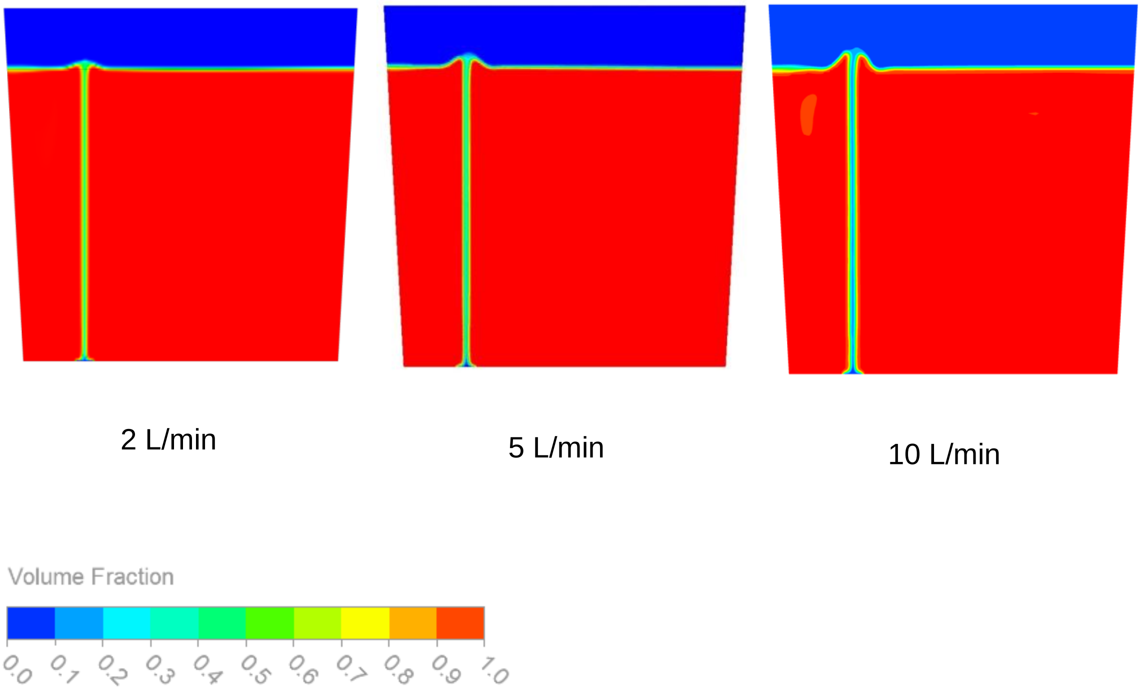

2 L/min

5 L/min

10 L/min

Figure 5.49: Water Volume Fraction results for VOF model cases.

Figure 5.50 shows the turbulence kinetic energy contours for the three cases. It is interesting to see that, for this model, the turbulent energy is restricted to the vicinity of the plume. It does not spread in the top surface like it was seen in the previous results shown in Figure 5.16 and Figure 5.17 (Page 82).

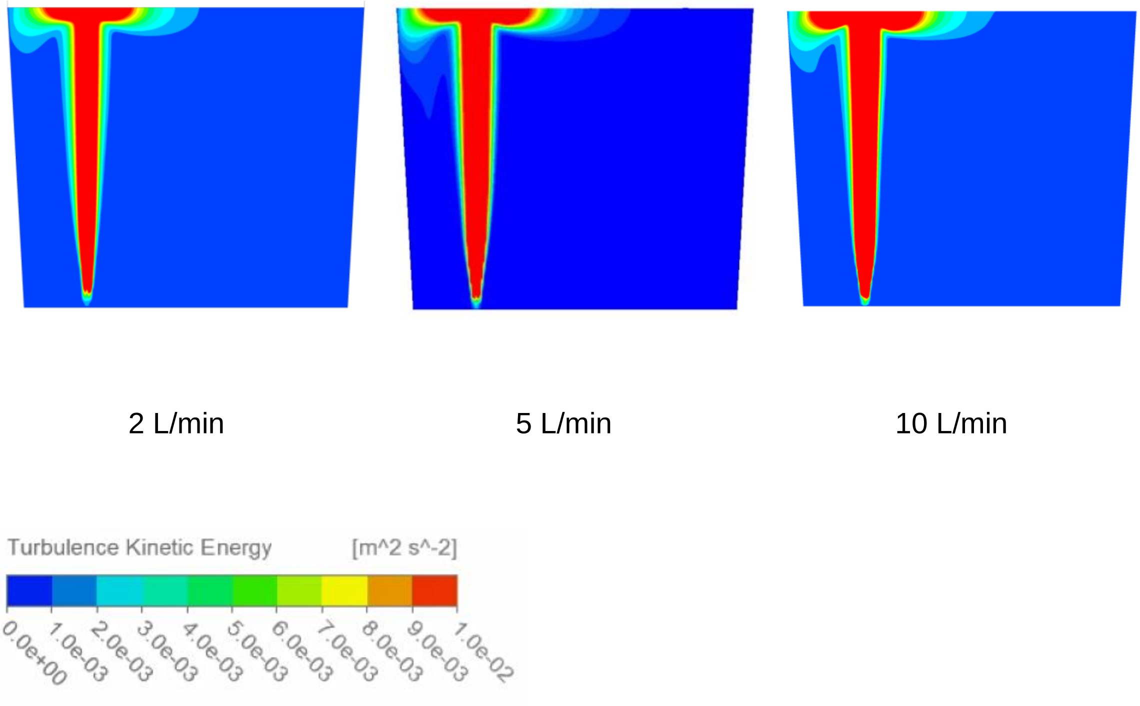

2 L/min 5 L/min 10 L/min

Figure 5.50: Turbulent Kinetic Energy results for the VOF model cases.

5.4.2 Inclusion removal efficiency during purging – VOF Model

In this section, the transient results of inclusion removal during purging considering the VOF model are going to be presented. Figure 5.51 shows the evolution of the inclusion distribution in the ladle during 80 seconds of purging treatment considering the flow rate of 2 L/min.

Figure 5.52 shows the results of inclusion distribution in the ladle for the 5 L/min flow rate, obtained through the VOF model for the purging stage.

Figure 5.53 shows the inclusion distribution results in the ladle for the 10 L/min flow rate, obtained through the VOF model for the purging stage.

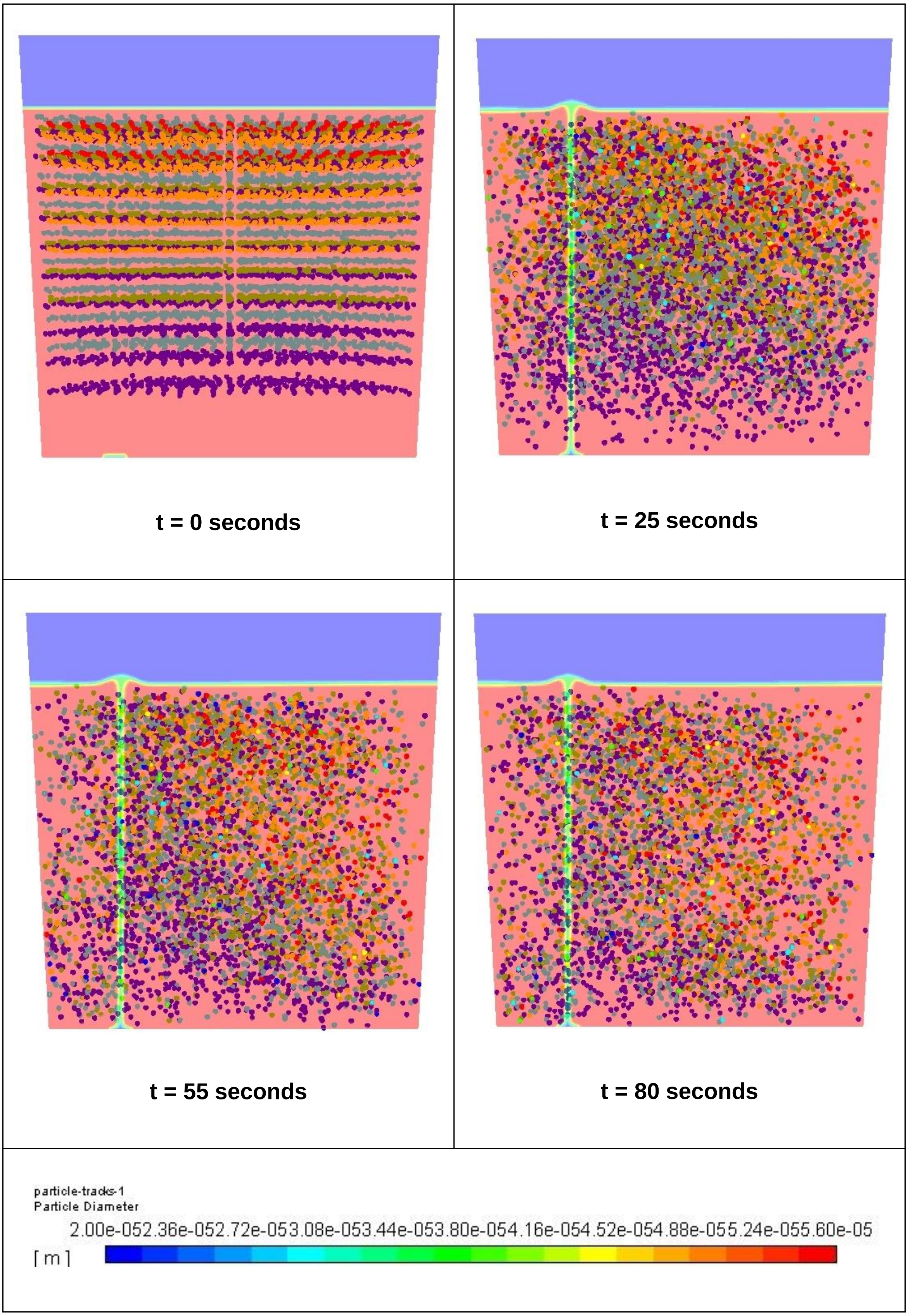

t = 0 seconds

t = 25 seconds

t = 55 seconds

t = 80 seconds

Figure 5.51: Inclusion Distribution during purging for the 2 L/min case. VOF model. Flow times of 0 seconds, 25 seconds, 55 seconds and 80 seconds.

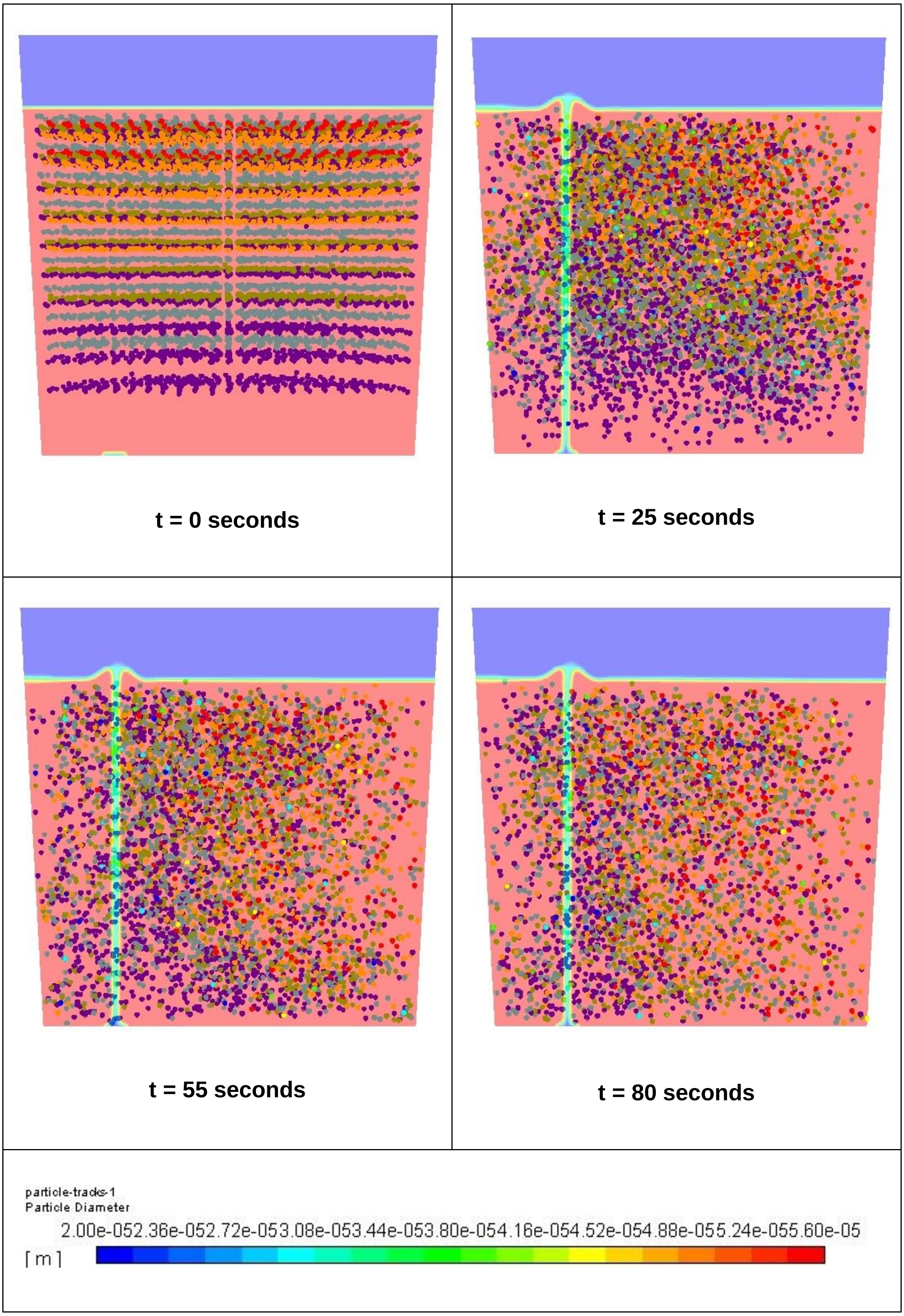

Figure 5.52: Inclusion Distribution during purging for the 5 L/min case. VOF model. Flow times of 0 seconds, 25 seconds, 55 seconds and 80 seconds.

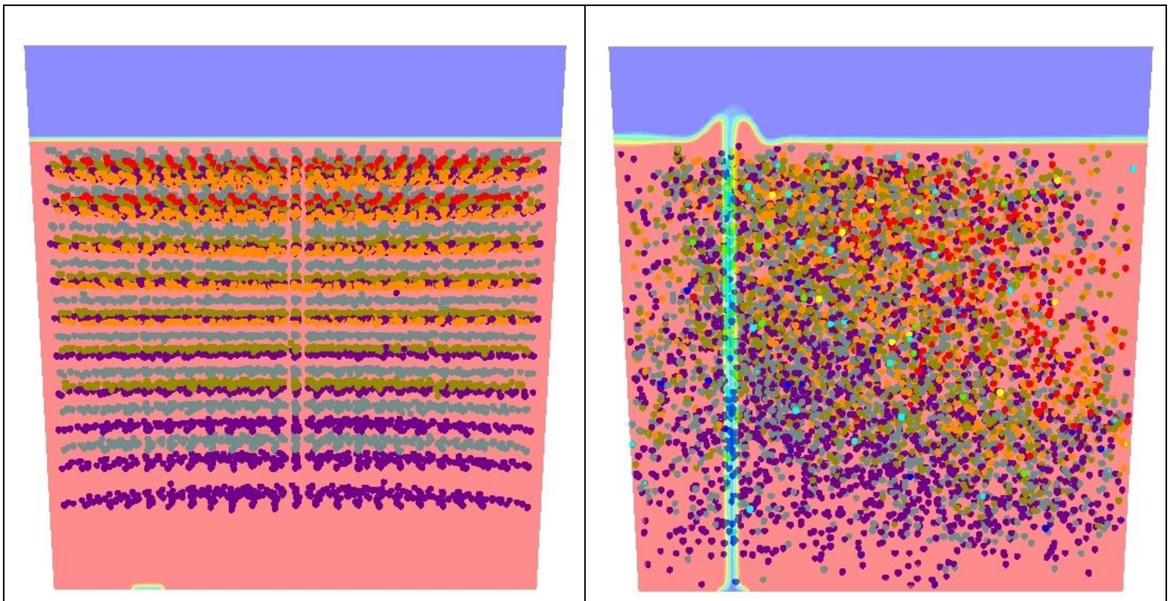

t = 0 seconds

t = 25 seconds

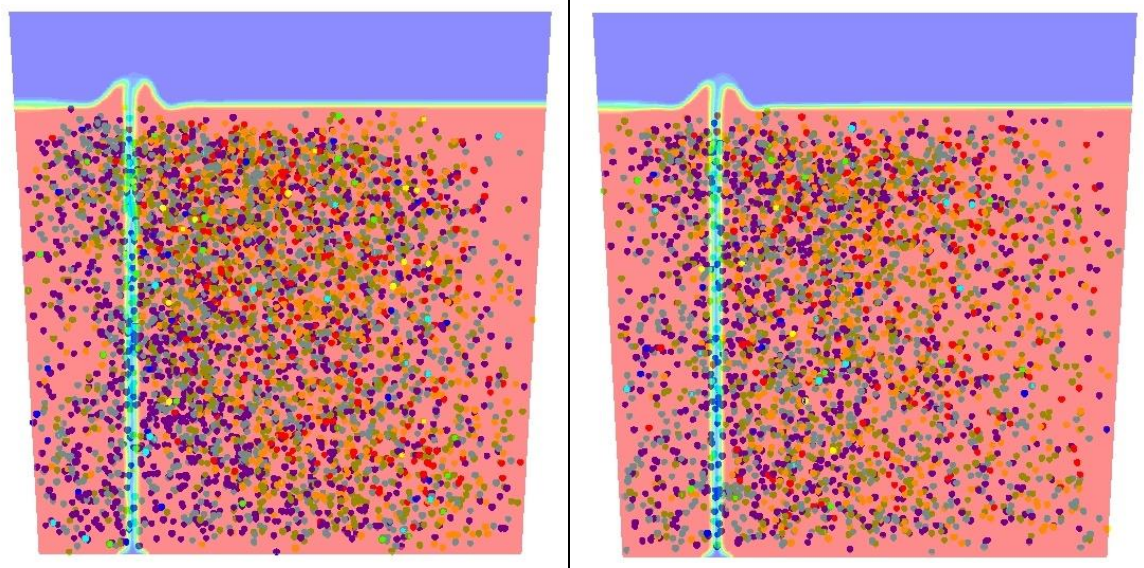

t = 55 seconds

t = 80 seconds

Figure 5.53: Inclusion Distribution during purging for the 10 L/min case. VOF model. Flow times of 0 seconds, 25 seconds, 55 seconds and 80 seconds.

From Figure 5.51 to Figure 5.53, it can be seen that the inclusions dispersion in the ladle is significantly less intense than what was observed for the Eulerian model with flat top surface. This becomes evident by looking at the motion of the larger inclusions, which are displaced around the ladle in an approximate orderly pattern, following the recirculation loop seen in the velocity results. In the inclusions distributions obtained through the Eulerian Flat Surface model shown previously, the inclusions were completely dispersed in the ladle and it was not possible to distinguish any region of higher concentration of the larger inclusions. This observation is consistent with the predictions for flow velocities and turbulence, which show significantly less agitation in the ladle when the VOF model is applied, compared to the previous approach. As a consequence, there is less turbulent dispersion of the particles which causes less randomness in the inclusions final positions.

Figure 5.54 shows the transient variation of the inclusion concentration in the ladle plotted versus the purging time. Such a curve is interesting to analyze since several authors have plotted similar curves[35,36,37]. These curves have been normalized considering a 100% value for the initial inclusion concentration at the start of the purging treatment. Therefore, these curves are not accounting for the removal of inclusions during the transport and teeming stages. This was done in order to have the curves in the same format as the results reported by other authors.

Figure 5.54 shows that the obtained curves adjust very well to exponential curve fits. This is in good agreement to other studies in the literature.[35,36,37] The purging treatment is most efficient at the beginning, when there are more inclusions in the ladle to be removed. After a certain time, the treatment removes fewer inclusions per unit of time, since there are fewer inclusions in the flow. The times studied in this work are shorter than what has been studied by other authors, who reported more dramatic decreases of efficiency of the purging treatment as time progressed. Nevertheless, the trend is clear, considering how well the negative exponential curves matched the results.

Table 5.8 shows the inclusion removal efficiencies (according to the *Absolute Purging PRI* definition) after 80 seconds of purging for the VOF model and compares it with the results obtained with the other previously adopted models. It can be seen that the VOF model yields the lowest values for inclusion removal efficiency. This can be explained considering that:

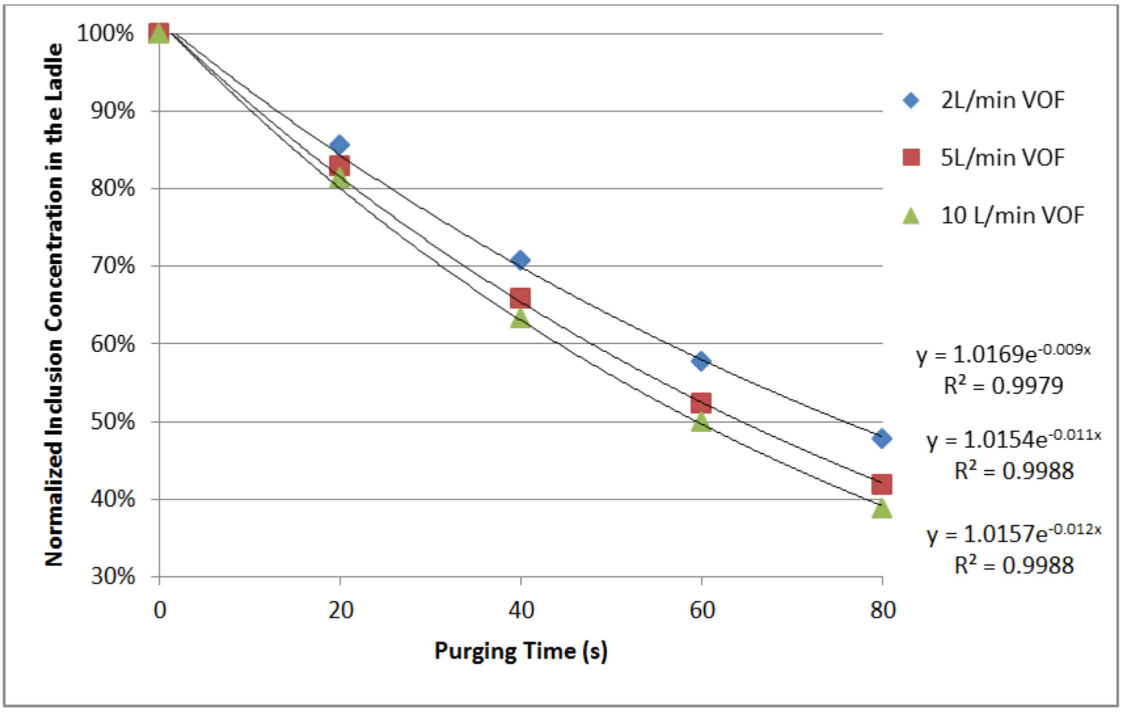

Figure 5.54: Curve fits for the inclusion concentration variation in the ladle with the purging time.

- The Eulerian models adopted in this study considered a steady-state solution where the flow was already fully developed from the start. However, it was seen in the transient results obtained through the VOF model simulations, that the flow takes some time to fully develop. With more stirring, there is a higher probability of collision between the inclusions and the top capturing surface, therefore this could have artificially enhanced the results obtained with the first two approaches.

- The capture criterion adopted in the VOF model simulations also includes the condition that the inclusion velocity magnitude should be less than 0.1 m/s for it to attach to the top surface.

- The modeling of the free surface allows the development of a spout above the plug, which causes a deformation in the water/air interface. As a consequence, a significant portion of the fluid does not flow closely parallel to the interface but acquires a downward velocity component. This effect likely drags some inclusions away from the capturing interface. When a flat surface is considered, this effect is not accounted for and the inclusion capture is probably enhanced.

Table 5.8: Inclusion removal efficiencies after 80s of purging. Values relative to initial inclusion concentration before transport stage (Absolute Purging PRI).

Configuration	Eulerian Flat Surface Standard Capture Criterion	Eulerian Flat Surface Custom Capture Criterion	VOF Custom Capture Criterion
2L_P1	72.3%	67.2%	64.5%
5L_P1	83.4%	72.2%	68.9%
10L_P1	89.1%	72.3%	71.2%

In the next section, the teeming simulations will be presented and discussed considering the inclusions distributions after 80 seconds of purging, obtained through the VOF model, as the initial conditions. It has been noticed previously in this study that the teeming simulations did not cause significant alterations in the inclusion removal efficiency results. This was due to the suction effect of the inclusions located on the interface when the liquid level decreased.

In order to circumvent this effect, a modification was introduced in the model. Through an UDF, it was defined that the inclusions which touched the interface would be eliminated, simulating what would happen in a real situation when an inclusion would be captured by an adequate steelmaking slag. With such an effect being considered, it would be expected that the teeming process would make a difference in the final inclusion removal efficiency obtained.

5.4.3 Inclusion removal efficiency after teeming – VOF Model

In order to evaluate the effect of the modification introduced by the inclusion capture UDF, the inclusion counting curves obtained for the reference configuration, in which no purging treatment was performed, are going to be compared accordingly to the two different approaches.

Figure 5.55 shows the curves obtained through the two procedures. The inclusion capture UDF significantly influences the inclusion removal efficiency at the end of teeming, since it eliminates the steepening of the curve that had been observed in the later stages of teeming. Figure 5.56 shows the inclusion distribution in the ladle after 9 minutes of teeming. Since the inclusions at the top surface have been removed from the calculations, they cannot be sucked into the nozzle anymore.

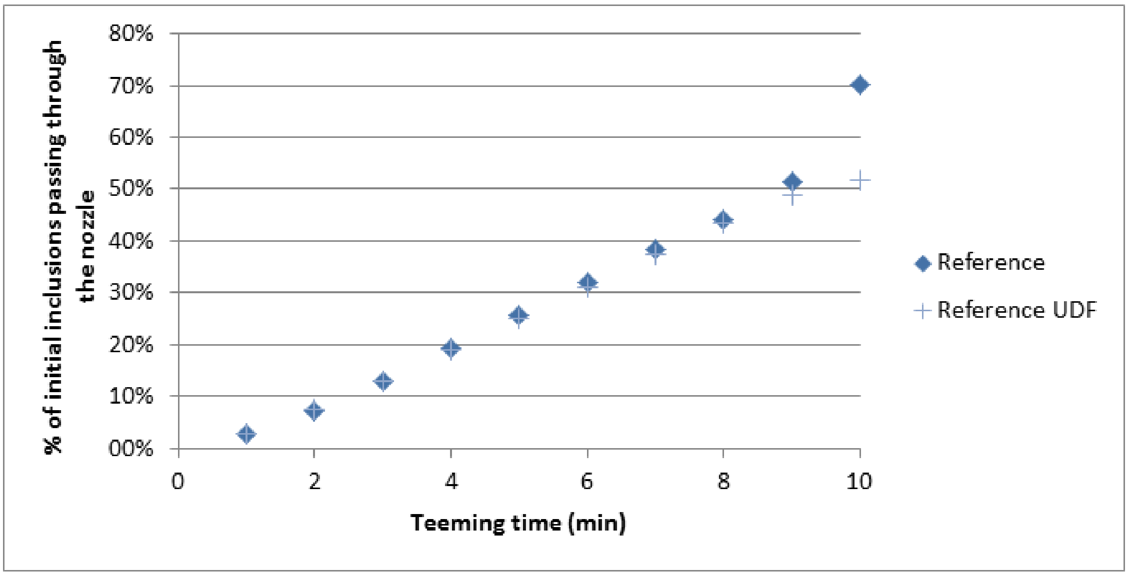

Figure 5.55: Effect of the Inclusion Capture UDF in the teeming simulations.

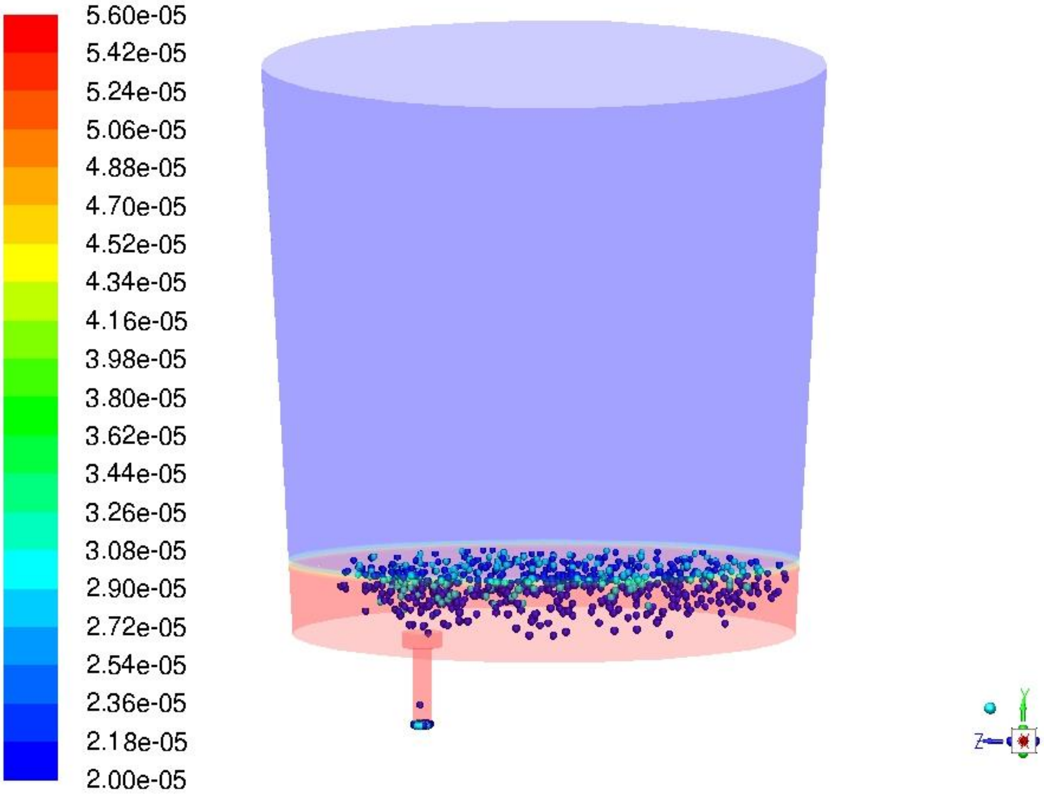

Figure 5.56: Inclusion distribution after 9 minutes of teeming for the reference configuration. Teeming model with UDF for inclusion capture at the interface. Colormap showing the inclusion size in [m].

Adopting this modified teeming model, the inclusion counting curves were obtained for the three configurations of purging, which were previously simulated through the VOF model. It can be seen that not only the final inclusion removal efficiencies are different from the results obtained previously with other modeling approaches, but the shape of the curve also became different. Now, instead of steepening in the later stages of teeming, the curve slope gets lower. This occurs since there are less inclusions in the upper portion of the ladle, since most of them were removed from the calculations when they touched the top surface. This effect reduced the amount of inclusions passing to the nozzle dramatically for the reference configuration. As for the configurations with gas purging, there is not enough data available for such conclusion, since the VOF purging model inclusion results have not been fed into the standard teeming model used before in this study. Most likely the inclusion capture during teeming had an effect towards increasing inclusion removal, but this was not enough to compensate the reduced effectiveness observed in the purging stage caused by the alternative modeling approaches. Table 5.9 shows the *Absolute PRI* results obtained after teeming considering the different modeling approaches presented in this study.

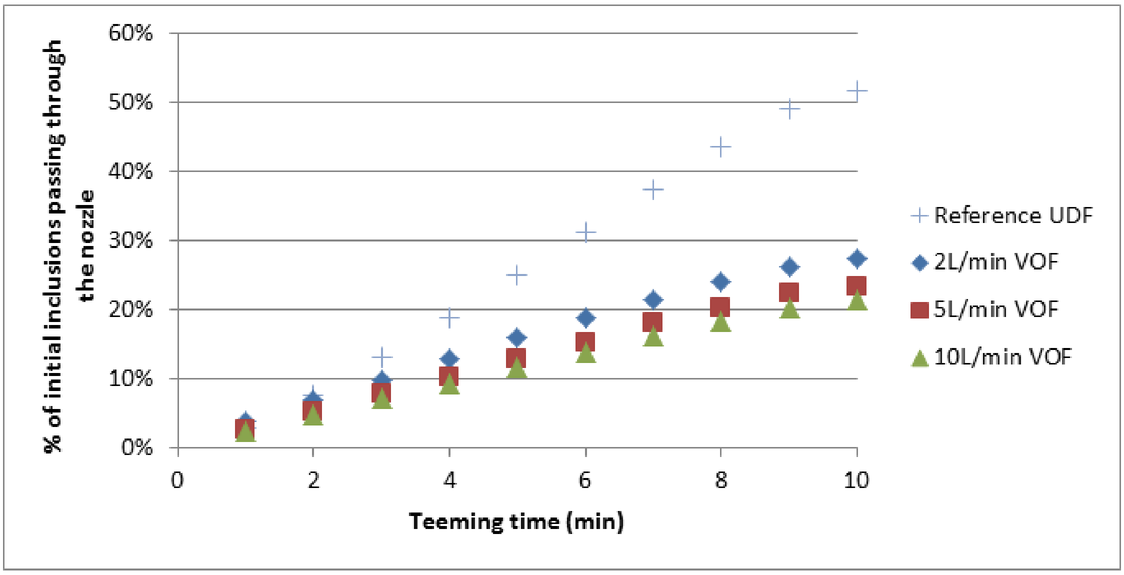

Figure 5.57: Inclusion Removal Efficiency obtained using the VOF model and including the inclusion capture UDF in the teeming simulations.

Table 5.9: Absolute PRI results comparing (1) the Eulerian Flat Surface model with Standard Teeming model (2) VOF purging model with Modified Teeming model.

Configuration	Absolute PRI Eulerian Flat Surface + Standard Teeming model	Absolute PRI VOF + Modified Teeming model
No purging	29.8%	48.4%
2L_P1	73.9%	72.7%
5L_P1	84.5%	76.6%
10L_P1	89.8%	78.7%

The Inclusion Removal results evaluated separately for each stage are shown in Table 5.10 and Table 5.11. The purging stage is clearly the step in which most inclusions are removed, regardless of the modeling approach.

Table 5.10: Inclusion Removal results in each stage of the process. Eulerian Flat Surface model.

Configuration	Inclusion Removal after Transport	Inclusion Removal after Purging	Inclusion Removal after Teeming
No purging	25.6%	25.6%	29.8%
2L_P1	25.6%	72.3%	73.9%
5L_P1	25.6%	83.4%	84.5%
10L_P1	25.6%	89.1%	89.8%

Table 5.11: Inclusion Removal results in each stage of the process. VOF model.

Configuration	Inclusion Removal after Transport	Inclusion Removal after Purging	Inclusion Removal after Teeming
No purging	25.6%	25.6%	48.4%
2L_P1	25.6%	64.5%	72.7%
5L_P1	25.6%	68.9%	76.6%
10L_P1	25.6%	71.2%	78.7%

In order to evaluate the effectiveness of the purging treatments, it is also interesting to evaluate the *Relative PRI* results. Table 5.12 shows the *Relative PR*I results obtained for each gas flow rate value, considering both mathematical models. It can be seen that the VOF model coupled with the modified teeming model predicted a lower Relative PRI for the treatments compared to the Eulerian Flat Surface model with Standard Teeming model.

This occurred due to two effects:

- The lower *Absolute PRI* obtained for the purging treatments when modeled through the VOF model, which can be seen in Table 5.9.

- The increased inclusion removal during teeming when the modified teeming model is adopted. This reduced significantly the number of inclusions passing through the nozzle in the reference configuration. Since the *Relative PRI* is obtained by the ratio between the number of inclusions removed in the case to be studied and the number of inclusions removed in the reference configuration, an increase in the latter causes a lower *Relative PRI*.

Table 5.12: Relative inclusion removal efficiencies obtained with each gas purging rate, considering the different modeling approaches.

Configuration	Relative PRI Eulerian Flat Surface + Standard Teeming model	Relative PRI VOF + Modified Teeming model
2L_P1	62.9%	47.1%
5L_P1	78.0%	54.7%
10L_P1	85.5%	58.7%

In this section, it was possible to see that the same physical phenomenon can be modeled through several different approaches and that the results can be significantly different. Consequently, it is necessary to validate the mathematical models. In the next chapter, some experimental results obtained by Silva[2] are going to be presented. These results were compared to the mathematical model results and this should provide additional insight about which modeling approaches better represent the physical phenomenon. The results were also compared to the published results from other authors in the literature.

5.5 Mathematical Model Validation

In this section, the results obtained through the mathematical model were compared to the experimental results by Silva[2]. The comparisons were divided into different sub-sections.

First, a qualitative comparison was done regarding the plume overall shape, which was compared to the gas volume fraction distributions obtained through the different modeling approaches.

Next, the results for the simulation of the inclusions entering the APS probe were analyzed. This was an important step to verify the correlation between the number of inclusions counted in the probe and the total number of inclusions passing through the nozzle in the experiments.

Then, the curves counting the inclusions passing through the nozzle were compared for the mathematical model and the experiments for the reference case, with no gas purging treatment. The advantage of analyzing this specific configuration first is that it is possible to exclude the influence of the purging stage simulations in the final results. Since the mathematical model for the purging stage suffers from several limitations, especially regarding the modeling of the gas bubbles and mechanisms of inclusion attachment to the turbulent top surface, it is advantageous to start the comparisons by the simplest case where no gas purging is performed.

Following the APS probe verification model, the influence of the gas flow rate on the inclusion removal results was compared according to what has been observed in the mathematical model and in the experiments.

Finally, the results from both the mathematical model developed in the present work and the physical model experiments developed by Silva[2] were compared to what has been reported by other authors.

5.5.1 Purging Stage

The first comparison to be made is between the plume shape of the experiments and the gas fraction distributions obtained in the simulations. Since the gas plume is what drives the entire flow, it is important to have its representation in the mathematical model as close as possible to the real plume.

Figure 5.58 shows the plume shapes obtained in the experiments for various gas flow rates. From left to right, the figure shows the plumes obtained for the following flow rates, respectively: 1, 2, 4, 6, 8 and 10 NL/min.

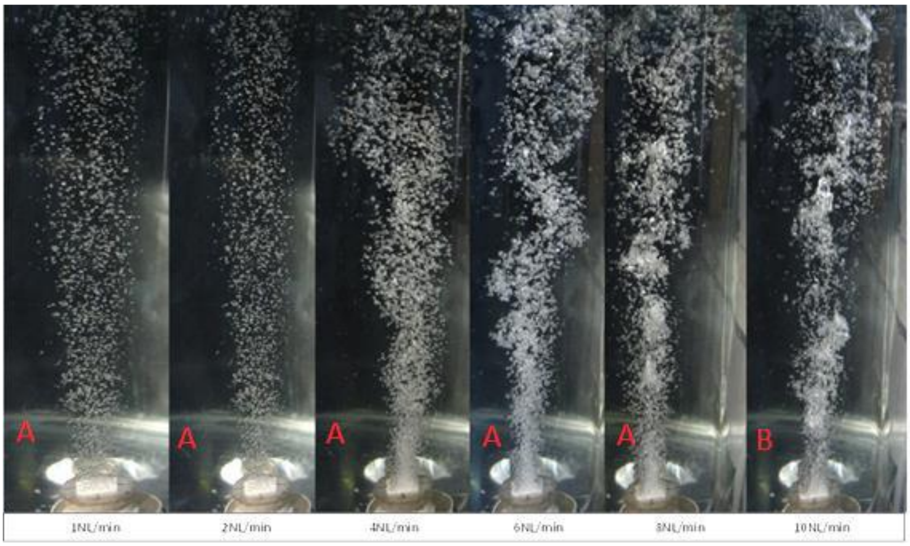

Figure 5.58: Evolution of the plume shape as the purging rate is increased. Silva (2018).[2]

Figure 5.59 shows the gas distribution obtained for the 10 NL/min purging rate for the Eulerian flat surface model and for the VOF model. It can be seen that, due to the turbulent dispersion effects that were included in the Eulerian model, the resulting plume was more disperse and consequently more similar to the real plume observed in the experiments. The possibility of considering non-drag forces in the model, such as the turbulent dispersion force, is a significant advantage of the Eulerian multiphase model over the VOF model, which does not allow for these considerations. On the other side, the VOF model captures the water/air interface dynamics, which the dispersed Eulerian model does not, and it is also a very important effect to consider for an accurate representation of the flow pattern in the ladle.

There are multiphase models which are able to consider both the plume dispersion effects and track the top interface dynamics. The Multi-Fluid VOF model is an extension of the Eulerian model in ANSYS Fluent and allows for the simulation of a free surface flow in some regions and dispersed flow in other regions. However, this model is also more complex to work with and the attempts performed in the present work to use the Multi-Fluid VOF model resulted in numerical divergence. It is suggested, for future work in this field, that the Multi-Fluid VOF model should be considered due to these advantages.

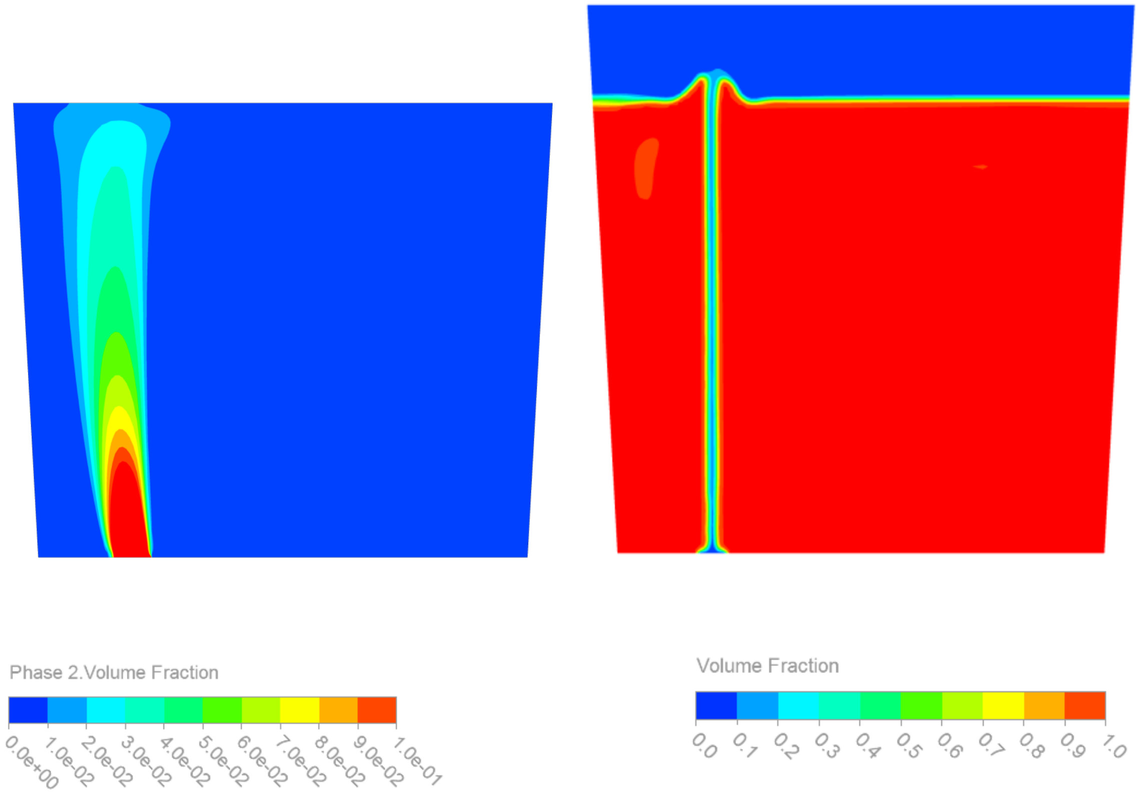

Figure 5.59: Volume Fraction distribution for the two different Modeling approaches. Gas Volume Fraction (phase-2) color map for the Eulerian Flat Surface Model (Left) and Water Volume Fraction for the VOF Model (Right).

5.5.2 APS Probe Model Results

In order to compare the experimental results of inclusion counting by the APS probe and the results from the mathematical model, it is necessary to understand the relationship between the number of inclusions counted by the probe and the total number of inclusions flowing through the nozzle.

Figure 5.60 shows the velocity contours for the mid plane of the nozzle. After this flow field has been obtained, a representative number of inclusions are injected at the top plane and follow this velocity field. The inclusions which enter the probe orifice eventually are entrapped and counted. The other inclusions leave the domain through the bottom boundary.

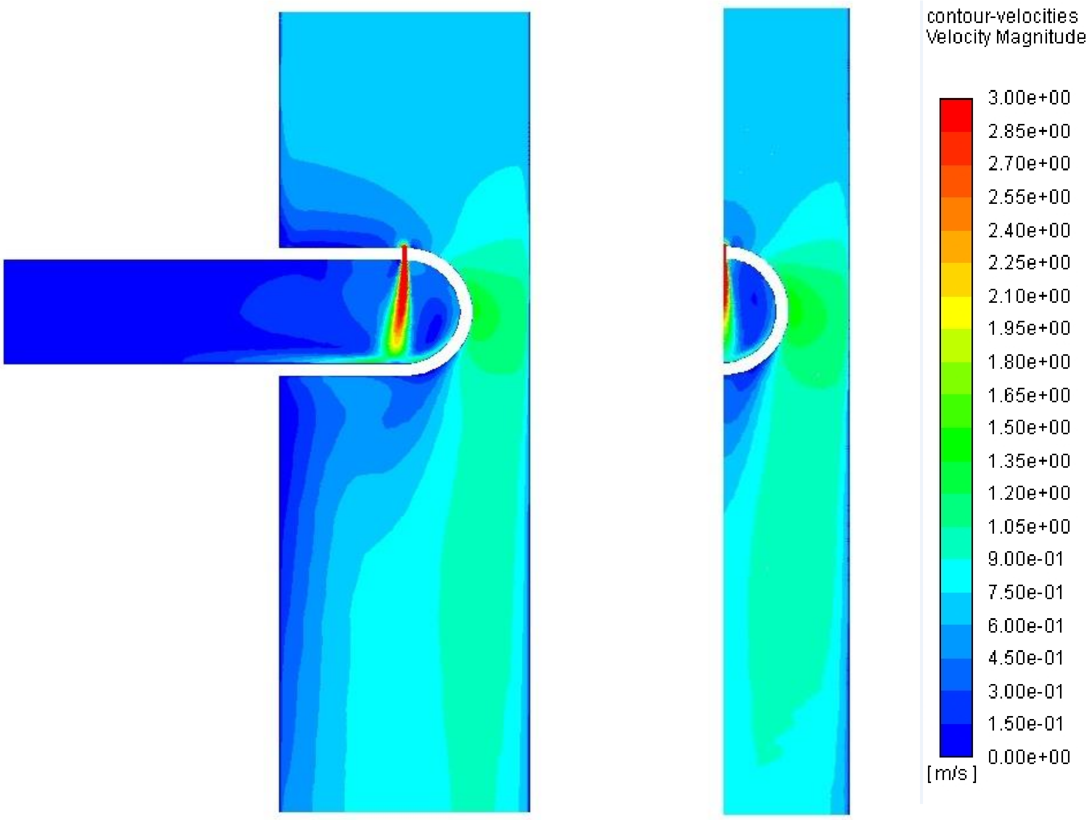

Figure 5.60: Velocity contours for the APS probe simulation.

Table 5.13 shows the results obtained through the APS probe simulations. From the 5041 inclusions of each size injected in the system, about 28 were counted by the probe, which gives a ratio of 0.56%. In other words, for every 179 inclusions passing through the nozzle, 1 would be counted. With this information, it is possible to relate the number of inclusions counted in the experiments to the total number of inclusions passing through the nozzle.

Table 5.13: Results for the ratio of inclusions counted by the APS Probe and the total number of inclusions passing through the system.

Diameter (µm)	Inclusions passing in the nozzle	Counted by APS probe	Ratio
20	5041	27	0.54%
30	5041	28	0.56%
38	5041	28	0.56%
45	5041	28	0.56%
56	5041	28	0.56%

It is interesting to notice that the average flow rate through the nozzle during teeming is approximately 20 L/min, while the average flow rate through the probe is approximately 0.09 L/min. The ratio between the flow rate through the probe and the flow rate through the nozzle is 0.0045, or 0.45%. This number is very close to the calculated ratio of inclusions counted in the probe and total number of inclusions in the nozzle. This is consistent with the fact that the inclusion sizes considered in this calculation are small and therefore follow closely the water flow.

5.5.3 Inclusions Counting for the Reference Case

Figure 5.61 shows the normalized inclusion counting results obtained by Silva[2] for the reference configuration. There were two main aspects worth analyzing in this curve: the number of inclusions counted and the shape of the curve.

Regarding the number of inclusions counted in the experiments, it is surprising how few inclusions have been counted for the case with no gas purging in the experiments. Recalling what has been described in the Methodology chapter of the present study, the total amount of countable inclusions at the start of the experiments is equal to 8.86 x 10^7 inclusions.

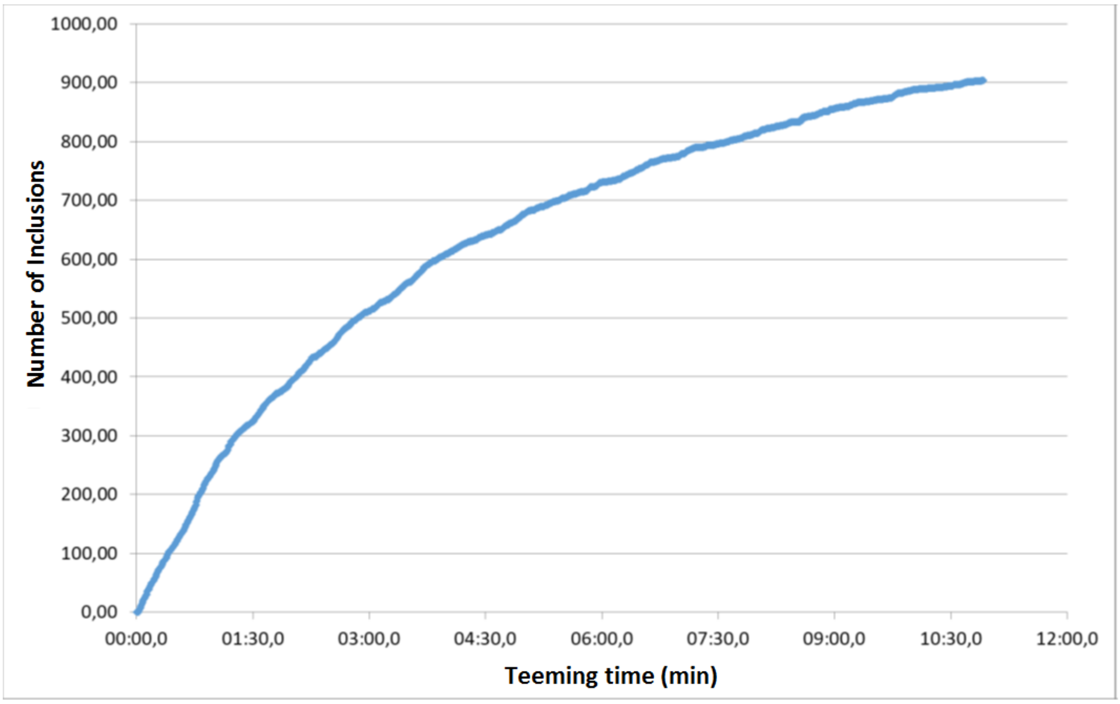

Figure 5.61: Normalized result for the inclusion counting for the reference case. Silva (2018)[2]

Considering the ratio of 1 inclusion counted for each 179 inclusions passing through the nozzle, calculated in the APS probe simulations, the total number of inclusions passing through the nozzle in Silva's[2] experiment for the reference case is given by Eq. 5.1:

$$900\ inclusions\ counted\ x\ 179 = 161{,}100\ total\ inclusions \tag{5.1}$$

Eq.5.2 gives the percentage of removed inclusions from the ladle, relative to the initial amount injected, for the case where no gas purging treatment was performed:

$$1 - \frac{1.61\ x\ 10^5}{8.86\ x\ 10^7} = 0.998 \tag{5.2}$$

Which means that 99.8% of the inclusions which were initially in the ladle have been removed exclusively due to buoyancy effects after 7 minutes of waiting time and during the teeming process, according to Silva's[2] results.

At this point, it is important to have in mind the terminal rising velocities of the inclusions considered in this study. The results shown previously in Table 5.5, when the inclusion counting results for the mathematical model were presented (Section 5.3.1), showed that during the 7 minutes of waiting time, a 20-µm diameter inclusion would float 6.79 cm, while a 30-µm diameter inclusion would cover 15.28 cm in the same time period.

Considering that these two inclusion sizes together make for more than 70% of the total amount of inclusions and that the liquid height is 60 cm, the total number of inclusions counted in the experiments seems to be significantly underestimated. The reasons for this deviation are not clear, however it is worth noticing the shape of the curve. The slope at the beginning is the highest and it gradually decreases with time. This suggests a higher concentration of inclusions near the ladle bottom at the start of teeming, since more inclusions are counted at the beginning. Since Silva[2] performed a normalization procedure of the inclusion counting results with the flow rate, the effect of the decreasing flow rate in the experiments has already been circumvented and does not provide an explanation for the curve slope. This behavior is different from what has been observed in the mathematical model, where the slope of the curve is approximately constant until the 8-9 minute mark, when it changes at the final stages of teeming.

If the inclusions are evenly distributed in the flow at the beginning of the experiments and if there is no gas purging to disturb the initial inclusion pattern, an inclusion counting curve with constant slope, as given by the mathematical model, is more consistent than a curve with decreasing slope, as given by the experiments. It has not been found a reason to explain why there would be more inclusions at the ladle bottom, if the particles were only subject to buoyancy effects. Therefore, it could be questioned whether the APS probe suffers some kind of saturation during the experiment. This would provide an explanation for the decreasing number of inclusions being counted as the experiments progressed and could also explain the overall low number of total inclusions counted in the experiments. Nevertheless, in the present study, only assumptions can be made about the reason behind the deviations observed in the experimental results.

Since an absolute match between the number of inclusions counted in the mathematical model and in the experiments could not be achieved, the comparisons are going to be performed regarding the effectiveness of the purging treatments, measured by the ratio between the number of inclusions counted during teeming after a purging treatment is performed and the number of inclusions counted in the reference configurations, where no purging treatment has been performed.

5.5.4 Effect of gas purging parameters on inclusion removal

5.5.4.1 Review of the experimental results by Silva[2]

In the work of Silva[2], there were made comparisons regarding the percentage of inclusion removal under different gas purging configurations. There were analyzed the effects of the plug surface area, time duration of the purging treatment and gas flow rate adopted, among others. Since the effect of the variation of the plug surface area was not studied in the present work, the main focus of analysis on the comparisons in this section was the time duration of the purging treatment and the gas flow rate. The plug surface area considered in the present study corresponds to the “Plug 1” in the nomenclature adopted in the work of Silva[2].

Figure 5.62 shows the percentage of removed inclusions (PRI) plotted against the different gas flow rates studied by Silva[2] (represented by the different symbols in the scale) for the three different plug types studied in the experiments considering a purging time of 81 seconds. It can be seen that the purging treatment effectiveness ranges between 40% and 70%. There is not a clear relationship between the studied gas flow rates and the PRI, according to the experimental results shown in Figure 5.62.

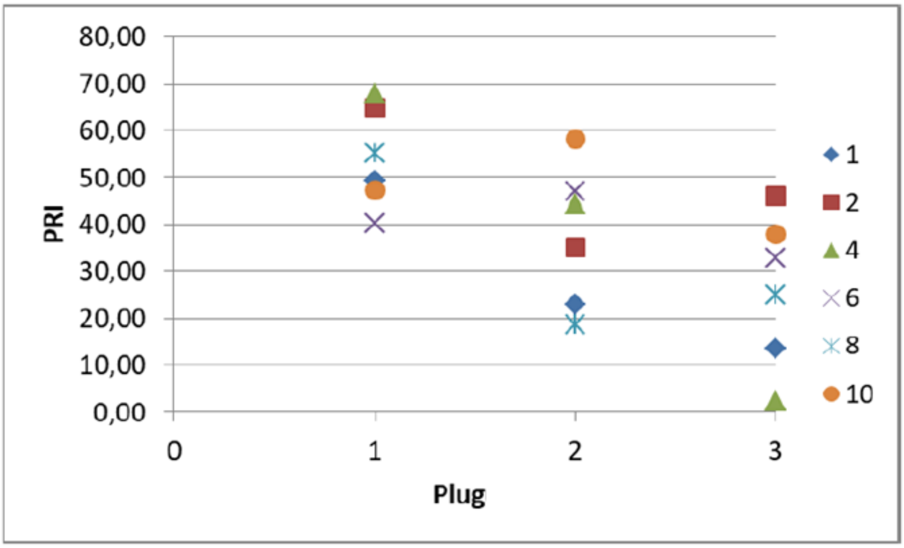

Figure 5.62: Inclusion Removal plotted against the plug type in the off-centered position after 81 seconds of purging time. Silva (2018)[2]

Figure 5.63 shows the average values of PRI obtained for each purging treatment time duration. The average PRI obtained for the plug 1 considering 81 seconds of purging was equal to approximately 55%. This value is higher than what has been obtained for the same plug when lower purging times were considered. For the other plugs, there is not a clear trend regarding the purging treatment time and the PRI. In his work, Silva considers that the dynamics of bubble formation might have played a significant role in the overall reduced effectiveness of plugs 2 and 3, which have a smaller surface area. Since the plugs 2 and 3 have not been the subject of study in the present work, further details about its results should be consulted in Silva[2].

Figure 5.64 shows the PRI results as the purging time is varied for the gas flow rates of 1 and 2 NL/min for the three different plugs. The nomenclatures adopted by Silva[2] in the curves are composed by two numbers. The first number is related to the plug type and the second number is related to the gas flow rate. For example, the curve 12 corresponds to the plug 1 with a 2 NL/min gas flow rate. For the plug 1, it can be seen that both flow rates show an increasing effectiveness of the purging treatment as its time duration is increased. The gas flow rate of 1 NL/min showed an overall higher effectiveness than the flow rate of 2 NL/min for the plug 1 in terms of the PRI for the purging times studied, according to Silva's[2] results.

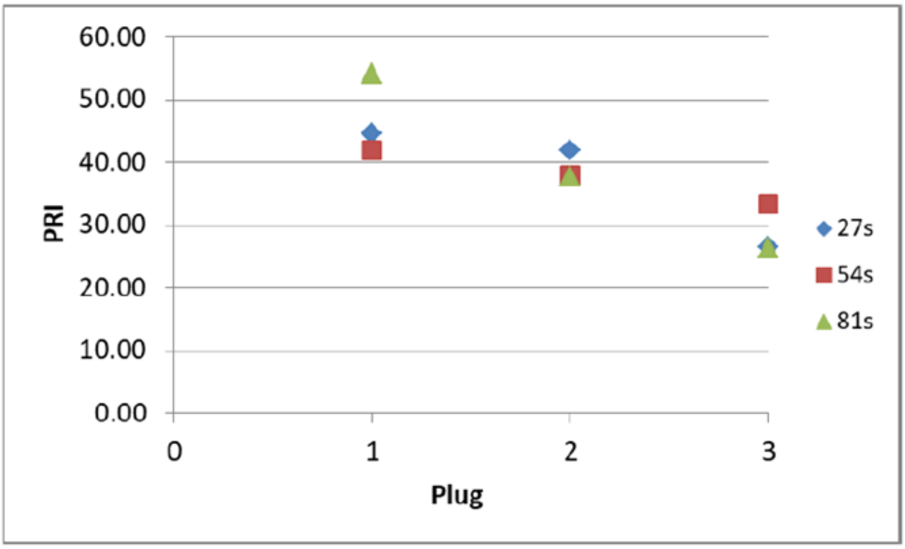

Figure 5.63: Averaged inclusion removal plotted against the purging time in the off-centered position. Silva (2018)[2]

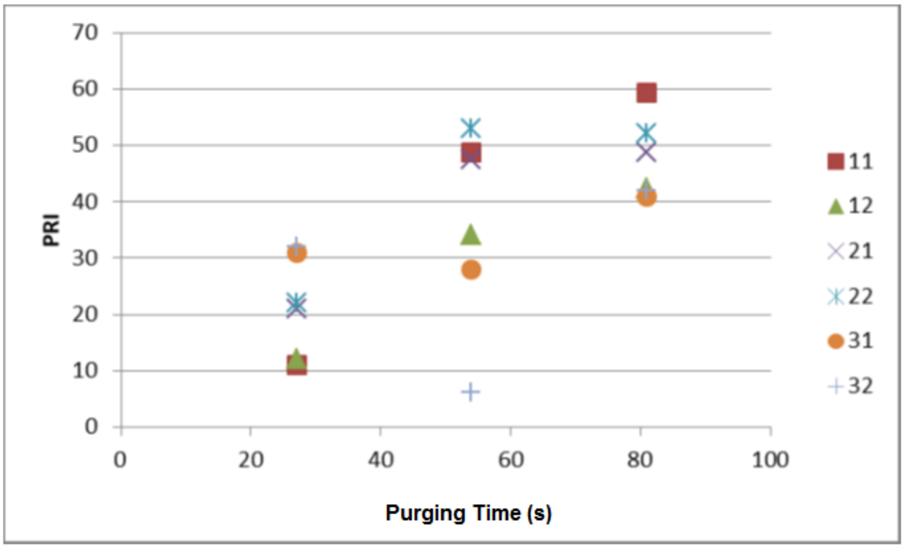

Figure 5.64: Inclusion removal in function of purging time for the gas flow rates of 1 and 2 NL/min. Silva (2018)[2].

Figure 5.65 shows the PRI results obtained for the higher flow rates adopted in the experiments: 8 and 10 NL/min. No clear relationship can be seen between the purging time neither the gas flow rate when comparing these two flow rate values for the plug 1. The results for the 8 NL/min flow rate show a low PRI for the shortest purging time

(27s), then increase sharply for the intermediate purging time (54s) and finally decrease slightly for the longer purging time (81s). The results for the 10 NL/min flow rate show a high PRI for the first two purging times studied (27 and 54s) and then sharply decrease for the longer purging time (81s).

The explanation provided by Silva[2] for the erratic behavior of the results was based on the phenomenon of inclusion reversal from the top surface towards the bulk flow. In order to investigate deeply the inclusion reversal phenomenon, Silva[2] performed additional experiments in the water model with a layer of particles in the top surface to simulate the slag layer. The particles were made of polystyrene and the same amount was injected in all experiments, simulating a slag layer of 2.5 cm in the ladle.

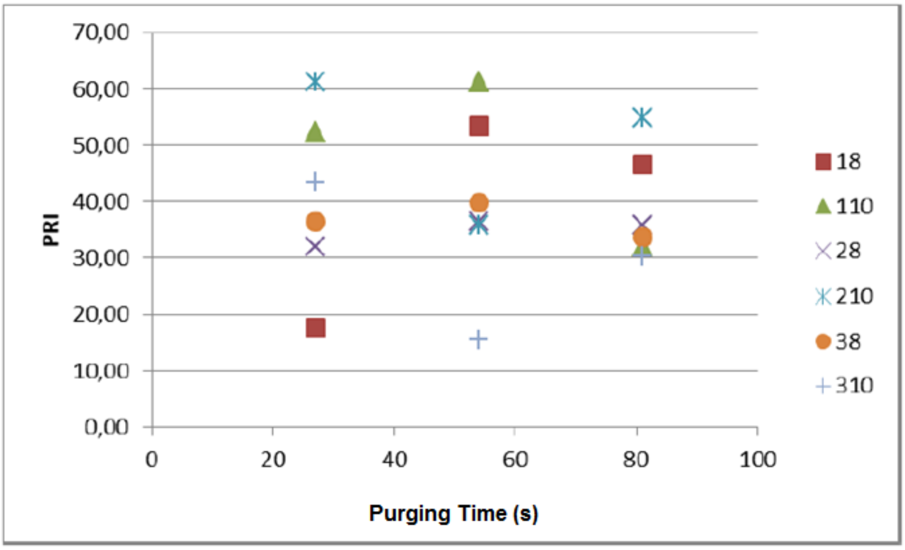

Figure 5.65: Inclusion removal in function of purging time for the gas flow rates of 8 and 10 NL/min. Silva (2018)[2].

Figure 5.66 shows the evolution of the particles recirculations in the ladle with the purging time. According to Silva[2], the results show that the gas purging initially opens the slag eye, dragging many particles back to the bulk flow. At the moment when the plume is stabilized and the slag eye is already formed, the recirculation of particle is reduced, as the gas passes directly from the liquid to the atmosphere, without getting in contact with the slag layer. This causes the inclusion reversal effect to be higher at the beginning and after some time, this effect tends to get lower. Figure 5.67 shows the inclusion reversal phenomenon at the moment of the slag eye stabilization and after some time of purging treatment.

As pointed by Silva[2], it can be seen in Figure 5.67 that the inclusion reversal effect is more pronounced at 30 seconds of purging than at 60 seconds of purging. It has been observed that after the slag eye stabilization, the inclusion reversal effect gets lower. Figure 5.68 shows the variation of the inclusion reversal as the gas flow rate increases. Overall, the lower gas flow rates showed a lower tendency of inclusion reversal, as it would be expected.

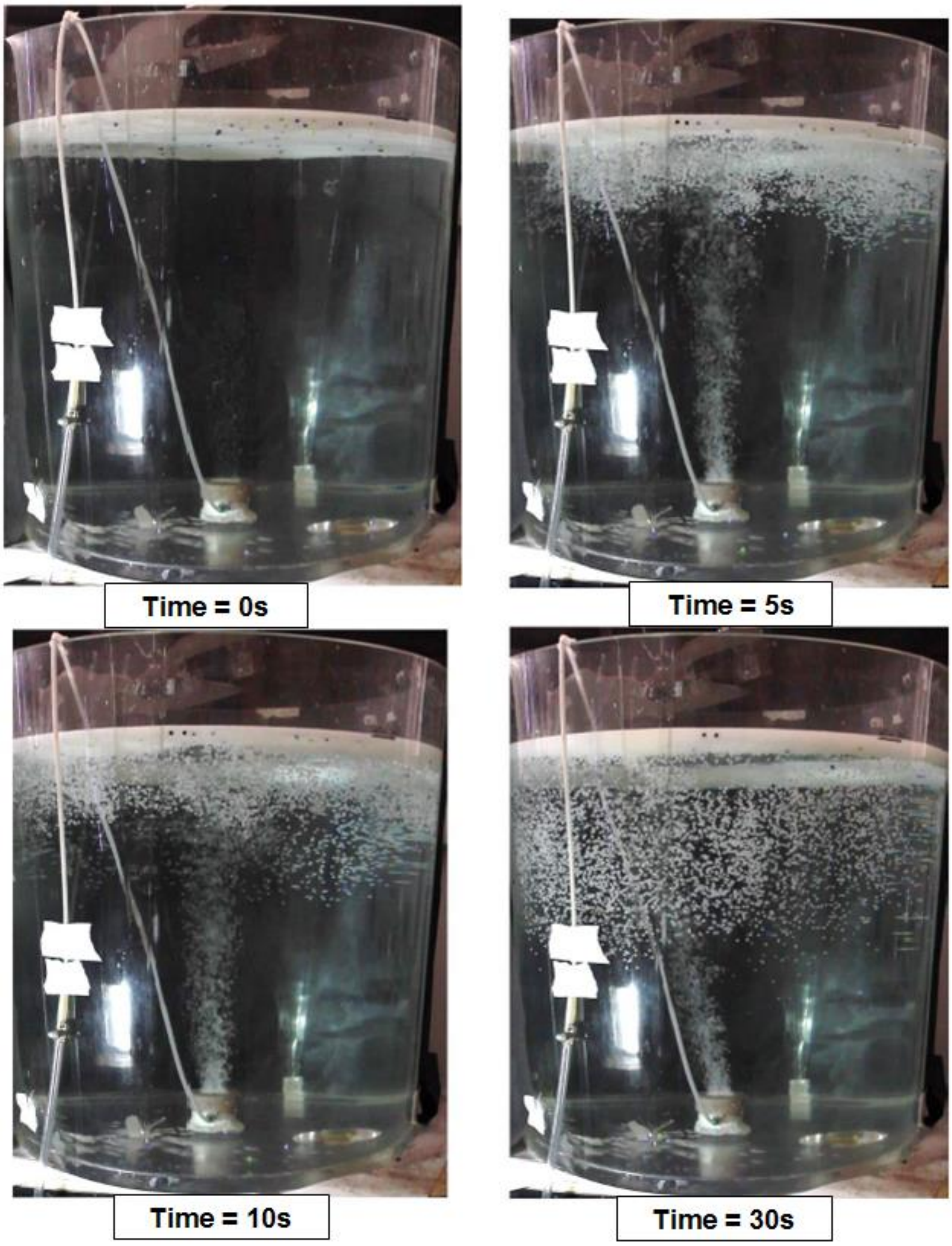
Time = 0s
Time = 5s
Time = 10s
Time = 30s

Figure 5.66: Evolution of the inclusion reversal during gas purging for the centered plug considering a gas flow rate of 8 NL/min. (Silva, 2018)[2]

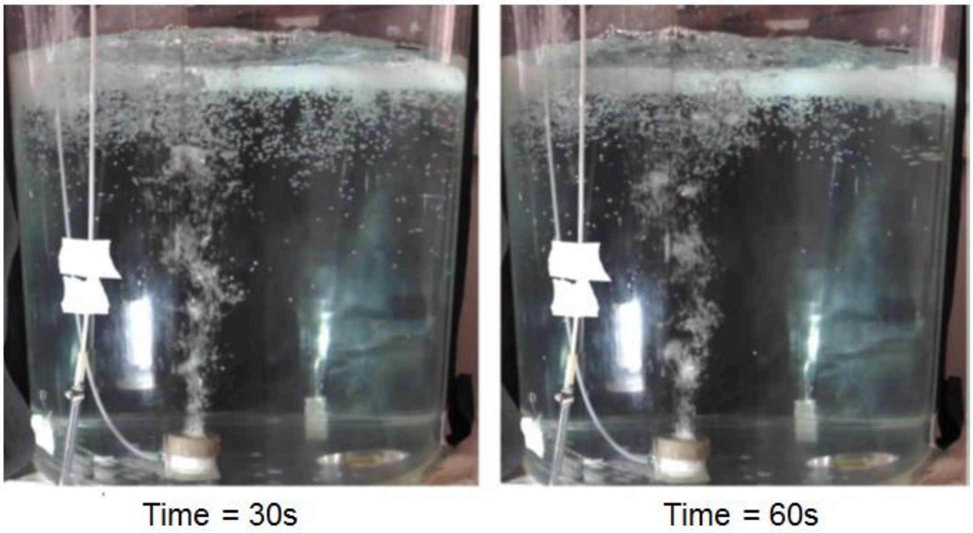

Figure 5.67: Inclusion reversal effect shown after 30 and 60 seconds of purging. Silva (2018)[2]

Silva[2] correlated the inclusion reversal phenomenon with the reduced effectiveness of the higher gas flow rates under longer purging treatment times. According to Silva[2], at the beginning of the purging treatment, there would be many inclusions distributed in the bath. This would cause the initial inclusion removal to be high. As the purging treatment progressed, the inclusion concentration in the bath would lower, increasing the inclusion reversal phenomenon. With higher bubble velocities this reversal would be higher. Therefore, under higher flow rates and longer purging treatment times, the effectiveness of the treatments would be worse.

The above statement by Silva[2] is partially consistent with the observations of the present study, regarding the fact that the rate of inclusion removal is indeed higher in the early stages of the treatment, due to the presence of more inclusions in the bath. The inverse exponential relationship between the PRI and the purging time found in the present study (Figure 5.54 in Section Inclusion removal efficiency during purging – VOF Model5.4.2) agrees with the proposition that the inclusion removal rate gets lower as the purging treatment progresses.

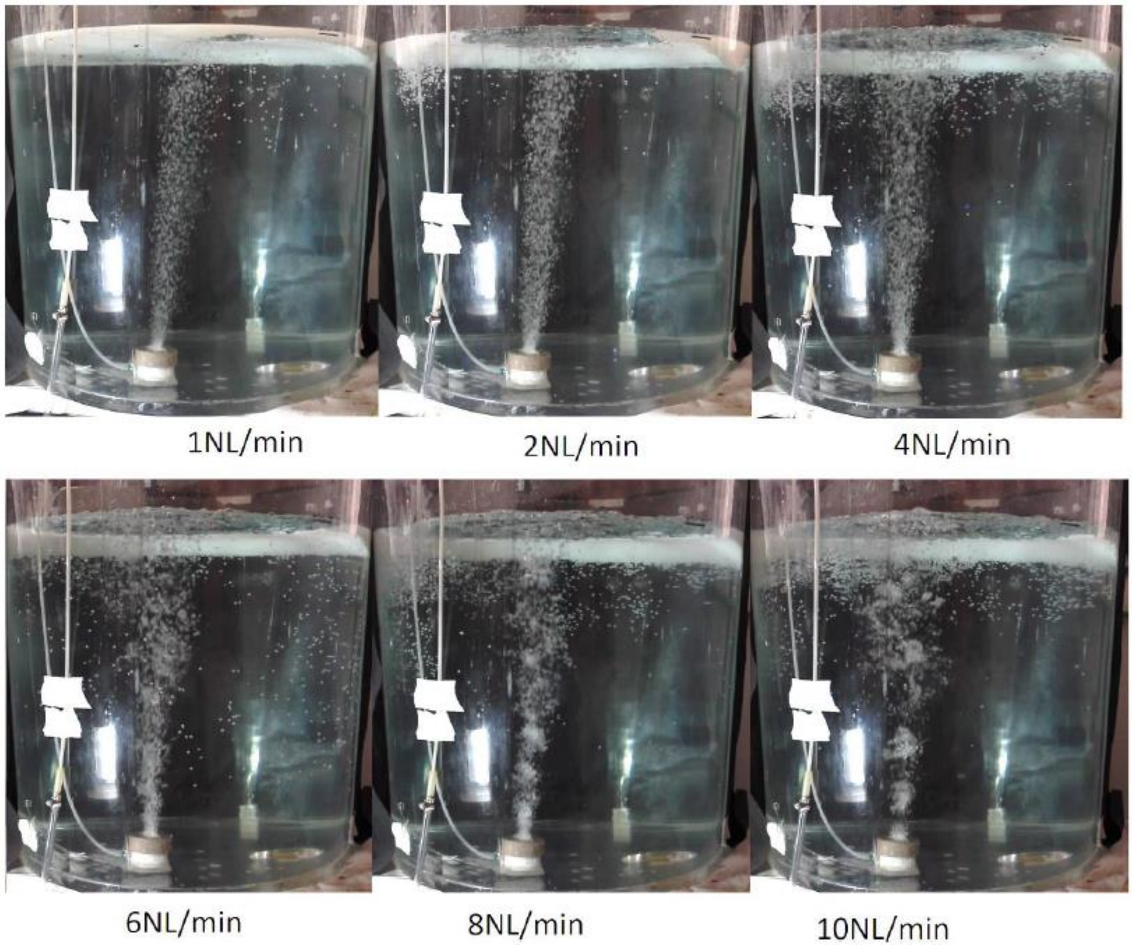

Figure 5.68: Variation of the inclusion reversal phenomenon as the gas flow rate is increased for the plug 2, considering a purging time of 30 seconds. Silva (2018)[2]

However, the explanation provided by Silva[2] for the reduced effectiveness of the purging treatments under high flow rates and longer purging times is not consistent with his own observations about the inclusion reversal phenomenon. As it has been described in the previous paragraphs, the inclusion reversal experiments performed by Silva[2] showed that the inclusion reversal would be the highest at the early instants of purging, showing a tendency of stabilization after some time.

Consequently, the inclusion reversal phenomenon is not a convincing explanation for the much lower PRI shown by the 10 NL/min treatment during 81 seconds, compared to the results for the same gas flow rate and 54 seconds of treatment. If the inclusion reversal were to stabilize after the initial instants of purging, as it would be expected according to the previous observations, then it would not cause a sudden loss of effectiveness in the purging treatment so long after the start of the treatment. The PRI at 54 seconds should be lower or at least equal to the PRI at 81 seconds according to this line of thought, which was not the case.

It is also difficult to justify why the PRI under 2 L/min is significantly lower than the PRI under 1 L/min for the plug 1 (Figure 5.64). Since these purging rates are in the lower range of the flow rates studied, it would not be expected that inclusion reversal would play a significant role in the obtained PRIs for these configurations. In Figure 5.68, it can also be seen that inclusion reversal is not as significant for these flow rates as it is for the higher purging rates.

The observations of the previous paragraphs suggest that there is a significant degree of variability in the experimental results obtained by Silva[2]. This could be explained by the strong sensitivity of the APS probe. Silva[2] reports that the APS probe is very sensitive and therefore all the experiments were carried in duplicates. Figure 5.69 shows the results of the duplicates for the cases considering the plug 1 and 2 NL/min flow rate. The nomenclature adopted by Silva[2] consists of characters representing sequentially: plug type, gas flow rate, purging time and duplicate. For example, “12a1” is the test code for plug 1, flow rate of 2 NL/min, purging time of 27s (“a” representing the shortest time studied, “b” the intermediate and “c” the longest) and the first duplicate. Comparing the curves 12a1 and 12a2, it can be seen that, for the same conditions, there could be very significant variations in the results registered by the probe.

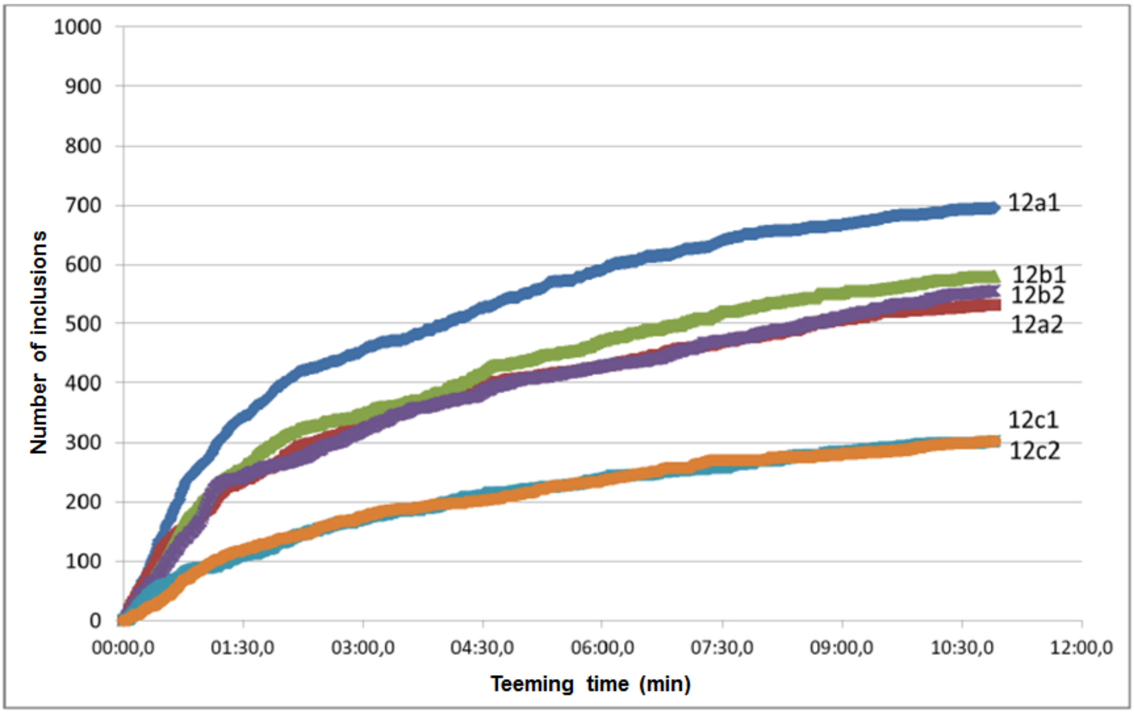

Figure 5.69:Results of the duplicates in the three purging treatment times for the plug 1 considering a 2 L/min flow rate. Silva (2018)[2]

A previous work by Silva[43], which used a very similar experimental system, showed even higher variability, as shown in Figure 5.70. It is evident that there was a significant improvement in the reduction of results variability comparing the most recent work (Silva[2]) with the past work (Silva[43]). However, these results show that the experimental system is prone to significant variability in the results, probably induced by the APS probe sensitivity, and performing the experiments only twice for each set of conditions might not have been enough to completely circumvent this effect. Not only should more experiments be performed for each set of conditions, but it would also be very important that the significant statistical data were provided for the experimental results, such as the degree of uncertainty or the standard deviation of the samples.

The randomness seen in the experimental results pose a challenge for the comparisons with the mathematical model results. Nevertheless, the mathematical model also has its own limitations and its results vary significantly depending on the modeling choices, as it was seen in the previous sections. Therefore, the available experimental data should be used judiciously to guide the selection of which mathematical model is the most appropriate to represent the phenomenon of inclusion removal in the ladle.

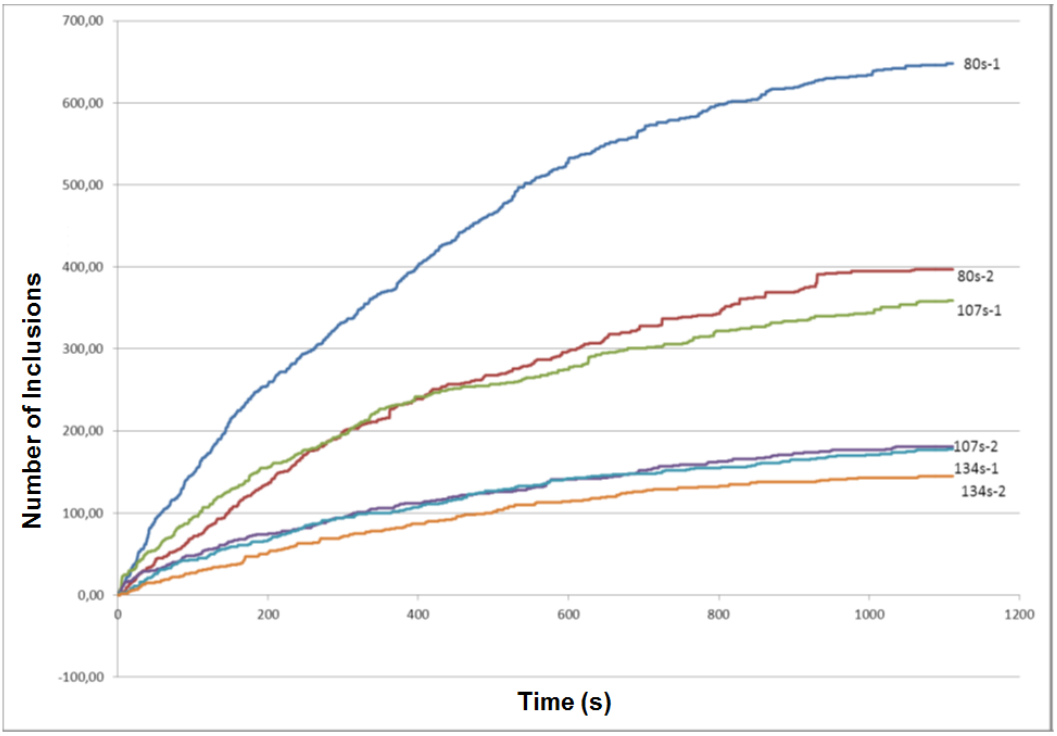

Figure 5.70: Inclusion counting results after a purging treatment considering a 5 NL/min gas flow rate. Silva (2014)[43]

5.5.4.2 Comparison between the mathematical model results and the experimental results

Table 5.14 shows a comparison between the obtained PRI at the end of teeming for the two mathematical modeling approaches adopted in the present work and the experimental results by Silva[2].

Table 5.14: PRI comparison at the end of teeming between the different mathematical modeling approaches and the experimental data.

Configuration	Relative Inclusion Removal Efficiency after Teeming (EE Flat Surface + Standard Teeming model)	Relative Inclusion Removal Efficiency after Teeming (VOF + Modified Teeming model)	Experimental data after 81s of purging time for the plug 1
1L/min	-	-	50%
2L/min	62.9%	47.1%	65%
4L/min	-	-	68%
5L/min	78.0%	54.7%	-
6L/min	-	-	40%
8L/min	-	-	55%
10L/min	85.5%	58.7%	47%

As it can be seen, there is not a direct match between the results when they are compared strictly for the same flow rate. However, keeping in mind the variability seen in the experimental results, it is interesting to notice that the results for the VOF model fit very well inside the range of variation of the experimental data. This is better seen in Figure 5.71, which shows the results from Table 5.14 in a curve.

From the curves it can be seen that the Eulerian (EE) Flat Surface approach gave PRI results outside the boundaries of the experimental data, which indicates that this mathematical model has overestimated the inclusion removal from the ladle. On the other side, the VOF model is well within the boundaries of the experimental data. If there were available information about the error bars of the experimental data, it is very likely that the VOF model results would be within the margin of error or at least close to that.

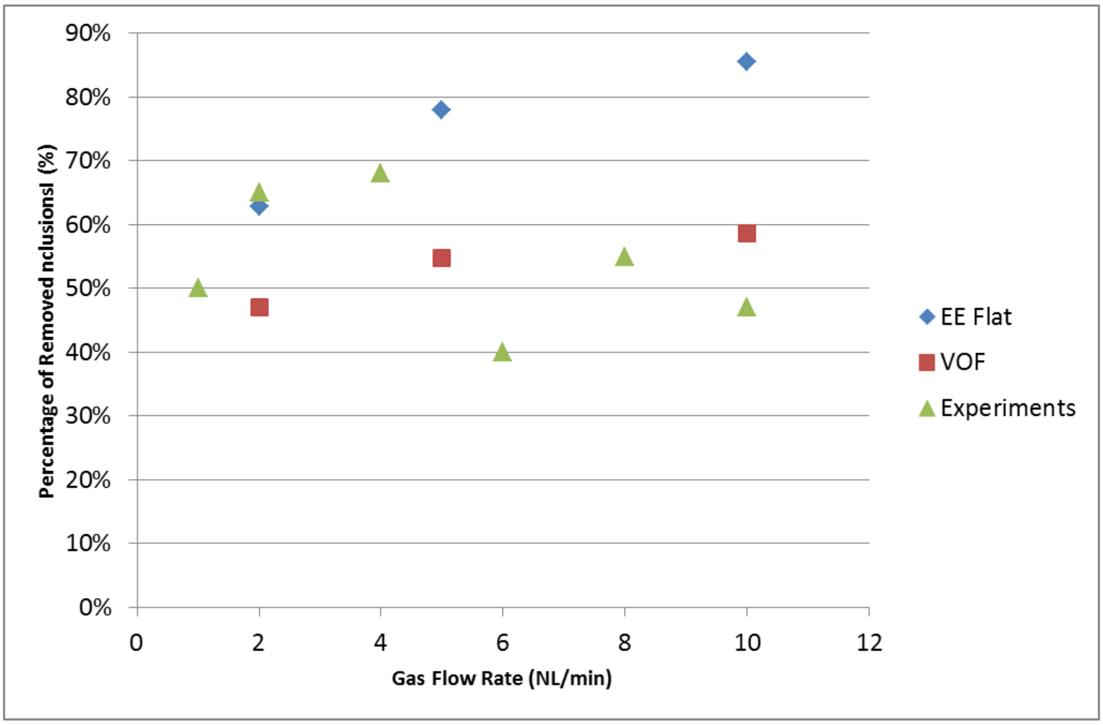

Figure 5.71: Curve showing the variation of the PRI with the gas flow rate for the mathematical models and experiments.

Another way to circumvent the variability of the experimental data for the purpose of validation of the mathematical model is to analyze the average PRI obtained for the purging time of 81 seconds and for the plug 1 in the experiments. By looking at the average over many experiments, the statistical randomness of the results is mitigated.

From Figure 5.63, it can be seen that the average PRI for the plug 1 considering 81 seconds of purging time is approximately 55%. This value is very consistent with the results obtained through the VOF model. Therefore, it can be concluded that, from the two mathematical modeling approaches adopted in the present study, the VOF model is the one that better fits the experimental data obtained by Silva[2] regarding the effect of the gas flow rate on the PRI.

As for the effect of the purging time on the PRI, other authors[35,36] have reported an approximate inverse exponential relationship between the PRI and the time duration of the purging treatment. This tendency has been well reproduced by the VOF modeling approach adopted in the present work. The experiments show this tendency only partially: in Figure 5.64, both curves for the plug 1 (curves 11 and 12) show a tendency similar to an inverse exponential relationship. The same cannot be said for the results shown in Figure 5.65, for the flow rates of 8 and 10 NL/min. Given the match between the mathematical model results and the results reported by other authors regarding this effect, it could be suggested that the experimental results shown in Figure 5.65 might have suffered with variability of the experimental results and lack of an appropriate number of repeated experiments.

Finally, the curves of inclusion counting during teeming should be compared between the experiments and the mathematical model. The adoption of the inclusion capture UDF during the teeming stage simulations caused a significant change in the shape of the inclusion counting curve for the mathematical model, by avoiding the occurrence of the steep section of the curve in the later stages of teeming. In this case, instead of the steepening of the curve, it was observed a flattening of the curve. The flattening of the curve fits better with the experimental data than the steepening behavior.

This analysis should not neglect the fact that the mathematical model still has several limitations, especially regarding the purging modeling. Among the limitations of the mathematical model, there are three which are most impacting on the relevant results of the present study. First is the limitation of not accounting for important effects such as the dynamics of bubble formation, breakup and coalescence. The behavior of the bubbles changes dramatically as the gas flow rate and plug type are varied, as shown in the work by Silva[2]. In order to properly account for these effects, more elaborate mathematical models should be adopted, such as a Population Balance Model. Another approach could be to adopt a VOF model with an extremely fine mesh, such as to completely resolve the bubbles interface. This would be extremely computationally expensive and not suitable for the present work.

Then, another limitation is the fact that the VOF model results, despite showing PRI results in the same range as the experiments, did not capture correctly the plume shape. The resulting gas plume in the VOF model is much narrower than it should be, according to the experiments. Whether a more disperse plume would have a significant effect on the PRI, perhaps displacing the results out of the experimental results boundaries, it would only be possible to know by running a simulation which considers both the VOF model at the top surface and the bubble dispersion effect at the plume region. Among others that could exist, two alternatives can be considered to achieve this in future works: the Multi-Fluid VOF model, which is a variant of the Eulerian model which is able to handle both disperse phases and free surface modeling or a coupled DPM model, treating the bubbles as a discrete phase, together with the VOF model for the free surface modeling. It is not clear whether the additional complexity introduced by these models would pay off in terms of a more accurate PRI result. Ideally, experiments for validation of the flow pattern in the ladle should also be performed. This way, the mathematical model can be validated on a more fundamental level, which would give more confidence when the PRI comparison was performed. By performing the validation studies only by comparing the PRI results, such as what has been done in the present work, it gets challenging to find the source of deviation when the experimental and numerical results do not match.

The other very important limitation of the mathematical model is the arbitrary criterion chosen for the inclusion capture at the top surface. The adopted criterion is consistent with the notion that a too high particle velocity at the moment of collision with the top surface might not allow for the particle flotation. However, it would be more appropriate if the criterion for particle removal at the top surface was based on the actual physical phenomenon taking place at the top surface, such as a hypothetical relationship between the surface tensions of the system water/air/inclusion which would possibly result in an equilibrium when the inclusion was entrapped in the interface. In a real steelmaking ladle, the inclusions would most likely be absorbed by the slag. In the physical model system, there is no slag to retain the inclusion, however, there seems to be still some kind of force acting towards keeping the inclusions close to the interface, otherwise they would just homogenize in the entire ladle under the effects of stirring, and the purging treatments would have no beneficial effect at all. In the present work, the arbitrary criterion was chosen with the purpose of analyzing the effect of excluding inclusion capture if the particle velocity was too high and the resulting PRI was consistent with the experiments. Nevertheless, there is still the necessity of studying better what really happens at the interface and applying this knowledge into developing a more elaborate criterion for inclusion removal in the mathematical model.

6. CONCLUSÕES

No presente trabalho, um modelo matemático foi desenvolvido para estudar a remoção de inclusões durante a drenagem da panela, logo após a injeção com gás inerte. Diferentes abordagens de modelagem matemática foram testadas com o objetivo de identificar quais reproduziriam melhor os resultados experimentais obtidos no trabalho de Silva[2]. Além disso, o modelo desenvolvido permitiu a avaliação de resultados relevantes, como padrões de velocidade e turbulência, os quais têm influência significativa na remoção da inclusão, mas não são facilmente obtidos a partir do modelo experimental. O modelo desenvolvido também foi adotado para estudar a influência das variáveis do processo de rinsagem na eficiência de remoção de inclusões, tais como: vazão de gás e tempo de rinsagem.

Existem várias opções de modelagem que precisam ser feitas quando um modelo matemático é desenvolvido. Para avaliar cada uma dessas escolhas de modelagem separadamente, seria necessário realizar um número impraticável de simulações, portanto dois modelos matemáticos diferentes foram desenvolvidos, cada um abrangendo decisões de modelagem variadas. Esses modelos são resumidos da seguinte forma:

I.
   a. Cálculo de um campo de fluxo em estado estacionário, seguido por um cálculo da trajetória de inclusões neste campo de fluxo durante o tempo de rinsagem a ser considerado.
   b. Modelo multifásico Euleriano para a fase gasosa nas simulações de rinsagem.
   c. Condição de contorno de parede plana na interface água / ar, considerando tensão de cisalhamento zero.
   d. Coeficiente de restituição das inclusões na superfície superior igual a zero. Isso significa que as inclusões perdem todo o seu momento quando colidem com a superfície superior e são capturadas e removidas de cálculos posteriores.
   e. Durante o estágio de drenagem, as inclusões que atingiram a superfície superior não foram removidas dos cálculos. Portanto, nos estágios finais de drenagem, essas inclusões foram sugadas para o bocal, resultando em um pico de inclusões contadas nos minutos finais.

II.
   a. Cálculo transiente do campo de fluxo durante o tempo de rinsagem a ser considerado, com cálculo simultâneo da trajetória de inclusão.
   b. Modelo multifásico VOF nas simulações de rinsagem de gás.
   c. Modelagem de superfície livre na interface água / ar.
   d. UDF para remover inclusões quando eles alcançaram a interface. A remoção teve uma condição na qual a partícula seria removida somente se sua velocidade fosse menor que 0,1 m/s. Caso contrário, retornaria ao fluxo considerando um coeficiente de restituição de 0,001 (significando que ele reteria 0,1% de seu momento antes da colisão).
   e. Durante o estágio de drenagem, uma UDF foi adotada para remover dos cálculos as inclusões que atingiram a superfície superior. Isso evitou o pico de inclusões contadas nos estágios finais da drenagem.

Das duas abordagens de modelagem matemática estudadas, a segunda (VOF) mostrou uma melhor correspondência com os resultados experimentais. A exceção foi na forma da pluma, onde a primeira abordagem (Eulerian Flat Surface) forneceu resultados mais consistentes. Os resultados do PRI obtidos foram superestimados para o modelo Eulerian Flat Surface, provavelmente pelas seguintes razões:

- Maior intensidade de agitação na panela, provavelmente causada pela condição de limite da parede plana. Com maior agitação, há uma maior probabilidade de colisão entre as inclusões e a superfície superior de captura.

- Condição simples para captura de inclusão. Como todas as inclusões que tocaram a superfície superior foram capturadas, mesmo aquelas com altas velocidades, o PRI foi superestimado.

O cálculo transiente do campo de fluxo com cálculo simultâneo da trajetória de inclusões foi considerado mais apropriado do que a abordagem segregada de calcular primeiro o campo de fluxo de estado estacionário e depois calcular o movimento de inclusões. Inicialmente, esperava-se que o cálculo do estado estacionário fosse significativamente mais rápido. No entanto, esse não foi o caso, já que fatores muito baixos de relaxamento foram necessários para evitar divergências nos cálculos. Considerando que, para resolver um fluxo bifásico através do modelo euleriano, seis equações de momento fortemente acopladas precisam ser resolvidas até a convergência, contra três para o modelo VOF, a conseqüência é que a demanda computacional para o modelo Euleriano é muito maior do que para o modelo VOF. Além disso, utilizando o esquema SIMPLE para o acoplamento pressão-velocidade, como foi feito no presente trabalho, não há uma referência do tempo físico decorrido desde o início dos cálculos. O cálculo transiente foi considerado mais conveniente e não significativamente mais computacionalmente intensivo, uma vez que não foi necessário julgar se o fluxo estava totalmente desenvolvido ou não. A simulação seria executada apenas para o tempo de rinsagem a ser estudado, independentemente do estágio de desenvolvimento do fluxo no final dos cálculos. Portanto, a abordagem transiente seria a mais recomendada, independentemente das outras opções de modelagem.

Quanto à escolha do modelo multifásico, os resultados do modelo VOF coincidiram melhor com os dados experimentais. Isto sugere que é muito importante contabilizar a influência da superfície livre no fluxo, especialmente desde que se observou que seus efeitos causam velocidades globais mais baixas na panela, o que tem um impacto direto no movimento das inclusões. No entanto, existem limitações nessa abordagem, principalmente em como ela lida com a interação entre as diferentes fases. O modelo VOF é mais adequado para modelagem da superfície livre, não para modelagem de fases dispersas, como as bolhas. Uma vez que o modelo VOF não tem a opção de incluir forças de não arrasto nos cálculos, a pluma resultante é muito mais fina do que deveria ser. Isso poderia ter um impacto negativo no cálculo do padrão de fluxo e, consequentemente, nos resultados de remoção de inclusão. Portanto, em uma comparação direta entre os dois modelos multifásicos estudados, o VOF seria a melhor escolha, entretanto uma abordagem de modelagem mais abrangente que englobe tanto um modelo apropriado para as fases dispersas quanto para a superfície livre seria a mais recomendada. Uma sugestão seria o modelo Multi Fluid VOF, que é uma variante do modelo Euleriano disponível no ANSYS Fluent. Um DPM acoplado para as bolhas, juntamente com o modelo VOF para a superfície livre, também poderia ser uma escolha mais adequada.

A condição de contorno para as inclusões na superfície superior também foi considerada muito influente para a previsão da eficácia dos tratamentos de rinsagem. Nas primeiras simulações realizadas no presente trabalho, concluiu-se que um critério simples não seria suficiente para representar o comportamento das inclusões na superfície superior. Considerando os critérios simples disponíveis no ANSYS Fluent para o comportamento de inclusão na superfície superior, existem dois tipos principais:

a) Se um coeficiente de restituição zero é definido para as inclusões, elas perdem todo o seu momento ao colidir com a superfície superior, sendo consideradas como capturadas e depois removidas de cálculos posteriores.
b) Se qualquer valor maior que zero for definido para o coeficiente de restituição, as inclusões retornam ao colidirem com a superfície superior, e sua velocidade após a colisão é calculada pelo coeficiente de restituição. Independentemente do valor escolhido para o coeficiente de restituição, as inclusões retornam ao fluxo e são dispersas pelo efeito das velocidades de fluxo e turbulência.

Nenhum desses dois critérios forneceu bons resultados. O primeiro causou resultados superestimados da remoção de inclusões, pois mesmo em áreas com turbulência excepcionalmente alta, como no topo da pluma, as inclusões seriam capturadas. Pior que isso, essas áreas apresentariam uma taxa de captura maior, já que a probabilidade de colisões entre as inclusões e a superfície superior seria maior nesses locais. Por outro lado, o segundo critério fez com que os tratamentos de rinsagem fossem completamente ineficazes, já que a rinsagem de gás teria apenas o efeito de homogeneizar as inclusões em toda a panela, revertendo qualquer efeito de flotação. Se um rebatimento absoluto fosse considerado no modelo, todas as configurações de rinsagem de gás mostrariam um PRI negativo, o que significa que seria melhor deixar o sistema para descansar por algum tempo do que adotar um tratamento de rinsagem. Tal comportamento vai contra os resultados experimentais de Silva[2] e também contra os resultados relatados por outros autores[35,36,37,39], todos relatando que os tratamentos de rinsagem com gás são benéficos em relação à remoção da inclusão. Portanto, o comportamento induzido pelo segundo critério também foi considerado incorreto.

A partir dos resultados acima mencionados, verificou-se que o comportamento correto das inclusões na interface seria algo entre os dois critérios simples descritos. Algumas inclusões que tocaram a superfície superior permaneceriam aderidas devido a algum mecanismo não claro no presente trabalho, mesmo em um sistema de água / ar, mas não todas as inclusões. Portanto, para avaliar os resultados considerando um critério de captura intermediário, um critério de captura arbitrário foi desenvolvido e implementado através de uma UDF. Foi definido que apenas as inclusões que tocaram a superfície a baixa velocidade (arbitrariamente definidas como inferiores a 0,1 m/s) permaneceriam ligadas à superfície superior. As outras inclusões seriam rebatidas e retornariam ao fluxo.

O critério de captura personalizado, quando aplicado ao modelo Eulerian Flat Surface, teve o efeito de fechar a lacuna entre os PRIs das taxas de rinsagem intermediária e mais alta (5 e 10 NL/min). Isso indica que, sob a maior taxa de fluxo, a maior agitação e turbulência contribuíram para o maior PRI obtido, provavelmente superestimado. O critério de captura personalizado também foi aplicado ao modelo VOF. Isso resultou em um aumento modesto do PRI à medida que o fluxo de gás foi aumentado. Tal comportamento teve uma correspondência razoável com os dados experimentais e com outros resultados da literatura. Embora haja necessidade de maior desenvolvimento do critério de captura de inclusão, o critério personalizado definido no presente trabalho mostrou resultados satisfatórios.

Finalmente, havia o modelo de drenagem. Quando não foram considerados efeitos de captura de inclusão no modelo, constatou-se que essa etapa não teve influência significativa nos PRIs finais obtidos, pois mesmo as inclusões na parte superior da panela seriam sugadas para o dreno eventualmente, mesmo antes da aspiração de ar ocorrer. Por outro lado, quando uma UDF foi aplicada para remover as inclusões na interface dos cálculos (simulando absorção por uma escória real e também uma suposta força interfacial possivelmente atuando nos experimentos), então o estágio de drenagem influenciou os resultados finais do PRI. Esta influência não foi claramente no sentido de aumentar nem diminuir o PRI, uma vez que a UDF melhorou a remoção de inclusão para todos os casos, incluindo o caso de referência sem rinsagem. Também vale a pena mencionar o fato de que a adoção da UDF fez com que a curva de contagem de inclusão se parecesse mais com a curva obtida nos experimentos. Embora o comportamento visto nas curvas experimentais possa ser questionado sobre as razões pelas quais as curvas teriam uma inclinação maior no início e especialmente em relação à baixa contagem geral de inclusão, elas ainda são a única fonte disponível de validação do modelo desenvolvido no presente trabalho. Consequentemente, leva à conclusão de que os resultados do modelo de drenagem foram melhorados pela adição da captura de inclusão UDF.

O modelo matemático desenvolvido foi aplicado na avaliação do efeito de dois parâmetros do processo de rinsagem: vazão de gás e tempo de duração do tratamento de rinsagem. Para as faixas de parâmetros consideradas no presente trabalho, ambas as variáveis apresentaram relação positiva com a eficácia do tratamento de rinsagem, ou seja, quanto maior a taxa de fluxo de rinsagem e a duração do tratamento, maior seria o PRI. As tendências observadas também mostraram que para maiores taxas de fluxo e tempos de rinsagem, aumentos adicionais nessas variáveis mostraram um aumento progressivamente menor no PRI.

O PRI foi avaliado como mais sensível ao tempo de duração do tratamento de rinsagem do que a taxa de fluxo de gás adotada. Pode ser visto na Figura 5.54 na Seção 5.4.2. que para cada 20 segundos de aumento na duração do tempo de tratamento da rinsagem, o PRI aumentou em aproximadamente 15% para os tempos mais baixos (de 0 a 20 segundos e de 20 a 40 segundos de tratamento) e 10% para os tempos mais longos (de 40 a 60 segundos e de 60 a 80 segundos). Quando uma análise semelhante é realizada para o fluxo de gás, pode ser visto na Tabela 5.12 que quando a taxa de rinsagem é aumentada de 2 para 5 NL/min, o PRI aumenta em torno de 7,6% e quando é aumentado de 5 para 5 10 NL/min, o PRI aumenta 4,0%. Também deve-se ter em mente que é mais arriscado aumentar o fluxo de gás do que aumentar o tempo de duração do tratamento, levando-se em conta que, com um fluxo de gás maior, há mais turbulência na parte superior da panela, o que poderia causar olho aberto e arrastamento de escória em uma panela industrial real. Se tais efeitos deletérios acontecessem, quaisquer ganhos proporcionados pelo tratamento de rinsagem seriam imediatamente perdidos devido à reoxidação do aço e / ou ao arrastamento de inclusões da escória para o aço fundido.

Portanto, a recomendação que pode ser obtida do presente trabalho em relação à aplicação de tratamentos de rinsagem de gás em panelas industriais reais é que a vazão de gás deve ser mantida em faixa de baixa a moderada, enquanto o tempo de duração do tratamento deve ser o mais longo que o processo permitir. Convertendo os valores considerados no presente trabalho para os valores equivalentes em uma panela industrial real, para uma panela de 150 toneladas, a taxa de rinsagem recomendada seria entre 35 e 87 NL/min e a duração recomendada do tratamento de rinsagem seria pelo menos 3 minutos, com uma tendência de resultados ainda melhores em tempos de tratamento mais longos.

6. CONCLUSIONS

In the present work, a mathematical model was developed to study the inclusion removal during ladle teeming, right after inert gas purging. Different mathematical modeling approaches were tested with the goal of identifying which would better reproduce the experimental results obtained in the work of Silva[2]. Moreover, the developed model allowed for the evaluation of relevant results such as velocity and turbulence patterns, which have a significant influence on inclusion removal but are not easily obtainable from the experimental model. The developed model was also adopted to study the influence of purging process variables on the inclusion removal efficiency, such as: gas flow rate and purging time.

There are several modeling choices that need to be made when a mathematical model is developed. To evaluate each of these modeling choices separately would make for a impracticable number of simulations to be performed, therefore two different mathematical models were developed, each encompassing varied modeling decisions. These models are summarized as follows:

III.

  a. Calculation of a steady-state flow field followed by a calculation of the inclusions trajectory in this flow field during the purging time to be considered.
  b. Eulerian multiphase model for the gas phase in the purging simulations.
  c. Flat wall boundary condition at the water/air interface, considering zero shear stress.
  d. Coefficient of restitution of the inclusions at the top surface equal to zero. This means that the inclusions lose all their momentum when they collide with the top surface and are captured and removed from further computations.
  e. During the teeming stage, the inclusions which reached the top surface were not removed from the computations. Therefore, at the final stages of teeming, these inclusions were sucked into the nozzle, resulting in a peak of counted inclusions at the final minutes.

IV.

  f. Transient calculation of the flow field during the purging time to be considered, with simultaneous calculation of the inclusion trajectory.
  g. VOF multiphase model in the gas purging simulations.

h. Free surface modeling at the water/air interface.
i. UDF to remove inclusions when they reached the interface. The removal had a condition in which the particle would only be removed if its velocity was less than 0.1 m/s. Otherwise, it would return to the flow considering a 0.1 restitution coefficient (meaning that it would retain 10% of its momentum prior to the collision).
j. During the teeming stage, an UDF was adopted to remove the inclusions which reached the top surface from the computations. This avoided the peak of counted inclusions at the final stages of teeming.

From the two mathematical modeling approaches studied, the second (VOF) showed a better match with the experimental results. The exception was in the plume shape, where the first approach (Eulerian Flat Surface) provided more consistent results. The PRI results obtained were overestimated for the Eulerian Flat Surface model, probably due to the following reasons:

- Higher stirring intensity in the ladle, probably caused by the flat wall boundary condition. With higher stirring, there is a higher probability of collision between inclusions and the capturing top surface.
- Simple condition for inclusion capture. Since every inclusion which touched the top surface was captured, even the ones with high velocities, the PRI was overestimated.

The transient calculation of the flow field with simultaneous calculation of the inclusions trajectory was found to be more appropriate than the segregated approach of first calculating the steady-state flow field and then later calculating the inclusions motion. At first, it was expected that the steady-state calculation would be significantly faster. However that was not the case, since very low under-relaxation factors were necessary to avoid divergence in the calculations. Considering that to solve a two-phase flow through the Eulerian model, six strongly coupled momentum equations need to be solved until convergence, against three for the VOF model, the consequence is that the computational demand for the Eulerian model is much higher than that for the VOF model. Moreover, by using the SIMPLE scheme for pressure-velocity coupling, as it was done in the present work, there is not a reference of the physical time elapsed since the beginning of the calculations. The transient calculation was found to be more convenient and not significantly more computationally intensive, since it was not necessary to judge whether the flow was fully developed or not. The simulation would just run for the purging time to be studied, regardless of the flow development stage at the end of the computations. Therefore, the transient approach would be the most recommended, regardless of the other modeling choices.

As for the multiphase model choice, the VOF model results matched better with the experimental data. This suggests that it is very important to account for the free surface influence on the flow, especially since it was observed that its effects cause overall lower velocities in the ladle, which has a direct impact on the inclusion’s motion. Nevertheless, there are limitations in this approach, most importantly in how it handles the interaction between the different phases. The VOF model is better suited for modeling of the free surface, not for modeling of disperse phases such as the bubbles. Since the VOF model lacks the option of including non-drag forces in the computations, the resulting plume is much thinner than it should be. This could have a negative impact on the flow pattern calculation and, consequently, on the inclusion removal results. Therefore, in a straight comparison between the two multiphase models studied, the VOF would be the better choice, however a more comprehensive modeling approach which encompasses both an appropriate model for the disperse phases and for the free surface would be the most recommended. A suggestion would be the Multi Fluid VOF model, which is a variant of the Eulerian model available in ANSYS Fluent. A coupled DPM for the bubbles together with the VOF model for the free surface could also be a more suitable choice.

The boundary condition for the inclusions at the top surface was also found to be very significant for the prediction of the effectiveness of the purging treatments. In the first simulations run in the present work, it was concluded that a simple criterion would not be enough to represent the behavior of the inclusions at the top surface. Considering the simple criteria available in ANSYS Fluent for the inclusion behavior at the top surface, there are two main types:

a) If a zero restitution coefficient is set for the inclusions, then they lose all their momentum as they collide with the top surface, being regarded as captured and then removed from further computations.

b) If any value higher than zero is set for the restitution coefficient, the inclusions rebound as they collide with the top surface, and their velocity after the collision is calculated by the restitution coefficient. Regardless of the value chosen for the restitution coefficient, the inclusions return to the bulk flow and are dispersed by the effect of the flow velocities and turbulence.

Neither of these two criteria provided good results. The first caused an overestimation of the inclusion removal, since even in areas with exceptionally high turbulence, such as in the plume spout, the inclusions would be captured. Worse than that, these areas would even show a higher capture ratio, since the probability of collisions between the inclusions and the top surface would be higher in these locations. On the other side, the second criterion caused the purging treatments to be completely ineffective, since the gas purging would have only the effect of homogenizing the inclusions in the entire ladle, reverting any flotation effects. If an absolute no attachment was considered in the model, all gas purging configurations would show a negative PRI, meaning that it would be better to just leave the system to rest for some time than to adopt a purging treatment. Such a behavior goes against the experimental results by Silva[2] and also against the reported results by other authors[35,36,37,39], all of which reporting that gas purging treatments are beneficial regarding inclusion removal. Therefore, the behavior induced by the second criterion was also regarded as incorrect.

From the results mentioned above, it was found that the correct behavior of the inclusions at the interface would be something in between the two simple criteria described. Some inclusions which touched the top surface would remain attached due to some mechanism not clear in the present work, even in a water/air system, but not all of them. Therefore, in order to assess the results considering an intermediate capture criterion, an arbitrary capture criterion was developed and implemented through an UDF. It was defined that only the inclusions which touched the surface at a low velocity (arbitrarily defined as less than 0.1 m/s) would remain attached to the top surface. The other inclusions would rebound and return to the bulk flow.

The custom capture criterion, when applied to the Eulerian Flat Surface model, had an effect of closing the gap between the PRIs of the intermediate and higher purging rates (5 and 10 NL/min). This indicates that, under the higher flow rate, the higher stirring and turbulence contributed to the higher PRI obtained, most likely overestimated. The custom capture criterion was also applied to the VOF model. It resulted in an modest increase of the PRI as the gas flow rate was increased. Such behavior had a reasonable match with the experimental data and with other results from the literature. Although there is a need for further development of the inclusion capture criterion, the custom criterion defined in the present work has shown satisfactory results.

Finally, there was the teeming model. When no inclusion capture effects where considered in the model, this stage was found to not have any significant influence in the final PRIs obtained, since even the inclusions at the upper part of the ladle would be sucked into the nozzle eventually, even before air aspiration occurred. On the other side, when an UDF was applied to remove the inclusions at the interface from the computations (simulating absorption by a real slag and also a supposed interfacial force possibly acting in the experiments), then the teeming stage influenced the final PRI results. This influence was not clearly in the direction of increasing neither decreasing the PRI, since the UDF enhanced inclusion removal for all cases, including the reference case with no purging. Also worth of mention is the fact that the adoption of the UDF caused the inclusion counting curve to look more alike the curve obtained in the experiments. Although the behavior seen in the experimental curves could be questioned regarding why the curves would have a higher slope at the start and especially regarding the low overall inclusion counting, they are still the only available source of validation of the model developed in the present work. Consequently, it leads to the conclusion that the teeming model results were improved by the addition of the inclusion capture UDF.

The developed mathematical model was applied in the evaluation of the effect of two purging process parameters: gas flow rate and time duration of the purging treatment. For the parameters ranges considered in the present work, both variables were found to have a positive relationship with the effectiveness of the purging treatment, meaning that the higher the purging flow rate and time duration of the treatment, the higher would be the PRI. The observed trends also showed that for higher flow rates and purging times, further increases in these variables showed a progressively lower increase in the PRI.

The PRI was found to be more sensitive to the time duration of the purging treatment than to the adopted gas flow rate. It can be seen in Figure 5.54 in Section 5.4.2. that for every 20 seconds of increase in the purging treatment time duration, the PRI increased by approximately 15% for the lower times (from 0 to 20 seconds and from 20 to 40 seconds of treatment) and 10% for the longer times (from 40 to 60 seconds and from 60 to 80 seconds). When a similar analysis is performed for the gas flow rate, it can be seen from Table 5.14 that when the gas purging rate is increased from 2 to 5 NL/min, the PRI increases about 7.6%, and when it is increased from 5 to 10 NL/min, the PRI increases 4.0%. It should also be kept in mind that it is more risky to increase the gas flow rate than to increase the time duration of the treatment, taking into account that with a higher gas flow rate, there is more turbulence in the upper part of the ladle, which could cause open eye and slag entrainment in a real industrial ladle. If such deleterious effects were to happen, any gains provided by the purging treatment would immediately be lost due to steel reoxidation and/or dragging of inclusions from the slag into the molten steel.

Therefore, the recommendation that can be obtained from the present work regarding the application of gas purging treatments in real industrial ladles is that the gas flow rate should be kept in a low to moderate range, while the time duration of the treatment should be as high as the process would allow. Converting the values considered in the present work to the equivalent values in a real industrial ladle, for a 150-ton ladle, the recommended purging rate would be between 35 and 87 NL/min and the recommended duration of the purging treatment would be at least 3 minutes, with a tendency of even better results under longer treatment times.

7. RECOMENDAÇÕES PARA TRABALHOS FUTUROS

- O tratamento de rinsagem recomendado no presente trabalho deve ser testado em uma panela industrial real e o número de inclusões no produto final deve ser comparado com e sem o tratamento de rinsagem. Um procedimento sugerido para validar as previsões do modelo na panela industrial seria coletar amostras do aço líquido em diferentes locais e tempos de processo e avaliar a quantidade de inclusões em cada uma das amostras. Estas podem ser: uma amostra da panela antes do tratamento de rinsagem, outra amostra da panela após o tratamento de rinsagem e finalmente uma amostra no distribuidor. Para minimizar os desvios estatísticos entre as diferentes corridas, a coleta de dados deve ser realizada em várias corridas diferentes.

- Um critério mais elaborado para remoção de inclusão deve ser desenvolvido. Como o comportamento de inclusão na interface é muito complexo, sugere-se que estudos futuros sejam realizados com foco nos aspectos fundamentais do comportamento das inclusões na interface. Isolando os fenômenos de interface e estreitando o escopo do estudo sobre a física fundamental da aderência e separação de inclusões na interface, será possível desenvolver um critério melhor para remoção de inclusão.

- O modelo matemático deve ser validado quanto ao padrão de fluxo, com medidas experimentais de velocidade. Somente comparando os resultados do PRI, não é possível realizar uma validação rigorosa do modelo.

- Um modelo matemático deve ser desenvolvido usando abordagens que representem corretamente a dispersão da pluma de gás e a superfície livre ao mesmo tempo. Recomendações possíveis seriam o modelo Multi-Fluid VOF ou um modelo DPM (para as bolhas) + VOF (para a superfície livre).

7. RECOMMENDATIONS FOR FUTURE WORK

- The purging treatment recommended in the present work should be tested in a real industrial ladle and the number of inclusions in the final product should be compared with and without the purging treatment. A suggested procedure to validate the model predictions in the industrial ladle would be to collect samples of the molten steel at different locations and process times and evaluate the amount of inclusions in each of the samples. These could be: one sample from the ladle before the purging treatment, another sample from the ladle after the purging treatment and finally one sample in the tundish. In order to minimize statistical deviations between different heats, the data collection should be performed in several different heats.

- A more elaborate criterion for inclusion removal should be developed. Since the inclusion behavior at the interface is very complex, it is suggested that future studies should be performed with focus on the fundamental aspects of the behavior of inclusions at the interface. By isolating the interface phenomena and narrowing the scope of the study on the fundamental physics of inclusion attachment and detachment from the interface, it will be possible to develop a better criterion for inclusion removal.

- The mathematical model should be validated regarding the flow pattern, with experimental measures of velocity. Only by comparing the PRI results, it is not possible to conduct a rigorous validation of the model.

- A mathematical model should be developed using approaches which represent correctly the gas plume dispersion and the free surface at the same time. Possible recommendations would be the Multi-Fluid VOF model or a DPM model (for the bubbles) + VOF model (for the free surface).

8. REFERENCES

[1]Worldsteel Association, London. SRO-2017; Short Range Outlook. London, April, 2017. 4p.

[2] P.H.Silva. *Análise da remoção de inclusões do aço durante o esgotamento da panela após injeção de gás inerte através de modelamento físico.* Belo Horizonte: Escola de Engenharia da UFMG, 2018. 120p. (Dissertação de Mestrado, Engenharia Metalúrgica).

[3]A.Ghosh. *Secondary Steelmaking Principles and Applications.* CRC Press, 2001. 344p.

[4]L.Holappa. *Secondary Steelmaking.* In: S.Seetharaman. *Treatise on Process Metallurgy*; Industrial Processes. Oxford, UK: Elsevier, 2014. Volume 3, Chapter 1.6, p301-345.

[5]L.Zhang and W.Pluschkell. *Nucleation and growth kinetics of inclusions during liquid steel deoxidation.* Ironmaking and Steelmaking. Vol.30 (2). 2003 p106-110.

[6]E.T.Turkdogan. *Fundamentals of Steelmaking.* London, The Institute of Materials, 1996. Chapter 9.

[7]M.Iguchi et al. *The Flow Field in Air-Water Vertical Bubbling Jets in a Cylindrical Vessel.* ISIJ International. Vol.31. No.3. 1991. P-246-253.

[8]M.Iguchi et al. *Bubble Characteristics in the Buoyancy Region of a Vertical Bubbling Jet.* ISIJ International. Vol.32. No.6. 1992. P747-754.

[9]Y.Xie et al. *Behaviour of Bubbles at Gas Blowing into Liquid Wood's Metal.* ISIJ International. Vol.32. No.1. 1992. p66-75.

[10]Y..Y.Sheng and G.A.Irons. *Measurements of the Internal Structure of Gas-Liquid Plumes.* Metallurgical Transactions B. Vol. 23B. December 1992. P779-788.

[11]V.Sahajwalla, A.H.Castillejos and J.K.Brimacombe. *The spout of air jets upwardly injected into a Water Bath.* Metallurgical Transactions B. Vol. 21B. February 1990. P-71-80.

[12]P.E.Anagbo and J.K.Brimacombe. *Plume Characteristics and Liquid Circulation in Gas Injection through a Porous Plug.* Metallurgical Transactions B. Vol. 21B. August 1990. P637-648.

[13]D.Mazumdar and R.I.L.Guthrie. *The Physical and Mathematical Modelling of Gas Stirred Ladle Systems.* ISIJ International. Vol.35. 1995. P1-20.

[14]D.Mazumdar, H.Nakajima and R.I.L.Guthrie. *Possible Roles of Upper Slag Phases on the Fluid Dynamics of Gas Stirred Ladles.* Metallurgical Transactions B. Vol. 19B. June 1988. P507-511

[15]D.Mazumdar. *Modeling of Secondary Steelmaking Processes.* In: A. Ghosh. *Secondary Steelmaking Principles and Applications.* CRC Press, 2001. Chapter 11. P299-317.

[16]R.W.Fox and A.T.McDonald. *Introdução à Mecânica dos Fluidos.* LTC, 1998. Chapter 7. P227-247.

[17]D.Mazumdar. *Dynamic Similarity Considerations in Gas-Stirred Ladle Systems.* Metallurgical Transactions B. Vol.21B. 1990. P925-928.

[18]Y.Sahai and T.Emi. *Criteria for Water Modeling of Melt Flow and Inclusion Removal in Continuous Casting Tundishes.* ISIJ International. Vol.36. 1996. P1166-1173.

[19]K.Chattopadhyay, M.Isac and R.I.L.Guthrie. *Physical and Mathematical Modeling of Steelmaking Tundish Operations: A Review of the Last Decade (1999-2009).* ISIJ International. Vol.50. 2010. No. 3. P331-348

[20]S.V.Patankar. *Numerical Heat Transfer and Fluid Flow.* Hemisphere Publishing Corporation, 1980. 197p.

[21]R.P.Tavares. *Metalurgia Fenômenos de Transporte*. Departamento de Engenharia Metalúrgica e de Materiais, UFMG. 2002. 337p.

[22]H.K.Versteeg and W.Malalasekera. *An Introduction to Computational Fluid Dynamics.* 2nd Ed. Pearson Education Limited, UK. 2007. 503p.

[23]C.R.Maliska. *Transferência de Calor e Mecânica dos Fluidos Computacional.* 2nd Ed. LTC, BR. 2004. 453p.

[24]R.P.Tavares. Modelamento Témico e Fluido-Dinâmico Aplicado a Sistemas Metalúrgicos. *Turbulência.* Slides de Aula. 2017. 44p.

[25]H. Tennekes and J.L.Lumley. *Length Scales in Turbulent Flows.* In: *A First Course in Turbulence*; The MIT Press. Massachusetts, US, 1972. Chapter 1.5, p14-23.

[26]ANSYS, Release 16.2, Help System, *Standard, RNG and Realizable k-ε Models*, ANSYS, Inc., 2015.

[27]ANSYS, Release 16.2, Help System, *The Standard k-ω Model*, ANSYS, Inc., 2015.

[28]F.R.Menter. *Two-Equation Eddy-Viscosity Turbulence Models for Engineering Applications.* AIAA Journal. 1994. Vol.32, No.8. p1598-1605.

[29]ANSYS, Release 16.2, Help System, *The Euler-Lagrange Approach*, ANSYS, Inc., 2015.

[30]ANSYS, Release 16.2, Help System, *The Euler-Euler Approach*, ANSYS, Inc., 2015.

[31]D.Y.Sheng, M.Söder, P.Jönsson and L.Jonsson. *Modeling Micro-Inclusions Growth and Separation in Gas-Stirred Ladles.* Scandinavian Journal of Metallurgy. 2002; 31: p134-147.

[32]M.Söder, P.Jönsson and L.Jonsson. *Inclusion Growth and Removal in Gas-Stirred Ladles.* Steel Research International. 75. 2004. No.2. p128-138

[33]J.Aoki, L.Zhang and B.G.Thomas. *Modeling of Inclusion Removal in Ladle Refining.* 3rd International Congress on Science & Technology of Steelmaking, Charlotte, USA. May 9-11, 2005. Association for Iron & Steel Technology, Warrendale, PA. p319-322.

[34]L.T.Wang, Q.Y.Zhang, S.H.Peng and Z.B.Li. *Mathematical Model for Growth and Removal of Inclusion in a Multi-tuyere Ladle during Gas Stirring.* ISIJ International. Vol.45, 2005, No.3. p331-337.

[35]S.Zheng and M.Zhu. *Physical Modeling of Inclusion Behavior in Secondary Refining with Argon Blowing.* Steel Research International. 79. 2008. No.9. p685-690.

[36]M.Ek, L.Wu, P.Valentin and D.Sichen. *Effect of Inert Gas Flow Rate on Homogenization and Inclusion Removal in a Gas Stirred Ladle.* Steel Research International. 81. 2010. No.12. p1056-1063.

[37]T.Qu, M.Jiang, C.Liu and Y.Komizo. *Transient Flow and Inclusion Removal in Gas Stirred Ladle during Teeming Process.* Steel Research International. 81. 2010. No.6. p434-445.

[38]A.M.F. Marins. Modelagem física e computacional do fluxo de aço em panela com agitação por gás inerte, com ênfase na separação de inclusões. Ouro Preto: Escola de Minas da Universidade Federal de Ouro Preto, 2011. 94p. (Dissertação de Mestrado, Rede Temática em Engenharia de Materiais).

[39]W.Lou and M.Zhu. *Numerical Simulations of Inclusion Behavior in Gas-Stirred Ladles.* Metallurgical and Materials Transactions B. Vol. 44B. 2013. p762-782.

[40]J.Bellot, V. De Felice, B.Dussoubs, A.Jardy and S.Hans. *Coupling of CFD and PBE Calculations to Simulate the Behavior of an Inclusion Population in a Gas-Stirring Ladle.* Metallurgical and Materials Transactions B. Vol. 45B. 2014. P13-21.

[41]A. Sá. Comportamento escória/metal em panela de refino de aço agitado por borbulhamento de gás inerte. Ouro Preto: Escola de Minas da Universidade Federal de Ouro Preto, 2015. 70p. (Dissertação de Mestrado, Rede Temática em Engenharia de Materiais).

[42]Y.Liu, M.Ersson, H.Liu, P.Jönsson and Y.Gan. *A Review of Physical and Numerical Approaches for the Study of Gas Stirring in Ladle Metallurgy.* Metallurgical and Materials Transactions B. November 2018. Published Online.

[43]P.H.Silva, T.Cardoso, A.Mendonça, A.A.Nascimento; R.Tavares. *Estudo da remoção de inclusões por injeção de gás inerte na panela por meio de modelamento físico*. In: ABM Week, 2015, Rio de Janeiro. Anais da ABM Week. São Paulo: Associação Brasileira de Metalurgia e Materiais, 2015. p. 1-10.

[44]P.H.Silva. *Estudo de remoção de inclusões por injeção de gás inerte na panela na torre giratória.* Belo Horizonte: Escola de Engenharia da UFMG, 2014. 47p. (Trabalho de Conclusão de Curso, Bacharelado em Engenharia Metalúrgica).

[45]O.Simonin and P.L.Viollet. *Modeling of turbulent two-phase jets loaded with discrete particles.* Phenomena in Multiphase Flows. 1990. p.259-269.

[46]ANSYS, Release 16.2, Help System, *Particle Motion Theory*, ANSYS, Inc., 2015.

[47]ANSYS, Release 16.2, Help System, *Eulerian Model Theory*, ANSYS, Inc., 2015.

[48]P.H.Silva, D.Jesus, I.Camargo, R.Alves, R.Tavares. *Caracterização das bolhas na panela de aciaria por modelamento físico.* In: ABM Week, 2017, São Paulo. Anais da ABM Week. São Paulo: Associação Brasileira de Metalurgia e Materiais, 2017. P.195-206.

[49]ANSYS, Release 16.2, Help System, *Modeling Discrete Phase*, ANSYS, Inc., 2015.

[50]ANSYS, Release 16.2, Help System, *Volume of Fluid (VOF) Model Theory*, ANSYS, Inc., 2015.

[51]A. Chakraborty. *Development of an online aqueous particle sensor to study the performance of inclusions in a 12 tonne, delta shaped full scale water model tundish.* Montreal: Department of Mining and Material Engineering, McGill University, 2010. 94p. Master Thesis.

[52]ANSYS, Release 16.2, Help System, *Determining Mesh Quality*, ANSYS, Inc., 2015.